Theoretical Studies on Terahertz Quantum Cascade Lasers for Device Design Guideline

by

Teppei Miyoshi

A thesis
presented to the University of Waterloo
in fulfillment of the
thesis requirement for the degree of
Doctor of Philosophy
in
Electrical and Computer Engineering

Waterloo, Ontario, Canada, 2023

© Teppei Miyoshi 2023

Examining Committee Membership

Internal Member:	Hamed Majedi Professor, Department of Electrical and Computer Engineering, University of Waterloo
Internal Member:	Youngki Yoon Associate professor, Department of Electrical and Computer Engineering, University of Waterloo
Internal-External Member:	Jonathan Baugh Professor, Institute for Quantum Computing / Department of Chemistry, University of Waterloo
External Examiner:	Christian Jirauschek Professor, School of Computation, Information and Technology, Technical University of Munich, Germany

Author’s declaration

I hereby declare that I am the sole author of this thesis. This is a true copy of the thesis, including any required final revisions, as accepted by my examiners.

I understand that my thesis may be made electronically available to the public.

Abstract

Terahertz (THz) quantum cascade laser (QCL) is the most promising THz light source for the next-generation THz technologies of imaging, spectroscopy, and wireless communication. However, room-temperature operation of THz QCLs, which is necessary for these applications, has yet been demonstrated, and the record value of the highest operation temperature of THz QCLs remains 250K. Thus, this issue has been tackled theoretically and experimentally by many researchers and institutions around the world nowadays. In this thesis, three theoretical research topics related to device design guideline for high-performance devices are presented. (1) development of fast and accurate device simulator, (2) investigation of the influence of impurity doping on device performance, and (3) investigation of the influence of barrier height on device performance.

First, a fast and accurate device simulator is developed based on a rate equation model introduced by Razavipour. This development implements speed-up of the calculation of electron-electron scattering rate, careful selection of a screening effect model, introduction of theoretical models of pure dephasing time, optical linewidth, and a leakage current. In calculation, the developed device simulator can reproduce the device characteristics of previously published devices accurately, and the simulated highest operation temperature of previously published devices are reasonable compared to the experimental values.

Second, the influence of ionized impurities on device performance is investigated based on a two-well resonant-phonon THz QCL designed by Khalatpour *et al.* Seven doping conditions determined by doping positions and distributions and an undoped condition are

simulated over a range of sheet doping density from 1.0×10^{10} to $1.0\times10^{12}cm^{-2}$ for a single module. By this simulation, optical linewidth is found to be small in the undoped condition due to absence of ionized-impurity scattering, resulting in the highest optical gain among all doping patterns. Among doped conditions, wide doping in a phonon-well shows the highest optical gain, and this is attributed to mitigation of band-bending effect. Based on these results, a modulation doping scheme is proposed.

Lastly, the influence of barrier height on device performance of two-well resonant-phonon THz QCLs is investigated through two steps of research, and a series of comprehensive research discovers a new device design concept featured by a thick radiation barrier which is around 40Å (Type-B). Furthermore, around 15% of Al-composition is found to provide the optimal barrier height conditions for two-well resonant-phonon structures under both the conventional design (Type-A) and Type-B concepts in device structure exploration. The reason for this feature is clarified by careful analysis of calculation data, and the optimal conditions are found to happen by complex behavior of componential parameters of optical gain, which varys with barrier height.

Acknowledgements

I would like to show my deep appreciation to Dr. Dayan Ban, Dr. Zbigniew Wasilewski, and Dr. Safieddin Safavi-Naeini for their supervision on my Ph.D. research. I also would like to thank my Ph.D. committee members: Dr. Hamed Majedi, Dr. Youngki Yoon, Dr. Jonathan Baugh, and Dr. Christian Jirauschek for their referee on my thesis, fruitful discussion, their coursework, and encouragement.

Next, in the beginning of my theoretical work, I developed a simulation tool thanks to assistance of the other exceptional members of Photonics and Nanoelectronics Laboratory in the University of Waterloo: Dr. Ghasem Razavipour, Dr. Chao Xu, Ms. Cathy (Kai Xi) Wang, and Ms. Manesa Kaniselvan. I also would like to express my sincere gratitude to Dr. Saeed Fathololoumi in Intel., Dr. Emmanuel Dupont in National Research Council of Canada, Dr. Martin Alexander Kainz in TU Wien, Dr. Ali Khalatpour in Massachusetts Institute of Technology, and Dr. Martin Frankié in ETH Zürich. Their kind and helpful sharing of technical information enabled me to obtain a deeper consideration about physics of THz QCLs and to enhance the accuracy of my simulation tool. In the final year of my program, I fortunately had a chance to learn the way to fabricate THz QCLs in Institute of Physical and Chemical Research (RIKEN) in Japan. Where, I was inspired by Dr. Tsung-Tse Lin's deep understanding and wide knowledge about THz QCLs and his enthusiasm for high-performance devices. Learning professional works of the exceptional researchers above, their sincere effort toward research, and their philosophy as engineering researchers is the most precious experience in my research life in the University of Waterloo.

I believe that my Ph.D. study could not be accomplished without assistance by

people in other technical fields and the administration of the department of electrical and computer engineering in the University of Waterloo. So, I would like to extend my sincere thanks to Dr. Kankar Bhattacharya, Dr. Christopher Nielsen, Dr. Christopher Backhouse, Dr. Irene Goldthorpe, Dr. Alfred Yu, Ms. Jessica Rossi, Ms. Susan Widdifield, and Ms. Cassandra Brett. Lastly, most language errors in my writing documentations were corrected and brushed up by Ms. Mary McPherson in Writing Center of the University of Waterloo. Her thorough check over my journal articles, her clear instruction about English writing, and encouragement gave me confidence and joy for submission. I would like to offer my special thanks to her. In addition to the people in Waterloo, I would like to thank my former coworkers: Dr. Mitiko Miura-Mattauch, Dr. Tetsuo Tsutsui, Dr. Hideo Yamagishi, and Dr. Hiroshi Tomiyasu for giving me a chance to pursue Ph.D.

Lastly, during my long journey for Ph.D., I have shared precious time and experience with many invaluable people in Hiroshima University, Mitsubishi Chemical Corporation, International Language School Canada - Montréal, the University of Waterloo, and — around the World. I would like to express my deep gratitude to all the people forming my life.

October 25, 2022

Teppei Miyoshi

Dedication

To my grandfather

Table of Contents

List of Figures xiii

List of Tables xx

List of Abbreviations xxi

Chapter 1 Introduction 1

1.1 Background 1

1.1.1 Electromagnetic Wave and Our Society 1

1.1.2 Terahertz Applications 4

1.1.3 Terahertz Light Sources 11

1.2 Quantum Cascade Laser 14

1.2.1 Overview 14

1.2.2 Principle 18

1.3 Terahertz Quantum Cascade Laser 25

1.3.1 Overview 25

1.3.2 Simulation Method 30

1.3.3 Active Core Study 33

1.4 Research Objective and Thesis Organization 48

Chapter 2 Theory and Modeling 53

2.1 Overview 53

2.2 Schrödinger Equation **57**
2.2.1 Finite Difference Method 58
2.2.2 Band Non-Parabolicity Effect 61
2.2.3 Non-Linear Finite Difference Method 63
2.2.4 Comparison of Numerical Calculations 66

2.3 Incoherent Carrier Transport **68**
2.3.1 Fermi's Golden Rule 70
2.3.2 Ando's Theory 84
2.3.3 Screening Effect 88

2.4 Coherent Carrier Transport **93**
2.4.1 Tight-Binding Theory 94
2.4.2 First-Order Tunneling Current Theory 99

2.5 Rate Equation **104**
2.5.1 Intra-Module Carrier Transport 104
2.5.2 Inter-Module Carrier Transport 105
2.5.3 Solution of the Rate Equation 107

2.6 Electrical Current Theory **108**
2.6.1 Second-Order Tunneling Current Theory 108
2.6.2 Third-Order Tunneling Current Theory 111

2.7 Optical Parameters **122**
2.7.1 Oscillator Strength 122
2.7.2 Optical Gain 124

2.8 Auxiliary Physical Phenomena **126**
2.8.1 Self-Heating Theory 126
2.8.2 Energy-Balance Theory 129
2.8.3 Electron Temperature in Continuum States 132
2.8.4 Dopant Activation Rate 133
2.8.5 Dopant Distribution Model 135
2.8.6 Schrödinger-Poisson Equation System 137

2.9 Calculation Flow **139**

2.10 Calculation Examples **142**

2.10.1 High-Performance Two-Well Resonant-Phonon THz QCL 142

2.10.2 Prediction of the Highest Operation Temperature 146

Chapter 3 Doping Study **149**

3.1 Introduction **149**

3.2 Method **153**

3.2.1 The Influence of Impurity-Doping on Device Parameters 153

3.2.2 Examined Doing Patterns 157

3.3 Simulation **159**

3.3.1 Simulation Results 159

3.3.2 Doping Position Dependence 163

3.3.3 Doping Distribution Dependence 166

3.4 Discussion **171**

3.5 Summary and Conclusion **174**

Chapter 4 Barrier Height Study - Part I **177**

4.1 Introduction **177**

4.2 Method and Simulation Results **180**

4.2.1 Validation of the Third-Order Tunneling Current Model 180

4.2.2 The Influence of Barrier Height on Device Characteristics 187

4.3 Discussion **192**

4.4 Summary and Conclusion **196**

Chapter 5 Barrier Height Study - Part II 199

5.1 Introduction 199

5.2 Method 201

5.2.1 Methodology of Device Structure Exploration 206

5.2.2 Rate Equation – Limited Model... 220

5.3 Results and Discussion 225

5.3.1 Optical Gain Map 225

5.3.2 Device Design Concepts.. 229

5.3.3 High-Performance Device Design 231

5.3.4 Full Model Analysis 235

5.4 Summary and Conclusion 250

Chapter 6 Conclusion and Future Work............................ 253

6.1 Conclusion.. 253

6.2 Future Works 255

Reference 258

List of Figures

Figure. 1.1 Electromagnetic wave and applications in our society. All pictures are downloaded from web sites for free images or taken by the author. 3

Figure. 1.2 THz transmissive imaging examples. (a) A railway payment card [13]. (b) A dried shrimp [10]. (c) A leather suitcase including a knife and pens [15]. (d) A shoe [15]. (e) A stainless-steel plate (upper figures) and a rubber band, a plastic button, a clip, and a cutter knife blade in envelopes (bottom figures) [12]. 5

Figure. 1.3 THz spectroscopy examples. (a) A spectrum from an explosive (tri-nitro toluene) [17]. (b) A spectrum from inflammable liquids [23]. (c) A spectrum from saccharides [20]. (d) MDMA (left), aspirin (center), and methamphetamine (right) [19]. (e) Cancer tissues [24]. (f) Porcine tissues. An optical image (up-left) and a spectroscopic image (bottom-right) [28]. 7

Figure. 1.4 Atmospheric window [33]. 8

Figure. 1.5 Conceptual illustration of future networks with THz link in the space [32]. 9

Figure. 1.6 (a) THz emission from an LSI 8-bit microprocessor (red and blue indicate positive and negative amplitudes of THz light) [37]. (b) Transmission microscope images of a polymer. (b-1) without THz irradiation, (b-2) with THz irradiation [39]. 10

Figure. 1.7 THz-emission power and frequency of reported THz light sources [53] 13

Figure. 1.8 Classification of quantum cascade laser devices. 15

Figure. 1.9 A relation between the highest operation temperature and lasing frequency of MIR and THz QCLs. 17

Figure. 1.10 Progress of DFG THz QCLs in output power. (a wiggly line is a trend curve.) 17

Figure. 1.11 A band diagram and its E-k dispersion of heterojunction and different types of carrier transports. 18

Figure. 1.12 Band diagrams for sequential resonant tunneling (a, b) and photocurrent and voltage characteristics (c) [82]. In this experiment, carriers are optically injected. (a) Resonant tunneling between a ground state (E_1) and a first excited state (E_2). (b) Resonant tunneling between a ground state and a second excited state (E_3). (c) Photocurrent -voltage characteristics. 19

Figure. 1.13 band diagram of the first MIR QCL [57]. 'Digitally graded alloy' is an injection region in this figure. 21

Figure. 1.14 Optical transition of quantum cascade laser (left) and semiconductor laser (right) [83]. 22

Figure. 1.15 Waveguide structures of QCLs. (a) SISP waveguide, and (b) MM waveguide. 24

Figure. 1.16 The difference of carrier transition mechanisms between MIR and THz QCLs. 26
Figure. 1.17 Progress of THz QCL research. (a) Chronological improvement of the highest operation temperature. (b) Lasing frequency vs the highest operation temperature. (c) Lasing frequency vs output power (under low temperature and pulsation condition). (d) Lasing frequency vs threshold current. 29
Figure. 1.18 Carrier transport methods. (a) Chirped superlattice [61], (b) Interlaced [147], (c) Bound-to-Continuum [141], (d) Hybrid [162], (e) Five-well resonant-phonon [165], (f) Three-well resonant-phonon [107], (g) Double resonant-phonon [192], (h) Scattering assisted [112], (i) Phonon-Photon-Phonon [200], and (j) Ground state structure [203]. 38
Figure. 1.19 The number of subbands per module vs carrier use efficiency. [111] 39
Figure. 1.20 The influence of barrier height [182]. 42
Figure. 1.21 Examples of structural complexity. (a) A stepped-well [212] (b) A split-well structure [210, 211]. (c) Different height of barriers [208]. 44
Figure. 1.22 Thermal-degradation processes in THz QCLs. ①Thermally activated LO-phonon scattering, ② Thermal backfilling, ③Leakage to high energy states, and ④Leakage to continuum states. 47
Figure. 1.23 Outline of this thesis 51
Figure. 2.1 Carrier transport considered in the rate equation model. 54
Figure. 2.2 Device parameters and a brief calculation procedure of the rate equation. For Hartree potential, electron temperature, and lattice temperature, iterative calculation is necessary. 56
Figure. 2.3 Comparison of calculated eigen-energy 67
Figure. 2.4 Incoherent carrier transport and related device parameters. 69
Figure. 2.5 A brief idea of a relation between scattering rate and componential parameters. (a) A large overlap between a large wavefunction overlap and a cause phenomenon. (b) A large overlap between a small wavefunction overlap and a cause phenomenon. (c) A large overlap between an almost zero wavefunction overlap and a cause phenomenon. (d) A small overlap between a large wavefunction overlap and a cause phenomenon. 71
Figure. 2.6 Quantum states before and after the electron-electron scattering. 76
Figure. 2.7 Calculation results for the electron-electron scattering rate in an infinite square quantum well. (a) Inter-subband scattering rate W_{2211}, and (b) Calculation time. 80
Figure. 2.8 Conditions for the two-dimensional Lindhard theories and three-dimensional theories. 90
Figure. 2.9 An image of tight-binding condition (a) Delocalized condition, and (b) Tight-binding condition. 93
Figure. 2.10 Decomposition of potential 95
Figure. 2.11 Intra-module carrier transition. Blue arrows describe income, and red arrows describe outcome for subband 1. 105

Figure. 2.12 Inter-module carrier transition. Blue arrows describe income, and red arrows describe outcome for subband 1. 106
Figure. 2.13 Thermal distribution of subband carriers in the second-order tunneling current theory. (a)$\hbar\Delta_{LR}\geq$ 0, and (b) $\hbar\Delta_{LR}<0$. 110
Figure. 2.14 Carrier leakage and tunneling paths from one subband in a quantum well. 111
Figure. 2.15 Electron tunneling to a triangle potential. 112
Figure. 2.16 Local potential barrier for leakage carriers. 113
Figure. 2.17 Comparison of thermally distributed electrons used for different theories of tunneling current. (a) First-order tunneling theory, (b) Second-order tunneling theory, and (c) Third-order tunneling theory. The carriers' thermal distribution shown in blue is applied to the tunneling current equation, and that shown in red contribute to the leakage current. 115
Figure. 2.18 Images for device parameters for optical gain. (a) Lorentzian function, and (b) the dependence of optical gain on electrical field. 125
Figure. 2.19 Heat flow from a QCL chip. A blue part is a QCL mesa structure, and a grey part is a GaAs-substrate. 128
Figure. 2.20 The self-consistent loop calculation for the electron temperature. 130
Figure. 2.21 Calculation flow for the electron temperature. $T_{conv.}$. Denotes a convergent temperature. 131
Figure. 2.22 Band diagram of n-type semiconductor with the donor level. 134
Figure. 2.23 Doping distributions. (a) Rectangular doping. (b) δ-doping. 136
Figure. 2.24 Calculation flowchart with self-consistent loop. 140
Figure. 2.25 Calculation flowchart without self-consistent loop (adopted in this work). 141
Figure. 2.26 A two-well resonant-phonon structure (G652). 143
Figure. 2.27 Calculation results of G652. (a) J-V characteristics. Experimental data was taken at 10K. (b) Population fraction calculated by the rate equation. (c) Tunneling component of population fraction. (d) Leakage component of population fraction. 144
Figure. 2.28 Scattering rate between main subbands. In this calculation, electron temperature of each subband is individually calculated and shows abrupt change to electrical field. That change influence the current density and appears as small dents. 145
Figure. 2.29 Comparison in the highest operation temperature between simulation and experiment. 147
Figure. 3.1 The influence of impurity doping on device parameters in theory. The parameters directly influenced by doping are described by red boxes. Indirect influence is described by blue boxes. Some parameters are affected both directly and indirectly. In calculation, three-dimensional doping profiles are determined based on sheet doping density. 154

Figure. 3.2 The influence of doping position on the ionized-impurity scattering rate and optical linewidth in a double-quantum-well. (a) Different doping positions. (b) The ionized-impurity scattering rate. (c) Optical linewidth due to ionized-impurity scattering. In all doping positions, 20Å-rectangular doping is assumed. 156
Figure. 3.3 A two-well resonant-phonon structure in the tight-binding condition and eight examined doping patterns. The layer thicknesses of the simulated structure are fixed as 33.5/72.0/18.5/145.0 in Å (Bold = barrier). Segregation is considered only in Pattern E. 158
Figure. 3.4 The dependence of optical gain peak on sheet doping/carrier density. (a) Narrow-rectangular doping patterns (A~D), (b) Other doping patterns (E~G), (c) Undoped pattern (H). The thick dots are optical gain peaks abstracted from the gain-filed characteristics for each sheet doping/carrier density, and wiggly lines are trend curves. In (c), the calculation result of pattern A is inserted as a reference with sheet doping density, and sheet carrier density, assumed to be injected from external modules, is swept as a variable for pattern H instead of constant sheet doping density (2.69×10^{8} cm^{-2}). 161
Figure. 3.5 The dependence of electrical current density on sheet doping/carrier density. (a) Narrow-rectangular doping patterns (A~D), (b) Other doping patterns (E~H). The plotted data are abstracted at the gain peak conditions. In (b), x-axis describes carrier density for pattern H and sheet doping density for others. 162
Figure. 3.6 The dependence of lasing frequency on sheet doping/carrier density. (a) Narrow-rectangular doping patterns (A~D), (b) Other doping patterns (E~H). The plotted data are abstracted at the gain peak conditions. In (b), x-axis describes carrier density for pattern H and sheet doping density for others. . 162
Figure. 3.7 The dependence of componential parameters and carrier transition rates on sheet doping density (A~D). (a) Oscillator strength. (b) Population inversion. (c) Optical linewidth. (d) Tunneling injection rate. (e) Non-radiative scattering rate. (f) Carrier extraction rate. The plotted data are abstracted at the gain peak conditions. 165
Figure. 3.8 The dependence of componential parameters and carrier transition rates on sheet doping/carrier density (E~H). (a) Oscillator strength. (b) Population inversion. (c) Optical linewidth. (d) Tunneling injection rate. (e) Non-radiative scattering rate. (f) Carrier extraction rate. The plotted data are abstracted at the gain peak conditions. The x-axis describes sheet carrier density for the condition (H). 168
Figure. 3.9 Potential profile including band-bending effect with $2.0\times10^{11}cm^{-2}$ at 25kV/cm. (a) Rectangular-doping. (b) Homogeneous-doping. (c) Undoped condition. Black dotted lines describe a flat potential (no band-bending), and colored solid lines describe the total potential. 169
Figure. 3.10 A proposed doping pattern for a single module. 171
Figure. 3.11 The modulated doping scheme. The magnitude of doping period toward the structural period is

described by NDP. For example, when all modules are doped, NDP = 1. When impurities are doped every two modules, it is described as NDP = 2. 173

Figure. 4.1 Band diagrams of two-well resonant-phonon THz QCLs in tight-binding condition. (a) Low-barrier device (TW246), (b) Middle-barrier device (EV2624), and (c) High-barrier device (G652). ... 179

Figure. 4.2 J-V characteristics. (a) Low-barrier device (TW246). (b) Middle-barrier device (EV2624). (c) High-barrier device (G652). 182

Figure. 4.3 Difference in resonant tunneling transport model between the rate equation and actual devices or the NEGF calculation. (a) a condition in the rate equation, and (b) in actual devices or the NEGF. 184

Figure. 4.4 Calculated temperature dependence. (a) Leakage current density. (b) Optical gain peak. The data are taken when optical gain peaks. 184

Figure. 4.5 Two-well resonant-phonon structure for barrier height study (A phonon-well + one module). The layer thicknesses are fixed as 33.5/72.0/18.5/145.0 in Å. (Bold = barrier, underline = doping)......... 187

Figure. 4.6 Barrier height (Al-composition) dependence in simulation. (a) Electrical current density, (b) Optical gain peak and population inversion $\Delta\rho_{32}$, (c) Population fraction, (d) Scattering rate between lasing states, (e) Optical linewidth between lasing states. In (c), $\rho_{parasite}$ is the sum of population fractions for all parasite subbands. In (d), Total = LO + IFR + IMP + AD + EE. Dot-lines indicate trend curves. 188

Figure. 4.7 Major carrier transition and population fraction. A unit of transition rate is 1/s. (a) Low barrier device (x = 15%), (b) High barrier device (x = 45%). The sum of population fraction of all parasite states is smaller than 1% in both cases, and their occupancy is not described. 194

Figure. 4.8 Population fraction without electrical field. 195

Figure. 5.1 A basic structure of a two-well resonant-phonon terahertz quantum cascade laser and design parameters. 201

Figure. 5.2 Variations of two-well resonant-phonon structures. 205

Figure. 5.3 The coupling energy between the ground-states of two coupled quantum-wells. (Solid line = coupling energy, Dashed line = detuning energy) [263]. 209

Figure. 5.4 Thermally averaged LO-phonon scattering rate versus subband energy difference in a 200Å-wide single quantum well structure [59]. Subband number 1 and 2 in this figure corresponds to a ground state and the first excited state of the 200Å-wide single quantum well. 211

Figure. 5.5 An image picture of condition screening process by true-false tables in a MATLAB program. Images ②, ③, ④ correspond to the screening conditions shown in the previous page. 212

Figure. 5.6 How to make an optical gain map. Conditions in black parts do not have optical gain peaks. In other parts, thicker colors mean higher optical gain. 213

Figure. 5.7 The relation between optical gain and design parameters. (a) Collection-well thickness dependence, (b) radiation-barrier thickness dependence, and (c) phonon-well thickness dependence.. 216
Figure. 5.8 A sketched image of Rough search and Fine search. ... 217
Figure. 5.9 Device structure exploration procedure – Part A. ... 218
Figure. 5.10 Device structure exploration procedure – Part B. ... 219
Figure. 5.11 Comparison between the rate equation – full model and – limited model in the dependence of optical gain on the heat-sink temperature. ... 222
Figure. 5.12 doping condition and electrical field conditions in device structure exploration. ... 223
Figure. 5.13 Difference of calculation procedures. ρ_n and V_H denote population fraction of a subband n and Hartree potential, respectively. ... 224
Figure. 5.14 Optical gain map of two-well resonant-phonon terahertz quantum cascade lasers by Rate equation – Limited model. ... 227
Figure. 5.15 Band diagrams of two types of devices. (20% of Al-composition under tight-binding condition.) (a) Type-A: 28/73.5/17.5/153 in Å (b) Type-B: 29/37.5/39.5/77.5 (Bold = barrier, underline = doping.). ... 229
Figure. 5.16 A relation between optical gain and lasing frequency in explored devices. ... 232
Figure. 5.17 The Al-composition dependence of design parameters. (a) Injection-barrier, (b) collection-well, (c) radiation-barrier, (d) phonon-well, (e) one period length, and (f) alignment field. ... 233
Figure. 5.18 The Al-composition dependence of optical gain maxima. ... 238
Figure. 5.19 The Al-composition dependence of electrical current at gain peak conditions. ... 239
Figure. 5.20 The Al-composition dependence of population fraction at gain peak conditions. $\rho_{parasite} = \rho_4 + \rho_5 + \rho_6 + \cdots$ ... 240
Figure. 5.21 The Al-composition dependence of componential parameters of thin injection-barrier devices at gain peak conditions. (▲= Type-A, ● = Type-B) (a) Oscillator strength, (b) population inversion, (c) optical linewidth, (d) carrier injection rate to ULS, (e) non-radiative scattering rate between lasing states, and (f) carrier extraction rate from LLS. ... 244
Figure. 5.22 The Al-composition dependence of optical gain maxima. ... 247
Figure. 5.23 The Al-composition dependence of electrical current at gain peak conditions calculated by the rate equation – full model. ... 248
Figure. 5.24 The Al-composition dependence of population fraction at gain peak conditions. $\rho_{parasite} = \rho_4 + \rho_5 + \rho_6 + \cdots$ ... 248
Figure. 5.25 The Al-composition dependence of componential parameters of thick injection-barrier devices at gain peak conditions. (▲= Type-A, ● = Type-B) (a) Oscillator strength, (b) population inversion, (c)

optical linewidth, (d) carrier injection rate to ULS, (e) non-radiative scattering rate between lasing states, and (f) carrier extraction rate from LLS.. 249

Figure. 6.1 Ideas of carrier transport by two subbands. (a) a ground state is used as ULS, and (b) a ground state is used as LLS.. 257

List of Tables

Table.1.1 Comparison of different material systems in conduction band offset and the highest operation temperature. 40
Table. 2.1 Calculation models for Schrödinger equation and calculation speed. 67
Table. 2.2 Screening effect models. 90
Table. 3.1 Previous doping studies of THz QCLs. (*Injection barriers are composed of $Al_{0.45}Ga_{0.55}As$, and phonon-wells are split.) 152
Table. 4.1 Device information for examined two-well resonant-phonon THz QCLs. (*Estimated in this work.) 181
Table. 4.2 Calculated device parameters at optical gain peak (T_{HS} = 200K). 190
Table. 5.1 Comparison of the rate equation – Full model and – Limited model. *A screening effect model is considered. 220
Table. 5.2 Features of device design concepts type -A and -B. 231
Table. 5.3 Device structures of high-performance THz-QCLs with a thin injection-barrier. 237
Table. 5.4 Device structures of high-performance THz-QCLs composed of thick injection-barrier. 246

List of Abbreviations

AD	Alloy-disorder
B-to-C	Bound-to-continuum
CW	Continuous wave
C.B.	Conduction band
DFB	Distributed feedback
DFG	Difference frequency generation
DM	Density matrix
EC	External cavity
EE	Electron-electron
EM	Electromagnetic
FD	Fermi-Dirac
FP	Fabry-Perot
FT-IR	Fourier transform infrared spectroscopy
FWHM	Full width half maximum
GHz	Gigahertz
IC	Integrated circuit
ICL	Interband cascade laser
IMPATT	Impact ionization avalanche transit-time diode
IDP	Indirectly pumped
IFR	Interface-roughness
IMP	Ionized-impurity
LA	Longitudinal acoustic
LLS	Lower lasing state
LO	Longitudinal optical
LTEM	Laser terahertz emission microscope
MBE	Molecular beam epitaxy

MC	Monte-Carlo
MIR	Mid-infrared
MM	Metal-metal
MOCVD	Metal organic chemical vapor deposition
NDR	Negative Differential Resistance
NEGF	Non-equilibrium green function
PD	Photodiode
PhC	Photonic crystal
QCL	Quantum cascade laser
QW	Quantum well
RE	Rate equation
RP	Resonant-phonon
RPA	random-phase-approximation
RT	Room-temperature
RTD	Resonant tunneling diode
SA	Scattering assisted
SE	Surface emitting
SISP	Semi-insulating surface-plasmon
THz	Terahertz
TO	Transverse optical
TUNNET	Tunnel injection transit time diode
ULS	Upper lasing state
UTC	Uni-travelling-carrier
V.B.	Valence band
WKB	Wentzel-Kramers-Brillouin
YAG	Yttrium Aluminum Garnet

When life seems hard, the courageous do not lie down and accept defeat; instead, they are all the more determined to struggle for a better future.

– Queen Elizabeth II

Chapter 1 Introduction

1.1 Background

The goal of this study — room-temperature operation of terahertz (THz) quantum cascade lasers (QCLs) — is one of the many research topics in development of terahertz light sources and advancement of quantum optoelectronics. To clarify the position of this work in such a large stream of research and development, the backgrounds behind this work in our society and technical fields of electromagnetic (EM) waves will be briefly introduced in this section. Following that, previous studies, fundamental physics, and device driving mechanisms of general QCLs are presented in Section 1.2. Based on previous THz QCL research, a two-well resonant-phonon device is selected as a base device structure for the works in Chapter 3~5. In Section 1.3, the progress of THz research and technical issues required to be resolved for room-temperature operation are described. Finally, the outline of this thesis is explained in Section 1.4 with objectives and summaries of each chapter.

1.1.1 Electromagnetic Wave and Our Society

It is no exaggeration that our society has been advanced by development of the EM wave technologies. The EM wave was theoretically proposed by Maxwell in 1864 and demonstrated by Hertz in 1888. After that, during approximately 130 years – when the human

society experienced rapid industrialization and two World Wars – academic fields of optics, electromagnetics, and quantum physics established the EM wave theories independently or mutually. Simultaneously, applied techniques were developed and commercialized in industry. Thanks to profits of such technological advancement, our life has become drastically enriched [1, 2].

Even though 'the EM wave technique' often means the information-and-communication technologies nowadays, this technology basically includes many kinds of electrical and/or optical products exploiting unique features of the EM waves to frequency or wavelength. On the one hand, for example, radio wave whose frequency is relatively low is advantageous for long-distance communication such as cell phones, TVs, radios, and so on because radio wave is less likely absorbed by the atmosphere (especially water vapor), and it is able to propagate diffractively even with obstacles. On the other hand, light wave whose frequency is high is not suitable for long-distance communication because it is attenuated by vapor and cannot divert obstacles. Despite such drawbacks, light has an advantage in sending a large amount of data rapidly in direct-and-short-distance communication. Rather high energy of light is also used for natural or industrial chemical reaction, infrared heaters, and ultraviolet disinfection systems. Furthermore, medical and security inspections exploits the X-rays or Γ-rays that can penetrate most substances due to high energy.

As described in Figure 1.1, around 100GHz to 10THz of the EM field frequency is called THz wave/light (GHz = 10^9Hz, and THz = 10^{12}Hz). THz light has been known well to have unique characteristics which are different from radio waves or light, and THz

applications such as transmissive imaging, spectroscopy, and wireless communication techniques has been expected to benefit many technical fields for advancement [3-8]. However, THz technologies has yet been prevailed in our society currently because of developmental delay of THz emission or detection devices. Therefore, THz light and the frequency range of it are also called ‘unexplored EM wave’ and ‘THz gap’, respectively [9]. The characteristics of THz light and THz applications will be introduced in the next subsection.

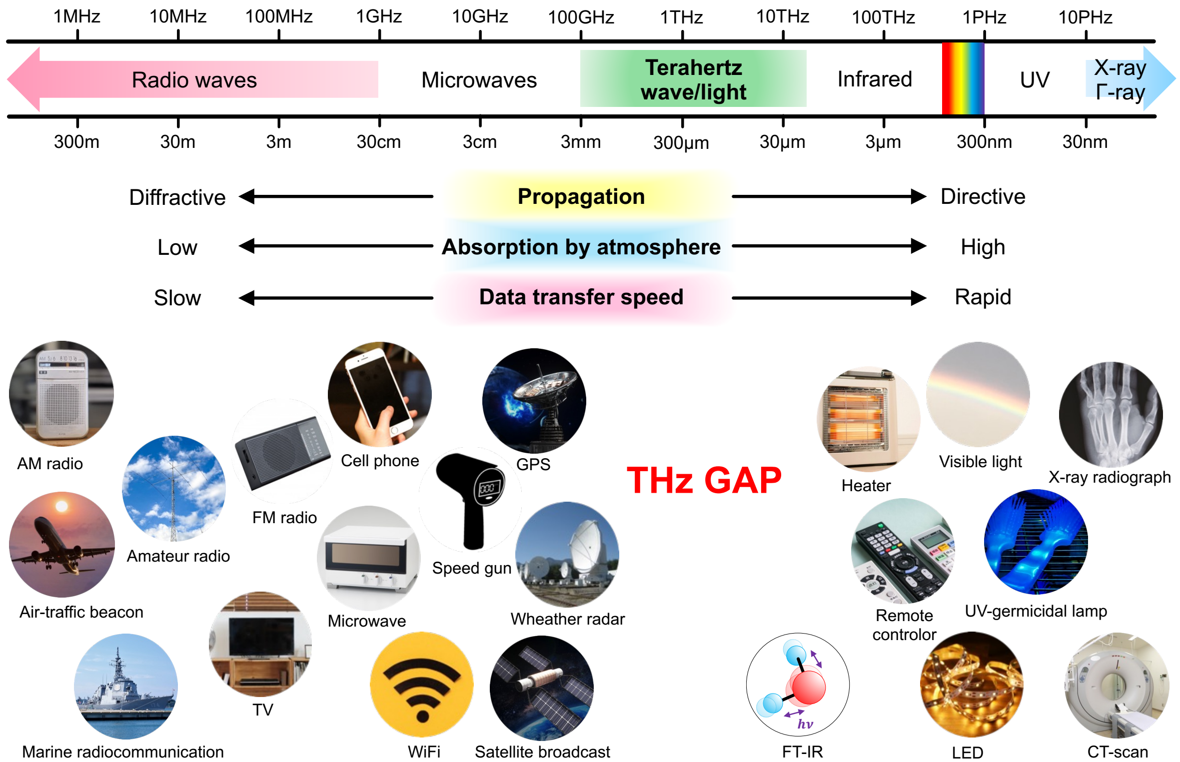

Figure. 1.1 Electromagnetic wave and applications in our society. All pictures are downloaded from web sites for free images or taken by the author.

1.1.2 Terahertz Applications

THz technologies have been expected to apply to transmissive imaging, spectroscopy, and wireless communication. Currently, these techniques using microwave or infrared light have already been prevailed in wide technical fields: arts, medical and pharmaceutical research, biotechnology, industry, architecture, agriculture, food, environment, communication and information, security/safety, space development, military defense, fundamental science, and engineering. Introduction of terahertz technologies is expected to evolve these existing techniques and enable more advanced development or a variety of inspection [3-39]. Not only these three THz applications but also other reported examples will be introduced in this subsection, and fundamental characteristics of THz light will also be explained together.

First of all, THz transmissive imaging will be introduced [10-15]. One of the unique characteristics of THz light is permeability to substances. As a natural feature, THz light can penetrate non-metal materials such as fabric, leather, wood, plastic, ceramics, and so on but is reflected by metal. So, THz transmissive imaging is suitable for non-contact and non-destructive inspection. For example, metal weapons concealed in leather or fabric bags, metal contamination in manufactured food, and electrical circuit in a plastic card [10, 11, 13, 15]. Even though such inspection is available even with the X-ray, the advantage of using THz light is safety for human body (non-invasiveness) because the energy of THz light is lower than the one of the X-ray. In addition, THz transmissive imaging is superior to the one using microwave in terms of spatial resolution. This is because spatial resolution is proportional to wavelength of light sources [9, 12]. Considering that special resolution of THz imaging is

around ten μm-order, we cannot use it for inspecting nano structures, but things in mm-order can be inspected with high quality by it. One of the demerits of THz light, easily absorbed by water vapor, turns to be an advantage for crop inspection in agriculture [9]. Non-destructive inspection of cultural assets such as paintings was also reported [14].

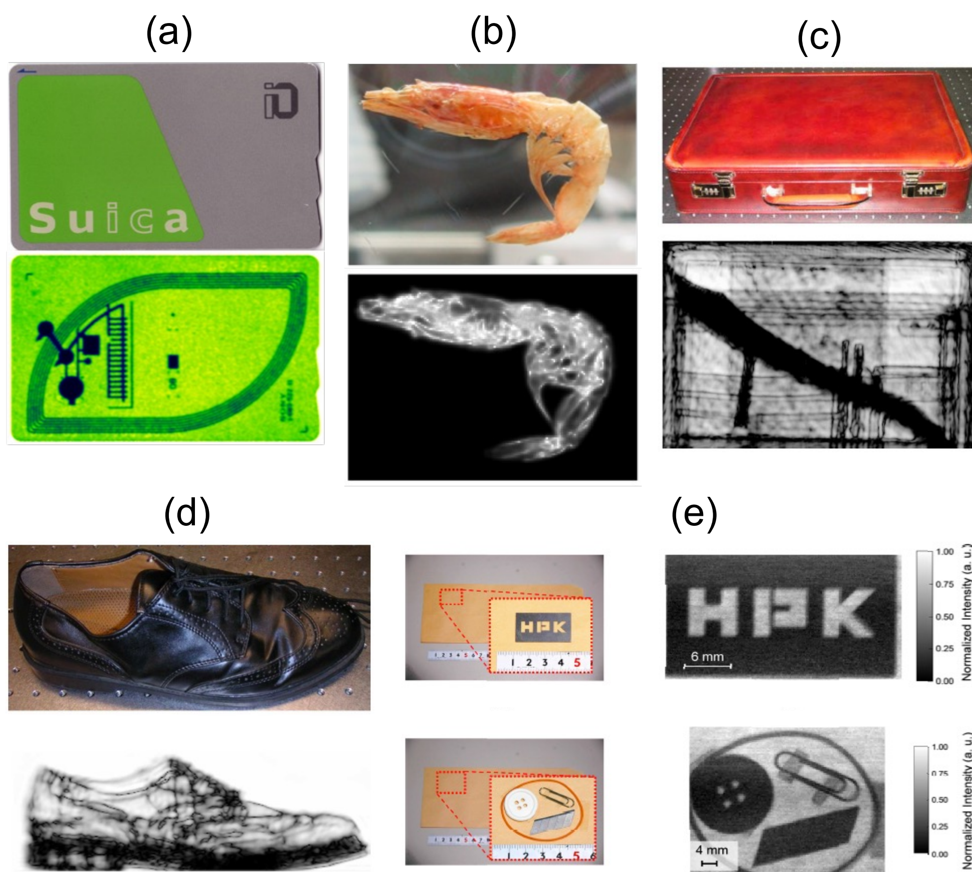

Figure. 1.2 THz transmissive imaging examples. (a) A railway payment card [13]. (b) A dried shrimp [10]. (c) A leather suitcase including a knife and pens [15]. (d) A shoe [15]. (e) A stainless-steel plate (upper figures) and a rubber band, a plastic button, a clip, and a cutter knife blade in envelopes (bottom figures) [12].

THz spectroscopy is another important THz technology. Spectroscopy is a technique to measure unique optical responses of substances such as emission or absorption, and spectrum analysis assists to identify molecular structures because spectra reflect intra-molecular and/or inter-molecular vibration. Currently, Fourier transform infrared spectroscopy (FT-IR), a prevailing technique using infrared light, has contributed to scientific or engineering research. However, identification of complicated molecular structures is difficult for FT-IR because the FT-IR spectra comes from chemical bonds amongst rather light chemical functional groups. On the other hand, a single THz spectrum can identify molecules solely, thus THz spectrum is called 'fingerprint spectrum' [16]. THz spectroscopy can be a powerful tool especially for organic molecule inspection because FT-IR cannot reach the THz frequency region where many organic molecules have absorption peaks. Furthermore, spectroscopic images, two-dimensional spatial plots of spectrum intensities for a specific frequency, are also available to recognize spatial distribution of substances [16].

Such strength of THz spectroscopy is suitable for inspection of many kinds of materials such as explosives, inflammables, medicine, saccharides, and so on [17-23]. It is also a merit that THz spectroscopy is able to evaluate wrapped targets by paper of plastic in non-destructive and non-contact inspections [19, 23]. Furthermore, THz spectroscopy can also detect subtle difference in molecular structures. For example, distinguishment of the difference in spectra between anhydrate and hydrate of trehalose has been reported [16]. In clinical research, detection of cancer or malignant tumors by THz spectroscopy have been reported, and application of it has been expected [24-27]. Inspection by THz spectroscopy is also useful in food mass manufacturing [28].

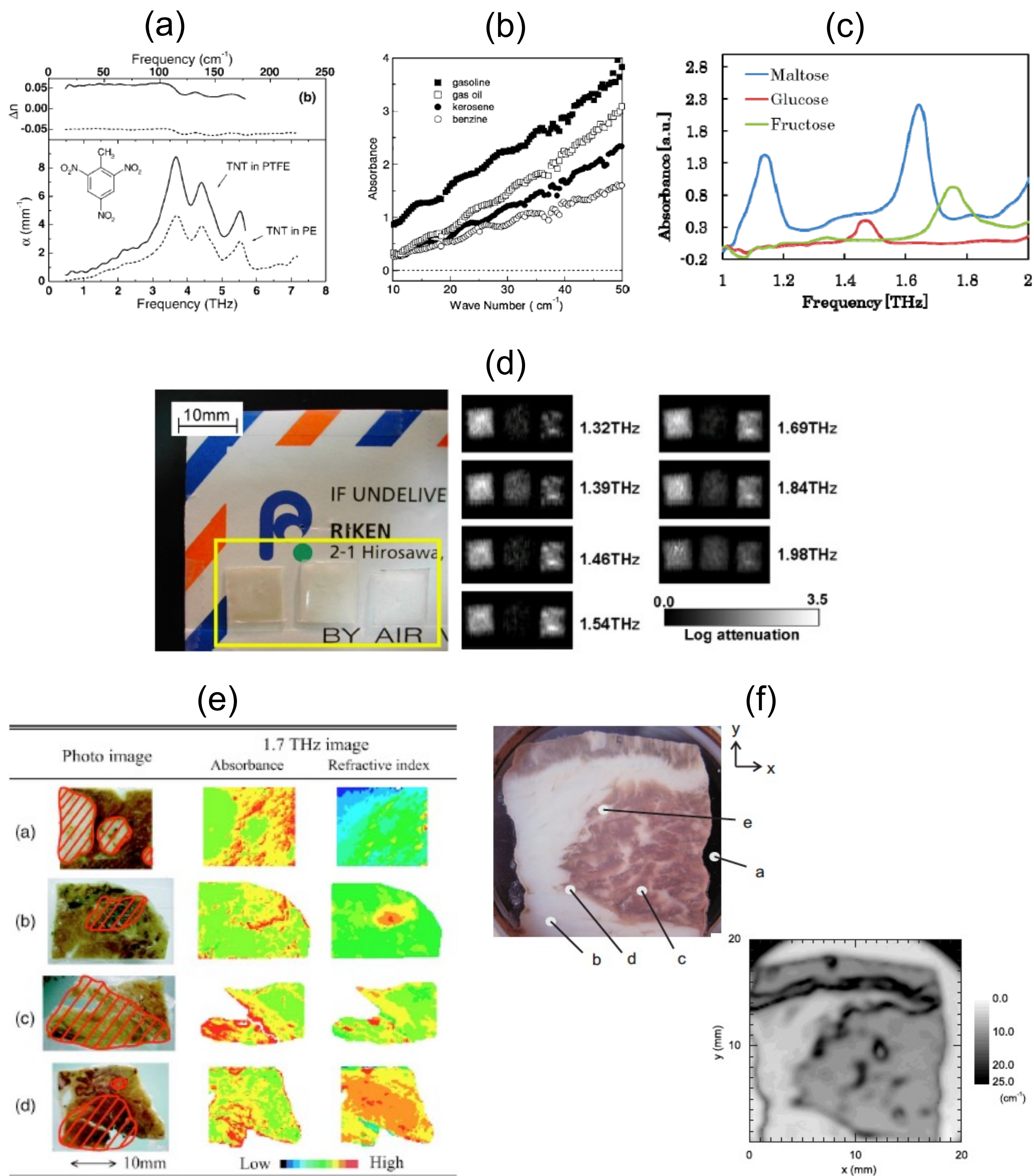

Figure. 1.3 THz spectroscopy examples. (a) A spectrum from an explosive (tri-nitro toluene) [17]. (b) A spectrum from inflammable liquids [23]. (c) A spectrum from saccharides [20]. (d) MDMA (left), aspirin (center), and methamphetamine (right) [19]. (e) Cancer tissues [24]. (f) Porcine tissues. An optical image (up-left) and a spectroscopic image (bottom-right) [28].

The third anticipating terahertz technology is terahertz wireless communication. Even though telecommunication is imperative in our society, spectrum crunch – scarcity of the available EM frequency ranges for wireless communication – is an apprehensive social issue due to current drastic increase of mobile terminals [29-31]. To resolve this issue, application of THz light to wireless communication is proposed as well as frequency sharing and efficient frequency allowance [32]. One of the reasons why THz light was not applied to wireless communication is developmental delay of THz light sources or detectors. In addition, atmospheric absorption is also a critical issue for it. Permittivity of the EM wave to atmosphere is unique depending on the EM wave frequency, and certain ranges of the EM waves: visible light, near-infrared light, and parts of radio waves are less likely absorbed by the atmosphere, but THz light is more likely absorbed (Atmospheric window [33]). Therefore, realization of THz telecommunications is challenging.

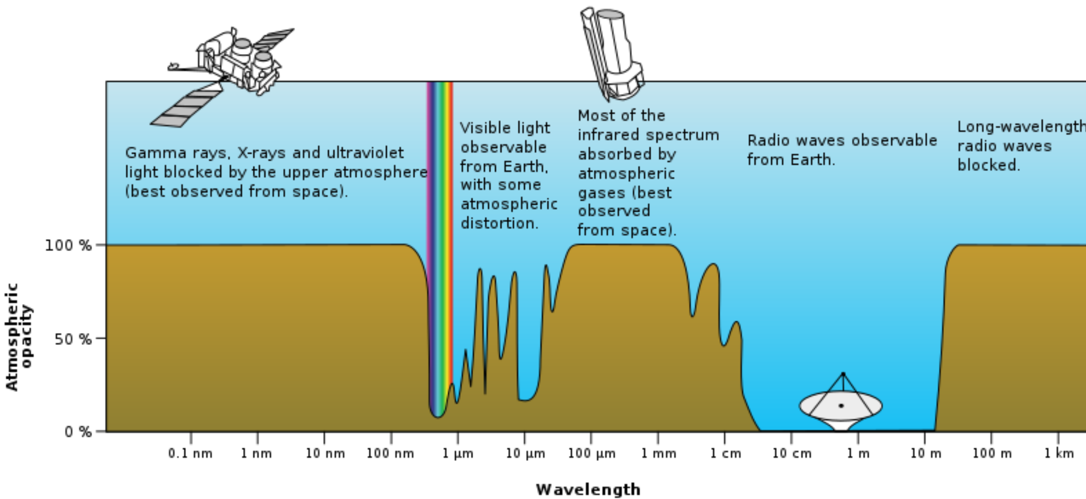

Figure. 1.4 Atmospheric window [33].

Having said that, rapid and large-volume data transferability of THz light is attractive for wireless communication. (In accordance with the Shannon-Hartley theorem.) In particular, high attenuation of THz light in atmosphere is considered to be suitable for localized and secret communication. To exploit such advantages, applied research of THz wireless communication for rather short-distance communication (shorter than 10m) have been developed [32]. In research for THz wireless communication, transfer frequency up to around 700GHz and data rate surpassing 200Gbit/s have been demonstrated [32, 34, 35], and some applications of THz communications have also been proposed: very short-distance communication between IC chips or printed wiring boards, short-distance communication for synchronism of the cloud service with mobile contents, inter-server communication in data centers, and indoor non-compression and high-quality video distribution [31]. Furthermore, THz long-distance wireless communication is available in the extraterrestrial space due to absence of the atmosphere. Where, down-sizing of antenna is also available [32].

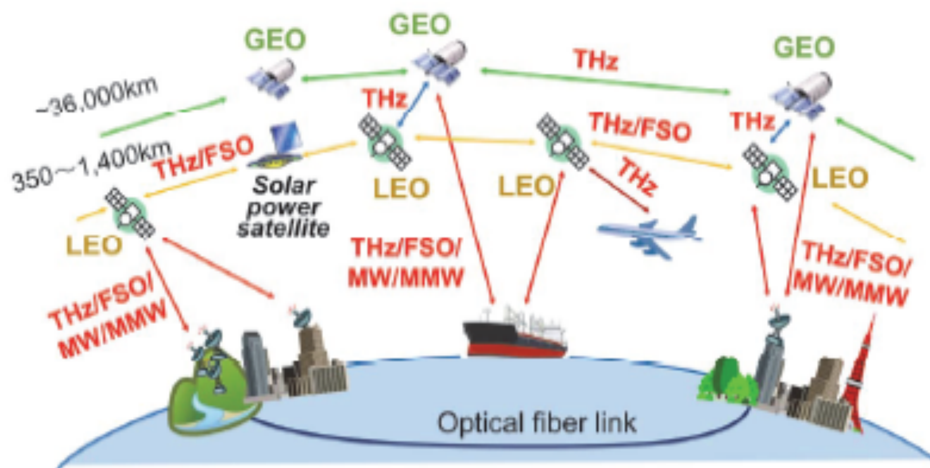

Figure. 1.5 Conceptual illustration of future networks with THz link in the space [32].

Lastly, other THz techniques except for transmissive imaging, spectroscopy, and wireless communications are briefly introduced. One of the THz sensing examples is defect detection of gallium nitride substrates by observation of a yellow band in photoluminescence which bases lattice defects in substrates and has a spectrum over THz frequency range [36]. Detection of electrical failure in integrated circuits (ICs) is also proposed by using the laser terahertz emission microscope (LTEM) as described in Figure 1.6(a). In this method, change of THz light amplitudes due to local electrical field is detected, and even very small structures of circuits can be observed without contact [37]. Furthermore, chemical structure deformation of materials by THz light is rather new and intriguing topics. Phase transition of vanadium dioxide from insulator to metal is reported, and conformational change of one type of polymers, poly(3-hydroxybutylate), is also demonstrated without chemical compositional change as depicted in Figure 1.6 (b) [38, 39]. These new features are anticipated to connect development of new functional materials.

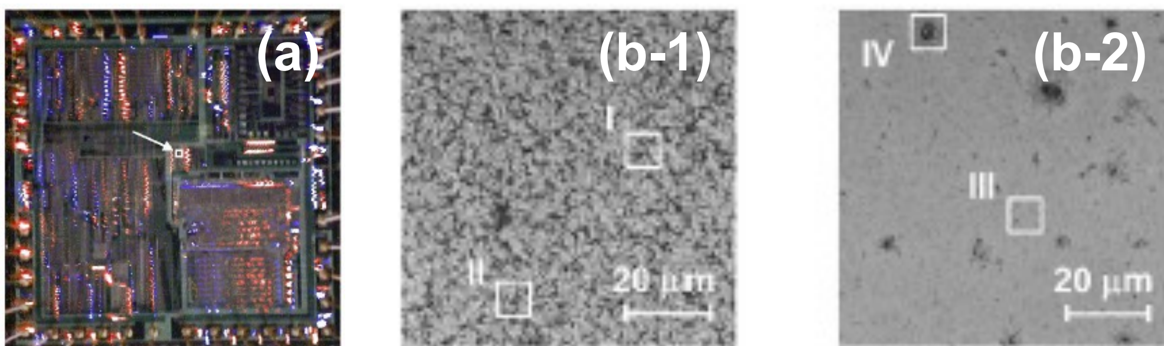

Figure. 1.6 (a) THz emission from an LSI 8-bit microprocessor (red and blue indicate positive and negative amplitudes of THz light) [37]. (b) Transmission microscope images of a polymer. (b-1) without THz irradiation, (b-2) with THz irradiation [39].

1.1.3 Terahertz Light Sources

As mentioned in the previous subsection, THz light has high anticipation to bring much benefit to many scientific and engineering fields due to its unique characteristics. However, development of THz light sources is a prolonged challenge, and a variety of methods for THz light generation have been attempted. Those methods fall into three categories: optical generation, solid-state devices, and lasers. [5, 40]

Due to directional propagation, terahertz light can be dealt with in optical measurement systems. Optical generation utilizes such characteristics of THz light. In the optical generation, two types of methods are known well. The one is optical parametric generation. In this method, excited laser light (e.g. generated by YAG laser) is radiated into the third-order nonlinear crystals and interacts with the dispersion and absorption of TO-phonon in the crystals, resulting in idler light and THz light, so that the energy conservation and momentum conservation laws are restored. The second-order materials are also used for difference-frequency generation (DFG) and four-wave-mixing. [41, 42] Another method is multiple photo-mixing, in which an optical beat composed of two componential frequencies is received by a photo-conductive antenna and is converted to electrical signal. So, when this frequency difference is designed to be THz frequency, THz signals can be obtained. These optical methods are applicable to a wide frequency range and can generate rather strong THz light depending on the intensity of the excited light. However, low power efficiency due to frequency conversion and bulky systems are bottlenecked [43].

Solid state devices can also generate THz signals which is dealt with as the EM

waves. Depending on photo-generation phenomena, many types of devices have been proposed so far. For instance, uni-travelling-carrier photodiodes (UTC-PDs) generate THz signals from input optical beats by photodiodes instead of antennas in optical generation [44,45]. Other electrical devices, Gunn diodes [46-48], tunnel injection transit time diodes (TUNNETs) [49, 50], impact ionization avalanche transit-time diodes (IMPATTs) [51], and resonant tunneling diodes (RTDs) [52, 53], commonly utilize the negative differential resistance (NDR) to generate THz waves. In terms of fabrication of these devices, conventional semiconductor device processes or facilities are available, so these devices are suitable for inexpensive mass production. However, operative frequency range of these devices are from about 100Hz to 300GHz, and the output power easily dwindles when the oscillation frequency gets close to the THz range as shown in Figure 1.7.

Lastly, some sorts of semiconductor lasers have also demonstrated THz radiation. p-type germanium (p-Ge) lasers can generate THz light from hole transitions amongst valence bands, and high output power has been reported although very low temperature (~20K) and strong magnetic field are necessary for operation [54, 55]. On the other hand, another applicant device, quantum cascade lasers (QCLs), utilize electrons transition amongst subbands in a conduction band for lasing. Details of QCLs will be explained in the next section.

As described above, many THz light sources have been demonstrated and improved to fulfill THz gap. However, all types of devices have pros and cons for THz applications and also have not satisfied enough level of requirements: high output power, high efficiency, compactness, room-temperature operation, wavelength tunability, narrow spectra,

inexpensiveness, needlessness of magnetic field, and so on [56]. Amongst these devices, THz QCL, that satisfies most requirements except for room-temperature operation due to its principle, have thought to be the most prospective THz light source and have attracted a great attention.

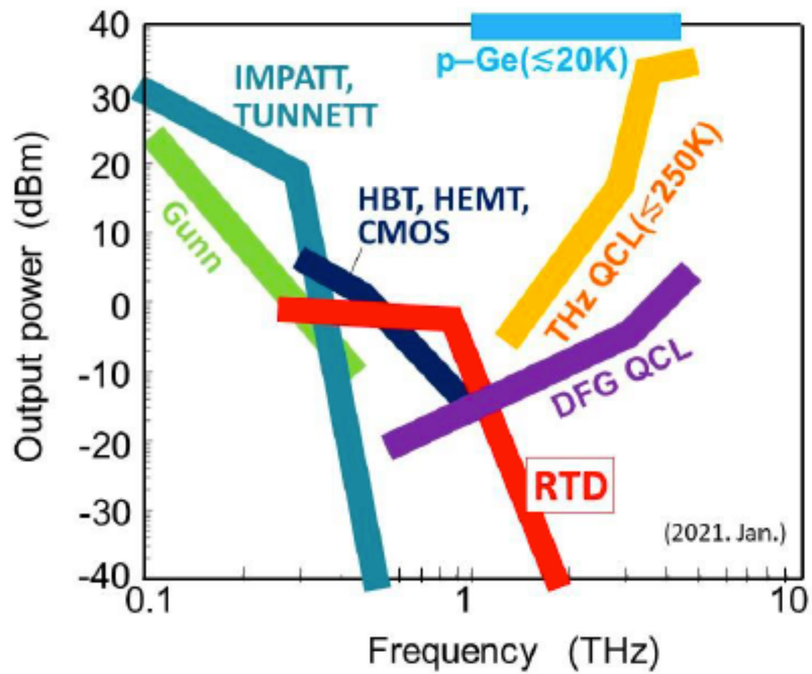

Figure. 1.7 THz-emission power and frequency of reported THz light sources [53]

1.2 Quantum Cascade Laser

The main research topic in this study, Terahertz (THz) quantum cascade laser (QCL), is one type of QCL devices, and most driving mechanisms and device structures are common to other QCL devices. Before explanation about THz QCLs in Section 1.3, fundamentals of QCL devices: classification, history, main carrier transports, device structures, research methods, and developmental progress will be explained in this section.

1.2.1 Overview

Quantum cascade laser device, one kind of semiconductor lasers, is featured by multiple quantum well structures composed of dissimilar semiconductor materials (double-hetero junction) and optical intersubband transition and are classified into several types depending on physical characteristics [57, 58]. First, quantum cascade lasers are divided into Type-I and Type-II depending on heterojunction [59]. On the one hand, Type-I devices, generally called 'quantum cascade laser', generate light by electrons' intersubband transition in conduction band. On the other hand, Type-II devices use recombination of electrons and holes for radiation and are called interband cascade lasers (ICLs) [60]. In the early day, these two types of devices have been studied for mid-infrared radiation. Next, Type-I QCL devices are divided into MIR-QCLs and THz QCLs depending on lasing frequency [61]. Lastly, THz radiation can be obtained by combining MIR radiation and differential frequency generation (DFG) in an active core. This method is called DFG THz QCL [62].

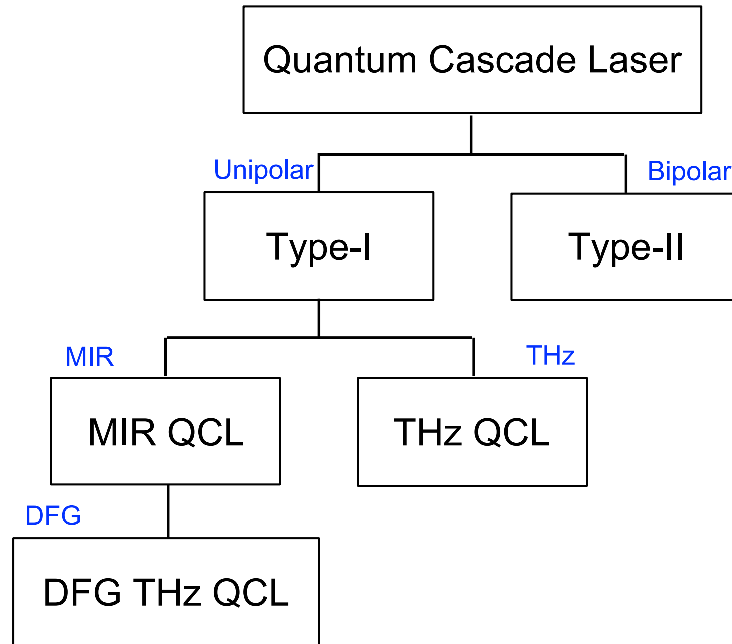

Figure. 1.8 Classification of quantum cascade laser devices.

The origin of QCLs stretches back to about fifty years ago. The first idea of optical transition by tunneling carrier transport was proposed by R. F. Kazarinov and R. A. Suris in 1971 [63]. However, the first MIR QCL could not be demonstrated until mature techniques of crystal growth for superlattice (SL) such as molecular beam epitaxy (MBE) and metal organic chemical vapor deposition (MOCVD) were invented [57]. Even though the first MIR QCL demonstrated by J. Faist *et al.* lased up to 90K with 4.3μm of lasing frequency in 1994, a great progress enabled MIR QCLs to lase over the room-temperature in 1996 [64] and at a wide range of lasing frequency from 2.7μm to 22.4μm [65-68]. In 1997, the first interband cascade laser was also demonstrated [60, 69]. Compared to MIR QCLs, development of THz QCLs is more challenging. The first THz QCL was demonstrated by R. Köhler *et al.* in 2002

[61], but the highest operation temperature remains at 261K instead of many challenges about device structure, material, and so on [70]. The lasing was reported from 1.2THz to 5.4THz [71, 72], and high-power operation is also studied. During stagnant development of THz QCLs, M. A. Belkin *et al.* demonstrated THz radiation by combing high power MIR QCLs and DFG phenomenon in 2007 [62]. In DFG THz QCLs, the room-temperature operation was demonstrated one year after the first demonstration, and the Cherenkov phase matching technique improves output power [73, 74]. However, due to low energy conversion efficiency, the reported highest power has not surpassed around 2mW since 2016 [75,76].

Crystal growth of stacked quantum well structures composed of III-V compound semiconductor materials are implemented by MBE or MOCVD with group-III material sources: aluminum, gallium, and/or indium and group-V material sources: nitrogen, arsenide, and/or antimonide. The advantage of MBE is sensitive control of layer thicknesses in the level of mono layer. On the other hand, MOCVD is suitable for mass production. As shown in Figure 1.9, high-performance MIR-QCLs were demonstrated with lattice-matched InGaAs/AlInAs system, which enable rather deep quantum wells, and most THz QCLs were demonstrated with GaAs/AlGaAs system which can change barrier height flexibly by Al-composition. Material systems with smaller effective mass is considered to be advantageous because optical gain is inversely proportional to effective mass. In THz QCLs, however, high-performance was obtained only with the GaAs material system (which has rather large effective mass). GaAs/AlGaAs system is not suitable for lasing at 5 to 10THz due to Reststrahlen band. So, gallium nitride, which has Reststrahlen band in a different range, has also been studied for THz QCLs [77, 78].

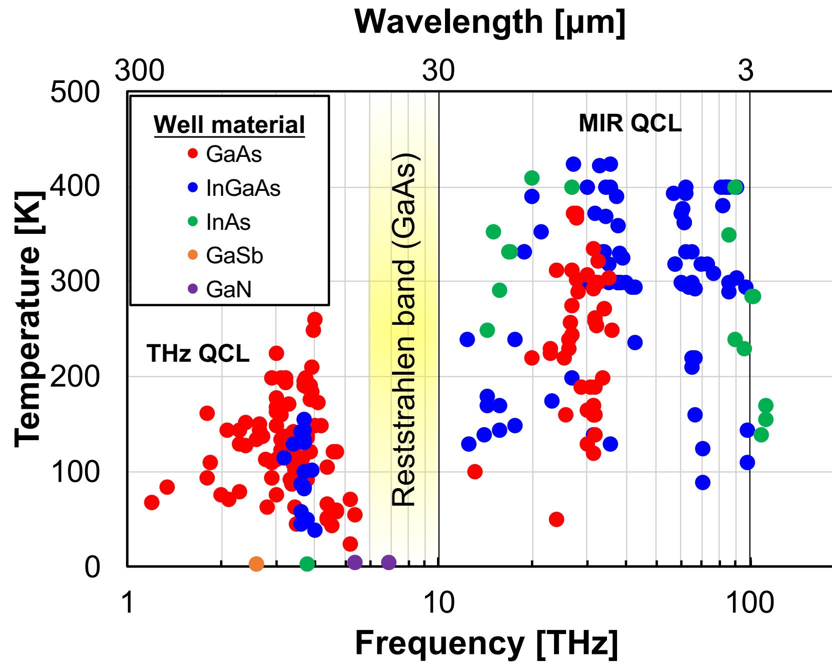

Figure. 1.9 A relation between the highest operation temperature and lasing frequency of MIR and THz QCLs.

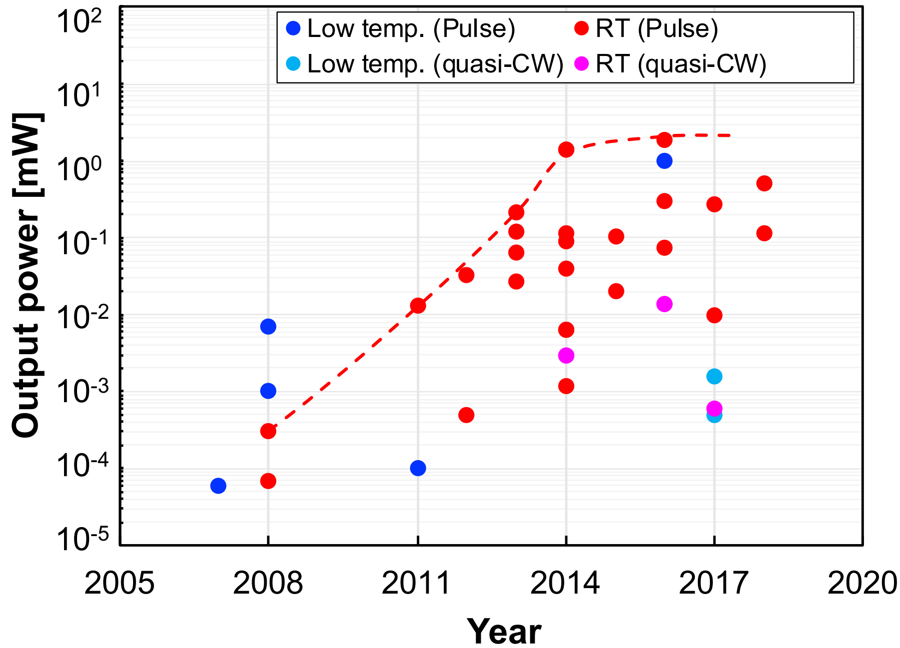

Figure. 1.10 Progress of DFG THz QCLs in output power. (a wiggly line is a trend curve.)

1.2.2 Principle

A quantum cascade laser is composed of an active core and a waveguide. An active core is comprised of stacked multiple layers by heterojunction with dissimilar semiconductor materials. Due to unique bandgaps of these materials, quantum wells appear in conduction band (C.B.) and valence band (V.B.), and electrons and holes are confined in quantum states happened in quantum wells as depicted in Figure 1.11. Quantum states, wavefunction and subband energy, can influence on electrical and optical characteristics of quantum well devices and are adjustable by tuning well or barrier thickness and materials.

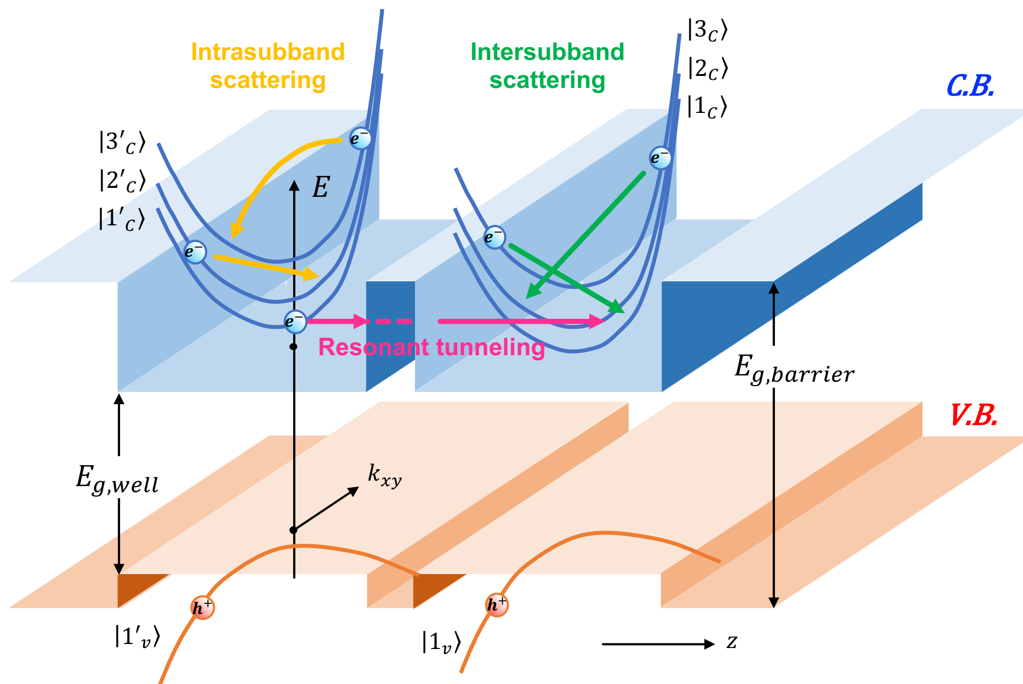

Figure. 1.11 A band diagram and its E-k dispersion of heterojunction and different types of carrier transports.

In QCLs, two types of carrier transition; carrier scattering and resonant tunneling are combined to establish population inversion between lasing states enabling stimulated emission. Incoherent/random carrier scattering happens inside a subband (intra-subband scattering) or between subbands (inter-subband scattering) even without subband alignment. Scattering rate is determined by an overlap of wavefunctions in the initial and final states and scattering phenomena [59]. Coherent resonant tunneling happens when two subbands are aligned, and electrical current tends to peak at the alignment condition resulting in negative differential resistance (NDR) [79-81]. After demonstration of sequential resonant tunneling described in Figure 1.12, research for quantum well devices such as RTDs or QCLs was accelerated [82].

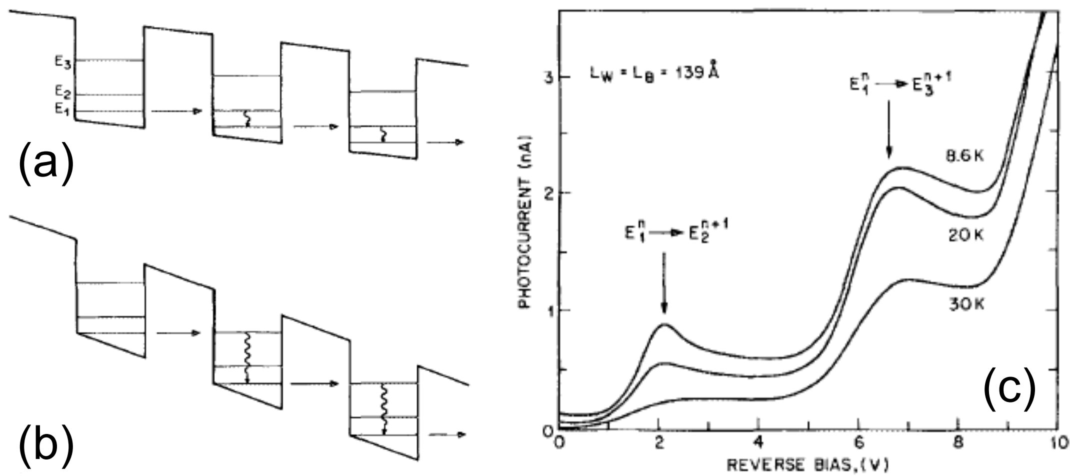

Figure. 1.12 Band diagrams for sequential resonant tunneling (a, b) and photocurrent and voltage characteristics (c) [82]. In this experiment, carriers are optically injected. (a) Resonant tunneling between a ground state (E_1) and a first excited state (E_2). (b) Resonant tunneling between a ground state and a second excited state (E_3). (c) Photocurrent -voltage characteristics.

Based on carrier transport mechanisms described above, active cores of QCLs are designed with repeated quantum well structures. One period/module is composed of an active region and an injection region separated by a thick injection barrier as described in Figure 1.13, and devices are designed on assumptions that inter-module carrier transport is resonant tunneling, and intra-module transport is carrier scattering [59]. In design, two lasing states, carrier injection to the upper lasing state (ULS), and carrier abstraction from the lower lasing state (LLS) are important for population inversion, which is a condition that carrier density of ULS is greater than the one of LLS. First, carrier injection to an active region from an injection region is often designed so that carriers are selectively injected to a specific subband by resonant tunneling. Where, there are two ways: direct injection to ULS by resonant tunneling and indirect one via LO-phonon scattering [84]. Instead of a bound state for injection, a mini band (a bundle of bound states) can also be used [85]. Large injection rate is required for high carrier density of ULS. Next, the energy difference between lasing states is designed to correspond to a target frequency of light. Where, an overlap of wave functions, determining radiative and non-radiative carrier transitions between lasing states, is important because a balance of these two types of carrier transition determines population inversion. Lastly, in order to create strong population inversion, scarcity of carriers in LLS is necessary. Carriers are designed to be abstracted rapidly from LLS by a mini-band or LO-phonon scattering [86]. In injection region, abstracted carriers from LLS are transferred. Besides, impurities are also doped to supply carriers. In MIR QCLs, an active region and an injection region are separated far enough, but these regions are close in THz QCLs, so ionized-impurity scattering is considered more likely to influence on device characteristics.

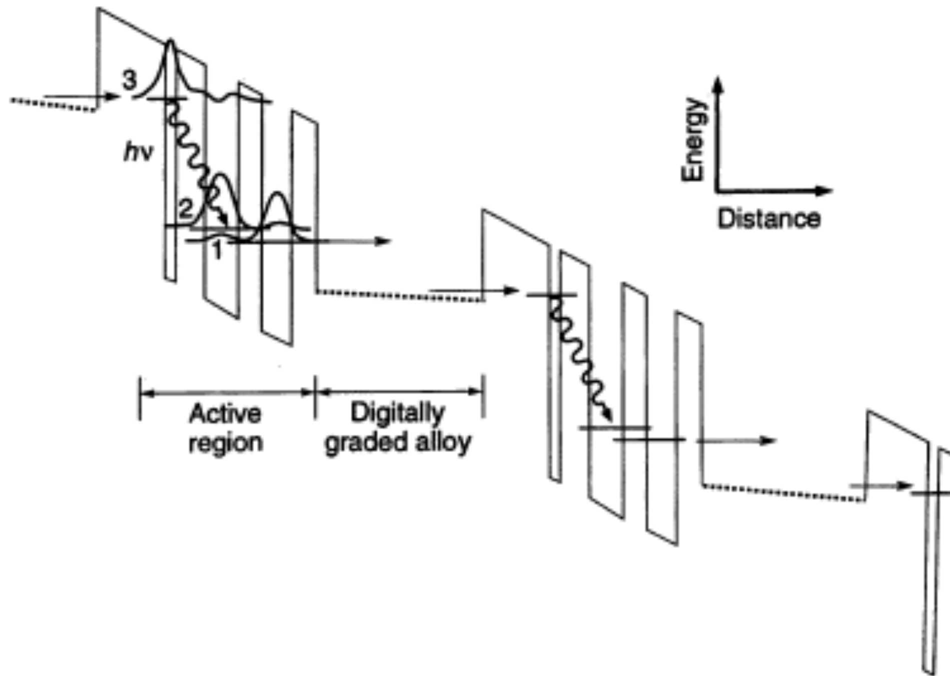

Figure. 1.13 band diagram of the first MIR QCL [57]. ‘Digitally graded alloy’ is an injection region in this figure.

On the one hand, QCLs are unipolar devices based on only electrons’ transport. (p-type QCLs have never been demonstrated due to complex valence bands.) On the other hand, conventional diode lasers are bipolar devices which use both electrons and holes for radiative recombination. Due to such difference, QCLs have unique characteristics as described below [83]. One of such characteristics is lasing frequency turnability. The lasing in diode lasers comes from recombination in band gap, which is a unique parameter of semiconductor materials. Thus, lasing frequency cannot flexibly be tuned. On the other hand, lasing frequency of QCLs is designable by adjusting device structures as far as conduction band difference allows. Technically, QCLs can cover a wide frequency range by different material

systems; GaAs-, InGaAs-, InAs, GaN-, and so on. The second feature is carrier recycling. In recombination process of diode lasers, electrons and holes annihilate each other after radiation. On the other hand, electrons in QCLs are recycled after radiation. Therefore, improvement of quantum efficiency is anticipated. In practice, undesirable carrier leakage between bound states or between a bound state and a continuum state can degrade quantum efficiency, so impurities are doped in every module in conventional device designs. Sharp optical linewidth is also expected in QCLs. Optical linewidth is dependent on curvature of the E-k dispersion curves, and optical transition can happen not only between the bottom of conduction band and the top of valence band but also between any other points of momentum. In diode lasers, curvatures of conduction and valence bands are opposite, so the range of optical transition energy can be wider as described in Figure 1.14, resulting in broad optical linewidth. On the other hand, in QCLs, subbands in conduction band have similar curvature. This can limit the optical transition energy range, resulting in sharp optical linewidth.

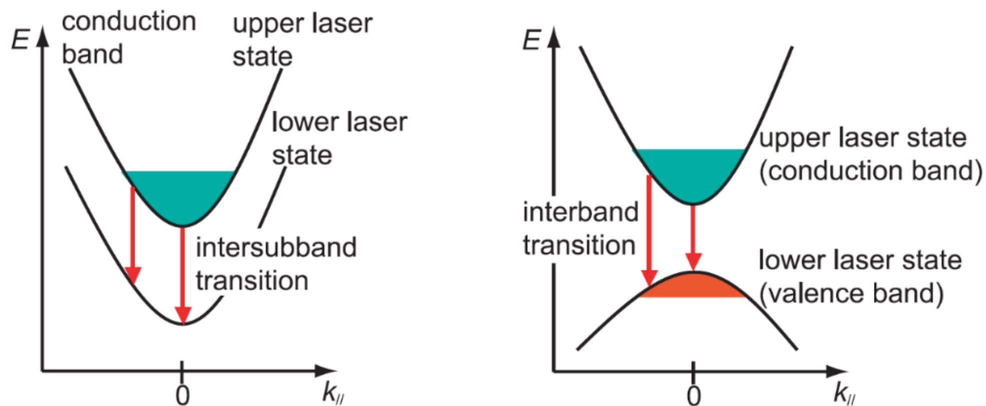

Figure. 1.14 Optical transition of quantum cascade laser (left) and semiconductor laser (right) [83].

Another important component is a waveguide. As described in Figure 1.13, optical transition in an active core is polarized to the crystal growth direction. So, metal or high-doped semiconductor layers stacked over and under an active core work as plasma to confine and amplify generated TM-polarized light inside the active core [58]. (An active core is sandwiched by waveguide materials. as depicted in Figure 1.15)

In QCLs, capability of lasing is judged by whether or not optical gain calculated from active core designs can surpass threshold gain, and threshold gain is calculated based on three design parameters: waveguide loss α_W, mirror loss α_M, and optical confinement factor Γ. Waveguide loss and confinement factor are estimated by using three-dimensional EM simulators [87]. Mirror loss is inversely proportional to a length of an active core L and calculated by Equation (1.1) with reflectivity of two facets, R_1 and R_2.

$$\alpha_M = -\frac{1}{2L}\ln(R_1 R_2) \tag{1.1}$$

Threshold gain is calculated by Equation (1.2).

$$g_{th} = \frac{\alpha_W + \alpha_M}{\Gamma} \tag{1.2}$$

As shown in Equation (1.2), three parameters are necessary for calculating threshold gain precisely, but mirror loss is much smaller than waveguide loss, so threshold gain is almost determined by the other two parameters in most cases. Kohen *et al.* showed that thicker and wider active cores are advantageous for low waveguide loss and threshold gain [87].

In recent THz QCL research, two types of waveguides have often been used: a semi-insulating single-plasmon (SISP) waveguide and a metal-metal (MM) waveguide. In terms of the confinement factor, the MM waveguide design are preferable because its confinement factor is almost unity ($\Gamma \sim 1 \rightarrow g_{th} \sim \alpha_W$) [87-92], but high-power devices have been reported by using the SISP waveguide design [93-95]. As for materials, theoretical and experimental studies have revealed that copper is advantageous for low waveguide loss instead of gold, and the highest operation temperature can be improved by 20~40K [91,92,96]. Waveguide loss can vary depending on waveguide geometry, the net doping density of waveguides, and lasing frequency, and around 20~30cm^{-1} of threshold gain is used as an indicating value for active core design of THz QCLs. In addition to a basic Fabry–Pérot resonator, distributed feedback (DFB) and external cavity (EC) resonators, and surface-emitting (SE) devices by photonic crystal (PhC) have also been applied to QCLs [97-101]. In this study, a Fabry–Pérot resonator is assumed for theoretical research shown in the following chapters.

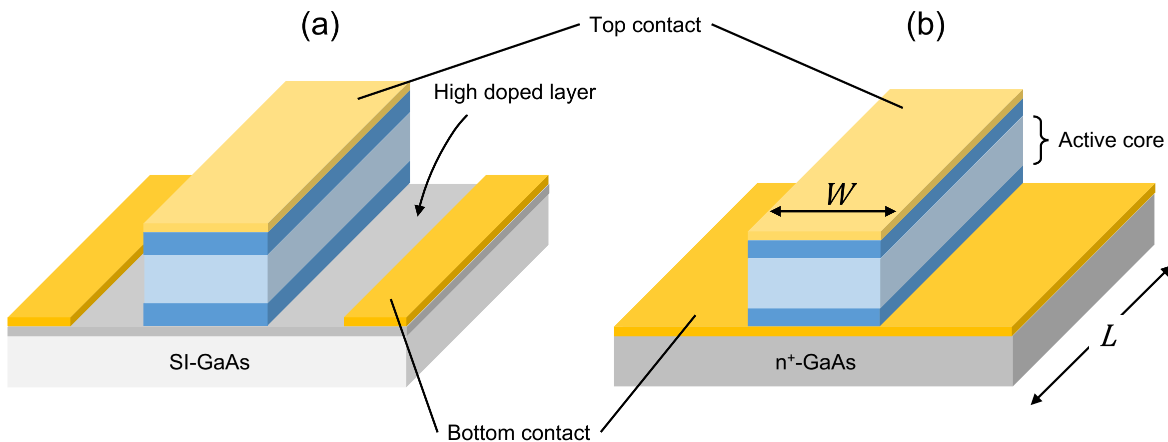

Figure. 1.15 Waveguide structures of QCLs. (a) SISP waveguide, and (b) MM waveguide.

1.3 Terahertz Quantum Cascade Laser

Details about THz QCL studies will be explained in this section. In general, the study of THz QCL is composed of simulation development, device design, crystal growth, device fabrication, characterization, and analysis, and many researchers have reported their theoretical and/or experimental works. In this section, background and previous research about simulation development and active core design will be introduced as a prologue of our research in Chapter 2 to 5. Research for waveguide, fabrication, and DFG THz QCLs are out of focus in this work.

1.3.1 Overview

THz QCLs have been expected to be applied to many THz applications, but the development of THz QCLs is rather challenging compared to MIR QCLs. In the past, it took several years to demonstrate the first THz QCL by Köhler *et al.* after MIR QCLs, and room-temperature operation has never been accomplished even though around twenty years have already passed since its first demonstration [61].

One of the reasons why THz QCL research is stagnant is efficient selective carrier injection to ULS [58]. As depicted in Figure 1.16, MIR QCLs have large energy difference between ULS and LLS. So, most carriers from an injection region are injected to ULS for large population inversion. On the other hand, the energy difference of lasing states needs to be designed much smaller in THz QCLs because the target frequency is 1~5THz (4~20meV).

In this case, carriers can be injected into LLS undesirably. Furthermore, carrier abstraction can happen not only from LLS but also from ULS. Usually, the energy difference between LLS and abstraction state (in most cases, a ground state) is designed to match LO-phonon vibration energy of materials. However, due to small energy difference between ULS and LLS, LO-phonon scattering rate between ULS and abstraction state can also be fast. Compared with MIR QCLs, therefore, THz QCLs are more difficult to create population inversion

Another issue is high waveguide loss. Waveguide loss is related to free carrier absorption which is determined by optical parameters of materials and lasing frequency or wavelength. Free carrier absorption increases with wavelength of light, so THz QCLs, whose wavelength is longer than the one of MIR QCL, have higher waveguide loss [102, 103]. Due to these two drawbacks, THz QCLs are more difficult to obtain high optical gain and low threshold gain.

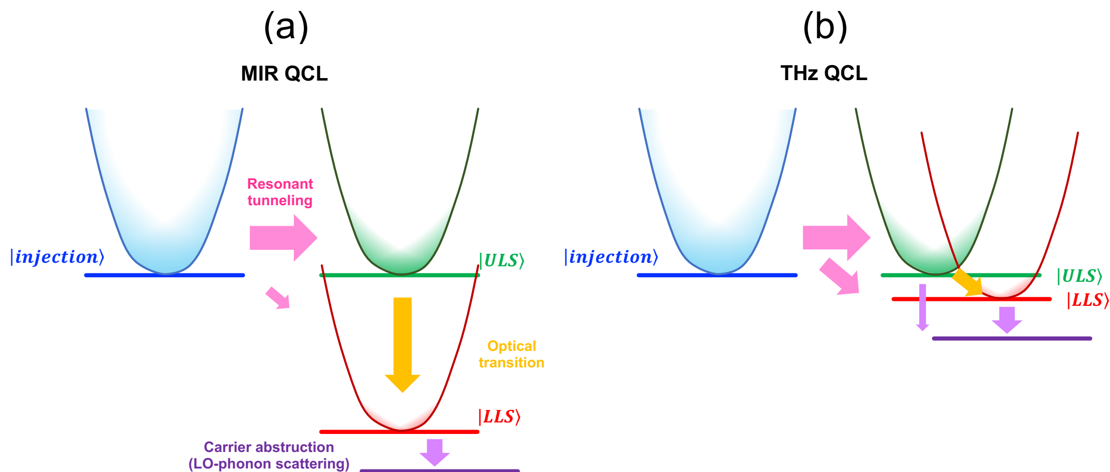

Figure. 1.16 The difference of carrier transition mechanisms between MIR and THz QCLs.

Instead of aforementioned technical difficulties, THz QCLs have had a great progress since the first demonstration by many researchers' theoretical and/or experimental approaches, and 250K of the highest operation temperature, 2.4W of the highest output power under low temperature and pulsation conditions, and from 1.2THz to 5.4THz of lasing frequency have been demonstrated until today (Figure 1.17).

Research for improving operation temperature has been most intensively implemented as shown in Figure 1.17(a). Even though the highest operation temperature of the first THz QCL, demonstrated with chirped-superlattice (Chirped-SL) structure by Köhler *et al.*, is just 50K [61], a four-well resonant-phonon structure (RP-4QW) and Cu-Cu waveguide were introduced in the year after [104, 105], and 164K of the highest operation temperature was achieve in 2005 [106]. After 2007, a three-well resonant-phonon (RP-3QW) structure has more likely been studied [107], and 199.5K of operation was reported by Fathololoumi *et al.* in 2012 [108]. In the same period, 225K of the highest operation temperature under magnetic field [109] and stacked active core devices were also demonstrated [110]. Although the progress was stagnant for a while, the highest temperature has started to be renewed after Bosco *et al.* discovered advantage of a two-well resonant-phonon (RP-2QW) structure in 2018 [111], and the current highest operation temperature is 261K achieved by Khalatpour *et al.* in 2020 [70].

As for lasing frequency, lasing at 3~4THz has frequently been reported, but a wide range of radiation, from 1.2THz to 5.4THz, has also been achieved [71, 72] as in Figure 1.17(b). THz QCLs have lasing frequency limits in low and high frequency regions. In low frequency region, selective injection to ULS limits the operation. The energy difference

between lasing states is very narrow in THz QCLs, so lasing under 2THz would be technically difficult, and the other THz light sources such as RTDs would be more advantageous in this region. The Reststrahlen band is also a limit in another end. GaAs and InGaAs, conventional materials for THz QCLs, has the Reststrahlen band approximately from 5THz to 10THz, and light is strongly absorbed in this frequency region. This issue has been approached by using GaN which has the Reststrahlen band in a different frequency region [78]. In the past, an empirical temperature limit ($T = \frac{\hbar\omega}{k_B}$) was also postulated, but many devices work over this limit [112].

Instead of resonant-phonon devices accelerating the research for high temperature operation, bound-to-continuum (B-to-C) and hybrid type devices combining B-to-C and LO-phonon abstraction (Hybrid) have often been studied for high output power, and three research have reported over 1W of output power under low temperature below 10K [93-95] as in Figure 1.17(c). A research group in Leeds University reported 1.01W and 2.4W of output power in 2014 and 2017, respectively [93, 94]. Lin *et al.* in RIKEN also demonstrated 1.31W by using a four-well resonant-phonon device [95].

As for threshold current, it is observed from Figure 1.17 (d) that device structures which use mini-band for carrier abstraction form LLS and need lower alignment field are advantageous. When LO-phonon scattering is used, voltage drop per module increases, resulting in higher threshold current.

As described above, development of THz QCLs has mostly been attributed to proposal or improvement of active core designs. On the other hand, device simulators play an important role for high-performance device design and has also been improved in the

calculation precision and speed. This study, aiming theoretical studies, develops a device simulator, so a background of simulation research and previous studies of active core designs will be explained in the next subsection.

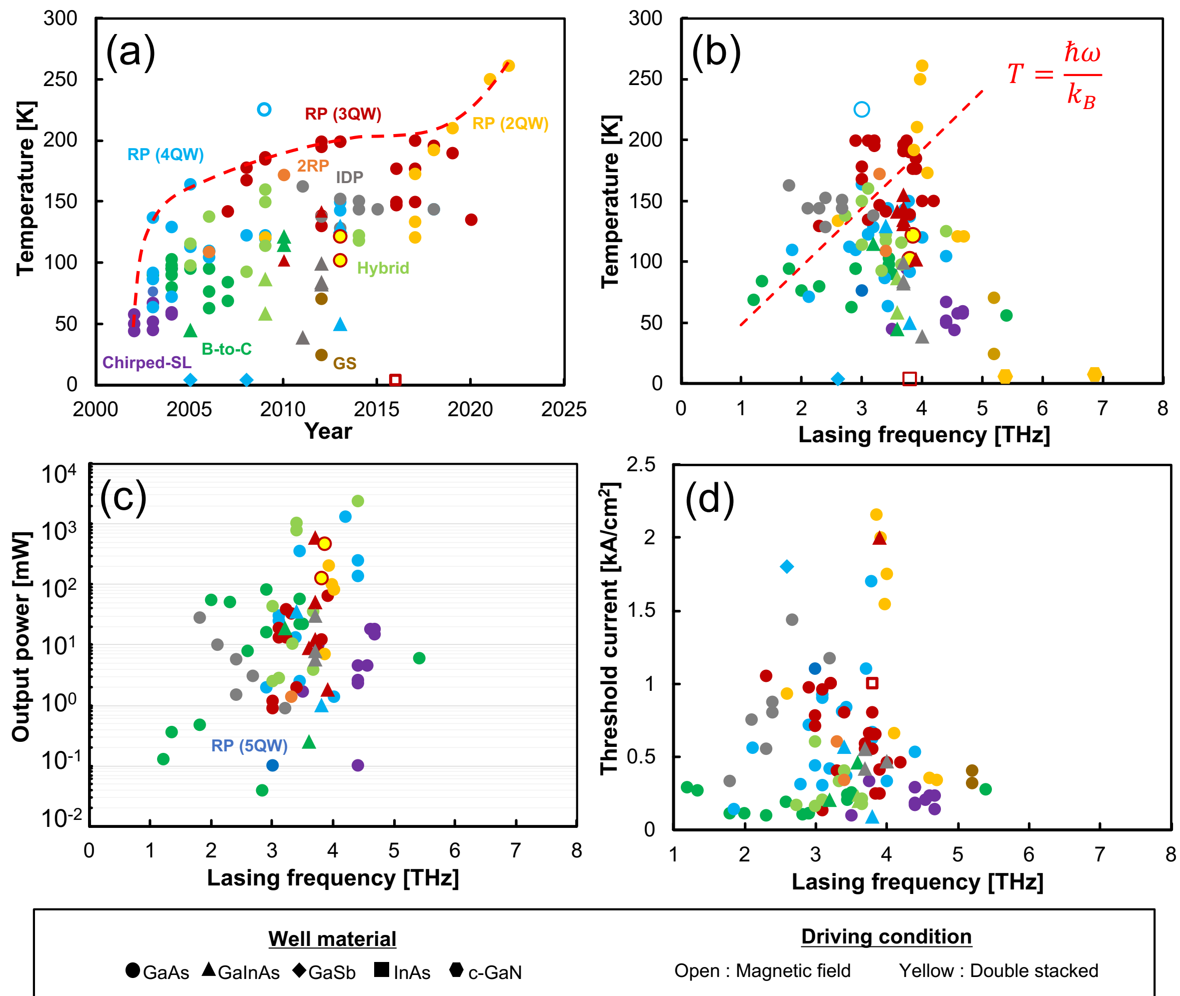

Figure. 1.17 Progress of THz QCL research. (a) Chronological improvement of the highest operation temperature. (b) Lasing frequency vs the highest operation temperature. (c) Lasing frequency vs output power (under low temperature and pulsation condition). (d) Lasing frequency vs threshold current.

1.3.2 Simulation Method

QCLs drive based on combination of many quantum physical phenomena, which cannot be observed directly by experiment, so it is very challenging to design device structures and analyze behaviors of devices intuitively or qualitatively. Thus, device simulators are indispensable to predict electrical and optical characteristics from device structures, material parameters, and driving conditions [113]. Such calculation has been studied long and is classified into four methods: the rate equation (RE) method [58, 59, 113-116], the density matrix (DM) method [113, 117-122], the Monte-Carlo (MC) method [113, 123-129], and the non-equilibrium green function (NEGF) method [113, 130-138]. Each method has advantages and disadvantages with respect to the calculation accuracy and speed.

The rate equation is a set of simultaneous differential equations to describe transient change of subband carrier density by carrier inflow and outflow rates, and the advantages of it are ease of understanding phenomena such as carrier transports inside devices, introducing new models of phenomena, and rapid calculation. Usually, carriers in subbands distributes complying with Fermi-Dirac distribution, and carrier scattering rate depends on kinetic energy (or momentum) as described in Figure 1.11. In rate equation, carrier scattering rate is thermally averaged, and a hopping model – carriers move between quantized sates instead of the E-k dispersion – is used for establishing the equations. In the early QCL works, only incoherent carrier scattering was considered in the rate equation, and such models were successful in MIR QCL works, to some extent, but it cannot describe electrical characteristics of THz QCLs properly [59]. This issue was resolved by introducing the tunneling time model

in the rate equation. The tunneling time model, which describes coherent transport, was derived by Scalari, *et al.* who applied the Liouville equation to the two-level problem in 2007 [139]. Despite simplicity, the rate equation is a little apprehensive in the accuracy because some parameters are calculated based on simplification or assumptions of complex quantum effects (e.g. quantum state broadening).

The density matrix method, developed based on the Liouville equation, is a quantum mechanical calculation method standardly considering coherence between subbands. Like the rate equation, assumptions and phenomenological parameters are used for this method [59]. From 2009 to 2011, the simplified density matrix method, which consider coherence between a ground state of a previous module and others of the next module, was frequently reported [117-120]. For precise description of inter-module carrier transport, however, coherence between all subbands are necessary, and the generalized density matrix method resolving this issue was published in 2012[121, 122]. In the generalized DM, calculation can be heavy when device structures are large because a considered matrix is a $N_{level}^3 \times N_{level}^3$ (N_{level} denotes the subband number per module.).

The Monte-Carlo method considers spatial and energetic distribution of carriers for the calculation precision unlike the rate equation and density matrix using thermally averaged carrier scattering rate [123-128]. This semi-classical method was often used for MIR QCL research but cannot deal with coherent transport solely. So, combination with the density matrix method was applied to THz studies [129].

The NEGF method, which is the most quantum mechanical and has been used in most recent research, bases the first principle calculation and is considered to be most reliable

in THz QCL study [130-138]. This is because the NEGF method can treat coherent and incoherent transport without the assumptions used in the rate equation and density matrix methods and with consideration of spatial and energetic carrier distribution like the Monte-Carlo method. On the other hand, the complexity of this method increases calculation time and makes it difficult for us to intuitively understand carrier dynamics. Furthermore, it is apprehensive if the NEGF can deal with semi-classical phenomena such as leakage current from bound states to continuums.

As described above, each calculation method has advantages and disadvantages in terms of calculation accuracy and speed. So, efficient choice of methods is required depending on purposes of research. For example, the rate equation or density matrix is suitable for rough comparison of many applicant device structures in short time. On the other hand, the NEGF method can be used to determine the best device structure or to analyze high-performance devices with detail. Generally, the rate equation is advantageous in calculation speed. However, this is dependent of considered physical phenomena. If the rate equation includes electron-electron or ionized-impurity scattering calculation, which is computationally heavy, total calculation time increases. On the other hand, development of computers assists more rapid calculation in the Monte-Carlo or NEGF method. As for the accuracy in calculation, many publication states that the NEGF is the most reliable. However, around 100K of difference in the highest operation temperature between simulation and experiment has also been reported [138]. In conclusion, simulation development still has room for improvement.

1.3.3 Active Core Study

Active cores of THz QCLs have been most intensively studied because the designs of active core directly influence on device characteristics. The study of active cores is roughly divided into two classifications: (1) Structure design, and (2) analysis of degradation mechanisms in high temperature conditions. Previous studies will be summarized below.

1.3.3.1 Active Core Design

Quantum well structures of active cores, determining electrical and optical characteristics of devices, have several design components and have been studied for high temperature or high output power operation [140, 141]. The design components are [A]carrier transport methods, [B] material systems, [C] impurity doping, [D] barrier height, [E] structural complexity, [F] alignment field and layer thicknesses. Devices need to be designed carefully because these design components can interfere each other depending on driving conditions.

[A] Carrier transport method

In the beginning of THz QCL research, many carrier transport methods used in MIR QCLs have been applied to THz QCLs, and device performance has been improved. Later, meeting with driving conditions or degradation mechanisms of THz QCLs, new carrier

transport methods have also been demonstrated.

Chirped-superlattice In 2002, Köhler *et al.* demonstrated the first THz QCL by adopting the chirped-superlattice (Chirped-SL) carrier transport, featured by lasing from optical transport between mini-bands as shown in Figure 1.18 (a) [61, 142-147]. A mini-band is composed of several bound states, and electrons in the top of a mini-band are quickly drained to the bottom via each state. The advantage of using a mini-band for carrier extraction form LLS is capability of designing alignment field to be low, resulting in low threshold current. On the other hand, device structures are long, compared to other carrier transport methods. The highest operation temperature of the first devices by Köhler *et al.* is just 50K, but the interlaced structure (Figure 1.18 (b)), combining the chirped-superlattice method and carrier extraction by LO-phonon scattering, recorded 95K of the highest operation temperature in 2004 [147]. Thermal backfilling and rather weak population inversion seem to be limitations for enhancement of device characteristics. 4~4.5THz of lasing frequency range and several ten mW of output power have been reported in the chirped-superlattice structures.

Bound-to-Continuum Another carrier transport method used in the early work of THz QCLs is the bound-to-continuum (B-to-C) carrier transport (Figure 1.18 (c)) [71, 72, 148-158]. Like Chirped-SL devices, B-to-C devices also use mini-bands, but an isolated bound state inside a miniband is used as ULS for population inversion. Diagonal optical transition of the B-to-C method, compared to Chirped-SL method, can reduce the non-radiative transport rate between lasing subbands, resulting in longer carrier lifetime of ULS and

enhancement of temperature characteristics. The highest operating temperature of B-to-C devices was recorded to be 122K by an InGaAs-based device [72], and the lasing frequency range is 1.2~3.5THz. Output power of B-to-C devices reported so far is under 100mW.

Hybrid Depopulation of LLS is enforced by adding LO-phonon carrier scattering into the lower mini-band of the B-to-C carrier transport method, and this is called hybrid (Hybrid) method as shown in Figure 1.18 (d) [93, 94, 139, 159-164]. In terms of the highest operation temperature, lasing up to 160K was achieved by this method [161], and this method is often used for high output power device research. 2.4W of the highest power has been reported under the low temperature conditions. Lasing frequency ranges from 3.0 to 4.5THz.

Resonant-phonon A carrier transport method most frequently reported, is the resonant-phonon (RP) transport method (Figure 1.18 (e) and (f)) [70, 90-92, 95, 96, 105- 107, 110, 111, 165-190]. Where, carriers transfer between subbands, and LLS is depopulated by LO-phonon scattering solely. One module is composed of two to five quantum wells, and the number of subband relating to optical transition is three to six. Because carriers are injected into ULS by resonant tunneling, the theoretical limit of carrier occupancy of ULS is 50%. However, the record highest operation has been renewed by this method: 164K by Williams *et al.* with a four-well device [106], 199.5K by Fathololoumi *et al.* with a three-well device [92], and 261K by Khalatpour with a two-well device [70]. High output power of 1.3W is also reported [95]. Reported lasing frequency of RP devices is from 2 to 4.5THz.

Double resonant-phonon The double resonant-phonon (Double RP) scheme was introduced to suppress carrier back-filling from an injection state to LLS by using LO-phonon scattering twice subsequently (Figure 1.18 (g)) [191, 192]. However, the highest operation temperature of the double RP method was not improved and remains 172K.

Indirectly-pumped Another method using LO-phonon scattering is the indirectly-pumped (IDP) or scattering assisted (SA) method (Figure 1.18 (h)) [112, 116, 136, 193-201]. In this method, carriers are first injected from the adjacent module to an injection state and are extracted by LO-phonon scattering to ULS. By this method, the injection limitation of the RP scheme is resolved. Furthermore, LO-phonon scattering can be used for carrier extraction from LLS of IDP devices, as described in Figure 1.18 (i). This method is called Phonon-Photon-Phonon (3P) scheme and is similar to the double RP scheme in a point of using LO-phonon carrier abstraction twice. In the recent research, carriers not only in an injection state but also in LLS are also proposed to be withdrawn by resonant tunneling [198, 199]. The highest operation temperature of IDP devices is 163K [112], and lasing frequency is 2~3THz.

Ground state In 2012, Chan *et al.* demonstrated the ground state (GS) scheme [203]. The carrier transport of this method is very similar to the one of RP devices but is established by only ground states in quantum wells as depicted in Figure 1.18 (j). Excited states, happen in high energy region, often align with other subbands in the adjacent modules, resulting in parallel leakage paths. The highest operation temperature demonstrated by Chan *et al.* is 71K.

(a)

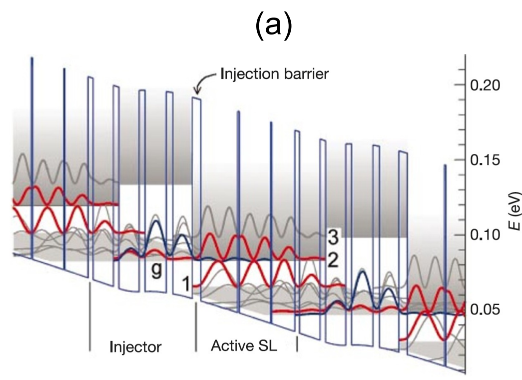

(b)

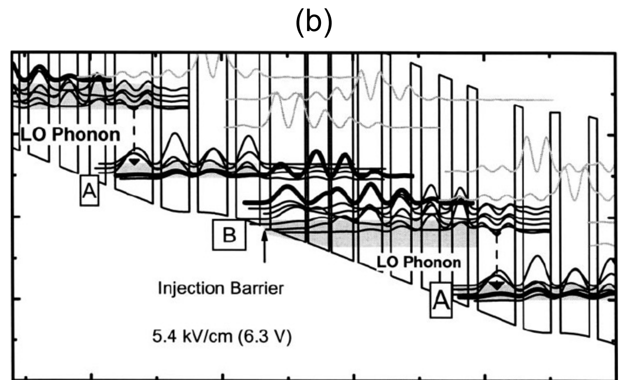

(c)

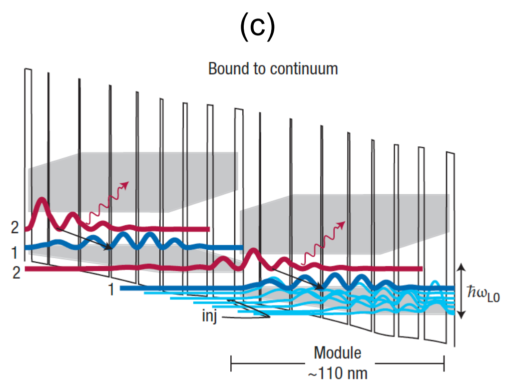

(d)

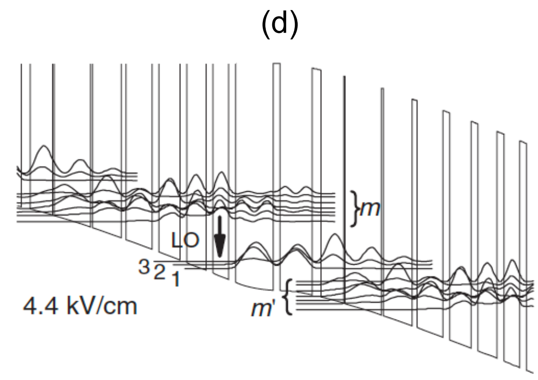

(e)

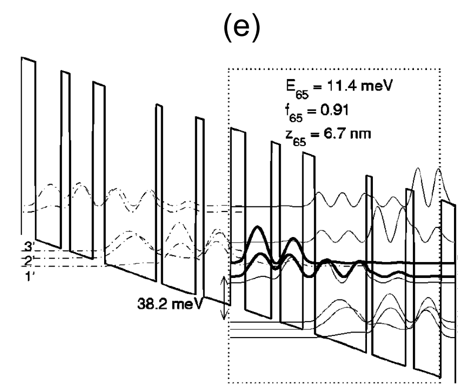

(f)

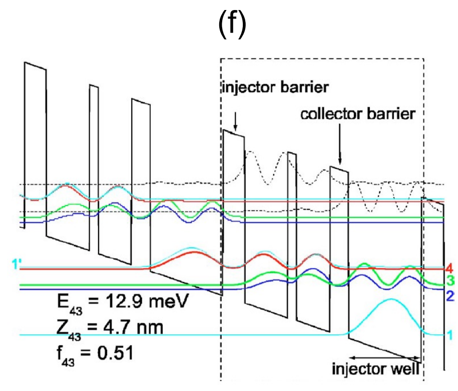

(g)

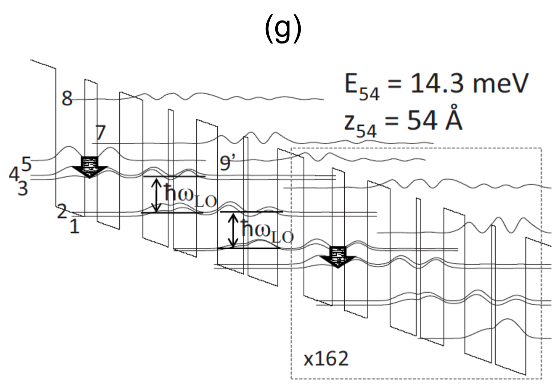

(h)

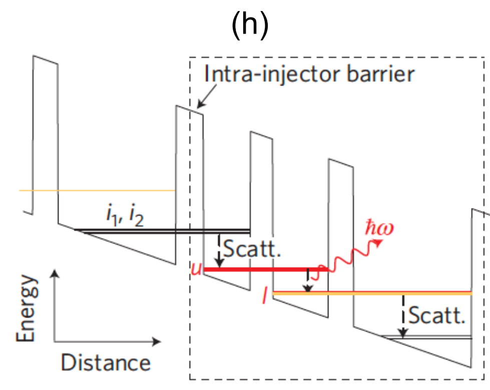

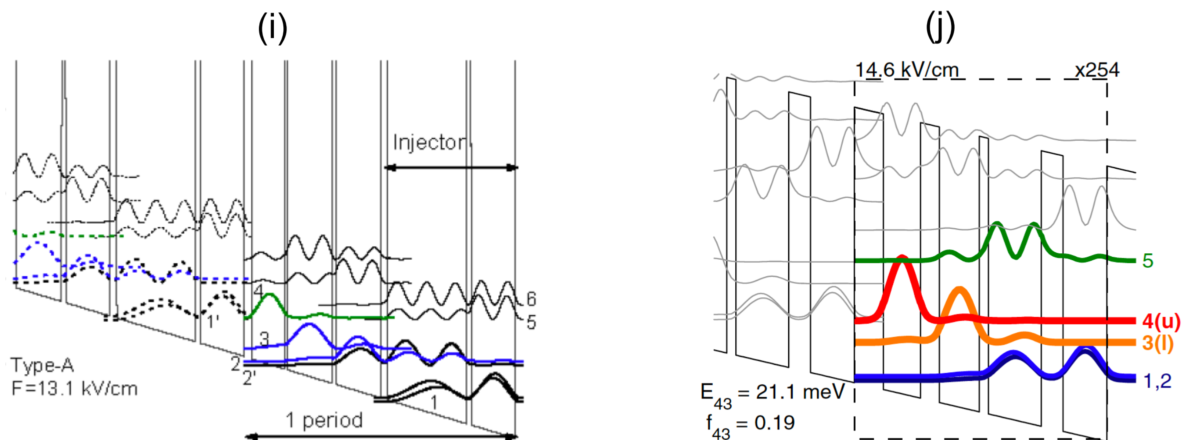

Figure. 1.18 Carrier transport methods. (a) Chirped superlattice [61], (b) Interlaced [147], (c) Bound-to-Continuum [141], (d) Hybrid [162], (e) Five-well resonant-phonon [165], (f) Three-well resonant-phonon [107], (g) Double resonant-phonon [192], (h) Scattering assisted [112], (i) Phonon-Photon-Phonon [200], and (j) Ground state structure [203].

Since the first demonstration, development of THz QCLs had been continued without confirmed assurance about the best carrier transport scheme though the record highest operation temperature had been renewed by the RP scheme. An answer for this question was indicated by Bosco *et al.*[111]. In their paper, they showed that the carrier use efficiency (a ratio of carrier density of ULS to total) is improved when the number of subbands per module is fewer, resulting in higher operation temperature. For example, the carrier use efficiency of B-to-C devices is 21%, and the highest operation temperature is 116K. In SA or RP scheme, these parameters increase to 30% and 199.5K. Ultimately, two-well resonant-phonon scheme has 37% of efficiency and 210.5K of the highest temperature as shown in Figure 1.19. Due to this discovery, two-well resonant-phonon scheme has been intensively investigated these days.

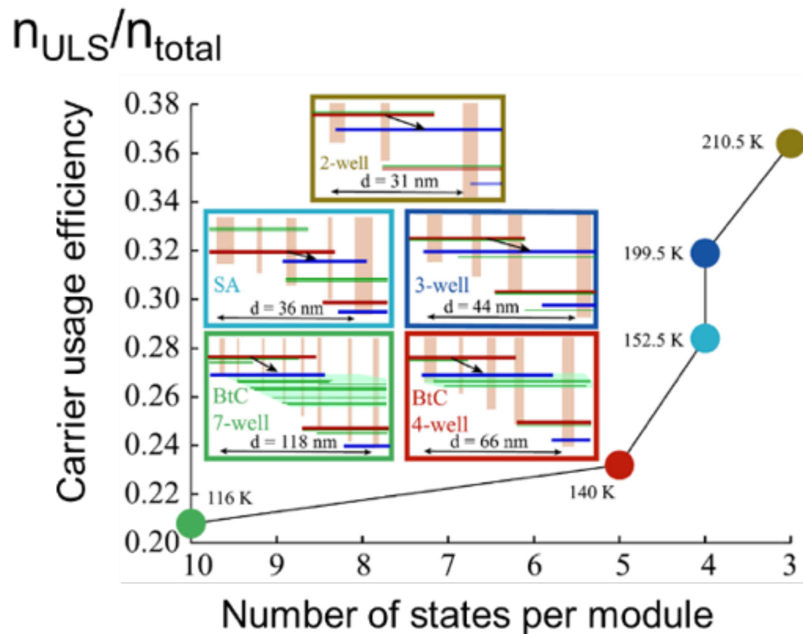

Figure. 1.19 The number of subbands per module vs carrier use efficiency. [111]

[B] Material System

In previous studies, THz QCLs are mostly fabricated with the GaAs/AlGaAs material system which has a small lattice constant mismatch between GaAs and AlGaAs and is suitable for lower barrier devices required for THz QCLs. On the other hand, other material systems have also been investigated: InGaAs/AlInAs, InGaAs/GaAsSb, InGaAs/AlInGaAs, GaSb/AlGaSb, and InAs/AlAsSb [77, 157, 158, 164, 176, 185-187, 200, 204-206]. Because optical gain is inversely proportional to the effective mass in theory, these material systems which have the smaller effective mass than the one of GaAs-based material systems are expected to improve the optical gain and the highest operation temperature. In contrast with

such expectation, the demonstrated operation temperatures of these devices have not been so high as the one of GaAs-based material system. Even though worse interface-roughness or inferior quality of crystals are pointed out as the reasons, this explanation would be inadequate because MIR QCLs have been successfully demonstrated and commercialized with these material systems, and clearer explanation is required. Material systems influence on barrier height (conduction band-offset), and Barrier height study of this work showed an idea relating to a relation between material systems and device characteristics in Chapter 4.

The other reason for using different material systems from GaAs-based system is to avoid the Reststrahlen band. As described above, devices composed of the III-V group materials which have zincblende crystal structures tend to have the Reststrahlen band over a range of 5 to 10THz and are considered to lase in this frequency range. To resolve this issue, GaN-based THz QCLs have already started to be investigated [78, 190].

Material system (Effective mass ratio)		Conduction band offset ΔE_c [meV]	Highest operation temperature [K]
Well	Barrier		
GaAs (0.067)	$Al_xGa_{1-x}As$ (0.079~0.104)	136.2 ~ 363.9	250
$In_{0.53}Ga_{0.47}As$ (0.043)	$Al_{0.48}In_{0.52}As$ (0.075)	520	155
$In_{0.53}Ga_{0.47}As$ (0.043)	$GaAs_{0.51}Sb_{0.49}$ (0.045)	360	142
$In_{0.53}Ga_{0.47}As$ (0.043)	$Al_{0.17}InGa_{0.83}As$ (0.057)	140	130
InAs (0.023)	$AlAs_{0.16}Sb_{0.84}$ (0.120)	2210	Low temperature

Table.1.1 Comparison of different material systems in conduction band offset and the highest operation temperature.

[C] Impurity Doping

Impurities need to be doped in an injection region of QCLs to supply carriers for optical carrier transport, and a certain level of doping (carrier) density is necessary for high optical gain or output power. (Output power is proportional to electrical current, and current is also proportional to carrier density.) However, too high doping density can increase non-radiative carrier transition between lasing subbands, optical linewidth broadening, band-bending, and waveguide loss, which are disadvantageous for lasing. These degradations are not so remarkable in MIR QCL or early THz QCL structures which separate doping and radiation regions far enough in a large structure, but recent THz QCLs such as RP devices have a doping region near a radiation region, so more attention is necessary for device design. In recent RP or other recent THz QCLs have a narrow-doped region in the center of a phonon-well.

Research for the influence of impurity doing is one of the main topics in this work (Doping study), and the details about background, simulation results, and discussion will be described in Chapter 3.

[D] Barrier Height

Most of recent THz QCLs, including the ones that have renewed the highest operation temperature, are composed of GaAs/AlGaAs material system with 15~30% of Al-composition. However, the influence of barrier height has yet been cleared enough because

many physical phenomena inside device can vary due to barrier height, and device characteristics are determined by complicated interaction of such phenomena. In 2018, Kainz *et al.* varied Al-composition from 12% to 24% of a three-well resonant-phonon THz QCLs experimentally and found that 20% of Al-composition provided the highest operation temperature [182]. However, in 2020, Khalatpour *et al.* demonstrated the higher operation temperature with 30% of Al-composition with a two-well resonant-phonon device [224]. As one of the clarified things, interface-roughness scattering is proportional to barrier height. So, if high barrier is used for a radiation barrier, increased interface-roughness scattering can enhance non-radiative transition and reduce carrier lifetime of ULS. On another front, when barrier is too low, carrier confinement becomes weak, which can increase leakage current from bound states to continuums as shown in Figure 1.20.

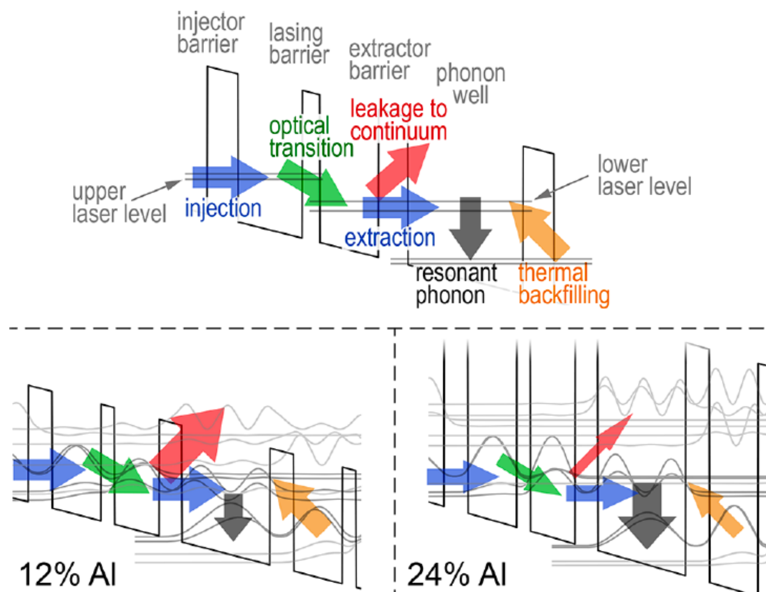

Figure. 1.20 The influence of barrier height [182].

Research for the influence of barrier height is also one of the main topics in this work (Barrier height study), and the details about background, simulation results, and discussion will be described in Chapter 4 and 5.

[E] Structural complexity

In THz QCL design, wavefunction and subband energy are basically designed by tuning barrier height, layer thickness, alignment field conditions, and so on, for high optical gain. In addition to simple device designs, structural complexities such as different barrier height or well depth and step-well structure enable more scrupulous tuning (Figure 1.21) [95, 188, 207-213]. For example, injection and radiation barriers can be designed with different Al-composition because these two barriers have different roles for carrier transport. On the one hand, an injection barrier can affect resonant tunneling rate. On the other hand, radiation barrier is a key to the balance between radiative and non-radiative transitions. Therefore, different barrier height is a reasonable design scheme. As another example, a split-well structure, where a very thin barrier is inserted in the middle of a well, is demonstrated by Albo *et al.* in 2019 [210, 211]. Split-well structures are useful to adjust the excited state which can be a leakage path from ULS. Structural complexities are introduced depending on focusing design parameters of standard structures, so various ideas are expected to be proposed in the future.

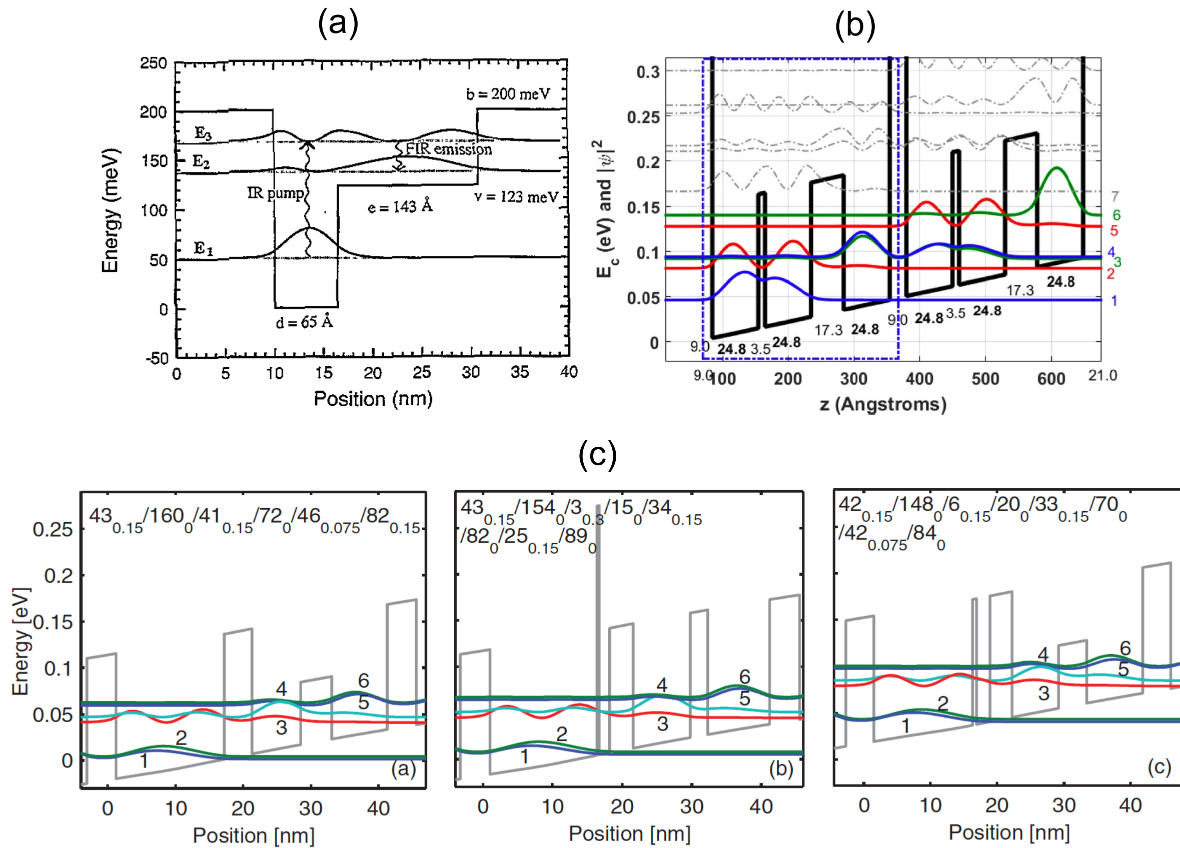

Figure. 1.21 Examples of structural complexity. (a) A stepped-well [212] (b) A split-well structure [210, 211]. (c) Different height of barriers [208].

[F] Others

Finally, device structures are determined by adjusting layer thicknesses and alignment field. Layer thickness affects spreading of wavefunction and carrier transition rate, so careful tuning is necessary. Too thick barrier may impede carrier transition, on the other hand, too thin barrier would deteriorate injection selectivity or impair thickness control by MBE. Alignment field is related to power consumption of devices and self-heating effect.

Electrical current tends to increase under high field, so output power can be enhanced as well.

Except for these design components, we can design devices based on some device parameters such as oscillator strength, coupling strength, LO-phonon scattering rate, and so on.

This work investigates the influence of layer thickness and alignment field, and the results will be described in Chapter 5.

1.3.3.2 Degradation Mechanism Analysis

Analysis of degradation mechanisms of THz QCLs under high temperature conditions has also been intensively examined because room-temperature operation, which is necessary for anticipated THz applications, is very challenging. So far, four degradation mechanisms have been studied: thermally activated LO-phonon scattering, thermal backfilling, carrier leakage to bound/continuum states, and optical linewidth broadening. Depending on carrier transport methods, some of these degradation mechanisms can be influential, and a consensus about dominant mechanisms is also not gained among researchers. Besides, waveguide loss, increases with temperature, is also considered as one of the temperature degradation mechanisms of THz QCLs.

Thermally activated LO-phonon scattering Among several degradation mechanisms of THz QCLs, thermally activated LO-phonon scattering is mostly accepted by many researchers [214-216]. Under high temperature, LO-phonon scattering between lasing

states increases, resulting in degradation of lifetime of ULS and population inversion. Because there is a trade-off between thermally activated LO-phonon scattering and radiative transition between lasing states, thermally activated LO-phonon scattering cannot completely suppressed even if other design components are carefully adjusted.

Thermal backfilling Population inversion can degrade by thermally agitated carriers into LLS from the lower state, and this mechanism is called thermal backfilling [217, 218]. This phenomenon is considered as the main degradation mechanism in Chirped-SL and B-to-C devices which include mini-bands. Although thermal backfilling can be considered to be the main degradation mechanism in other types of devices, it is also difficult to distinguish the effect of thermally activated LO-phonon scattering and thermal backfilling because both degradation mechanisms can increase carrier density of LLS. In RP devices, it is considered that thermal backfilling is not the main degradation factor based on a fact that the energy difference between LLS and injection state is wide enough compared to Chirped-SL and B-to-C devices and that the temperature characteristics are not improved in double-RP and IDP devices, which adopt two times of LO-phonon depopulation per module.

Carrier leakage from ULS Carrier leakage from ULS can also degrade population inversion, and two leakage paths have been studied: ULS to continuums, and ULS to high energy bound states of an adjacent module [179, 181, 219, 220]. For example, Albo *et al.* demonstrated that devices composed of 30% of Al-composition can supress carrier leakage into continuums instead of 15% devices. In a different study implemented by Lin *et al.* they

avoided subband alignment between ULS and a high energy state in an adjacent module by adjusting device structures, and successfully enhanced device performance.

Optical linewidth broadening In addition to population inversion, optical linewidth is also one of the componential parameters of optical gain, and optical gain is inversely proportional to optical linewidth in theory. Optical linewidth is determined by several scattering phenomena, so temperature-sensitive scattering phenomena can broaden optical linewidth under high temperature conditions. So far, the influence of ionized-impurity and interface-roughness scatterings have been reported [221-223].

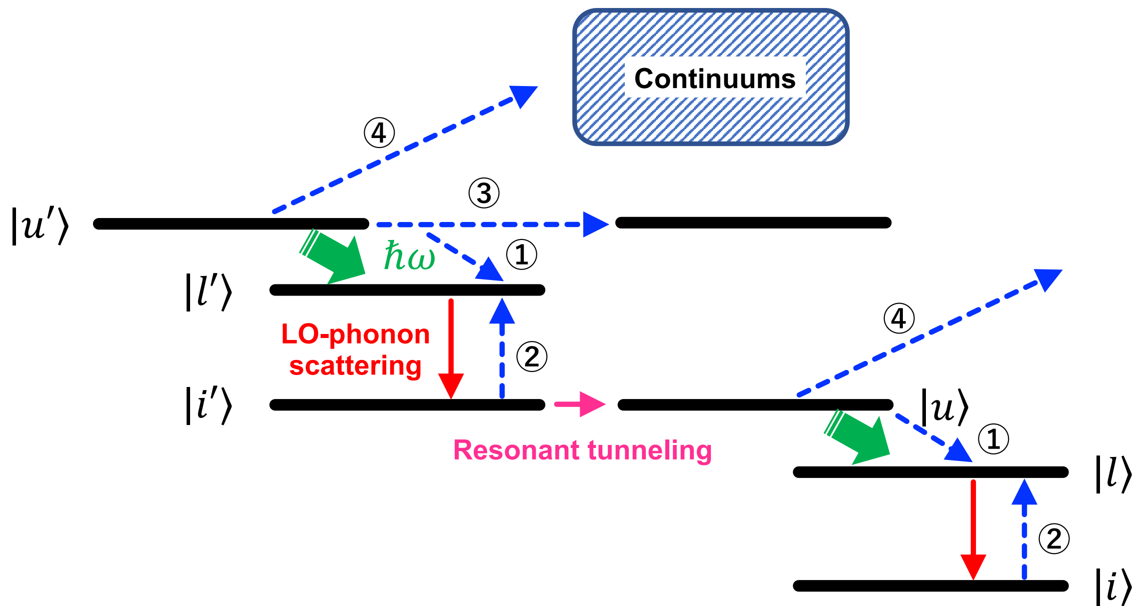

Figure. 1.22 Thermal-degradation processes in THz QCLs. ①Thermally activated LO-phonon scattering, ②Thermal backfilling, ③Leakage to high energy states, and ④Leakage to continuum states.

1.4 Research Objective and Thesis Organization

The objective of this work is to establish device design guidelines for high-performance THz QCLs. QCLs are designed by considering a balance of design components: carrier transport methods, material systems, impurity doping, barrier height, structural complexity, layer thickness, and alignment field. Among these design components, Bosco *et al.* demonstrated that carrier transport methods with fewer number of subbands are advantageous for high temperature operation, but preferable design ideas about other components remain unclear.

Thus, this work bases two-well resonant-phonon devices to thoroughly investigate the influence of impurity doping and barrier height on device characteristics theoretically and find optimal design conditions. Although the best conditions of aforementioned components could vary depending on carrier transport methods, the two-well resonant-phonon scheme is selected for this work due to some advantages of it: ease of observing and understanding essential impacts of design components on device characteristics due to structural simplicity, and possibility to use obtained results in research on more complicated structures such as several-well RP or IDP devices. Even though the focus of this work is ionized-impurity and barrier height, the influence of other components: material system, alignment field, and layer thickness are also investigated as side-topics and discussed as much as possible. Through this work, GaAs/AlGaAs material system is consistently used.

A device simulator is developed in this work based on a rate equation model proposed by Razavipour. The simulator developed by Razavipour is able to reproduce

characteristics of IDP devices well, but calculation errors are observed in simulation for RP devices in terms of current density and highest operation temperature. This would be attributed not to fundamental limitation of the rate equation but to lack of some important physical phenomena. So, this work improves the calculation accuracy by introducing such models of physical phenomena. As for physical phenomena which have several mathematical models, this work traces the derivation process and incorporates ones considered optimal in simulation.

These objectives in this thesis are organized as follows.

Chapter 2 A device simulator is developed for this work based on the rate equation. In development, several models of physical phenomena are incorporated. Electron-electron scattering model is modified by using Fourier transform for speed-up of calculation. As for the screening effect, several models are compared in terms of versatility, and reasonable one is selected. Optical linewidth and pure dephasing time, which are assumed to be constant in the base simulation method, are modeled based on Ando's theory and incorporated in the developed simulator. Leakage current to continuum and its influence on subband carrier density are described by the third-order tunneling current theory and reflects the influence of barrier height. The lattice temperature is also modeled for a mesa structure of waveguides. Lastly, example calculation for previously published devices is demonstrated.

Chapter 3 Based on a high-performance two-well resonant-phonon THz QCL structure published by Khalatpour *et al.*, the influence of impurity doping (the amount,

position, and distribution) on device characteristics is investigated. Sheet doping density varys from 1.0×10^{10} to 1.0×10^{12} cm^{-2}, and optical gain is calculated as a figure-of-merit. Seven doping profiles are composed of doping position and distribution and are simulated to investigate the influence of doping. An undoped condition, considering only natural doping, is also calculated. From the results, effective doping methods for a single module and for an active core are proposed.

Chapter 4 The influence of barrier height, determined by Al-composition, on two-well resonant-phonon THz QCLs is investigated. In the first half part, leakage current of different devices published in the past is estimated by introducing the third-order tunneling current theory. Later, based on the high-performance device designed by Khalatpour, only barrier height is changed from 12.5% to 45% of Al-composition with fixed layer thicknesses to investigate the influence of barrier height on device characteristics. Based on the calculation results, the influence of material systems which can also influence barrier height, is discussed.

Chapter 5 Following Chapter 4, discussion over the optimal barrier height for two-well resonant-phonon devices continues. Device structure exploration is implemented over a range of Al-composition from 5% to 45%, and high-performance devices are sought by changing layer thickness and alignment field flexibly. In exploration, optical gain is used as a figure-of-merit, and optical gain maps which visualize the relation between the optical gain and design parameters is introduced. Structural tolerance against difference between design and demonstration is also discussed. A new design concept is also discovered and

investigated by simulaiton.

Chapter 6 Lastly, conclusion from Chapter 2 to 5 is summarized.

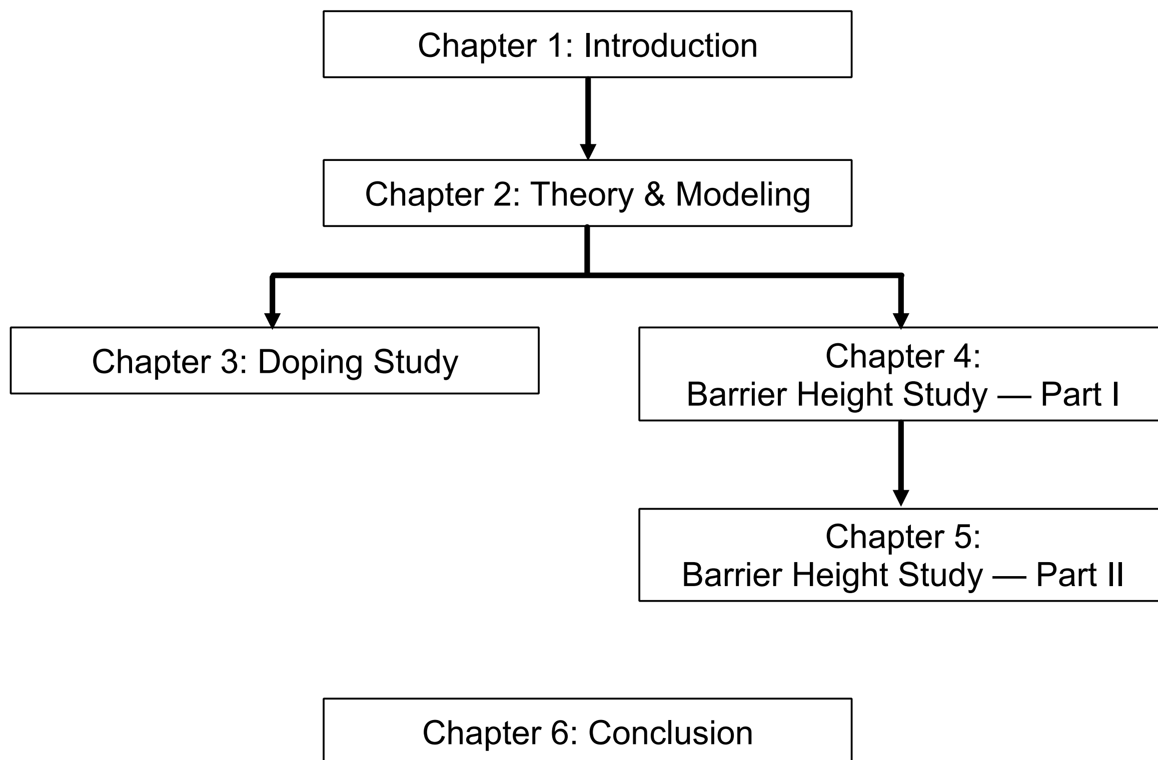

Figure. 1.23 Outline of this thesis

When one’s expectations are reduced to zero, one really appreciates everything one does have.

– Stephen William Hawking

Chapter 2 Theory and Modeling

A device simulator developed in this study will be described in this Chapter. The device simulator adopts the rate equation, which is advantageous in terms of simplicity and speed in calculation, is developed by adding some physical phenomena to a base model introduced by Razavipour for expansion and further accuracy [225]. This calculation, Rate equation – Full model, is used in our theoretical works shown in Chapter 3 to 5, and a modified model is also used to enhance calculation speed by omitting a couple of phenomena in the first half part of Chapter 5 as Rate equation – Limited model.

2.1 Overview

First of all, the background and calculation flow of the developed device simulator will be explained. The rate equation method, adopted in this work, has often been used for the research on semiconductor lasers by many researchers since olden days and has contributed to advancement of research and development of semiconductor lasers [58]. The rate equation, which is a semi-classical calculation, is advantageous in terms of clear description of physical phenomena and calculation speed. Even though resonant-tunneling carrier transport between modules cannot be described by Fermi's golden rule in the rate equation, this issue was resolved by Scalari *et al.* introducing a tunneling time model derived from the Liouville equation [59,139].

The rate equation is a set of simultaneous differential equations to calculate subband carrier density, and inflow and outflow of carriers in subbands are described by coherent and incoherent carrier transport rates. On the one hand, coherent carrier transport means resonant tunneling which happens when subbands are aligned. On the other hand, incoherent carrier transport means carrier scattering which is a random move of carriers due to the environmental factors in QCLs. There is a precondition in Razavipour's model. Where intra-module carrier transport is described by incoherent transport, and the one between modules is described by coherent transport as described in Figure 2.1. This precondition is considered to be determined on an assumption that incoherent carrier transport can happen between modules in reality but do not happen in simulation due to thick barrier defining a single module (in most cases, injection barrier).

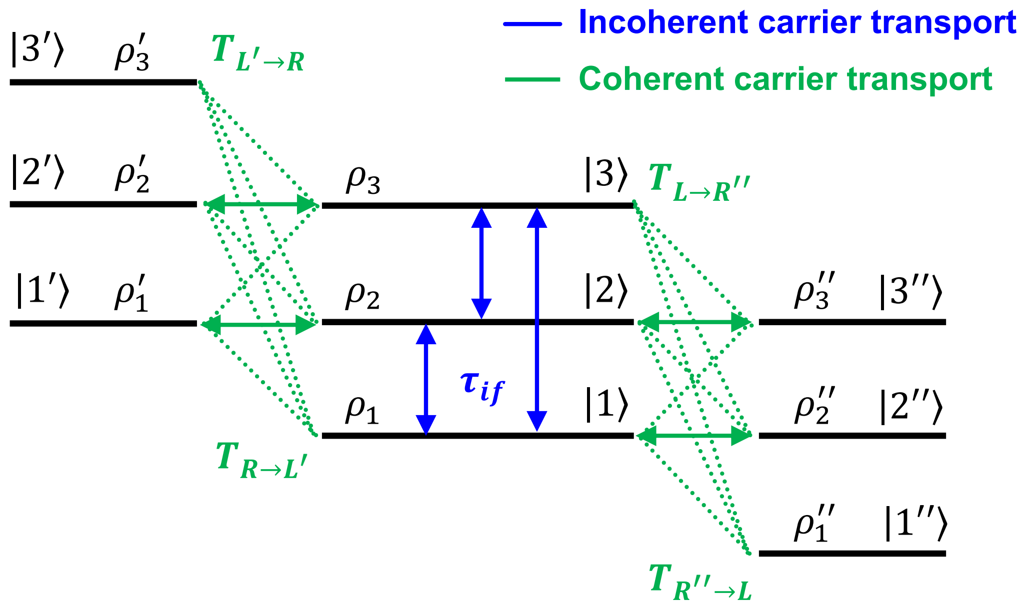

Figure. 2.1 Carrier transport considered in the rate equation model.

The structure of the device simulator is composed of two steps: (1) building and solving the rate equation, and (2) calculating device parameters such as current density and optical gain by using obtained subband carrier density. Each step is also established by several theories and device parameters, which makes the whole calculation very complicated. Furthermore, self-consistent loop calculation is preferred for some device parameters. For example, band-bending effect is calculated based on localized carriers and ionized dopants. The electron temperature is also calculated by using subband carrier density. However, in order to obtain spatial carrier distribution or subband carrier density, the rate equation needs to be solved with assumed values of band-bending or the electron temperature. So, the rate equation itself is very simple, but a series of device simulation can be complicated as described in Figure 2.2. In Figure 2.2, the calculation procedure for device characteristics with main device parameters is briefly described although parts of relation between device parameters are omitted.

In calculation of device parameters shown in Figure 2.2, there are several approaches for some parameters even though others are calculated by steady ways. So, details about the theories and calculation methods used in this work are described from Section 2.2 ~ 2.8. The calculation procedure coded by using MATLAB is also explained in Section 2.9. Self-consistent loop calculation suggested in Figure 2.2 is altered by different ways. Finally, an example of two-well resonant-phonon device designed by Khalatpour *et al.* is also calculated and detailed data is described in Section 2.10 [224].

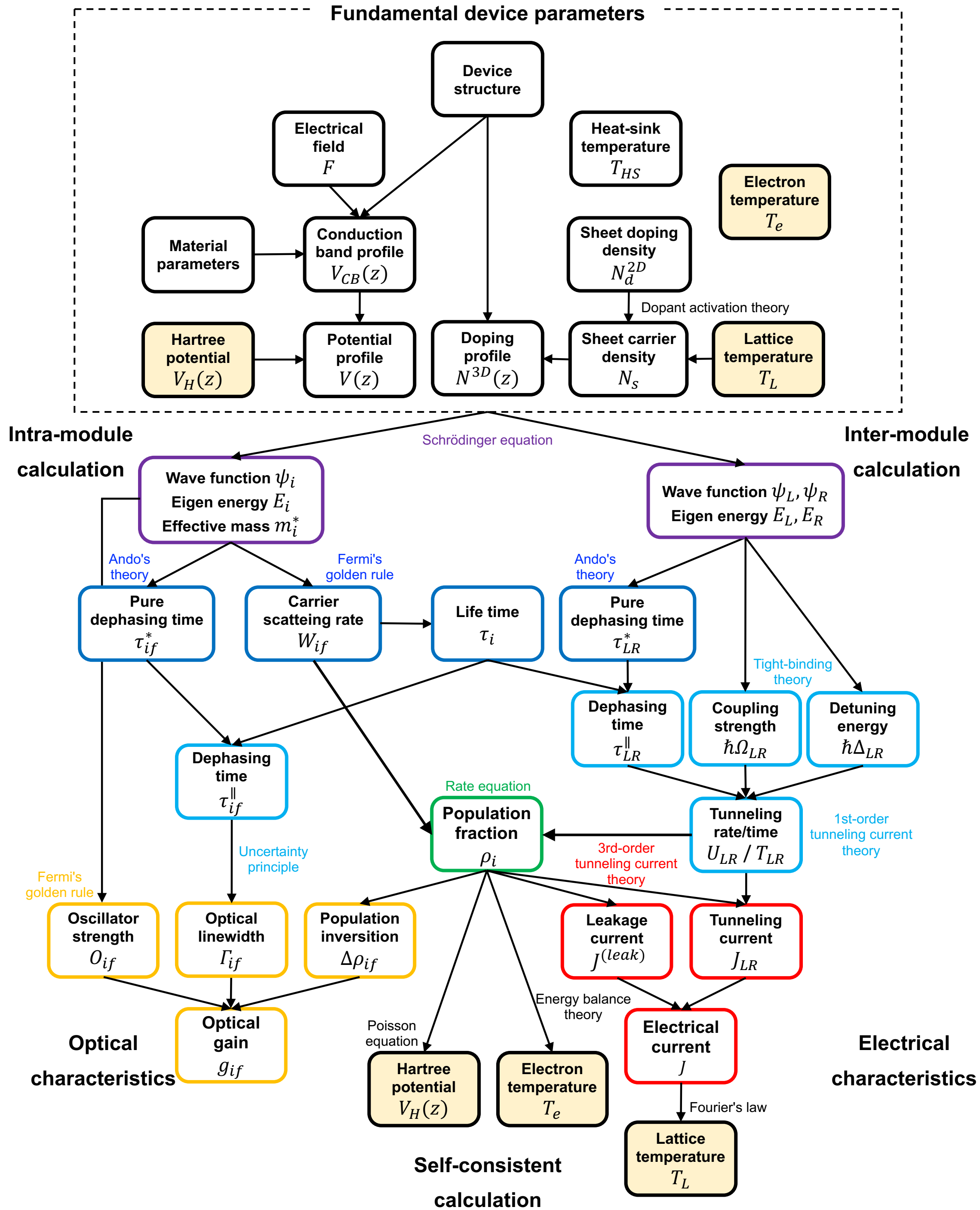

Figure. 2.2 Device parameters and a brief calculation procedure of the rate equation. For Hartree potential, electron temperature, and lattice temperature, iterative calculation is necessary.

2.2 Schrödinger Equation

Wavefunction and subbands are indispensable to calculate other device parameters of QCLs and are calculated by solving the Schrödinger equation. Due to different mathematical views, there are several solutions for the Schrödinger equation: the transfer matrix method (TMM), shooting method, finite difference method (FDM), and so on [59,113]. Furthermore, the band non-parabolicity effect, a phenomenon that the E-k dispersion relation has difference from a quadratic function for high-energy electrons, also needs to be considered in calculation [59]. In addition to several solutions for the Schrödinger equation, different methods for introducing the band non-parabolicity effect are also proposed. So, a variety of calculation methods for the Schrödinger equation are considered. In this study, a finite different calculation proposed by Cooper *et al.* is adopted in the simulation due to less phenomenological parameters [226], and several calculation methods are compared.

The calculation starts with the one-dimensional time-independent Schrödinger equation. In double-hetero junctions, the effective mass of well material and barrier material is different, so the effective mass is dealt with as a function of the position. In here, $\hbar$ is the reduced Plank constant, m^* is the electrons' effective mass at the bottom of the conduction band, ψ is a wave function, V is the potential profile of the conduction band, and E is the eigen-energy.

$$-\frac{\hbar^2}{2}\left(\frac{\partial}{\partial z}\frac{1}{m^*(z,E)}\frac{\partial \psi}{\partial z}\right)+V(z)\psi(z)=E\psi(z) \tag{2.1}$$

2.2.1 Finite Difference Method

The finite difference method is one of the most popular approximations to solve differential equations numerically, and there are several variations depending on the accuracy. For example, the simplest method considers only difference between two terms based on the definition of differentiation and is described with discretization number n.

$$\frac{df}{dz} \equiv \lim_{\delta z \to 0} \frac{f(z+\delta z) - f(z)}{(z+\delta z) - z} \to \frac{f_{n+1} - f_n}{\Delta z} \tag{2.2}$$

This approximation is effective for many differential equations but can lead calculation errors in the Schrödinger equation. Thus, the second-order approximation using half-integers is applied in this work.

$$\frac{df}{dz} \equiv \lim_{\frac{\delta z}{2} \to 0} \frac{f\left(z+\frac{\delta z}{2}\right) - f\left(z-\frac{\delta z}{2}\right)}{\left(z+\frac{\delta z}{2}\right) - \left(z-\frac{\delta z}{2}\right)} \to \frac{f_{n+\frac{1}{2}} - f_{n-\frac{1}{2}}}{\Delta z} \tag{2.3}$$

Using Eq. (2.3), the Schrödinger equation is solved without band non-parabolicity effect. First, only second-order differential term is modified. Here, the energy-dependence of effective mass is ignored.

$$\frac{\partial\left\{\frac{1}{m^*(z,E)}\frac{\partial\psi}{\partial z}\right\}}{\partial z} \to \frac{\frac{1}{m^*(z+\Delta z)}\left(\frac{\partial\psi}{\partial z}\right)_{z+\Delta z} - \frac{1}{m^*(z-\Delta z)}\left(\frac{\partial\psi}{\partial z}\right)_{z-\Delta z}}{2\Delta z}$$

$$= \frac{\frac{1}{m^*(z+\ \Delta z)}\cdot\frac{\psi(z+\ 2\Delta z)-\ \psi(z)}{2\Delta z}\ -\ \frac{1}{m^*(z-\ \Delta z)}\cdot\frac{\psi(z)-\ \psi(z-\ 2\Delta z)}{2\Delta z}}{2\Delta z}$$

$$= \frac{1}{(2\Delta z)^2}\left[\frac{\psi(z+\ 2\Delta z)-\ \psi(z)}{m^*(z+\ \Delta z)} - \frac{\psi(z)-\ \psi(z-\ 2\Delta z)}{m^*(z-\ \Delta z)}\right]$$

Now, $2\Delta z\ \rightarrow\ \delta z$.

$$\rightarrow \frac{1}{(\delta z)^2}\left[\frac{\psi(z+\ \delta z)-\ \psi(z)}{m^*\left(z+\frac{\delta z}{2}\right)} - \frac{\psi(z)-\ \psi(z-\ \delta z)}{m^*\left(z-\frac{\delta z}{2}\right)}\right]$$

$\delta z\ \rightarrow\ \Delta z$.

$$\rightarrow \frac{1}{(\Delta z)^2}\left[\frac{\psi_{n+1}-\ \psi_n}{m^*_{n+\frac{1}{2}}} - \frac{\psi_n-\ \psi_{n-1}}{m^*_{n-\frac{1}{2}}}\right]$$

$$= \frac{1}{(\Delta z)^2}\left[\frac{1}{m^*_{n+\frac{1}{2}}}\psi_{n+1} - \left(\frac{1}{m^*_{n+\frac{1}{2}}} + \frac{1}{m^*_{n-\frac{1}{2}}}\right)\psi_n + \frac{1}{m^*_{n-\frac{1}{2}}}\psi_{n-1}\right]$$

Plug this relation into Eq. (2.1).

$$-\frac{\hbar^2}{2}\frac{1}{(\Delta z)^2}\left[\frac{1}{m^*_{n+\frac{1}{2}}}\psi_{n+1} - \left(\frac{1}{m^*_{n+\frac{1}{2}}} + \frac{1}{m^*_{n-\frac{1}{2}}}\right)\psi_n + \frac{1}{m^*_{n-\frac{1}{2}}}\psi_{n-1}\right] + V_n\psi_n = E\psi_n$$

$$-\frac{\hbar^2}{2(\Delta z)^2}\frac{1}{m^*_{n+\frac{1}{2}}}\psi_{n+1} + \left[\frac{\hbar^2}{2(\Delta z)^2}\left(\frac{1}{m^*_{n+\frac{1}{2}}} + \frac{1}{m^*_{n-\frac{1}{2}}}\right) + V_n\right]\psi_n - \frac{\hbar^2}{2(\Delta z)^2}\frac{1}{m^*_{n-\frac{1}{2}}}\psi_{n-1} = E\psi_n$$

Using a relation $m^*_{n+\frac{1}{2}} = \frac{1}{2}(m^*_{n+1} + m^*_n)$.

$$-\frac{\hbar^2}{(\Delta z)^2}\frac{1}{(m^*_{n+1} + m^*_n)}\psi_{n+1} + \left[\frac{\hbar^2}{(\Delta z)^2}\left(\frac{1}{m^*_{n+1} + m^*_n} + \frac{1}{m^*_n + m^*_{n-1}}\right) + V_n\right]\psi_n - \frac{\hbar^2}{(\Delta z)^2}\frac{1}{(m^*_n + m^*_{n-1})}\psi_{n-1} = E\psi_n$$

$$\therefore\ -s_{n+1}\psi_{n+1} + d_n\psi_n - s_n\psi_{n-1} = E\psi_n \tag{2.4}$$

In Eq. (2.4),

$$\begin{cases} s_n = \dfrac{\hbar^2}{(\Delta z)^2}\dfrac{1}{(m^*_n + m^*_{n-1})} \\ d_n = \dfrac{\hbar^2}{(\Delta z)^2}\left(\dfrac{1}{m^*_{n+1} + m^*_n} + \dfrac{1}{m^*_n + m^*_{n-1}}\right) + V_n \end{cases}$$

When the position discretization is $n = 1 \sim N$, Equation (2.4) is written as below.

$$\begin{cases} -s_1\psi_0 + d_1\psi_1 - s_2\psi_2 = E\psi_1 \\ -s_2\psi_1 + d_2\psi_2 - s_3\psi_3 = E\psi_2 \\ -s_3\psi_2 + d_3\psi_3 - s_4\psi_4 = E\psi_3 \\ \vdots \\ -s_{N-1}\psi_{N-2} + d_{N-1}\psi_{N-1} - s_N\psi_N = E\psi_{N-1} \\ -s_N\psi_{N-1} + d_N\psi_N - s_{N+1}\psi_{N+1} = E\psi_N \end{cases}$$

Wavefunction is assumed to be converged in the end of the structure. So, $\psi_0 = \psi_{N+1} = 0$.

A set of these equations are summed as an eigenvalue-eigenvector problem.

$$\therefore \boldsymbol{H}\psi = E\psi \tag{2.5}$$

In Eq. (2.5),

$$\boldsymbol{H} = \begin{bmatrix} d_1 & -s_2 & 0 & 0 & \dots & 0 \\ -s_2 & d_2 & -s_3 & 0 & \dots & 0 \\ 0 & -s_3 & d_3 & -s_4 & \dots & 0 \\ \vdots & \vdots & \ddots & \ddots & \ddots & \vdots \\ 0 & 0 & \dots & -s_{N-1} & d_{N-1} & -s_N \\ 0 & 0 & \dots & 0 & -s_N & d_N \end{bmatrix}, \quad \boldsymbol{\psi} = \begin{bmatrix} \psi_1 \\ \psi_2 \\ \psi_3 \\ \vdots \\ \psi_{N-1} \\ \psi_N \end{bmatrix}$$

Eq. (2.5) can be solved very rapidly by using eigenvalue-eigenvector solver of MATLAB.

2.2.2 Band Non-Parabolicity Effect

The E-k dispersion of an electron, which describes a relation between electron's kinetics energy E^K and momentum k, is derived from the Schrödinger equation under the effective mass approximation and is described by Equation (2.6).

$$E^K = \frac{\hbar^2 k^2}{2m^*} \tag{2.6}$$

Although this relation can be available for explaining many physical phenomena, it is known well that this relation is collapsed for high-energy electrons because the effective mass is influenced by electrons' energy. For high-energy electrons, the kinetic energy of electrons become lower than the one of Equation (2.6), and this phenomenon is called band non-

parabolicity. There are several ways to described band non-parabolicity effect by mathematical forms, and the single band approximation method (1BM) is chosen in this work [59, 224, 226-230]. The energy dependent effective mass of the 1BM is described by Equation (2.7). Where, $E_g(z)$ denotes energy gap.

$$m^*(z,E) = m^*(z)\left[1 + \frac{E - V(z)}{E_g(z)}\right] \tag{2.7}$$

Other methods, two-band method (2BM) [228], three-band method (3BM) [224, 229], and eight-band method (8BM) [230], base the k·p theory to include the band non-parabolicity effect, and input parameters are different from the ones in the 1BM. In these k·p-based methods, a phenomenological parameter, Kane's energy, is necessary. However, compared to effective mass (in the bottom of the conduction band) and band gap which are necessary for the 1BM, the reports for Kane's energy are few and the reported values shows difference among the information sources.

To solve the Schrödinger equation including the band non-parabolicity effect, Equation (2.7) is discretized and incorporated into Equation (2.1), then the equation become non-linear. So, this study uses the solution for a non-linear finite difference method proposed by Cooper *et al.* [226].

2.2.3 Non-Linear Finite Difference Method

Equation (2.7) is discretized as below.

$$m_n^* \rightarrow m_n^*[1 + \alpha_n(E - V_n)] \tag{2.8}$$

In Equation (2.8), α_n is a band non-parabolicity parameter and is described in Equation (2.9)

$$\alpha_n = \frac{1}{E_{g_n}} \tag{2.9}$$

In addition, all half-integer terms are described below.

$$m^*_{n+\frac{1}{2}} = \frac{1}{2}(m^*_{n+1} + m^*_n), \qquad V_{n+\frac{1}{2}} = \frac{1}{2}(V_{n+1} + V_n), \qquad \alpha_{n+\frac{1}{2}} = \frac{1}{2}(\alpha_{n+1} + \alpha_n)$$

Applying these relations to Eq. (2.1), Eq (2.10) is obtained.

$$A_0 + A_1E + A_2E^2 + A_3E^3 = 0 \tag{2.10}$$

In Eq. (2.10),

$$A_0 = a_n\psi_{n-1} + b_n\psi_n + c_n\psi_{n+1} \qquad A_1 = d_n\psi_{n-1} + e_n\psi_n + f_n\psi_{n+1}$$

$$A_2 = g_n\psi_n \qquad\qquad A_3 = h_n\psi_n$$

Furthermore, $a_n \sim h_n$ in $A_0 \sim A_3$ are described below.

$$a_n = -\frac{\hbar^2}{2\Delta z^2}\cdot\frac{1-\alpha_{n+\frac{1}{2}}V_{n+\frac{1}{2}}}{m^*_{n-\frac{1}{2}}}$$

$$b_n = \frac{\hbar^2}{2\Delta z^2}\left(\frac{1-\alpha_{n-\frac{1}{2}}V_{n-\frac{1}{2}}}{m^*_{n+\frac{1}{2}}}+\frac{1-\alpha_{n+\frac{1}{2}}V_{n+\frac{1}{2}}}{m^*_{n-\frac{1}{2}}}\right)$$

$$c_n = -\frac{\hbar^2}{2\Delta z^2}\cdot\frac{1-\alpha_{n-\frac{1}{2}}V_{n-\frac{1}{2}}}{m^*_{n+\frac{1}{2}}} \qquad\qquad d_n = -\frac{\hbar^2}{2\Delta z^2}\cdot\frac{\alpha_{n+\frac{1}{2}}}{m^*_{n-\frac{1}{2}}}$$

$$e_n = \frac{\hbar^2}{2\Delta z^2}\left(\frac{\alpha_{n-\frac{1}{2}}}{m^*_{n+\frac{1}{2}}}+\frac{\alpha_{n+\frac{1}{2}}}{m^*_{n-\frac{1}{2}}}\right)+\left\{\left(1-\alpha_{n+\frac{1}{2}}V_{n+\frac{1}{2}}\right)\alpha_{n-\frac{1}{2}}+\left(1-\alpha_{n-\frac{1}{2}}V_{n-\frac{1}{2}}\right)\alpha_{n+\frac{1}{2}}\right\}V_n - \left(1-\alpha_{n-\frac{1}{2}}V_{n-\frac{1}{2}}\right)\left(1-\alpha_{n+\frac{1}{2}}V_{n+\frac{1}{2}}\right)$$

$$f_n = -\frac{\hbar^2}{2\Delta z^2}\cdot\frac{\alpha_{n-\frac{1}{2}}}{m^*_{n+\frac{1}{2}}}$$

$$g_n = \alpha_{n-\frac{1}{2}}\alpha_{n+\frac{1}{2}}V_n - \left(1-\alpha_{n+\frac{1}{2}}V_{n+\frac{1}{2}}\right)\alpha_{n-\frac{1}{2}}+\left(1-\alpha_{n-\frac{1}{2}}V_{n-\frac{1}{2}}\right)\alpha_{n+\frac{1}{2}}$$

$$h_n = -\alpha_{n-\frac{1}{2}}\alpha_{n+\frac{1}{2}}$$

When the position discretization is $n = 1 \sim N$, Equation (2.10) is described by N×N-matrice, $\mathbf{A}_0 \sim \mathbf{A}_3$.

$$(\boldsymbol{A}_0 + E\boldsymbol{A}_1 + E^2\boldsymbol{A}_2 + E^3\boldsymbol{A}_3)\boldsymbol{\psi} = \boldsymbol{0} \tag{2.11}$$

In Equation (2.11), $\mathbf{A}_0 \sim \mathbf{A}_3$ are described as below.

$$\boldsymbol{A_0} = \begin{bmatrix} b_1 & c_1 & 0 & 0 & \cdots & 0 \\ a_2 & b_2 & c_2 & 0 & \cdots & 0 \\ 0 & a_3 & b_3 & c_3 & \cdots & 0 \\ \vdots & \vdots & \vdots & \ddots & \ddots & \vdots \\ 0 & 0 & 0 & \cdots & b_{N-1} & c_{N-1} \\ 0 & 0 & 0 & \cdots & a_N & b_N \end{bmatrix}, \quad \boldsymbol{A_1} = \begin{bmatrix} e_1 & f_1 & 0 & 0 & \cdots & 0 \\ d_2 & e_2 & f_2 & 0 & \cdots & 0 \\ 0 & d_3 & e_3 & f_3 & \cdots & 0 \\ \vdots & \vdots & \vdots & \ddots & \ddots & \vdots \\ 0 & 0 & 0 & \cdots & e_{N-1} & f_{N-1} \\ 0 & 0 & 0 & \cdots & d_N & e_N \end{bmatrix}$$

$$\boldsymbol{A_2} = \begin{bmatrix} g_1 & 0 & 0 & 0 & \cdots & 0 \\ 0 & g_2 & 0 & 0 & \cdots & 0 \\ 0 & 0 & g_3 & 0 & \cdots & 0 \\ \vdots & \vdots & \vdots & \ddots & \ddots & \vdots \\ 0 & 0 & 0 & \cdots & g_{N-1} & 0 \\ 0 & 0 & 0 & \cdots & 0 & g_N \end{bmatrix}, \quad \boldsymbol{A_3} = \begin{bmatrix} h_1 & 0 & 0 & 0 & \cdots & 0 \\ 0 & h_2 & 0 & 0 & \cdots & 0 \\ 0 & 0 & h_3 & 0 & \cdots & 0 \\ \vdots & \vdots & \vdots & \ddots & \ddots & \vdots \\ 0 & 0 & 0 & \cdots & h_{N-1} & 0 \\ 0 & 0 & 0 & \cdots & 0 & h_N \end{bmatrix}$$

Equation (2.11) is modified, and an expansive matrix is formed.

$$(\boldsymbol{A}_0 + E\boldsymbol{A}_1 + E^2\boldsymbol{A}_2)\boldsymbol{\psi} = -\,E^3\boldsymbol{A}_3\boldsymbol{\psi}$$

$$\Leftrightarrow \begin{bmatrix} \boldsymbol{O_N} & \boldsymbol{I_N} & \boldsymbol{O_N} \\ \boldsymbol{O_N} & \boldsymbol{O_N} & \boldsymbol{I_N} \\ \boldsymbol{A_0} & \boldsymbol{A_1} & \boldsymbol{A_2} \end{bmatrix} \begin{bmatrix} \boldsymbol{\psi} \\ E\boldsymbol{\psi} \\ E^2\boldsymbol{\psi} \end{bmatrix} = E \begin{bmatrix} \boldsymbol{I_N} & \boldsymbol{O_N} & \boldsymbol{O_N} \\ \boldsymbol{O_N} & \boldsymbol{I_N} & \boldsymbol{O_N} \\ \boldsymbol{O_N} & \boldsymbol{O_N} & -\boldsymbol{A_3} \end{bmatrix} \begin{bmatrix} \boldsymbol{\psi} \\ E\boldsymbol{\psi} \\ E^2\boldsymbol{\psi} \end{bmatrix}$$

$$\therefore \begin{bmatrix} \boldsymbol{O_N} & \boldsymbol{I_N} & \boldsymbol{O_N} \\ \boldsymbol{O_N} & \boldsymbol{O_N} & \boldsymbol{I_N} \\ -\boldsymbol{A_3^{-1}A_0} & -\boldsymbol{A_3^{-1}A_1} & -\boldsymbol{A_3^{-1}A_2} \end{bmatrix} \begin{bmatrix} \boldsymbol{\psi} \\ E\boldsymbol{\psi} \\ E^2\boldsymbol{\psi} \end{bmatrix} = E \begin{bmatrix} \boldsymbol{\psi} \\ E\boldsymbol{\psi} \\ E^2\boldsymbol{\psi} \end{bmatrix} \tag{2.12}$$

This linearized equation, Equation (2.12), can be solved by the eigenvalue - eigenvector solver of MATLAB. Even though this method requires a very large PC memory due to a $3N \times 3N$ matrix, the calculation time is very short compared to the transfer matrix method.

2.2.4 Comparison of Numerical Calculations

In this subsection, several methods for solving the Schrödinger equation are compared in terms of eigen energy and calculation time. Calculation methods are determined by several factors, and the major difference is whether it is transfer matrix method (TMM) or finite difference method (FDM). Both TMM and FDM have variations. For example, in TMM, band non-parabolicity or self-consistent loop calculation are optional, and different solution basis, exponential (EXP) and triagonal (TRI) functions, gives a variety in calculation.

To compare these calculation methods, a single quantum well structure composed of a 200Å GaAs-well with $Al_{0.3}Ga_{0.7}As$-barriers are calculated by these methods under no electrical field. As a result, it turns out that the FDM-based calculation is advantageous compared to the TMM-based ones. In comparison, there is no significant difference in eigen energies between the FDM- and TMM-based methods. However, the FDM-based calculations are much faster than the ones of the TMM-based methods. In the TMM-based methods, it is found that the influence of the solution basis (EXP or TRI) is not so impactful on the calculation results, but the calculation speed is faster with the EXP. In addition, the self-consistent loop, which increases calculation time, also does not give so large difference in eigen energy. The 1BM without self-consistent loop can give similar results to the ones calculated with self-consistent loop. (TMM-based calculations could become faster when a parallel computation technique is used.) In the FDM-based methods (1BM, 2BM, and 3BM), there is negligible difference in eigen energy. Among them, the two-band model is the fastest. In all cases, when band non-parabolicity is considered, calculated eigen energy becomes

lower than the ones calculated without band non-parabolicity.

Model #	0	1	2	3	4	5	6	7	8	9
Method	Transfer Matrix Method						Finite Difference Method			
BNP	w/o BNP		1BM (Single band model)				w/o BNP	1BM	2BM	3BM
			No self-consistent loop		Self-consistent loop					
Basis	EXP	TRI	EXP	TRI	EXP	TRI	-	-	-	-
Time [s]	28	53	32	51	803	1615	2	15	4	5

Table. 2.1 Calculation models for Schrödinger equation and calculation speed.

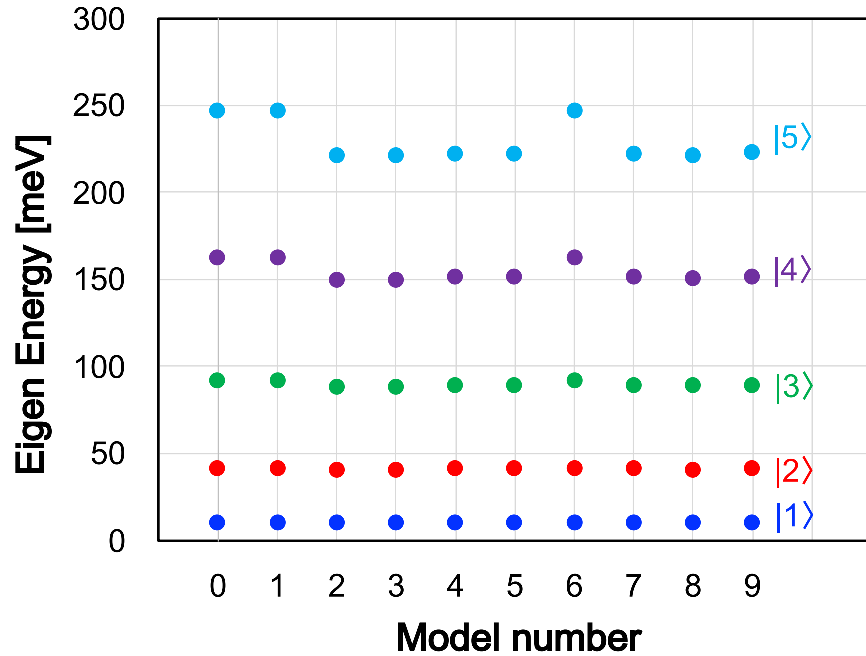

Figure. 2.3 Comparison of calculated eigen-energy

2.3 Incoherent Carrier Transport

Carrier transport in QCLs falls into two types: coherent and incoherent transports, and both types are mathematically described and incorporated in the rate equation. In this section, incoherent carrier transport is explained. Incoherent carrier transport is carrier scattering between subbands, which randomly occurs due to several environmental cause factors, and affects not only subband carrier density but also optical linewidth.

Carrier scattering rate and optical linewidth are calculated by applying the perturbation potential of scattering phenomena to Fermi's golden rule and Ando's theory, respectively [59, 231-234]. This work includes theoretical models of five scattering phenomena: LO-phonon (LO) scattering, electron-electron (EE) scattering, ionized-impurity (IMP) scattering, alloy-disorder (AD) scattering, and interface-roughness (IFR) scattering. In other work, acoustic-phonon (AP) scattering and radiative transition rate are also often included, but these phenomena are not included in the device simulator developed in this work because of its ignorable influence compared to other scattering phenomena. Furthermore, the screening effect is also considered in LO-phonon and Coulomb scatterings. These phenomena are influenced by the Coulomb force from the external components (e.g. other electrons or dopants). The screening effect model has been discussed for long years and has several variations, so the validity of these models is also considered in the later subsection. Based on scattering rate and optical linewidth, carrier lifetime in subbands and pure-dephasing time (or energy blurring) are calculated.

Several factors relating incoherent transport, which are not included the base model

by Razavipour, are considered in this work. First, although the original model of electron-electron scattering rate takes a lot of calculation time, this model is modified by the Fourier transform and successfully reduces calculation time by reducing the number of variables. Optical linewidth and pure dephasing time, not dealt with in many previous studies, are also modeled and incorporated in the rate equation.

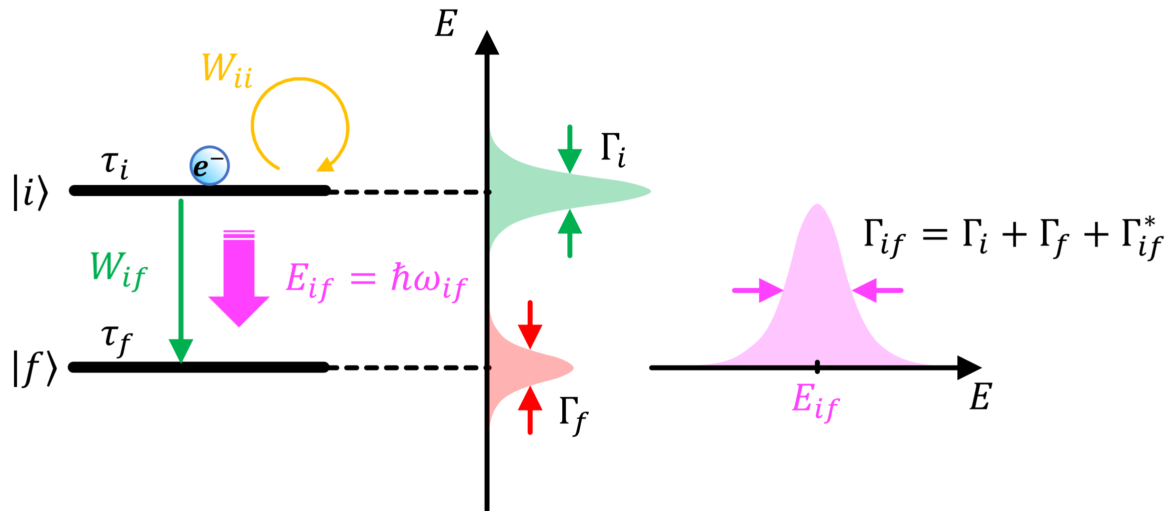

Figure. 2.4 Incoherent carrier transport and related device parameters.

2.3.1 Fermi's Golden Rule

Fermi's golden rule describes carrier transition rate between two subbands and is originally derived from the time-dependent Schrödinger equation by applying a scattering potential as a perturbation Hamiltonian. When an electron transfers from subband $|i\rangle$ to $|f\rangle$ due to a cause scattering phenomenon X (LO, EE, IMP, AD, or IFR), its scattering rate $W_{if}^{(X)}$ is described in Equation (2.13) [59].

$$W_{if}^{(X)}(k_i) = \frac{1}{\tau_{if}^{(X)}} = \frac{2\pi}{\hbar}\left|\langle f\middle|\tilde{H}_s^{(X)}\middle|i\rangle\right|^2 \delta\left(E_i^T - E_f^T\right) \tag{2.13}$$

In Equation (2.13), $\tilde{H}_s^{(X)}$ denotes a scattering potential due to a cause scattering phenomenon X, and E_i^T and E_f^T are total energy (a sum of kinetic and potential energies) of electrons in the initial and final states, respectively. From this equation, it is confirmed that scattering happens only when electrons' energy is conserved before and after scattering (Energy conservation law), and scattering rate is roughly predicted to be large when a spatial overlap of two wavefunctions ψ_i and ψ_f and a cause scattering phenomenon is wide (Scattering matrix element) as described in Figure 2.5. In order to obtain the final form of carrier scattering rate from Equation (2.13), several approximations or simplifications are necessary, and the detail of derivation is described in a reference book [59].

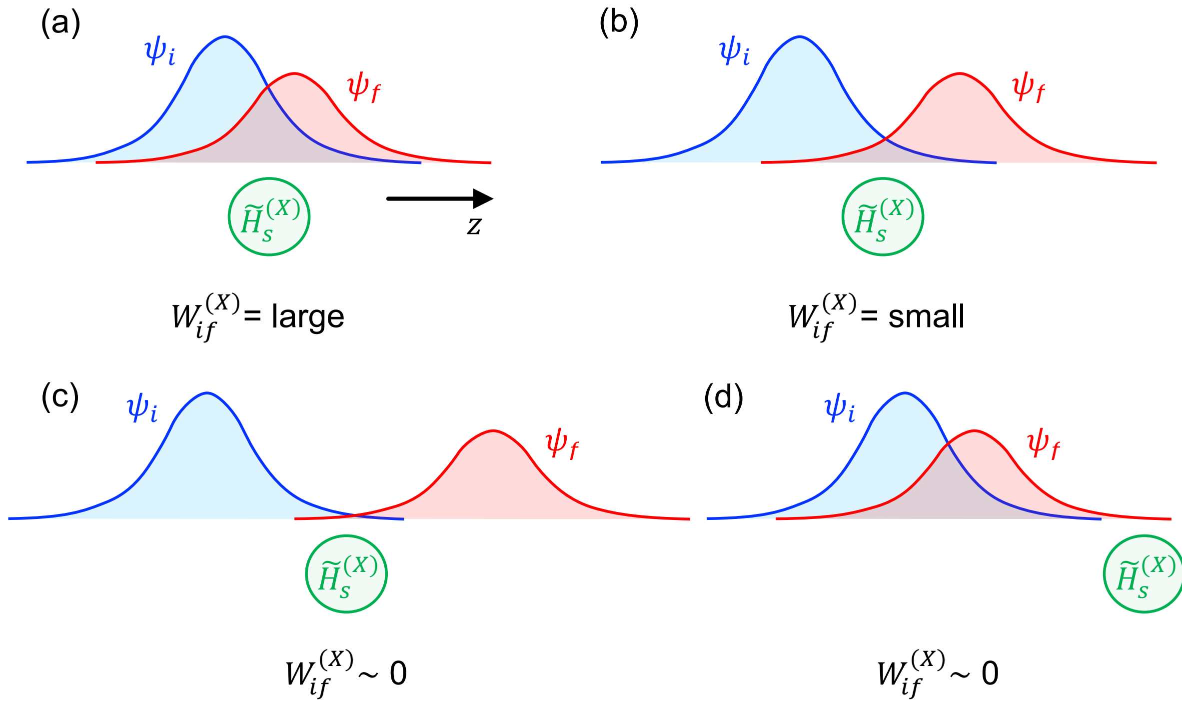

Figure. 2.5 A brief idea of a relation between scattering rate and componential parameters. (a) A large overlap between a large wavefunction overlap and a cause phenomenon. (b) A large overlap between a small wavefunction overlap and a cause phenomenon. (c) A large overlap between an almost zero wavefunction overlap and a cause phenomenon. (d) A small overlap between a large wavefunction overlap and a cause phenomenon.

The carrier scattering rates calculated by Fermi's golden rule is a function of the kinetic energy of the initial state. This form is directly used for the Monte-Carlo method, but thermally averaged values are used for the rate equation and density matrix methods. Electrons distribute energetically following the Fermi-Dirac distribution function $f_i^{FD}(k_i)$, so the effective scattering rate is averaged by the kinetic energy, and the carrier occupying rate in the final state is also considered (the final-state-blocking).

$$\overline{W_{if}^{(X)}} = \frac{\int W_{if}^{(X)}(k_i) f_i^{FD}(k_i)\left[1 - f_f^{FD}(k_f)\right] k_i dk_i}{\int f_i^{FD}(k_i)\, k_i dk_i} \tag{2.14}$$

After calculating the individual scattering rates caused by different phenomena, the net scattering rate W_{if} is calculated as below.

$$W_{if} = \sum_X \overline{W_{if}^{(X)}} = \overline{W_{if}^{(LO)}} + \overline{W_{if}^{(IFR)}} + \overline{W_{if}^{(IMP)}} + \overline{W_{if}^{(AD)}} + \overline{W_{if}^{(EE)}} = \frac{1}{\tau_{if}} \tag{2.15}$$

In Equation (2.15), τ_{if} denotes the net scattering time. Lastly, the carrier lifetime of a subband $|i\rangle$ is a sum of the times for carriers to transfer $|i\rangle$ to other subbands.

$$\frac{1}{\tau_i} = \sum_{f \neq i} \frac{1}{\tau_{if}} \tag{2.16}$$

In the latter sections, the net carrier scattering rate $\overline{W_{if}}$ is described by just W_{if}. Effective mass also varys depending on subbands, but this work uses the value at the bottom of the conduction band ($m_i \approx m_f \approx m^*$).

2.3.1.1 LO-phonon scattering rate

The LO-phonon scattering (Longitudinal optical phonon scattering), occurred due to lattice vibration, is a dominant carrier transport in QCLs and always needs to be considered in device design. When the energy difference between two subbands E_{if} corresponds to the LO-phonon vibration energy of materials, the LO-phonon scattering rate is maximized due to energy resonance, and the LO-phonon scattering rate is fast (ps order) compared to other scattering mechanisms and is often used for carrier abstraction from LLS. However, the LO-phonon scattering rate greatly increases under high temperature conditions, and the increase of scattering rate in radiation path causes degradation of device performance [188]. To calculate the LO-phonon scattering rate by Fermi's golden rule, the energy conservation law needs to be rewritten with the LO-phonon vibration energy of material E_{LO} as below because the LO-phonon scattering is an elastic phenomenon.

$$E_f + \frac{\hbar^2 k_f^2}{2m_f^*} - E_i - \frac{\hbar^2 k_i^2}{2m_i^*} \rightarrow E_f + \frac{\hbar^2 k_f^2}{2m_f^*} - E_i - \frac{\hbar^2 k_i^2}{2m_i^*} \pm E_{LO}$$

(- = emission, + = absorption)

The scattering Hamiltonian of the LO-phonon scattering is given in Equation (2.17).

$$\widetilde{H}_s^{(LO)} = q_0 \sum_{\boldsymbol{K_{xy}}} \sum_{K_z} \left[\frac{(\hbar\omega)\left(\frac{1}{\varepsilon_\infty} - \frac{1}{\varepsilon_s}\right)\left(N_0 + \frac{1}{2} \pm \frac{1}{2}\right)}{2\left(\left|\boldsymbol{K_{xy}}\right|^2 + |K_z|^2\right)} \right]^{\frac{1}{2}} \frac{e^{-i\boldsymbol{K_{xy}}\cdot\boldsymbol{r_{xy}}}}{A^{\frac{1}{2}}} \frac{e^{-iK_z z}}{L^{\frac{1}{2}}} \qquad (2.17)$$

In Equation (2.17), the upper sign (+) means LO-phonon emission, and the lower sign (-) means absorption, and both cases need to be solved. By applying Equation (2.17) to (2.13), the non-averaged scattering rate is derived in Equation (2.18).

$$W_{if}^{(LO)}(k_i) = \frac{\pi m^* q_0^2(\hbar\omega)}{(2\pi)^2\hbar^3}\left(\frac{1}{\varepsilon_\infty} - \frac{1}{\varepsilon_s}\right)\left(N_0 + \frac{1}{2} \pm \frac{1}{2}\right)\Theta\left(k_i^2 - \frac{2m^*\Delta}{\hbar^2}\right) \times \int_{-\infty}^{\infty} \frac{\left|G_{if}(K_z)\right|^2 dK_z}{\sqrt{K_z^4 + 2K_z^2\left(2k_i^2 - \frac{2m^*\Delta}{\hbar^2}\right) + \left(\frac{2m^*\Delta}{\hbar^2}\right)^2}} \tag{2.18}$$

(+ = emission, - = absorption)

In Equation (2.18), some parameters are calculated as below.

$$N_0 = \frac{1}{\exp(\hbar\omega/k_B T_L) - 1} \qquad G_{if}(K_z) = \int \psi_f^*(z) e^{-iK_z z} \psi_i(z) dz$$

$$\Delta = E_f - E_i \mp E_{LO}$$

(-=emission, +=absorption)

In the above equations, ε_∞ is the high-frequency permittivity, ε_s is the low-frequency (static) permittivity, N_0 is the phonon density of the crystal, G_{if} is the form factor, K_z is the z-direction wave vector, and Δ is the electron energy difference between the bottom of the initial state and the bottom of the final state.

2.3.1.2 Electron-electron scattering rate

The electron-electron scattering is caused by the conflict of two electrons, and this process is similar to the ionized-impurity scattering in terms of the influence of the Coulomb force. The scattering Hamiltonian of the electron-electron scattering is described below [59]. Where, $\boldsymbol{R}$ denotes the three-dimensional position of carriers ($\boldsymbol{R} = (x, y, z)^T$).

$$\widetilde{H}_s^{(EE)} = \frac{q_0^2}{4\pi\varepsilon_s\sqrt{|\boldsymbol{R} - \boldsymbol{R}'|^2}} \tag{2.19}$$

However, unlike the ionized-impurity scattering, the quantum conditions of the two electrons can change, so the four total quantum conditions, two initial conditions ($|i\rangle$ and $|j\rangle$) and two final conditions ($|f\rangle$ and $|g\rangle$), need to be considered in Fermi's golden rule. So, when the number of subbands per module is N_{level}, N_{level}^4 of the number of scattering paths exist. (In other scattering phenomena, the number of scattering paths is N_{level}^2.) The scattering rate of the electron-electron scattering is obtained by applying Equation (2.19) to (2.13).

$$W_{ijfg}^{(EE)}(k_i) = \frac{m^* q_0^4}{64\pi^3\hbar^3\varepsilon_s^2}\int_0^\infty f_j^{FD}(k_j)\int_0^{2\pi}\int_0^{2\pi}\frac{\left|A_{ijfg}(K_{xy})\right|^2}{K_{xy}^2}d\theta d\alpha k_j dk_j \tag{2.20}$$

In Equation (2.20), the momentum conservation law is described by K_{xy}, but the derivation is a little complicated. In the below equations, k_i, k_j, k_f, and k_g are the absolute values of wave vectors of electrons in the subbands, $|i\rangle$, $|j\rangle$, $|f\rangle$, and $|g\rangle$, respectively, and the angles,

α and β are made by the vectors, $\boldsymbol{k_i}$ and $\boldsymbol{k_j}$, and $\boldsymbol{k_f}$ and $\boldsymbol{k_g}$, respectively.

$$k_{ij}^2 = k_i^2 + k_j^2 - 2k_i k_j \cos(\alpha)$$

$$k_{fg}^2 = k_f^2 + k_g^2 - 2k_f k_g \cos(\beta)$$

$$(2K_{xy})^2 = k_{ij}^2 + k_{fg}^2 - 2k_{ij}k_{fg}cos\theta$$

A_{ijfg} is the form factor of the electron-electron scattering. Using these parameters, the electron-electron scattering rate can be calculated. However, this calculation is time-consuming and not practical with usual spec of computers. This issue is resolved by using Fourier transform. z and z' denote positions for carriers transporting from $|i\rangle$ to $|f\rangle$ and from $|j\rangle$ to $|g\rangle$, respectively.

$$A_{ijfg}(K_{xy}) = \int_{-\infty}^{\infty}\int_{-\infty}^{\infty} \psi_i(z)\psi_j(z')\psi_f^*(z)\psi_g^*(z')e^{-K_{xy}|z-z'|}dzdz' \qquad (2.21)$$

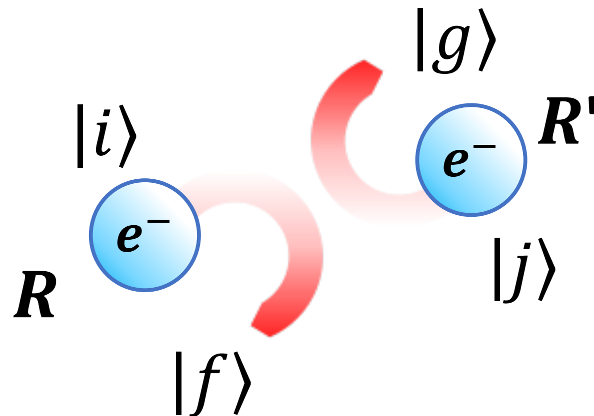

Figure. 2.6 Quantum states before and after the electron-electron scattering.

Due to the six variables in Equation (2.20) and (2.21), the calculation of the electron-electron scattering rate is a lengthy process. However, this issue is mitigated by applying the discretized Fourier transform proposed by Bonno, *et al.* [235]. In their work, integration range of the form factor is limited to one period of a device. Based on their methods, this work takes advantage of the wavefunction's characteristics that wavefunction converges at infinity, the integration range is expanded as in Equation (2.21) to derive the Fourier form of the form factor. Firstly, the following wave function products need to be introduced.

$$\begin{cases} \psi_n^{if} = \psi_i(z_n)\psi_f^*(z_n) \\ \psi_m^{jg} = \psi_j(z_m)\psi_g^*(z_m) \end{cases}$$

ψ_n^{if} and ψ_m^{jg}, and the corresponding Fourier coefficients, Ψ_a^{if} and Ψ_b^{jg}, are written as below by applying the discretized Fourier transform and the inverse Fourier transform. z and z' are also replaced by z_n and z_m.

$$\begin{cases} \Psi_a^{if} = \sum_{n=-N_f}^{N_f} \psi_n^{if}\, e^{-i\frac{2\pi an}{N}} \\ \Psi_b^{jg} = \sum_{m=-N_f}^{N_f} \psi_m^{jg}\, e^{-i\frac{2\pi bm}{N}} \end{cases} \qquad \begin{cases} \psi_n^{if} = \frac{1}{N}\sum_{a=-N_f}^{N_f} \Psi_a^{if} e^{i\frac{2\pi an}{N}} \\ \psi_m^{jg} = \frac{1}{N}\sum_{b=-N_f}^{N_f} \Psi_b^{jg} e^{i\frac{2\pi bm}{N}} \end{cases}$$

$$a, b = -N_f, -(N_f - 1), \cdots, (N_f - 1), N_f$$

$$N = 2N_f + 1$$

Then, Equation (2.21) is modified as below.

$$A_{ijfg}(K_{xy}) = \frac{1}{N^2}\sum_{a=-N_f}^{N_f}\sum_{b=-N_f}^{N_f}\Psi_a^{if}\,\Psi_b^{jg}\int_{-\infty}^{\infty}\int_{-\infty}^{\infty} e^{i\frac{2\pi an}{N}}e^{i\frac{2\pi bm}{N}}e^{-K_{xy}|z-z'|}dzdz'$$

where n and m are expressed by discretized positions z_n and z_m, respectively, then they are returned to the corresponding continuous positions, z and z'. Furthermore, these positions are respectively replaced with u and v.

$$\begin{cases} n = \dfrac{z_n - z_{-N_f} - N_f\Delta z}{\Delta z} \rightarrow \dfrac{z - z_{-N_f} - N_f\Delta z}{\Delta z} = \dfrac{u}{\Delta z} \\ m = \dfrac{z_m - z_{-N_f} - N_f\Delta z}{\Delta z} \rightarrow \dfrac{z' - z_{-N_f} - N_f\Delta z}{\Delta z} = \dfrac{v}{\Delta z} \end{cases}$$

Then, the form factor is modified as below.

$$A_{ijfg}(K_{xy}) = \frac{1}{N^2}\sum_{a=-N_f}^{N_f}\sum_{b=-N_f}^{N_f}\Psi_a^{if}\,\Psi_b^{jg}\int_{-\infty}^{\infty}\int_{-\infty}^{\infty} e^{i\frac{2\pi a}{N\Delta z}u}e^{i\frac{2\pi b}{N\Delta z}v}e^{-K_{xy}|u-v|}dudv$$

Finally, v is replaced by w $(w = u - v)$ for variable separation, and the Fourier transform is used to obtain Equation (2.22).

$$A_{ijfg}(K_{xy}) = \frac{1}{N^2}\sum_{a=-N_f}^{N_f}\sum_{b=-N_f}^{N_f}\Psi_a^{if}\,\Psi_b^{jg}\int_{-\infty}^{\infty}\int_{-\infty}^{\infty} e^{i\frac{2\pi a}{N\Delta z}u} e^{i\frac{2\pi b}{N\Delta z}(u-w)} e^{-K_{xy}|w|}dudw$$

$$= \frac{1}{N^2}\sum_{a=-N_f}^{N_f}\sum_{b=-N_f}^{N_f}\Psi_a^{if}\,\Psi_b^{jg}\int_{-\infty}^{\infty} e^{i\frac{2\pi(a+b)}{N\Delta z}u}du\int_{-\infty}^{\infty} e^{-K_{xy}|w|}e^{-i\frac{2\pi b}{N\Delta z}w}dw$$

$$\therefore\ A_{ijfg}(K_{xy}) = 2NK_{xy}\Delta z^3\sum_{c=-N_f}^{N_f}\frac{\Psi_c^{if}\Psi_{-c}^{jg}}{\left(K_{xy}N\Delta z\right)^2+(2\pi c)^2} \tag{2.22}$$

By this method, the calculation time is reduced by three orders and the electron-electron scattering model becomes more practical [236]. At last, the net electron-electron scattering rate between two subbands is calculated by the below equation.

$$\overline{W_{if}} = \overline{W_{iiff}} - \overline{W_{iffi}} + \sum_{j,g}\overline{W_{ijfg}} \tag{2.23}$$

To verify the calculation accuracy and speed, a 400Å-wide infinite square quantum well is simulated as an example. In this simulation, inter-subband scattering rate $W_{2211}^{(EE)}$ is calculated by the original and Fourier models and compared in Figure 2.7. The data points for the calculation are determined by a product of discretization points of k_i, k_j, α, and θ in Equation (2.20). The subband carrier density is assumed to be 1.0×10^{10}cm^{-2} in each subband. As shown in Figure 2.7(a), the calculation results with the original form and the DFT form match well. In Figure 2.7(b), on the other hand, the calculation time with the DFT form is almost three orders shorter. It changes from 1.08×10^4 s to 30s when the data points are 1.14×10^6. This result demonstrates the superiority of the DFT calculation.

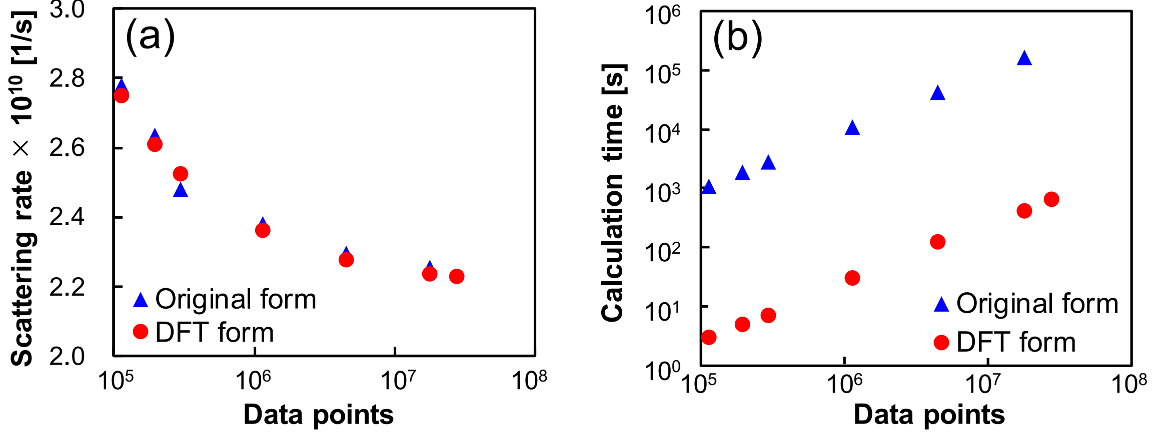

Figure. 2.7 Calculation results for the electron-electron scattering rate in an infinite square quantum well. (a) Inter-subband scattering rate W_{2211}, and (b) Calculation time.

2.3.1.3 Ionized-impurity scattering rate

The ionized-impurity scattering happens between an electron and ionized dopant atom. Even though the quantum conditions of two particles can change due to this scattering process like the electron-electron scattering, the change of quantum condition of the ionized atom is ignored due to its large mass compared to the one of electrons in theory. In order to calculate the scattering rate, the scattering Hamiltonian of the ionized-impurity scattering is described as the Coulomb potential [59]. $\boldsymbol{R_0}$ denotes the position of ionized impurities ($\boldsymbol{R_0} = (x_0, y_0, z_0)$).

$$\widetilde{H}_s^{(IMP)} = -\frac{q_0^2}{4\pi\varepsilon_s\sqrt{|\boldsymbol{R} - \boldsymbol{R_0}|^2}} \tag{2.24}$$

The scattering rate is calculated by using Fermi's golden rule.

$$W_{if}^{(IMP)}(k_i) = \frac{m^* q_0^4}{4\pi\hbar^3}\Theta(k_f^2)\int_0^{\pi}\frac{J_{if}(K_{xy})}{K_{xy}^2}d\theta \tag{2.25}$$

J_{if} and K_{xy} are the form factor and the scattering momentum exchange, as described below.

$$K_{xy}^2 = k_f^2 + k_i^2 - 2k_i k_f cos\theta$$

$$J_{if}(K_{xy}) = \int N^{3D}(z_0)\left|\int \frac{\psi_f^*(z)\psi_i(z)e^{-K_{xy}|z-z_0|}}{\varepsilon_s(z)}dz\right|^2 dz_0$$

2.3.1.4 Alloy-disorder scattering rate

The alloy-disorder scattering, happens due to inhomogeneity of compounds, needs to be considered when alloy crystals (ternary or quaternary) are used. In theory, the scattering rate of the alloy-disorder scattering is maximized when the alloy composition is 50% but is not so significant in most GaAs-based THz QCLs. The scattering Hamiltonian of the alloy-disorder scattering is derived based on the virtual crystal approximation by dealing with the real (random) and virtual (ideal) crystal potentials for a ternary material $A_xB_{1-x}C$ [59].

$$\widetilde{H}_s^{(AD)}(\boldsymbol{R}) = \Omega\Delta V_{ad}\left[\sum_{\boldsymbol{R_i}\in R_A}(1-x)\delta(\boldsymbol{R}-\boldsymbol{R_i}) - \sum_{\boldsymbol{R_i}\in R_B}x\delta(\boldsymbol{R}-\boldsymbol{R_i})\right] \tag{2.26}$$

In Equation (2.26), Ω and ΔV_{ad} denotes the volume of a unit-cell and the spatial average

of the potential difference between the two materials. The volume of a unit-cell is defined as below with a lattice constant a [59].

$$\begin{cases} \Omega(\text{zinc blende}) = \dfrac{a^3}{4} \\ \Omega(\text{diamond}) = \dfrac{a^3}{8} \end{cases}$$

As for the spatially-averaged potential difference, there are two definitions [59, 237], and this work selects the one proposed by Harrison *et al.* with the conduction band offset ΔE_C [59].

$$\Delta V_{ad} \sim \Delta E_C$$

By plugging these material parameters and Equation (2.26) into Fermi's golden rule, the alloy-disorder scattering rate is derived as in Equation (2.27).

$$W_{if}^{(AD)}(k_i) = \frac{m^* \Omega \Delta V_{ad}^2}{\hbar^3} \Theta(k_f^2) \int |\psi_f(z)|^2 x(z)[1 - x(z)] |\psi_i(z)|^2 dz \tag{2.27}$$

2.3.1.5 Interface-roughness scattering rate

The interface-roughness scattering originates from the inhomogeneity of the hetero-junction interfaces, and this phenomenon can be influential depending on device conditions such as barrier height, surface-roughness parameters (roughness height and correlation

length), and the driving temperature.

The scattering Hamiltonian of the interface-roughness scattering is defined as the potential difference at the interface whose range is defined as $z_I^L \leq z \leq z_I^U$. I denotes the number of interfaces.

$$\widetilde{H}_s^{(IFR)}(\boldsymbol{R}) = -\Delta_z(\boldsymbol{r})\frac{dV(z)}{dz}\mathrm{rect}\left(\frac{z - z_I}{z_I^U - z_I^L}\right) \tag{2.28}$$

Where, $\Delta_z(\boldsymbol{r})$ is the fluctuation of the interface ($\boldsymbol{r} = (x, y)^{\boldsymbol{T}}$), and the Gaussian shaped self-correlation function is assumed with the roughness height Δ and correlation length Λ [59]. In the simulation in this work, $\Delta = 2\,\text{Å}$ and $\Lambda = 100\,\text{Å}$ are used. As for the self-correlation function, the other variations are also proposed [238, 239].

$$\langle \Delta_z(\boldsymbol{r})\Delta_z(\boldsymbol{r}')\rangle = \Delta^2 exp\left(-\frac{|\boldsymbol{r} - \boldsymbol{r}'|^2}{\Lambda^2}\right)$$

For the net scattering rate, each rate at the interfaces per module is summed up. $I = 1 \sim All\ interfaces$. In Equation (2.29), V_0 denotes the potential drop (barrier height) over a range of $z_I^L \leq z \leq z_I^U$.

$$W_{if}^{(IFR)}(k_i) = \frac{m^*(\Delta\Lambda)^2}{\hbar^3}\Theta(k_f^2)e^{-\frac{\Lambda^2}{4}\left(k_i^2 + k_f^2\right)}\int_0^\pi e^{\frac{\Lambda^2}{2}k_i k_f cos\theta}d\theta \sum_I \left(\psi_f^*(z_I)V_0\psi_i(z_I)\right)^2 \tag{2.29}$$

2.3.2 Ando's Theory

One more important theory about incoherent carrier transport is Ando's theory, and optical linewidth (FWHM) is calculated by this theory. The theoretical form of optical linewidth for optical transition from $|i\rangle$ to $|f\rangle$, derived from the first principal calculation by Ando, is described in Equation (2.30) [231, 232]. Instead of the total energy E_i^T and E_f^T in Fermi's golden rule, the kinetic energies E_i^K and E_f^K are used in the delta function. By applying the same Hamiltonian potential corresponding to each scattering phenomenon to Ando's theory, optical linewidth is calculated.

$$\Gamma_{if}^{(X)}(k_i) = 2\pi \sum_{\boldsymbol{k_f}} \langle \left| \langle i\boldsymbol{k_f} \middle| \widetilde{H}_s^{(X)} \middle| i\boldsymbol{k_i} \rangle - \langle f\boldsymbol{k_f} \middle| \widetilde{H}_s^{(X)} \middle| f\boldsymbol{k_i} \rangle \right|^2 \rangle_{avg} \, \delta\left(E_f^K - E_i^K\right) \qquad (2.30)$$

Like scattering rate, optical linewidth is also thermally averaged by using the Fermi-Dirac distribution function $f_i^{FD}(k_i)$.

$$\overline{\Gamma_{if}^{(X)}} = \frac{\int \Gamma_{if}^{(X)}(k_i) \left| f_i^{FD}(k_i) - f_f^{FD}(k_i) \right| k_i dk_i}{\int \left| f_i^{FD}(k_i) - f_f^{FD}(k_i) \right| k_i dk_i} \qquad (2.31)$$

The total linewidth Γ_{if}^* is a sum of linewidths due to each scattering phenomenon.

$$\Gamma_{if}^* = \sum_X \overline{\Gamma_{if}^{(X)}} = \frac{2\hbar}{\tau_{if}^*} \qquad (2.32)$$

A device parameter related to optical linewidth is dephasing time. Dephasing is a mechanism that recovers classical behavior from a quantum system. When coherence decays by perturbation over time, the system returns to the state before perturbation. The time that it takes for the conducting electrons to lose their quantum behavior is dephasing time [240], and usually an experimental equation below is used for transition from $|i\rangle$ to $|f\rangle$ [241].

$$\frac{1}{\tau_{if}^{\parallel}} = \frac{1}{2}\left(\frac{1}{\tau_i} + \frac{1}{\tau_f}\right) + \frac{1}{\tau_{if}^{*}} \tag{2.33}$$

In Equation (2.33), $\tau_{if}^{\parallel}$ denotes the total dephasing time, and τ_i and τ_f are carrier lifetime calculated from intersubband scattering rate in Equation (2.16). τ_{if}^{*} in Equation (2.32) and (2.33) denotes the pure dephasing time [242, 243]. In the previous studies, phenomenological values are used for the pure dephasing time [118, 119, 129, 207, 244]. However, this method is a little cautious. Usually, phenomenological values are experimentally obtained from optical measurement, so using such values to simulate optical linewidth would not have so critical problems. On the other hand, pure dephasing time is also used for coherent transport between modules. In this case, phenomenological values would cause significant errors because wavefunction distribution inside a module and between modules are very different. Between carrier lifetime and band broadening due to inter-subband scattering, the uncertainty principle ($\Gamma_n \cdot \tau_n \sim \hbar$) can be used. Then, the total optical linewidth is described as in Equation (2.34).

$$\Gamma_{if} = \Gamma_i + \Gamma_f + \Gamma_{if}^{*} \tag{2.34}$$

In this work, optical linewidth due to the LO-phonon, ionized-impurity, alloy-disorder, and interface-roughness scatterings is calculated by using Ando's theory and the almost same mathematical procedure with Fermi's golden rule, and theoretical forms of them are introduced below. The optical linewidth due to the electron-electron scattering is not included in this work.

2.3.2.1 Optical linewidth by LO-phonon scattering

The optical linewidth due to the LO-phonon scattering is derived by applying Equation (2.17) to Ando's theory.

$$\Gamma_{if}^{(LO)}(k_i) = \frac{\pi m^* q_0^2(\hbar\omega)}{(2\pi)^2\hbar^2}\left(\frac{1}{\varepsilon_\infty}-\frac{1}{\varepsilon_s}\right)\left(N_0+\frac{1}{2}\pm\frac{1}{2}\right)\Theta\left(k_i^2\mp\frac{2m^*E_{LO}}{\hbar^2}\right) \times\int_{-\infty}^{\infty}\frac{\left|H_{if}(K_z)\right|^2 dK_z}{\sqrt{K_z^4+2K_z^2\left(2k_i^2\mp\frac{2m^*E_{LO}}{\hbar^2}\right)+\left(\frac{2m^*E_{LO}}{\hbar^2}\right)^2}} \tag{2.35}$$

(The upper sign = emission, the lower sign = absorption)

In Equation (2.35), the Heaviside function can be omitted for absorption because the inside of a parentheses is always plus, and the form factor is described below.

$$H_{if}(K_z) = \int\left(|\psi_i(z)|^2-\left|\psi_f(z)\right|^2\right)e^{-iK_z z}dz$$

2.3.2.2 Optical linewidth by ionized-impurity scattering

The optical linewidth due to the ionized-impurity scattering is often studied and is found to be influential on the optical gain [243, 245, 246]. The theoretical form is described in Equation (2.36). K_{xy} and I_{if} are also shown below.

$$\Gamma_{if}^{(IMP)}(k_i) = \frac{m^* q_0^4}{4\pi\hbar^2}\int_0^\pi \frac{I_{if}(K_{xy})}{K_{xy}^2} d\theta \qquad (2.36)$$

$$K_{xy}^2 = 2k_i^2(1 - cos\theta)$$

$$I_{if}(K_{xy}) = \int N_d^{3D}(z_0)\left|\int \frac{|\psi_i(z)|^2 - |\psi_f(z)|^2}{\varepsilon_s(z)} e^{-K_{xy}|z - z_0|} dz\right|^2 dz_0$$

A relation between optical linewidth and doping conditions is investigated in Chapter 3.

2.3.2.3 Optical linewidth by alloy-disorder scattering

The optical linewidth due to the alloy-disorder scattering is also derived by the same way. Alloy-disorder scattering is not so influential on both scattering rate and optical linewidth [242].

$$\Gamma_{if}^{(AD)}(k_i) = \frac{m^*\Omega\Delta V_{ad}^2}{\hbar^2}\int x(z)[1 - x(z)]\left[|\psi_i(z)|^2 - |\psi_f(z)|^2\right]^2 dz \qquad (2.37)$$

2.3.2.4 Optical linewidth by interface-roughness scattering

Interface-roughness scattering is also considered to be influential on optical linewidth and has been often studied with the ionized-impurity scattering [242, 243, 245, 247-250].

$$\Gamma_{if}^{(IFR)}(k_i) = \frac{m^* \Delta^2 \Lambda^2}{\hbar^2} \left(\sum_I G_{I,if}{}^2 \right) \int_0^{\pi} e^{-\frac{\Lambda^2}{2} k_i^2 cos\theta} d\theta \qquad (2.38)$$

The form factor $G_{I,if}$ is given as below.

$$G_{I,if} = \int_{z_I^L}^{z_I^U} \left(|\psi_i(z)|^2 - \left|\psi_f(z)\right|^2 \right) \left(\frac{dV}{dz} \right) dz$$

2.3.3 Screening Effect

In order to correctly calculate the carrier scattering rate of Coulomb scatterings (LO, IMP, and EE), it is vital to consider a screening effect model, without which the intra-subband scattering rate diverges at $K = 0$. Existing screening effect theories have generally been derived from the random-phase-approximation (RPA) and can be divided into two main categories: Dyson equation and Lindhard theory [251]. The screened Coulomb potential can be calculated by using either theory, but it can be an exacting task to select an appropriate

model [246, 252-254].

In the Dyson equation, the screened Coulomb potential is calculated from the RPA without any auxiliary assumptions, hence considered to have higher theoretical validity. However, this method leads to complicated simultaneous equations that can be computationally expensive. The Lindhard theory has the advantage of easy and swift calculation for the scattering rate by modifying the wave vector K_{xy} or K_z using the screened wave vector K_{sc}.

$$K \rightarrow \sqrt{K^2 + K_{sc}^2} \cdots 3D\ theory$$

$$K \rightarrow K + K_{sc} \cdots 2D\ theory$$

This modification of the wave vector varys according to the dimension being considered. As for the shortcomings of this theory, the accuracy of its calculation has been questioned because of the approximations being used to derive most of its models.

Even though the two-dimensional Lindhard theory has been widely used in previous works, this work adopts the three-dimensional theory because of the limitation in the application of the two-dimensional theory in device physics. Indeed, the Coulomb potential is defined in both two- and three-dimensions. In order to define the two-dimensional Coulomb potential, the carriers need to distribute homogeneously along the direction of current flow. Under this condition, the electrical field to the z-axis is canceled out, and the two-dimensional Coulomb potential can be defined (Figure 2.8). In QCLs, however, the spatial distribution of electrons is heterogeneous because it is determined by wave functions.

In this sense, the two-dimensional theory can be said to be plagued by contradiction.

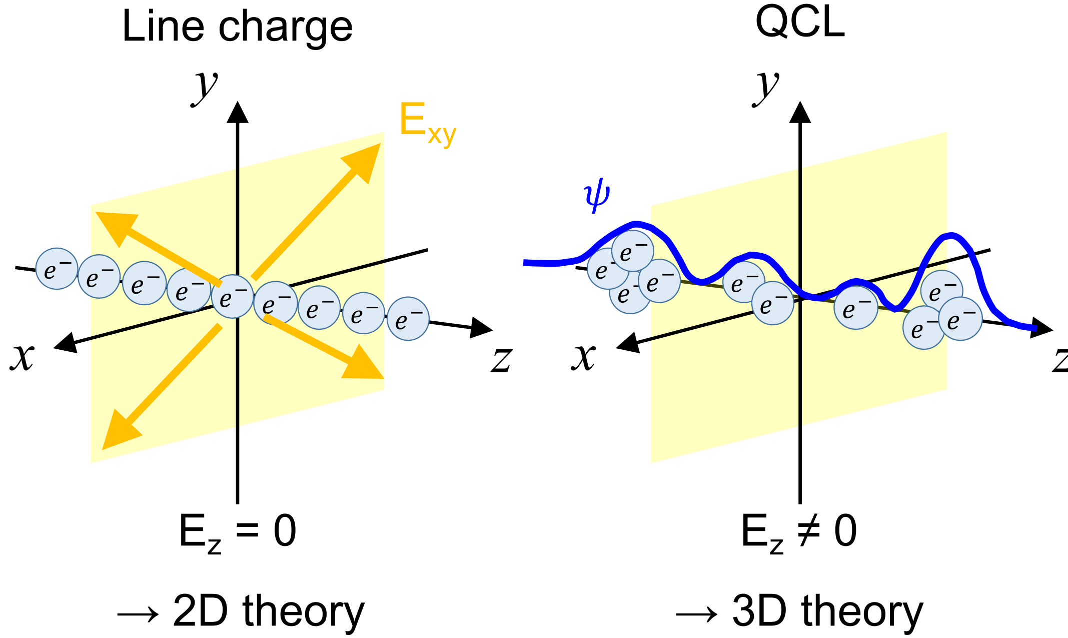

Figure. 2.8 Conditions for the two-dimensional Lindhard theories and three-dimensional theories.

Screening model		Approximation	Calculation time	Reference
Dyson equation	Full model	-	(Long)	[255]
	Long wavelength limit	Long wavelength limit		[113]
3D-Lindhard theory	Debye model	$\mathrm{E} - \mu \gg k_B T$	Short	[246]
	Thomas-Fermi model	$T_e \to 0$		[252]
	Ezhov model	-		
	Modified Debye model	Based on Debye model		
	Asada model	For only infinite square quantum well		[256]
2D-Lindhard theory	Straight model	-		[253]
	Thomas-Fermi model	$T_e \to 0$		[59]
	Maldague-Smet model	Similarity in equation	Long	[257, 258]

Table. 2.2 Screening effect models.

A thorough search of the relevant literature yielded five three-dimensional screening models (Table 2.2). These models can be derived based on the definition of three-dimensional screened wave vector in Equation (2.39) [259], where N_d^{3D} and μ denote the three-dimensional carrier density and chemical potential, respectively.

$$K_{sc}^2 = \frac{q_0^2}{\varepsilon_s}\left(\frac{\partial N_d^{3D}}{\partial \mu}\right) \tag{2.39}$$

Among the five models, the one by Ezhov *et al.* appears to the authors to make the fewest auxiliary assumptions, and thus has a wider range of applicability [252]. Ezhov model describes the three-dimensional carrier density as in Equation (2.40), with the subband carrier density N_i^{2D} and the length of one period of devices L_p.

$$N^{3D} = \sum_i \frac{N_i^{2D}}{L_p} \tag{2.40}$$

The subband carrier density is also described in Equation (2.41) with the subband effective mass m_i and eigen energy E_i.

$$N_i^{2D} = \int_{E_i}^{\infty} f_i^{FD}(E)\frac{m_i}{\pi\hbar^2}dE \tag{2.41}$$

From these equations, the three-dimensional carrier density is described as in Equation (2.42).

$$N^{3D} = \frac{1}{\pi\hbar^2 L_p}\sum_i m_i \int_{E_i}^{\infty} f_i^{FD}(E)dE \tag{2.42}$$

Equation (2.41) is then plugged into Equation (2.39) to obtain Equation (2.43).

$$K_{sc}^2 = \frac{q_0^2}{\pi\hbar^2\varepsilon_s L_p}\sum_i m_i \int_{E_i}^{\infty}\left(\frac{\partial f_i^{FD}(E)}{\partial\mu}\right)dE = \frac{q_0^2}{\pi\hbar^2\varepsilon_s L_p}\sum_i m_i \int_{E_i}^{\infty}\left(-\frac{\partial f_i^{FD}(E)}{\partial E}\right)dE$$

$$= \frac{q_0^2}{\pi\hbar^2\varepsilon_s L_p}\sum_i m_i[-f_i^{FD}(E)]_{E_i}^{\infty}$$

$$\therefore\ K_{sc}^2 = \frac{q_0^2}{\pi\hbar^2\varepsilon_s L_p}\sum_i m_i f_i^{FD}(E_i) \tag{2.43}$$

As for the other four models, the worrying thing is their inaccurate calculations due to approximations or simplifications. First, the Debye model approximates the Fermi-Dirac function by the Boltzmann distribution function, a condition that is not appropriate to high-energy electrons. The modified Debye model [252] is kindred to the Debye model. Second, the Thomas-Fermi model [252, 260] is based on low temperature conditions. Third, the Asada model [59, 256, 261] is similar to the Ezhov model [252] in the derivation process but uses effective well widths instead of the one period length in Equation (2.40). As a result, the approximation is not appropriate for complicated device structures, such as those of QCLs.

2.4 Coherent Carrier Transport

In this section, the theories related to coherent carrier transport will be described. The inter-module carrier propagation in the rate equation of this work is assumed to be only coherent resonant tunneling, and this carrier transition is described by the tunneling time/rate derived by Scalari *et al.* [139]. Tunneling time, which is obtained in derivation of the tunneling current by quantum mechanical approach (The first-order tunneling current theory), is composed of coupling strength, detuning energy, and dephasing time, and the tight-binding theory describes coupling strength and detuning energy. These theories will be explained below.

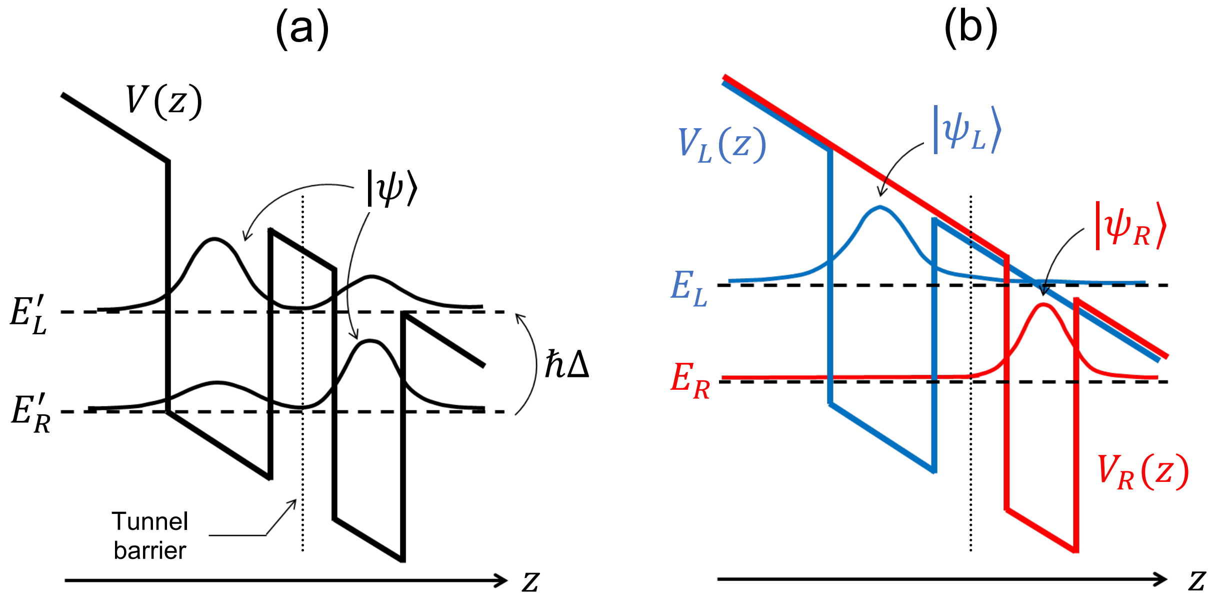

Figure. 2.9 An image of tight-binding condition (a) Delocalized condition, and (b) Tight-binding condition.

2.4.1 Tight-Binding Theory

The detuning energy and coupling strength are described by considering the delocalized condition where two modules are connected and the tight-binding condition where two independent modules are superposed [225]. Detuning energy is the energy difference between two coupled quantum states, and coupling strength describes how strongly two subbands are related. In the alignment condition, detuning energy is close to zero, and coupling strength shows a large value.

To describe the detuning energy and coupling strength between two subbands $|L\rangle$ and $|R\rangle$, a delocalized condition and tight-binding condition are considered as depicted in Figure 2.9. Now, the wave function in the original condition is assumed to be written as a superposition of two basis in a tight-binding condition as in Equation (2.44). Where, α and β are complexed binding coefficients and satisfy a relation ($|\alpha|^2 + |\beta|^2 = 1$).

$$\psi(z) = \alpha\psi_L(z) + \beta\psi_R(z) \tag{2.44}$$

In the tight-binding condition, Schrodinger equation can be applied into each quantum condition.

$$\begin{cases} \left[-\dfrac{\hbar^2}{2m^*}\dfrac{\partial^2}{\partial z^2} + V_L(z)\right]\psi_L(z) = E_L\psi_L(z) \\ \left[-\dfrac{\hbar^2}{2m^*}\dfrac{\partial^2}{\partial z^2} + V_R(z)\right]\psi_R(z) = E_R\psi_R(z) \end{cases} \tag{2.45}$$

The Schrodinger equation can also be applied to the original condition (Equation (2.44)). Then, the Hamiltonian is decomposed into the potential profiles in the tight-binding condition [262].

$$\widetilde{H}\psi(z) = E\psi(z) \tag{2.46}$$

$$\widetilde{H} = -\frac{\hbar^2}{2m^*}\frac{\partial^2}{\partial z^2} + V_L(z) + V_R(z) - V_0(z) \tag{2.47}$$

Plug Equation (2.44) into (2.46).

$$\widetilde{H}\big(\alpha\psi_L(z) + \beta\psi_R(z)\big) = E\big(\alpha\psi_L(z) + \beta\psi_R(z)\big)$$

$$\Leftrightarrow \alpha\widetilde{H}\psi_L(z) + \beta\widetilde{H}\psi_R(z) = \alpha E\psi_L(z) + \beta E\psi_R(z)$$

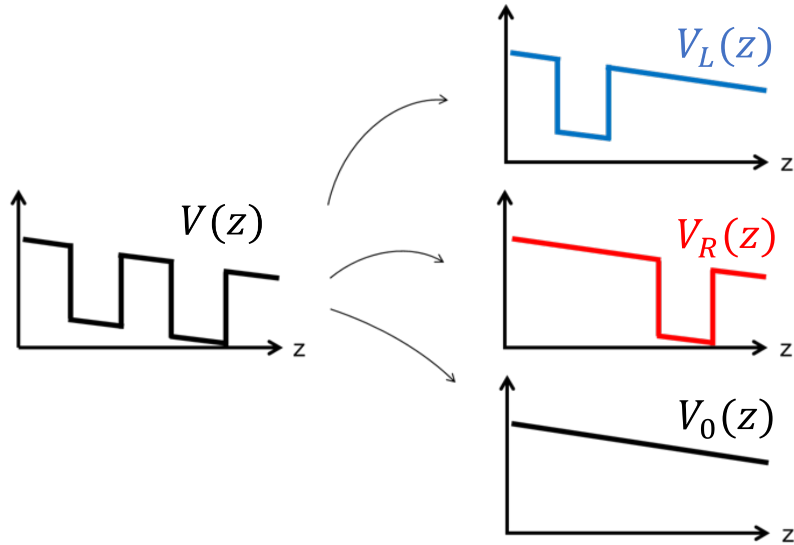

Figure. 2.10 Decomposition of potential

Multiply $\psi_L^*(z)$ from the left side, and integrate by z.

$$\alpha \int \psi_L^*(z)\widetilde{H}\psi_L(z)dz + \beta \int \psi_L^*(z)\widetilde{H}\psi_R(z)dz = \alpha E \int \psi_L^*(z)\,\psi_L(z)dz + \beta E \int \psi_L^*(z)\psi_R(z)dz$$

$$\Leftrightarrow\ H_{LL}\alpha + H_{LR}\beta = E(\alpha + r_{LR}\beta) \tag{2.48}$$

Multiply $\psi_R^*(z)$ from the left side, and integrate by z.

$$\alpha \int \psi_R^*(z)\widetilde{H}\psi_L(z)dz + \beta \int \psi_R^*(z)\widetilde{H}\psi_R(z)dz = \alpha E \int \psi_R^*(z)\,\psi_L(z)dz + \beta E \int \psi_R^*(z)\psi_R(z)dz$$

$$\Leftrightarrow\ H_{RL}\alpha + H_{RR}\beta = E(r_{RL}\alpha + \beta) \tag{2.49}$$

In Equation (2.48) and (2.49),

$$H_{LL} = \int \psi_L^*(z)\widetilde{H}\psi_L(z)dz = \int \psi_L^*(z)\left(-\frac{\hbar^2}{2m^*}\frac{\partial^2}{\partial z^2} + V_L(z) + V_R(z) - V_0(z)\right)\psi_L(z)dz$$

$$= \int \psi_L^*(z)\left[-\frac{\hbar^2}{2m^*}\frac{\partial^2}{\partial z^2} + V_L(z)\right]\psi_L(z)dz + \int \psi_L^*(z)\big(V_R(z) - V_0(z)\big)\,\psi_L(z)dz$$

$$= E_L \int \psi_L^*(z)\psi_L(z)dz + \int \psi_L^*(z)\big(V_R(z) - V_0(z)\big)\,\psi_L(z)dz = E_L + s_{LRL}$$

$$H_{LR} = \int \psi_L^*(z)\widetilde{H}\psi_R(z)dz = \int \psi_L^*(z)\left(-\frac{\hbar^2}{2m^*}\frac{\partial^2}{\partial z^2} + V_L(z) + V_R(z) - V_0(z)\right)\psi_R(z)dz$$

$$= \int \psi_L^*(z)\left[-\frac{\hbar^2}{2m^*}\frac{\partial^2}{\partial z^2} + V_R(z)\right]\psi_R(z)dz + \int \psi_L^*(z)\big(V_L(z) - V_0(z)\big)\psi_R(z)dz$$

$$= E_R \int \psi_L^*(z)\psi_R(z)dz + \int \psi_L^*(z)\big(V_L(z) - V_0(z)\big)\psi_R(z)dz = r_{LR}E_R + t_{LLR}$$

$$H_{RL} = \int \psi_R^*(z)\widetilde{H}\psi_L(z)dz = \int \psi_R^*(z)\left(-\frac{\hbar^2}{2m^*}\frac{\partial^2}{\partial z^2} + V_L(z) + V_R(z) - V_0(z)\right)\psi_L(z)dz$$

$$= \int \psi_R^*(z)\left(-\frac{\hbar^2}{2m^*}\frac{\partial^2}{\partial z^2} + V_L(z)\right)\psi_L(z)dz + \int \psi_R^*(z)\big(V_R(z) - V_0(z)\big)\psi_L(z)dz$$

$$= E_L\int \psi_R^*(z)\psi_L(z)dz + \int \psi_R^*(z)\big(V_R(z) - V_0(z)\big)\psi_L(z)dz = r_{RL}E_L + t_{RRL}$$

$$H_{RR} = \int \psi_R^*(z)\widetilde{H}\psi_R(z)dz = \int \psi_R^*(z)\left(-\frac{\hbar^2}{2m^*}\frac{\partial^2}{\partial z^2} + V_L(z) + V_R(z) - V_0(z)\right)\psi_R(z)dz$$

$$= \int \psi_R^*(z)\left(-\frac{\hbar^2}{2m^*}\frac{\partial^2}{\partial z^2} + V_R(z)\right)\psi_R(z)dz + \int \psi_R^*(z)\big(V_L(z) - V_0(z)\big)\psi_R(z)dz$$

$$= E_R\int \psi_R^*(z)\psi_R(z)dz + \int \psi_R^*(z)\big(V_L(z) - V_0(z)\big)\psi_R(z)dz = E_R + s_{RLR}$$

$$\therefore \boldsymbol{H} = \begin{bmatrix} H_{LL} & H_{LR} \\ H_{RL} & H_{RR} \end{bmatrix} = \begin{bmatrix} E_L + s_{LRL} & r_{LR}E_R + t_{LLR} \\ r_{RL}E_L + t_{RRL} & E_R + s_{RLR} \end{bmatrix} \tag{2.50}$$

$$\text{Overlap integral: } \begin{cases} r_{LR} = \int \psi_L^*(z)\psi_R(z)dz \\ r_{RL} = \int \psi_R^*(z)\,\psi_L(z)dz \end{cases}$$

$$\text{Shift integral: } \begin{cases} s_{LRL} = \int \psi_L^*(z)\big(V_R(z) - V_0(z)\big)\psi_L(z)dz \\ s_{RLR} = \int \psi_R^*(z)\big(V_L(z) - V_0(z)\big)\psi_R(z)dz \end{cases}$$

$$\text{Transfer integral: } \begin{cases} t_{LLR} = \int \psi_L^*(z)\big(V_L(z) - V_0(z)\big)\psi_R(z)dz \\ t_{RRL} = \int \psi_R^*(z)\big(V_R(z) - V_0(z)\big)\psi_L(z)dz \end{cases}$$

Equation (2.48) and (2.49) can be written in a matrix form.

$$\begin{bmatrix} H_{LL} & H_{LR} \\ H_{RL} & H_{RR} \end{bmatrix} \begin{bmatrix} \alpha \\ \beta \end{bmatrix} = E \begin{bmatrix} 1 & r_{LR} \\ r_{RL} & 1 \end{bmatrix} \begin{bmatrix} \alpha \\ \beta \end{bmatrix} \tag{2.51}$$

Multiply $\begin{bmatrix} 1 & r_{LR} \\ r_{RL} & 1 \end{bmatrix}^{-1}$ from the left side of Equation (2.51).

$$L.H.S = \frac{1}{1 - r_{LR} r_{RL}} \begin{bmatrix} H_{LL} - r_{LR} H_{RL} & H_{LR} - r_{LR} H_{RR} \\ H_{RL} - r_{RL} H_{LL} & H_{RR} - r_{RL} H_{LR} \end{bmatrix} \begin{bmatrix} \alpha \\ \beta \end{bmatrix} = \begin{bmatrix} H'_{LL} & H'_{LR} \\ H'_{RL} & H'_{RR} \end{bmatrix} \begin{bmatrix} \alpha \\ \beta \end{bmatrix}$$

$$\therefore \begin{bmatrix} H'_{LL} - E & H'_{LR} \\ H'_{RL} & H'_{RR} - E \end{bmatrix} \begin{bmatrix} \alpha \\ \beta \end{bmatrix} = \boldsymbol{O} \tag{2.52}$$

$$H'_{LL} = \frac{H_{LL} - r_{LR} H_{RL}}{1 - r_{LR} r_{RL}} \quad H'_{LR} = \frac{H_{LR} - r_{LR} H_{RR}}{1 - r_{LR} r_{RL}}$$
$$H'_{RL} = \frac{H_{RL} - r_{RL} H_{LL}}{1 - r_{LR} r_{RL}} \quad H'_{RR} = \frac{H_{RR} - r_{RL} H_{LR}}{1 - r_{LR} r_{RL}}$$

In order to satisfy Equation (2.52),

$$det \begin{bmatrix} H'_{LL} - E & H'_{LR} \\ H'_{RL} & H'_{RR} - E \end{bmatrix} = E^2 - (H'_{LL} + H'_{RR})E + H'_{LL} H'_{RR} - H'_{LR} H'_{RL} = 0$$

$$\therefore \begin{cases} E_+ = \dfrac{1}{2}\left(H'_{LL} + H'_{RR} + \sqrt{(H'_{LL} - H'_{RR})^2 + 4H'_{LR} H'_{RL}}\right) \\ E_- = \dfrac{1}{2}\left(H'_{LL} + H'_{RR} - \sqrt{(H'_{LL} - H'_{RR})^2 + 4H'_{LR} H'_{RL}}\right) \end{cases}$$

By using these parameters, the detuning energy $\hbar\Delta_{LR}$ and coupling strength $\hbar\Omega_{LR}$ are described below. These parameters are related to oscillation of carrier between the two states (Rabi oscillation). Rabi frequency and dephasing time are respectively related to frequency and dumping coefficient of attenuating oscillation of a quantum system.

$$\begin{cases} \hbar\Delta = H'_{LL} - H'_{RR} \\ \hbar\Omega = \sqrt{H'_{LR}H'_{RL}} = \frac{1}{2}\sqrt{(E_+ - E_-)^2 - (\hbar\Delta_{LR})^2} \end{cases} \tag{2.53}$$

2.4.2 First-Order Tunneling Current Theory

The tunneling time and the first-order tunneling current density are derived from a classic electrical current density model by a quantum mechanical approach [263]. In classical method, the current density J is described with the sheet carrier density N_s and the group velocity of electrons v, and the current density operator $\hat{J}$ is described as in Equation (2.54).

$$J = q_0 \frac{N_s}{L_p} v \Longrightarrow \hat{J} = q_0 \frac{N_s}{L_p} \hat{v} \tag{2.54}$$

The expectation value of the current density is derived from Equation (2.54) with the density matrix operator $\hat{\rho}$.

$$\langle \hat{J} \rangle = q_0 \frac{N_s}{L_p} \langle \hat{v} \rangle = q_0 \frac{N_s}{L_p} \langle \frac{d\hat{z}}{dt} \rangle = q_0 \frac{N_s}{L_p} Tr\left(\hat{\rho} \frac{d\hat{z}}{dt}\right) \tag{2.55}$$

Use the Heisenberg's equation of motion,

$$i\hbar\frac{d\hat{z}}{dt} = [\hat{z},\hat{H}] = -[\hat{H},\hat{z}] \Leftrightarrow \frac{d\hat{z}}{dt} = \frac{i}{\hbar}[\hat{H},\hat{z}] \quad (2.56)$$

Plug Equation (2.56) into (2.55).

$$\langle\hat{J}\rangle = q_0\frac{N_s}{L_p}Tr\left(\hat{\rho}\frac{d\hat{z}}{dt}\right) = q_0\frac{N_s}{L_p}Tr\left(\hat{\rho}\frac{i}{\hbar}[\hat{H},\hat{z}]\right) = Tr\left(\hat{\rho}\left\{q_0\frac{N_s}{L_p}\frac{i}{\hbar}[\hat{H},\hat{z}]\right\}\right) = Tr(\hat{\rho}\hat{J})$$

$$\therefore \hat{J} = q_0\frac{N_s}{L_p}\frac{i}{\hbar}[\hat{H},\hat{z}]$$

In the matrix description,

$$\boldsymbol{J} = q_0\frac{N_s}{L_p}\frac{i}{\hbar}[\boldsymbol{H},\boldsymbol{Z}] = \begin{bmatrix} J_{LL} & J_{LR} \\ J_{RL} & J_{RR} \end{bmatrix} \quad (2.57)$$

In Equation (2.57), $\boldsymbol{Z}$ is a transition dipole moment matrix, and $[\boldsymbol{H},\boldsymbol{Z}]$ is also calculated.

$$\boldsymbol{Z} = \begin{bmatrix} Z_{LL} & Z_{LR} \\ Z_{RL} & Z_{RR} \end{bmatrix} = \begin{bmatrix} \int \psi_L^*(z)z\psi_L(z)dz & \int \psi_L^*(z)z\psi_R(z)dz \\ \int \psi_R^*(z)z\psi_L(z)dz & \int \psi_R^*(z)z\psi_R(z)dz \end{bmatrix}$$

$$[\boldsymbol{H},\boldsymbol{Z}] = \boldsymbol{HZ} - \boldsymbol{ZH} = \begin{bmatrix} H_{LL} & H_{LR} \\ H_{RL} & H_{RR} \end{bmatrix}\begin{bmatrix} Z_{LL} & Z_{LR} \\ Z_{RL} & Z_{RR} \end{bmatrix} - \begin{bmatrix} Z_{LL} & Z_{LR} \\ Z_{RL} & Z_{RR} \end{bmatrix}\begin{bmatrix} H_{LL} & H_{LR} \\ H_{RL} & H_{RR} \end{bmatrix}$$

$$= \begin{bmatrix} H_{LR}Z_{RL} - H_{RL}Z_{LR} & (H_{LL} - H_{RR})Z_{LR} - H_{LR}(Z_{LL} - Z_{RR}) \\ -(H_{LL} - H_{RR})Z_{RL} + H_{RL}(Z_{LL} - Z_{RR}) & H_{RL}Z_{LR} - H_{LR}Z_{RL} \end{bmatrix}$$

$$\boldsymbol{\rho J} = \begin{bmatrix} \rho_{LL} & \rho_{LR} \\ \rho_{RL} & \rho_{RR} \end{bmatrix} \begin{bmatrix} J_{LL} & J_{LR} \\ J_{RL} & J_{RR} \end{bmatrix} = \begin{bmatrix} \rho_{LL}J_{LL} + \rho_{LR}J_{RL} & \rho_{LL}J_{LR} + \rho_{LR}J_{RR} \\ \rho_{RL}J_{LL} + \rho_{RR}J_{RL} & \rho_{RL}J_{LR} + \rho_{RR}J_{RR} \end{bmatrix}$$

$$J = Tr(\boldsymbol{\rho J}) = \rho_{LL}J_{LL} + \rho_{LR}J_{RL} + \rho_{RL}J_{LR} + \rho_{RR}J_{RR} = (\rho_{LL} - \rho_{RR})J_{LL} + J_{RL}\rho_{LR} + J_{LR}\rho_{RL}$$

Due to the diagonal components of $[\boldsymbol{H}, \boldsymbol{Z}]$, $J_{RR} = -J_{LL}$. $Z_{LR} = Z_{LR} = Z$.

$$J = q_0 \frac{N_s}{L_p} \frac{i}{\hbar} [(H_{LR} - H_{RL})Z(\rho_{LL} - \rho_{RR}) + (H_{LL} - H_{RR})Z(\rho_{RL} - \rho_{LR}) + (Z_{LL} - Z_{RR})(H_{RL}\rho_{LR} - H_{LR}\rho_{RL})] \tag{2.58}$$

Use the Liouville equation,

$$\frac{d\boldsymbol{\rho}}{dt} = -\frac{i}{\hbar}[\boldsymbol{H}, \boldsymbol{\rho}]$$
$$= -\frac{i}{\hbar} \begin{bmatrix} H_{LR}\rho_{RL} - H_{RL}\rho_{LR} & (H_{LL} - H_{RR})\rho_{LR} - H_{LR}(\rho_{LL} - \rho_{RR}) \\ -(H_{LL} - H_{RR})\rho_{RL} + H_{RL}(\rho_{LL} - \rho_{RR}) & H_{RL}\rho_{LR} - H_{LR}\rho_{RL} \end{bmatrix}$$

Consider the relaxation terms,

$$\begin{cases} \dfrac{d\rho_{LL}}{dt} = -\dfrac{i}{\hbar}(H_{LR}\rho_{RL} - H_{RL}\rho_{LR}) + \left(\dfrac{d\rho_{LL}}{dt}\right)_{relax} \\ \dfrac{d\rho_{LR}}{dt} = -\dfrac{i}{\hbar}[(H_{LL} - H_{RR})\rho_{LR} - H_{LR}(\rho_{LL} - \rho_{RR})] - \dfrac{\rho_{LR}}{\tau^{\parallel}} \\ \dfrac{d\rho_{RL}}{dt} = \dfrac{i}{\hbar}[(H_{LL} - H_{RR})\rho_{RL} - H_{RL}(\rho_{LL} - \rho_{RR})] - \dfrac{\rho_{RL}}{\tau^{\parallel}} \\ \dfrac{d\rho_{RR}}{dt} = \dfrac{i}{\hbar}(H_{LR}\rho_{RL} - H_{RL}\rho_{LR}) + \left(\dfrac{d\rho_{RR}}{dt}\right)_{relax} \end{cases} \tag{2.59}$$

At the steady state, the second and third terms of Equation (2.59) give ρ_{LR} and ρ_{RL}.

$$\rho_{LR} = \frac{H_{LR}\left(H_{LL} - H_{RR} + \frac{i\hbar}{\tau^{\parallel}}\right)}{(H_{LL} - H_{RR})^2 + \frac{\hbar^2}{\tau^{\parallel 2}}}(\rho_{LL} - \rho_{RR})$$

$$\rho_{RL} = \frac{H_{RL}\left(H_{LL} - H_{RR} - \frac{i\hbar}{\tau^{\parallel}}\right)}{(H_{LL} - H_{RR})^2 + \frac{\hbar^2}{\tau^{\parallel 2}}}(\rho_{LL} - \rho_{RR})$$

By using these values,

$$\rho_{RL} - \rho_{LR} = \frac{(H_{LL} - H_{RR})(H_{RL} - H_{LR}) - \frac{i\hbar}{\tau^{\parallel}}(H_{RL} + H_{LR})}{(H_{LL} - H_{RR})^2 + \frac{\hbar^2}{\tau^{\parallel 2}}}(\rho_{LL} - \rho_{RR})$$

$$H_{RL}\rho_{LR} - H_{LR}\rho_{RL} = \frac{-2\frac{i\hbar}{\tau^{\parallel}}H_{LR}H_{RL}}{(H_{LL} - H_{RR})^2 + \frac{\hbar^2}{\tau^{\parallel 2}}}(\rho_{LL} - \rho_{RR})$$

Plug these terms into Equation (2.58).

$$J = q_0 \frac{N_s}{L_p}\frac{i}{\hbar}\frac{\frac{\hbar^2}{\tau^{\parallel 2}}(H_{LR} - H_{RL})Z - \frac{i\hbar}{\tau^{\parallel}}[(H_{LR} + H_{RL})(H_{LL} - H_{RR})Z - 2H_{LR}H_{RL}(Z_{LL} - Z_{RR})]}{(H_{LL} - H_{RR})^2 + \frac{\hbar^2}{\tau^{\parallel 2}}}(\rho_{LL} - \rho_{RR})$$

$$Re(J) = q_0 \frac{N_s}{L_p}\frac{[(H_{LR} + H_{RL})(H_{LL} - H_{RR})Z - 2H_{LR}H_{RL}(Z_{LL} - Z_{RR})]}{\tau^{\parallel}\left[(H_{LL} - H_{RR})^2 + \frac{\hbar^2}{\tau^{\parallel 2}}\right]}(\rho_{LL} - \rho_{RR})$$

$$Im(J) = q_0 \frac{N_s}{L_p}\frac{\frac{\hbar}{\tau^{\parallel 2}}(H_{LR} - H_{RL})Z}{(H_{LL} - H_{RR})^2 + \frac{\hbar^2}{\tau^{\parallel 2}}}(\rho_{LL} - \rho_{RR})$$

Now, assume $Im(J) = 0$, then $H_{LR} = H_{RL}$. Furthermore, assume that $r_{LR} = r_{RL} \sim 0$, $s_{LRL} = s_{RLR} \sim 0$ in Equation (2.50), and Substitute $Z_{LL} - Z_{RR}$ with d_{LR} $(= Z_{LL} - Z_{RR})$.

$$H_{LR} = H_{RL} = t_{LLR} = t_{RRL} = \hbar\Omega \qquad\qquad H_{LL} - H_{RR} = E_L - E_R = \hbar\Delta$$

$$J = Re(J) = q_0 \frac{N_s}{L_p} \frac{[2(\hbar\Omega)(\hbar\Delta)Z - 2(\hbar\Omega)^2 d_{LR}]}{\tau^{\parallel}\left[(\hbar\Delta)^2 + \frac{\hbar^2}{\tau^{\parallel 2}}\right]} (\rho_{LL} - \rho_{RR})$$

$$= q_0 \frac{N_s}{L_p} (\Delta Z + \Omega d_{LR}) \frac{2\Omega\tau^{\parallel}}{1 + \Delta^2 \tau^{\parallel 2}} (\rho_{LL} - \rho_{RR})$$

At the alignment conditions of $|L\rangle$ and $R\rangle$, $\hbar\Delta \sim 0$, and assume $d_{LR} \sim L_p$, the first-order current density is obtained.

$$J \sim q_0 N_s \frac{2\Omega^2 \tau^{\parallel}}{1 + \Delta^2 \tau^{\parallel 2}} (\rho_{LL} - \rho_{RR})$$

Where, the tunneling time T_{LR} and rate U_{LR} are defined in Equation (2.60). With the population fraction of $|L\rangle$ and $|R\rangle$ ($\rho_L^{(1)}$ and $\rho_R^{(1)}$), the first-order current density is rewritten.

$$T_{LR} = \frac{1 + \Delta^2 \tau^{\parallel 2}}{2\Omega^2 \tau^{\parallel}} = \frac{1}{U_{LR}} \tag{2.60}$$

$$J_{LR}^{(1)} = q_0 N_s \frac{\rho_L^{(1)} - \rho_R^{(1)}}{T_{LR}} \tag{2.61}$$

2.5 Rate Equation

The rate equation is described by using carrier scattering time $\tau_{if}\ \left(= {}^{1}\!/_{W_{if}}\right)$ and tunneling rate T_{LR} obtained in Section 2.3 and 2.4 [225]. Because the optical gain is used as a figure-of-merit in Chapter 3~5, the photon density and optical output power are ignored in the rate equation developed in this work, and only intra-module carrier transition and inter-module transitions amongst adjacent modules are considered to describe the temporal change of the population fraction. In this section, the case when the number of subbands per module N_{level} is three is described, but it can be easily expanded for more subbands.

2.5.1 Intra-Module Carrier Transport

By, considering the income and outcome of carriers in subbands, the temporal change of the population fraction is described below. The sheet carrier density of a subband $|n\rangle$ is described as $N_n = N_s\rho_n$ with the sheet carrier density N_s and the population fraction ρ_n.

$$\left(\frac{d\rho_1}{dt}\right)_{intra} = \frac{\rho_2}{\tau_{21}} + \frac{\rho_3}{\tau_{31}} - \frac{\rho_1}{\tau_{12}} - \frac{\rho_1}{\tau_{13}} = -\frac{\rho_1}{\tau_1} + \frac{\rho_2}{\tau_{21}} + \frac{\rho_3}{\tau_{31}}$$

$$\left(\frac{d\rho_2}{dt}\right)_{intra} = \frac{\rho_1}{\tau_{12}} + \frac{\rho_3}{\tau_{32}} - \frac{\rho_2}{\tau_{21}} - \frac{\rho_2}{\tau_{23}} = \frac{\rho_1}{\tau_{12}} - \frac{\rho_2}{\tau_2} + \frac{\rho_3}{\tau_{31}}$$

$$\left(\frac{d\rho_3}{dt}\right)_{intra} = \frac{\rho_1}{\tau_{13}} + \frac{\rho_2}{\tau_{23}} - \frac{\rho_3}{\tau_{31}} - \frac{\rho_3}{\tau_{32}} = \frac{\rho_1}{\tau_{13}} + \frac{\rho_2}{\tau_{23}} - \frac{\rho_3}{\tau_3}$$

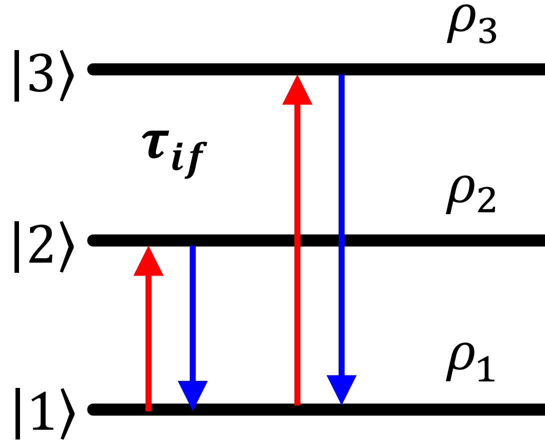

Figure. 2.11 Intra-module carrier transition. Blue arrows describe income, and red arrows describe outcome for subband $|1\rangle$.

This series of equations can be written in the matrix form with $\boldsymbol{\rho} = [\rho_1, \rho_2, \rho_3]^T$.

$$\left(\frac{d}{dt}\begin{bmatrix}\rho_1\\ \rho_2\\ \rho_3\end{bmatrix}\right)_{intra} = \begin{bmatrix} -\frac{1}{\tau_1} & \frac{1}{\tau_{21}} & \frac{1}{\tau_{31}} \\ \frac{1}{\tau_{12}} & -\frac{1}{\tau_2} & \frac{1}{\tau_{32}} \\ \frac{1}{\tau_{13}} & \frac{1}{\tau_{23}} & -\frac{1}{\tau_3} \end{bmatrix}\begin{bmatrix}\rho_1\\ \rho_2\\ \rho_3\end{bmatrix}$$

$$\therefore \left(\frac{d\boldsymbol{\rho}}{dt}\right)_{intra} = \boldsymbol{W}\cdot\boldsymbol{\rho} \tag{2.62}$$

2.5.2 Inter-Module Carrier Transport

In the inter-module transition, the temporal change of the population fractions is described by the tunneling time between the central module and two adjacent modules as

described in Figure 2.12. For example, the temporal change of population fraction of the subband $|1\rangle$ is described as below.

$$\left(\frac{dN_1}{dt}\right)_{inter} = \frac{\rho'_1}{T_{1'1}} - \frac{\rho_1}{T_{11'}} + \frac{\rho'_2}{T_{2'1}} - \frac{\rho_1}{T_{12'}} + \frac{\rho'_3}{T_{3'1}} - \frac{\rho_1}{T_{13'}} + \frac{\rho''_1}{T_{1''1}} - \frac{\rho_1}{T_{11''}} + \frac{\rho''_2}{T_{2''1}} - \frac{\rho_1}{T_{12''}} + \frac{\rho''_3}{T_{3''1}} - \frac{\rho_1}{T_{13''}}$$

Assume $T_{1''1} = T_{11'}$, $T_{11''} = T_{1'1}$, $T_{2''1} = T_{21'}$, $T_{12''} = T_{1'2}$, $T_{3''1} = T_{31'}$, $T_{13''} = T_{1'3}$, $\rho'_1 \approx \rho''_1 \approx \rho_1$, $\rho'_2 \approx \rho''_2 \approx \rho_2$, and $\rho'_3 \approx \rho''_3 \approx \rho_3$ at the steady-state.

$$\therefore \left(\frac{dN_1}{dt}\right)_{inter} = -\left(\frac{1}{T_{12'}} + \frac{1}{T_{13'}} + \frac{1}{T_{1'2}} + \frac{1}{T_{1'3}}\right)\rho_1 + \left(\frac{1}{T_{2'1}} + \frac{1}{T_{21'}}\right)\rho_2 + \left(\frac{1}{T_{3'1}} + \frac{1}{T_{31'}}\right)\rho_3$$

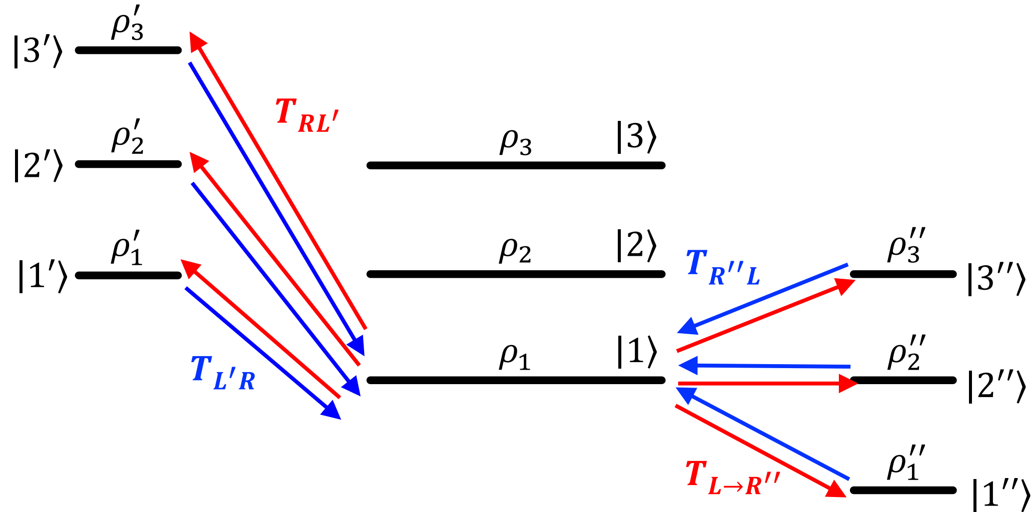

Figure. 2.12 Inter-module carrier transition. Blue arrows describe income, and red arrows describe outcome for subband $|1\rangle$.

$\left(\frac{dN_2}{dt}\right)_{inter}$ and $\left(\frac{dN_3}{dt}\right)_{inter}$ are also calculated, and the matrix form is Equation (2.63).

$$\left(\frac{d\boldsymbol{\rho}}{dt}\right)_{inter} = \boldsymbol{U} \cdot \boldsymbol{\rho} \tag{2.63}$$

$$\boldsymbol{U} = \begin{bmatrix} -\left(\frac{1}{T_{12'}} + \frac{1}{T_{13'}} + \frac{1}{T_{1'2}} + \frac{1}{T_{1'3}}\right) & \frac{1}{T_{2'1}} + \frac{1}{T_{21'}} & \frac{1}{T_{3'1}} + \frac{1}{T_{31'}} \\ \frac{1}{T_{1'2}} + \frac{1}{T_{12'}} & -\left(\frac{1}{T_{21'}} + \frac{1}{T_{23'}} + \frac{1}{T_{2'1}} + \frac{1}{T_{2'3}}\right) & \frac{1}{T_{3'2}} + \frac{1}{T_{32'}} \\ \frac{1}{T_{1'3}} + \frac{1}{T_{13'}} & \frac{1}{T_{2'3}} + \frac{1}{T_{23'}} & -\left(\frac{1}{T_{31'}} + \frac{1}{T_{32'}} + \frac{1}{T_{3'1}} + \frac{1}{T_{3'2}}\right) \end{bmatrix}$$

2.5.3 Solution of the Rate Equation

The net temporal change of the population fractions is the sum of the ones in Equation (2.62) and (2.63) and it is assumed to be zero at the steady state.

$$\frac{d\boldsymbol{\rho}}{dt} = \left(\frac{d\boldsymbol{\rho}}{dt}\right)_{intra} + \left(\frac{d\boldsymbol{\rho}}{dt}\right)_{inter} = (\boldsymbol{W} + \boldsymbol{U}) \cdot \boldsymbol{\rho} = \boldsymbol{0} \tag{2.64}$$

This simultaneous equation can be solved by replacing one of the equations with the carrier conservation law as described below.

$$\sum_n \rho_n = 1$$

2.6 Electrical Current Theory

The electrical current density of QCLs is calculated with population fraction obtained from the rate equation and the electrical current density model. Even though the first-order current density model shown in Equation (2.61) can reproduce experimental values to some extent, this model can also show a large error sometimes due to ignoring carriers' thermal distribution energy. Carrier leakage from bound states to continuum states is also not considered in this model. These phenomena are modeled in the second- [263,264] and third-order tunneling current models [265].

2.6.1 Second-Order Tunneling Current Theory

The second-order tunneling current model, considering carriers' thermal distribution, is proposed by Terazzi *et al.* in 2008 [263,264]. As described in Equation (2.65), the fundamental equation is almost the same as the first-order model, but thermal distribution of carriers is reflected in population fraction $\rho_L^{(2)}$ and $\rho_R^{(2)}$. Carriers in a subband complies with the Fermi-Dirac function described in Equation (2.66).

$$J_{LR}^{(2)} = q_0 N_{2D} \frac{\rho_L^{(2)} - \rho_R^{(2)}}{T_{LR}} \tag{2.65}$$

$$f_i^{FD}(E, \mu_i) = \frac{1}{1 + exp\left[\frac{E - \mu_i}{k_B T_{e_i}}\right]} \tag{2.66}$$

In Equation (2.66), μ_i is the two-dimensional chemical potential of a subband $|i\rangle$. The effective population fractions $\rho_L^{(2)}$ and $\rho_R^{(2)}$ are calculated considering the two cases depending on the subband energy shown in Figure 2.13. For example, in the case (a), all carriers in the left module contribute to the tunnel current. However, in the right module, only high energy carriers can affect. $D(E)$ denotes the two-dimensional density of state.

(a) $\hbar\Delta_{LR} \geq 0$

$$\rho_L^{(2)} = \rho_L$$

$$\rho_R^{(2)} = \rho_R \frac{\int_{E_L}^{\infty} D^R(E) f_R^{FD}(E, \mu_R) dE}{\int_0^{\infty} D^R(E) f_R^{FD}(E, \mu_R) dE}$$

$$D^R(E) = \frac{m_R^*}{\pi\hbar^2} \Theta(E - E_R)$$

(b) $\hbar\Delta_{LR} < 0$

$$\rho_L^{(2)} = \rho_L \frac{\int_{E_R}^{\infty} D^L(E) f_L^{FD}(E, \mu_L) dE}{\int_0^{\infty} D^L(E) f_L^{FD}(E, \mu_L) dE}$$

$$\rho_R^{(2)} = \rho_R$$

$$D^L(E) = \frac{m_L^*}{\pi\hbar^2} \Theta(E - E_L)$$

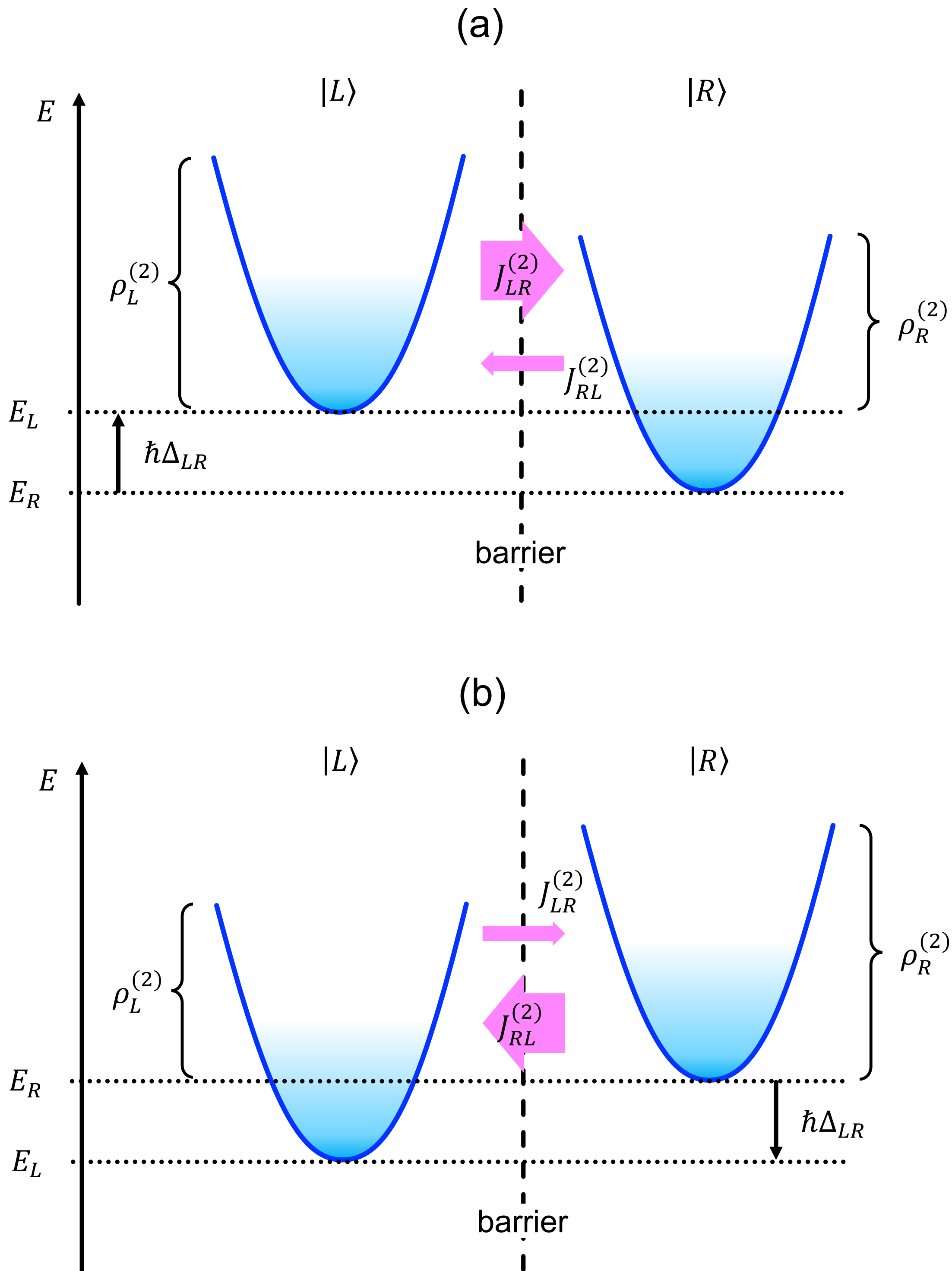

Figure. 2.13 Thermal distribution of subband carriers in the second-order tunneling current theory. (a)$\hbar\Delta_{LR} \geq 0$, and (b) $\hbar\Delta_{LR} < 0$.

2.6.2 Third-Order Tunneling Current Theory

Derivation of the third-order tunneling current model is described below. Because the energy distribution of bounded carriers complies with the Fermi-Dirac distribution as shown in Figure 2.14, carriers having higher energy over a potential barrier can escape to continuum states (leak A) and contribute to leakage current. It is also intuitively understood that most carriers below a potential barrier remain inside wells and contribute to the tunneling current. However, in devices based on quantum-wells, it is known that carriers inside wells can partially contribute to the leakage current by tunneling effect, too (leak B), and subband population is also influenced. The new model is developed to deal with such effects quantitatively.

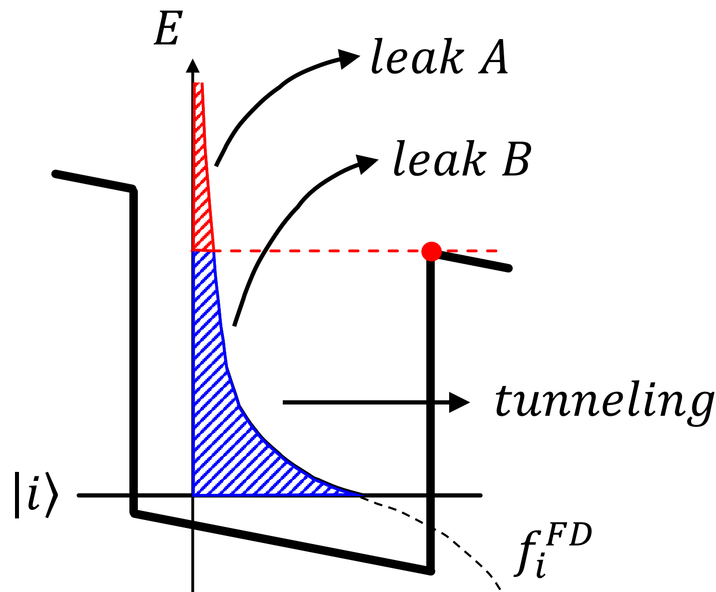

Figure. 2.14 Carrier leakage and tunneling paths from one subband in a quantum well.

2.6.2.1 The third-order tunneling current density

First, electrons' transmission coefficient toward a triangle barrier, often seen in quantum-well devices, is described by semi-classical Wentzel-Kramers-Brillouin (WKB) approximation [266]. When an electron injects into a potential barrier V_0 located at $z' = 0$ as shown in Figure 2.15, the transmission coefficient P is described by Equation (2.67), in which the elementary charge and the reduced Plank's constant are denoted by q_0 and $\hbar$, respectively, and the tunneling rate depends on the electrical field F and effective mass of the barrier material m_b, as well.

$$P = exp\left[-2\int_{0}^{z_c} \frac{\sqrt{2m_b(V_0 - q_0 F z')}}{\hbar} dz'\right] \tag{2.67}$$

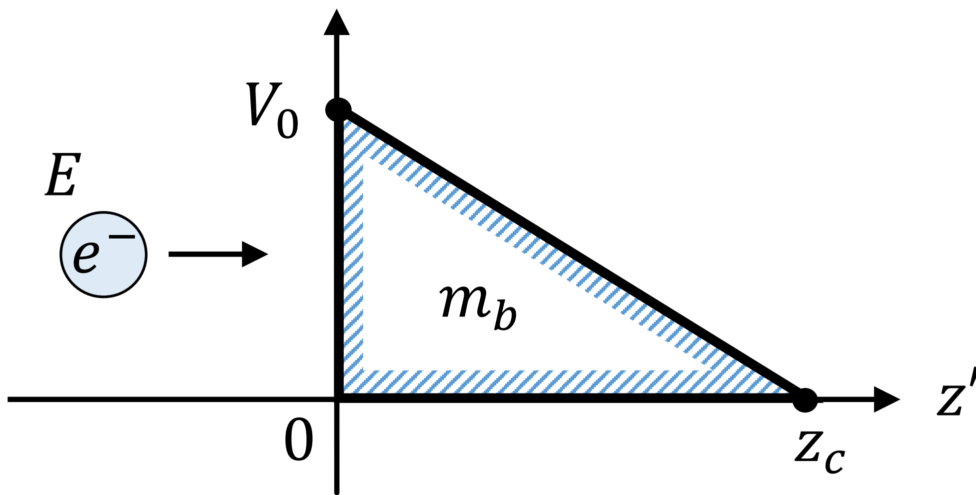

Figure. 2.15 Electron tunneling to a triangle potential.

Due to the linearity of a potential barrier, z_c, where potential becomes zero in z'-axis, is also described by Equation (2.68), and the integration in Equation (2.67) is calculated in (2.69).

$$z_c = \frac{V_0}{q_0 F} \tag{2.68}$$

$$P = exp\left[-\frac{4\sqrt{2m_b}}{3\hbar}\frac{V_0^{\frac{3}{2}}}{q_0 F}\right] \tag{2.69}$$

When an electron has the total energy E (= Potential energy + Kinetic energy), an efficient barrier height toward this electron V_0 is described by $V_0 = V_B - E$ using a local potential barrier height V_B. Therefore, the transmission coefficient is dependent on electrons' energy.

$$P(E) = exp\left[-\frac{4\sqrt{2m_b}}{3\hbar}\frac{(V_B - E)^{\frac{3}{2}}}{q_0 F}\right] \tag{2.70}$$

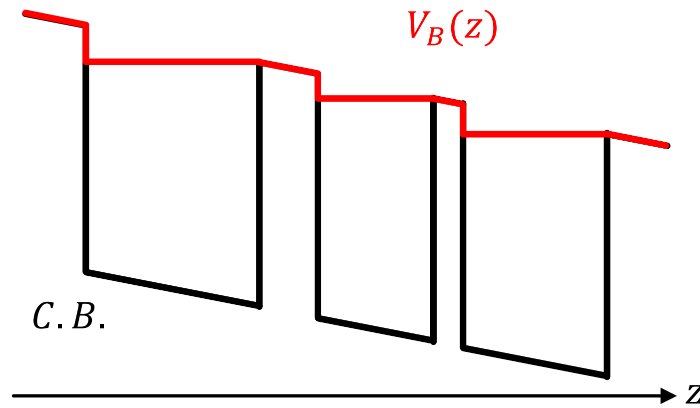

Figure. 2.16 Local potential barrier for leakage carriers.

Furthermore, considering that V_B depends on position as described in Figure 2.16, the energy-and-position dependent transmission coefficient is derived. The coefficient for the leak A is assumed to be unity, and the one for the leak B is estimated by Equation (2.70). These relations are integrated and described by Equation (2.71) with a Heaviside function Θ.

$$P(z,E) = \Theta\big(E - V_B(z)\big) + \Theta(V_B(z) - E)exp\left[-\frac{4\sqrt{2m_b}}{3\hbar}\frac{(V_B(z) - E)^{\frac{3}{2}}}{q_0 F}\right] \tag{2.71}$$

Next, the population fraction contributing to the tunneling and leakage current will be described using Equation (2.71) and the total population fraction of a bound state $|i\rangle$, whose eigenenergy and wavefunction are denoted by E_i and ψ_i. Due to nature of the wavefunction, the spatial distribution of population fraction is described by Equation (2.72).

$$\rho_i(z) = \rho_i|\psi_i(z)|^2 \tag{2.72}$$

When Fermi-Dirac function for subband $|i\rangle$, given in Equation (2.66), is denoted by f_i^{FD}, the energy-dependent population fraction is described by Equation (2.73).

$$\rho_i(z,E) = \rho_i(z)\frac{f_i^{FD}(E)\Theta(E - E_i)}{\int_0^\infty f_i^{FD}(E)\Theta(E - E_i)\, dE} \tag{2.73}$$

Using Equation (2.71) and (2.73), the tunneling component of the population fraction is written by Equation (2.74).

$$\rho_i^{(tun)}(z,E) = \rho_i(z,E)\big(1 - P(z,E)\big) \tag{2.74}$$

By integrating Equation (2.74) spatially, the energy-dependent electron distribution is obtained in (2.75), and the tunneling current and optical gain are calculated by using it.

$$\rho_i^{(tun)}(E) = \int \rho_i^{(tun)}(z,E)\, dz \tag{2.75}$$

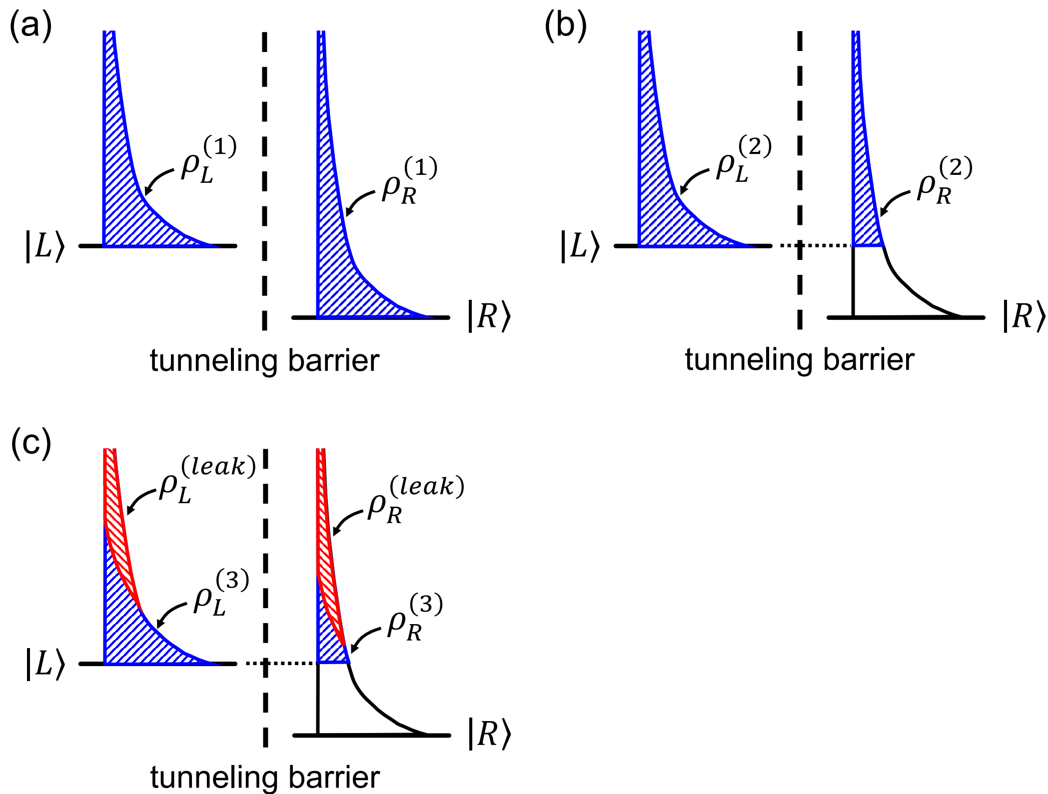

Figure. 2.17 Comparison of thermally distributed electrons used for different theories of tunneling current. (a) First-order tunneling theory, (b) Second-order tunneling theory, and (c) Third-order tunneling theory. The carriers' thermal distribution shown in blue is applied to the tunneling current equation, and that shown in red contribute to the leakage current.

We call the tunneling current considering the influence of carrier leakage the third-order tunneling current. For calculating it, tunneling time T_{LR} in Equation (2.60) and the first-order tunneling current equation proposed by Scalari *et al.* [139] in Equation (2.61) are used adopting the concept of the second-order tunneling current theory proposed by Terazzi *et al.* [263, 264] and the theory described in Equation (2.75), resulting in Equation (2.76). Where, $\rho_L^{(3)}$ and $\rho_R^{(3)}$ are population fractions of subbands $|L\rangle$ and $|R\rangle$ reflecting the influence of carrier leakage to continuum states depicted in Figure 2.17.

$$J_{LR}^{(3)} = q_0 N_s \frac{\rho_L^{(3)} - \rho_R^{(3)}}{T_{LR}} \tag{2.76}$$

2.6.2.2 Bound-to-Continuum Leakage Current

The leakage current, composed of leakage carriers into continuum states, is derived as the drift current in bulk crystal. The leakage component of the population fraction for subband $|i\rangle$ is described by Equation (2.77) using (2.71) and (2.73).

$$\rho_i^{(leak)}(z,E) = \rho_i(z,E)\, P(z,E) \tag{2.77}$$

By integrating spatially and energetically, the total leakage population fraction per module is obtained as in Equation (2.78).

$$\rho^{(leak)} = \sum_i \iint \rho_i^{(leak)}(z,E)dEdz \tag{2.78}$$

The volumetric leakage carrier density is calculated using Equation (2.78).

$$N_{3D}^{(leak)} = \frac{N_s \rho^{(leak)}}{L_p} \tag{2.79}$$

The drift velocity, another important parameter for the drift current calculation, is determined by mobility μ_e and saturated velocity v_{sat} [267]. In terms of electron mobility, LO-phonon scattering, acoustic-phonon scattering (AP), piezo-electric scattering (PZ), ionized-impurity scattering, and interface-roughness scattering are considered, and the theoretical models for bulk crystal are applied to the calculation [268]. The effective mobility μ_e is calculated by Matthiessen's rule in Equation (2.80) [268]. Among these scattering phenomena, LO-phonon scattering is predominant beyond around 100K, and interface-roughness and ionized-impurity scatterings become dominant at lower temperature conditions for GaAs. For thermal averaging, the electron temperature in continuums, explained in Section 2.8, is used.

$$\frac{1}{\mu_e} = \frac{1}{\mu^{(LO)}} + \frac{1}{\mu^{(AP)}} + \frac{1}{\mu^{(PZ)}} + \frac{1}{\mu^{(IMP)}} + \frac{1}{\mu^{(IFR)}} \tag{2.80}$$

In the calculation for the drift velocity in Equation (2.81), a theoretically calculated saturated velocity is also used [269].

$$v_d = \frac{\mu_e F}{\sqrt{1 + \left(\frac{\mu_e F}{v_{sat}}\right)^2}} \quad (2.81)$$

Finally, the leakage current is calculated by Equation (2.82).

$$J^{(leak)} = q_0 v_d N_{3D}^{(leak)} \quad (2.82)$$

2.6.2.3 Electron mobility for leakage current

The bound-to-continuum leakage current described in the previous subsection is defined as drift current in bulk crystal, so the electron's mobility caused by scattering mechanisms is also modeled in the three-dimensional system [268]. The abstract of the derivation of the mobility is briefly introduced in this subsection. The mobility $\mu^{(X)}$ due to a scattering phenomenon X is described in Equation (2.83) with a carrier relaxation time $\tau^{(X)}$.

$$\mu^{(X)} = \frac{q_0}{m^*}\tau^{(X)} \quad (2.83)$$

The energy-dependent carrier relaxation time $\tau^{(X)}(E_{\boldsymbol{k}})$ is described in Equation (2.84) obtained from a discussion about the distribution function in the Boltzmann equation with the carrier scattering rate $W^{(X)}(\boldsymbol{k}, \boldsymbol{k}')$ described by Fermi's golden rule as in Equation

(2.85). In these equations, $\boldsymbol{k}$ and $\boldsymbol{k'}$ respectively denotes three-dimensional momentums before and after scattering, and $\theta_{\boldsymbol{k},\boldsymbol{k'}}$ is an angle made by $\boldsymbol{k}$ and $\boldsymbol{k'}$.

$$\frac{1}{\tau^{(X)}(E_{\boldsymbol{k}})} = \sum_{\boldsymbol{k'}} W^{(X)}(\boldsymbol{k},\boldsymbol{k'})\left(1 - cos\theta_{\boldsymbol{k},\boldsymbol{k'}}\right) \tag{2.84}$$

$$W^{(X)}(\boldsymbol{k},\boldsymbol{k'}) = \frac{2\pi}{\hbar}\left|\left\langle \boldsymbol{k'}\middle|\widetilde{H}_s^{(X)}\middle|\boldsymbol{k}\right\rangle\right|^2 \delta(E_{\boldsymbol{k}} - E_{\boldsymbol{k'}}) \tag{2.85}$$

The thermally averaged relaxation time $\tau^{(X)}$ is derived from a discussion about thermal averaging of group velocity and is described in Equation (2.86).

$$\tau^{(X)} = \frac{\int_0^\infty \tau^{(X)}(E_{\boldsymbol{k}})\, f_{3d}^{FD}(1 - f_{3d}^{FD})E_{\boldsymbol{k}}^{\frac{3}{2}} dE_{\boldsymbol{k}}}{\int_0^\infty f_{3d}^{FD}(1 - f_{3d}^{FD})E_{\boldsymbol{k}}^{\frac{3}{2}}\, dE_{\boldsymbol{k}}} \tag{2.86}$$

$f_{3d}^{FD}(E_{\boldsymbol{k}})$ denotes the three-dimensional Fermi-Dirac function and is described in Equation (2.87). Where, E_F is the Fermi level of bulk crystal, and $T_{e,C}$ is the electron temperature of continuum states.

$$f_{3d}^{FD}(E_{\boldsymbol{k}}) = \frac{1}{1 + \exp\left(\frac{E_{\boldsymbol{k}} - E_F}{k_B T_{e,C}}\right)} \tag{2.87}$$

Carrier relaxation rate for each scattering mechanism is calculated based on these equations with the scattering Hamiltonian. In this work, LO-phonon, acoustic-phonon (AP), piezo-electric (PZ), ionized-impurity, and interface-roughness scatterings are considered for the

three-dimensional carrier mobility, and the relaxation rate for these phenomena is listed below. The derivation process is shown in a reference [268].

Relaxation time due to LO-phonon scattering

$$\tau^{(LO)}(E_{\boldsymbol{k}}) = \frac{8\pi\hbar^2}{\sqrt{2m^*}q_0^2 E_{LO}}\left(\frac{1}{\varepsilon_\infty} - \frac{1}{\varepsilon_s}\right)^{-1}\left[(N_0+1)\frac{\sqrt{E_{\boldsymbol{k}} - E_{LO}}}{E_{\boldsymbol{k}}}\Theta(E_{\boldsymbol{k}} - E_{LO}) + N_0\frac{\sqrt{E_{\boldsymbol{k}} + E_{LO}}}{E_{\boldsymbol{k}}}\right]^{-1} \quad (2.88)$$

Relaxation time due to Acoustic-phonon scattering

$$\tau^{(AP)}(E_{\boldsymbol{k}}) = \frac{2\pi\hbar^4 c_{ii}}{(2m^*)^{\frac{3}{2}} D_A^2 k_B T_L} E_{\boldsymbol{k}}{}^{-\frac{1}{2}} \quad (2.89)$$

In Equation (2.89), D_A denotes the acoustic-phonon potential deformation, and c_{ii} denotes the averaged longitudinal elastic constant.

Relaxation time due to Piezo-electric scattering

$$\tau^{(PZ)}(E_{\boldsymbol{k}}) = \frac{5\pi\varepsilon_s^2\hbar^2 c_{ii}}{\sqrt{2m^*}q_0^2 e_{14}^2 k_B T_L} E_{\boldsymbol{k}}{}^{-\frac{1}{2}} \quad (2.90)$$

In Equation (2.90), e_{14} denotes piezo-electric coefficient.

Relaxation time due to Ionized-impurity scattering

$$\tau^{(IMP)}(E_{\boldsymbol{k}}) = \frac{16\sqrt{2}\pi\varepsilon_s^2\sqrt{m^*}E_{\boldsymbol{k}}^{\frac{3}{2}}}{q_0^4 n_i}\left[ln\left(1+\frac{8m^*E_{\boldsymbol{k}}}{\hbar^2 K_{sc}^2}\right) - \frac{1}{1+\frac{\hbar^2 K_{sc}^2}{8m^*E_{\boldsymbol{k}}}}\right]^{-1} \quad (2.91)$$

In Equation (2.91), n_i is the three-dimensional driving carrier density.

Relaxation time due to Interface-Roughness scattering

$$\tau^{(IFR)}(E_{\boldsymbol{k}}) = \frac{\hbar^3}{m^*(q_0 F\Delta\Lambda)^2}\left[\int_0^{\pi}\left(1-cos\theta_{\boldsymbol{k},\boldsymbol{k}'}\right)exp\left[-\frac{m^*\Lambda^2 E_{\boldsymbol{k}}}{\hbar^2}\left(1-cos\theta_{\boldsymbol{k},\boldsymbol{k}'}\right)\right]d\theta_{\boldsymbol{k},\boldsymbol{k}'}\right]^{-1} \quad (2.92)$$

2.7 Optical Parameters

In this section, important design parameters, oscillator strength and optical gain, are explained.

2.7.1 Oscillator Strength

Oscillator strength is an un-dimensional parameter to describe the strength of optical transition and is determined by the energy difference and the degree of wavefunction overlap between two subbands. Optical gain is linearly related to oscillator strength, so large oscillator strength is considered to be advantageous. However, non-radiative transition (scattering) rate, described by Fermi's golden rule, is also dependent on wavefunction overlap, resulting in a trade-off. Therefore, THz QCLs are often designed so that the optical transition is diagonal, which means that oscillator strength is not so large.

Oscillator strength between subbands $|i\rangle$ and $|f\rangle$ is defined in Equation (2.93) with a momentum operator $\boldsymbol{P}$ [59, 229].

$$O_{if} = \frac{2}{m^*}\frac{\left|\langle\psi_i(z)\middle|\boldsymbol{P}\middle|\psi_f(z)\rangle\right|^2}{E_i - E_f} \tag{2.93}$$

Now, use Heisenberg equation of motion in Equation (2.93).

$$i\hbar \frac{d\boldsymbol{Z}}{dt} = [\boldsymbol{Z}, \boldsymbol{H}] = \boldsymbol{ZH} - \boldsymbol{HZ} \tag{2.94}$$

From a classical theory, the momentum operator is related to the position operator.

$$\boldsymbol{P} = m^* \frac{d\boldsymbol{Z}}{dt} \tag{2.95}$$

Combine Equations (2.94) and (2.95).

$$\boldsymbol{P} = \frac{im^*}{\hbar}(\boldsymbol{HZ} - \boldsymbol{ZH}) \tag{2.96}$$

By using Equation (2.96), Equation (2.93) is re-written as below.

$$\langle \psi_i(z)|\boldsymbol{P}|\psi_f(z)\rangle = \left\langle \psi_i(z)\middle| \frac{im^*}{\hbar}(\boldsymbol{HZ} - \boldsymbol{ZH})\middle|\psi_f(z)\right\rangle$$

$$= \frac{im^*}{\hbar}\left(\langle \psi_i(z)|\boldsymbol{HZ}|\psi_f(z)\rangle - \langle \psi_i(z)|\boldsymbol{ZH}|\psi_f(z)\rangle\right)$$

$$= \frac{im^*}{\hbar}\left(\langle \psi_f(z)|\boldsymbol{ZH}|\psi_i(z)\rangle^* - \langle \psi_i(z)|\boldsymbol{ZH}|\psi_f(z)\rangle\right)$$

$$= \frac{im^*}{\hbar}\left(E_i\langle \psi_f(z)|\boldsymbol{Z}|\psi_i(z)\rangle^* - E_f\langle \psi_i(z)|\boldsymbol{Z}|\psi_f(z)\rangle\right) = \frac{im^*}{\hbar}\left(E_i - E_f\right)\langle \psi_i(z)|\boldsymbol{Z}|\psi_f(z)\rangle$$

Plug this relation into (2.93) to obtain Equation (2.97).

$$O_{if} = \frac{2m^*}{\hbar^2}\left(E_i - E_f\right)\left|\langle \psi_i(z)|\boldsymbol{Z}|\psi_f(z)\rangle\right|^2 \tag{2.97}$$

2.7.2 Optical Gain

The optical gain is a parameter describing photon generation efficiency due to optical transition of carriers and is originally defined as a ratio of the number of photons generated per volume to the number of photons supplied to a surface.

$$gain \equiv \frac{Number\ of\ photons\ generated\ per\ volume\ [\#/cm^3]}{Number\ of\ photons\ supplied\ to\ a\ surface\ [\#/cm^2]}$$

The theoretical model is derived based on Fermi's golden rule and Lambert-Beer's law and is described in Equation (2.98) [59]. In this equation, N_i and N_f are subband carrier density ($N_i = N_s \Delta\rho_i,\ N_f = N_s \Delta\rho_f$), and $\mathcal{L}(\hbar\omega, \hbar\omega_{if})$ is a normalized Lorentzian function described below and Figure 2.18(a).

$$\begin{aligned} g_{if} &= \frac{\pi q_0^2}{n_r \varepsilon_0 c \hbar L_p}(\hbar\omega_{if})\left|\langle\psi_i(z)|\boldsymbol{Z}|\psi_f(z)\rangle\right|^2 \mathcal{L}(\hbar\omega, \hbar\omega_{if})(N_i - N_f) \\ &= \frac{\pi q_0^2 \hbar}{2m^* n_r \varepsilon_0 c L_p} O_{if} \mathcal{L}(\hbar\omega, \hbar\omega_{if})(N_i - N_f) \end{aligned} \quad (2.98)$$

$$\mathcal{L}(\hbar\omega, \hbar\omega_{if}) = \frac{\Gamma_{if}/2\pi}{(\hbar\omega - \hbar\omega_0)^2 + (\Gamma_{if}/2)^2} \xrightarrow[\hbar\omega = \hbar\omega_0]{} \frac{2}{\pi\Gamma_{if}}$$

Optical gain peaks when $\hbar\omega = \hbar\omega_0$. Then,

$$g_{if}^{peak} = \frac{q_0^2 \hbar}{m^* n_r \varepsilon_0 c L_p} O_{if} \frac{N_i - N_f}{\Gamma_{if}} = \frac{q_0^2 \hbar}{m^* n_r \varepsilon_0 c L_p} N_s O_{if} \frac{\rho_i - \rho_f}{\Gamma_{if}} \quad (2.99)$$

In Equation (2.99), the relation between the optical gain and some device parameters is important for device design: optical gain is proportional to oscillator strength and population inversion, and inversely proportional to optical linewidth and one period length. In device design, it is a key whether optical gain peak calculated in Equation can surpass threshold gain in Equation (1.2) as described in Figure 2.18 (b).

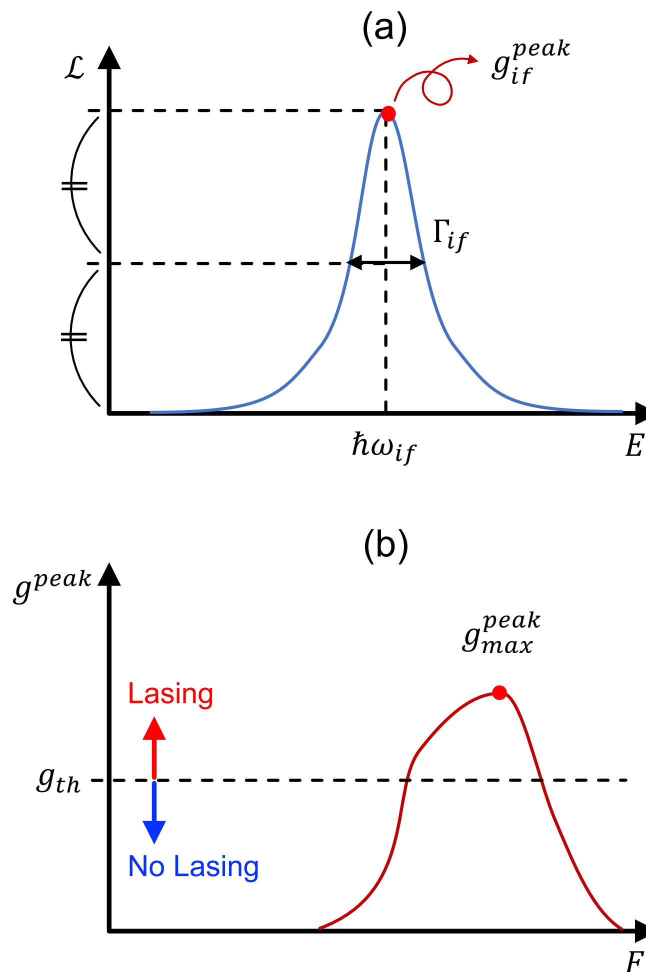

Figure. 2.18 Images for device parameters for optical gain. (a) Lorentzian function, and (b) the dependence of optical gain on electrical field.

2.8 Auxiliary Physical Phenomena

QCLs can be designed by adjusting the essential device parameters explained in Section 2.1 ~ 2.7. However, other phenomena can also influence on the device parameters greatly depending on a driving condition. So, it is important to consider these parameters in device simulation to predict device performance more accurately. In this section, the below auxiliary physical phenomena are introduced with the models and theories of them: the lattice temperature, electron temperature in bound state and continuum state, band-bending effect, and dopant activation ratio.

2.8.1 Self-Heating Theory

Even though the lattice temperature is often assumed to be the same as the heat-sink temperature in simulation, the lattice temperature can become higher than the heat-sink temperature due to self-heating effect in real devices, and an analytical model for it is preferred to be used [270, 271].

In this work, a QCL is assumed as a mesa structure. Then, generated heat diffuses to six directions as depicted in Figure 2.19. In this setting, only the bottom of the device touches a GaAs substrate whose thermal conductivity is κ_{sub} = 55W/Km, and the air or vacuum encompassing it has 0.024 W/Km and 5×10^{-4} W/Km thermal conductivity, respectively. Therefore, electrically generated heat is thought to flow mainly down to the substrate when it is not significant. (In Figure 2.19, heat flow in five directions: q_{+x}, q_{-x},

q_{+y}, q_{-y}, and q_{-z} are ignored, and only heat transfer q_{+z} is considered.) The cross-plane thermal transfer is also ignored in this work, but it is necessary for CW operation [285]. Then, a relation about the heat flow is described by Equation (2.100) using Fourier's law. The effective thermal flux generated per time is denoted by $\bar{Q}$, and L and W are a length and width of the mesa structure.

$$-\kappa_{sub}\frac{\partial T}{\partial z} = \frac{\bar{Q}}{LW} \tag{2.100}$$

Now, an axis z is determined and the boundary between the device and substrate is set as z = 0. In addition, assuming that the device temperature is homogeneous and corresponding to the lattice temperature T_L, and the temperature of the bottom of the device, whose thickness H_{sub}, matches the heat-sink temperature T_{HS}, solution of Equation (2.100) gives (2.101).

$$\begin{cases} T_L = T_{HS} + \Delta T \\ \Delta T = \dfrac{H_{sub}}{\kappa_{sub}LW}\bar{Q} \end{cases} \tag{2.101}$$

The effective thermal flux is dependent on several device parameters such as electrical field, current density, pulsation period T_{pulse}, and pulse width τ_{pulse}. Here, voltage applied in the device V and electrical current I are described in Equation (2.102). The total period of QCL structure is denoted by N_p.

$$\begin{cases} V = N_p F L_p \\ I = JLW \end{cases} \tag{2.102}$$

Using Equation (2.102), the effective thermal flux is described by (2.103), and the temperature difference between the heat-sink and lattice temperature ΔT is calculated by Eq. (2.104).

$$\bar{Q} = N_p L_p F J (LW) \left(\frac{\tau_{pulse}}{T_{pulse}} \right) \tag{2.103}$$

$$\therefore \Delta T = N_p L_p F J \left(\frac{H_{sub}}{\kappa_{sub}} \right) \left(\frac{\tau_{pulse}}{T_{pulse}} \right) \tag{2.104}$$

As for the accuracy of these equations, caution would be necessary because when the generated heat becomes substantial, heat could dissipate into the air or vacuum, as well.

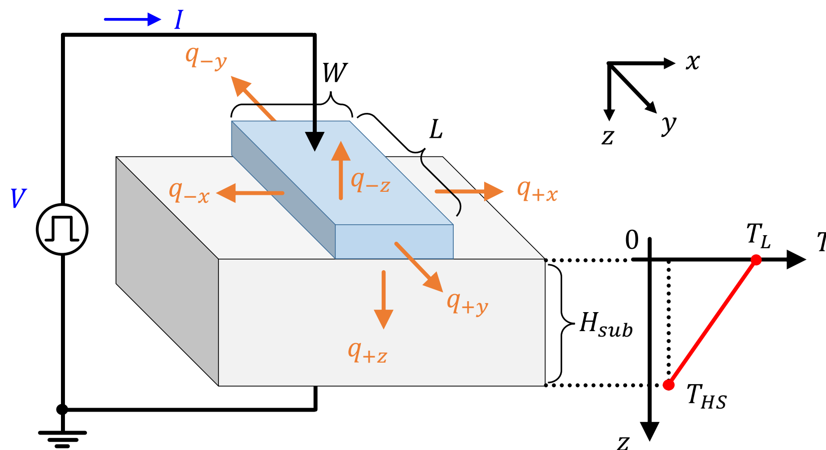

Figure. 2.19 Heat flow from a QCL chip. A blue part is a QCL mesa structure, and a grey part is a GaAs-substrate.

2.8.2 Energy-Balance Theory

Even though the electron temperature is important because it can influence thermal distribution of carriers as described in Fermi-Dirac function, it is often assumed to be the same value as the lattice temperature. Calculation for the electron temperature is proposed by Harrison *et al.*, and this work also adopts their method, the energy-balance theory [59, 272-274]. In this method, the electron temperature of all subbands is assumed to be the same value (The averaged electron temperature). Although alternative method has also been proposed to calculate the electron temperature for each subband, the work in Chapter 3~5 do not adopt this method because it does not always get converged in a loop calculation, or the electron temperature can abruptly vary to electrical field [275-278].

Now consider carrier scattering from subband $|i\rangle$ to $|f\rangle$ (Including the intra-subband scattering). Then, the energy that an electron obtains or loses through this transition is written in Equation (2.105).

$$\Delta E_{if} = E_i - E_f + \delta E \tag{2.105}$$

In Equation (2.105), δE is an additional energy depending on scattering phenomena and is described as below.

$$\delta E = \begin{cases} -E_{LO}\ (LO - phonon\ emission) \\ E_{LO}\ (LO - phonon\ absorption) \\ 0\ (elastic\ scattering) \end{cases}$$

The net energy balance due to all carrier transition is described below.

$$\Delta = \sum_{X}\sum_{f}\sum_{i}\frac{N_i}{\tau_{if}}\Delta E_{if} \tag{2.106}$$

In Equation (2.106), scattering time τ_{if} is dependent on the electron temperature, and this energy balance needs to be zero ($\Delta = 0$) at the steady state. So, the optimal electron temperature value is sought by changing T_e until it satisfies $\Delta \sim 0$ in a loop calculation. The calculation image and flow are described in Figure 2.20 and 2.21. Considering the influence of scattering rate on device performance, only LO-phonon and interface-roughness scatterings are included in the developed simulation in this work.

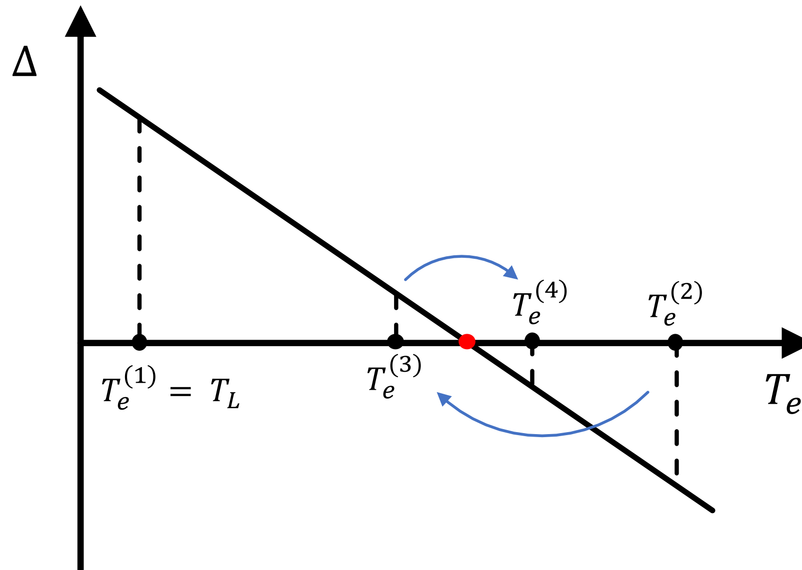

Figure. 2.20 The self-consistent loop calculation for the electron temperature.

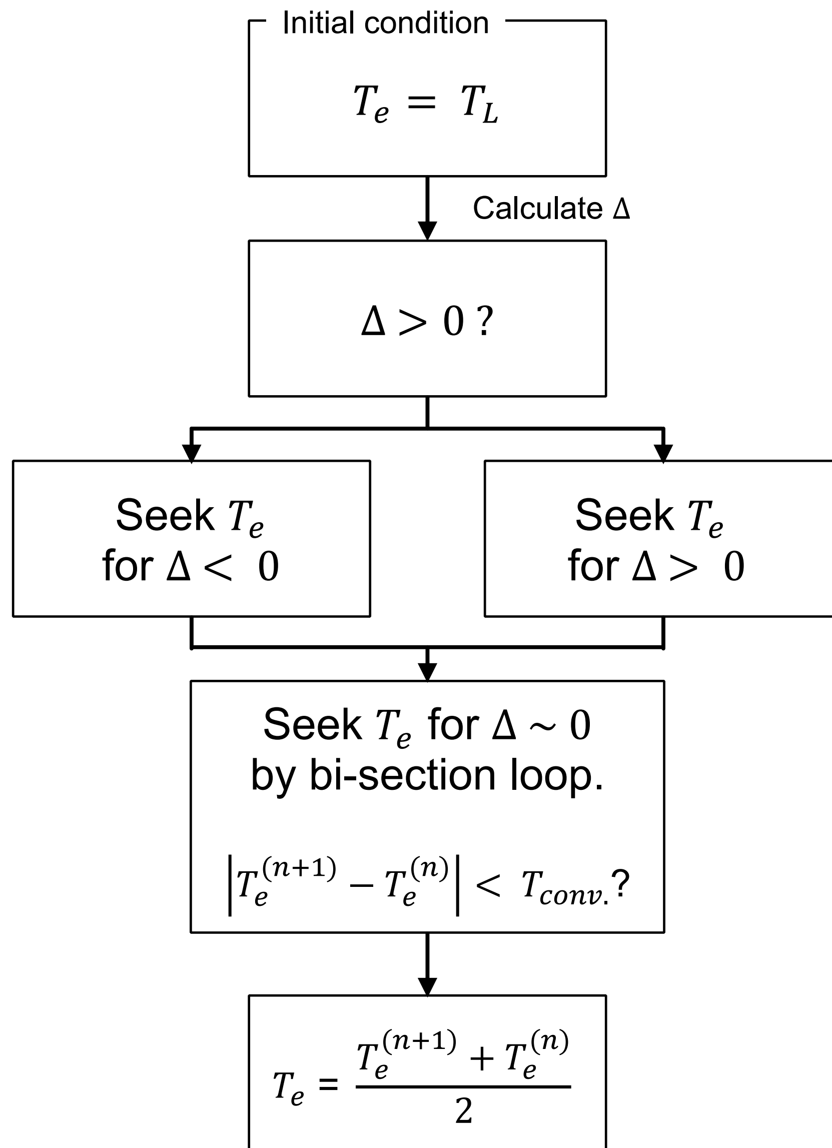

Figure. 2.21 Calculation flow for the electron temperature. $T_{conv.}$ Denotes a convergent temperature.

2.8.3 Electron Temperature in Continuum States

The electron temperature for the continuum states $T_{e,C}$ is also necessary for calculating bound-to-continuum leakage current. The theoretical model for this parameter is derived based on a semiclassical theory of bulk crystal.

Under a certain voltage, electron's kinetic energy is assumed to be a sum of thermal energy from lattice and kinetic energy due to electrical acceleration, and Equation (2.107) is obtained.

$$\frac{3}{2}k_B T_L + \frac{1}{2}m^* v_d^2 = \frac{3}{2}k_B T_{e,C} \tag{2.107}$$

By solving Equation (2.107), the electron temperature is given as below.

$$\therefore\ T_{e,C} = T_L + \frac{m^* v_d^2}{3k_B} \tag{2.108}$$

2.8.4 Dopant Activation Rate

As is often the case with QCL simulation, carrier density is assumed to be the same as doping density. However, even at room-temperature, not all dopants are activated. So, a self-consistent calculation is necessary to estimate the net carrier density. In the case of n-type semiconductor materials, the activated dopant density N_d^+ depends on the donor level E_D generated between the conduction band E_C and Fermi level E_F due to impurity doping and is described by Equation (2.109).

$$N_d^+ = \frac{N_d}{1 + 2\exp\left(\frac{E_F - E_D}{k_B T_L}\right)} \tag{2.109}$$

In Equation (2.109), the three-dimensional doping density is denoted by N_d, and k_B is the Boltzmann constant. As seen in this equation, the dopant activation ratio is influenced by the lattice temperature T_L. For the band diagram in Figure 2.22, the energy difference between the Fermi level and donor level is described by Equation (2.110).

$$E_F - E_D = (E_C - E_D) - (E_C - E_F) \tag{2.110}$$

The ionization energy of doped Si in GaAs is described by $E_C - E_D$, and its value is 5.85meV [267, 279]. $E_C - E_F$ is the energy difference between the conduction band and Fermi level and is obtained in Equation (2.111) by using the effective density of state N_C.

$$E_C - E_F = k_B T_L ln\left(\frac{N_C}{n^{3D}}\right) \quad (2.111)$$

$$N_C = 2\left(\frac{m^* k_B T_L}{2\pi\hbar^2}\right)^{\frac{3}{2}} \quad (2.112)$$

Finally, the value of the net three-dimensional carrier density n^{3D} is assumed to be the same as the calculated activated doping density described in Equation (2.113).

$$n^{3D} \approx N_d^+ \quad (2.113)$$

Having said that, to calculate N_d^+ by Equation (2.113), n^{3D} is required in Equation (2.111). Therefore, these calculations are self-consistently processed with an initial assumption of $n^{3D} \approx N_d$. The dopant activation ratios of Si in GaAs at 200K and 300K are approximately 84% and 91%, respectively [279].

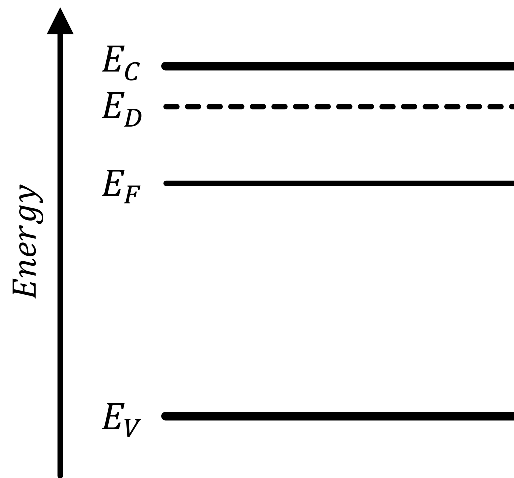

Figure. 2.22 Band diagram of n-type semiconductor with the donor level.

2.8.5 Dopant Distribution Model

In this study, conventional rectangular doping and δ-dope distributions are examined considering the back-ground doping (1.0×10^{14}cm^{-3}), and these doping distributions are determined by simple theoretical models and the sheet doping density N_d^{2D}. In this section, the relation between the volumetric dopant distribution $N_d^{3D}(z)$ and the sheet doping density is explained. In general, these two parameters have the relation described as below.

$$N_d^{2D} = \int_{1period} N_d^{3D}(z)dz \tag{2.114}$$

In rectangular doping, dopants are doped homogeneously over a range of L_{dope} described in Figure 2.23(a), and the sheet doping density is calculated using a local doping density $N_{d,0}^{3D}$. In actual situations, segregation happens as depicted by a wiggly line in Figure 2.23(a).

$$N_d^{2D} = N_{d,0}^{3D} L_{dope} \tag{2.115}$$

For δ-doping, an experimental model considering dopant migration is adopted as described in Equation (2.116) [280, 281]. In Figure 2.23(b), $N_{d,peak}^{3D}$ is a peak of doping density and z_p is a position of the doping peak. Dumping coefficients of exponential curves are denoted by α and β. In this study, $\alpha = 4\text{Å}$ and $\beta = 24\text{Å}$ are extracted from the reference data [281]. From Equation (2.116), the sheet doping density is calculated as in (2.117).

$$N_d^{3D}(z) = \begin{cases} N_{d,peak}^{3D} exp\left(\frac{z - z_p}{\alpha}\right) & (z < z_p) \\ N_{d,peak}^{3D} exp\left(-\frac{z - z_p}{\beta}\right) & (z \geq z_p) \end{cases} \tag{2.116}$$

$$N_d^{2D} = N_{d,peak}^{3D}(\alpha + \beta) \tag{2.117}$$

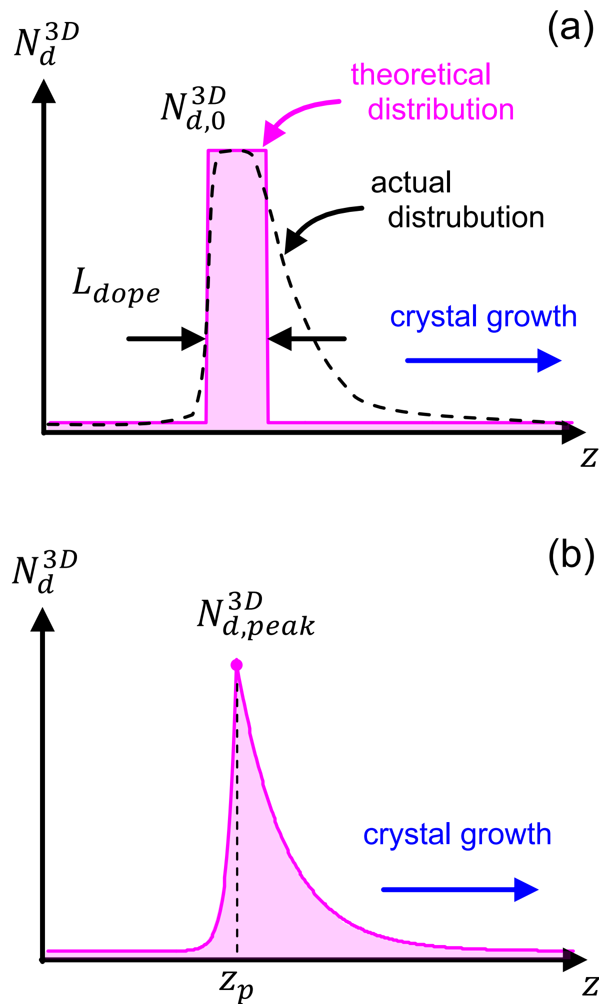

Figure. 2.23 Doping distributions. (a) Rectangular doping. (b) δ-doping.

2.8.6 Schrödinger-Poisson Equation System

Quantum-well potential in QCLs are basically determined by the conduction band edge and heterojunction. However, an electron in QCLs is influenced by other electrons and ionized donors, and the actual potential can be different from the one defined by only materials. Such space-charge effect is incorporated in calculation by the Hartree approximation [59].

Now, the potential made by surrounding electrons and ionized donors (the Hartree potential) is described by $V_H(z)$ and is calculated by Poisson equation in Equation (2.118).

$$\frac{\partial^2 V_H(z)}{\partial z^2} = -\frac{q_0}{\varepsilon_s}\left[p(z) - n(z) + N_d^+(z) - N_a^-(z)\right] \tag{2.118}$$

In equation (2.118), $p(z)$, $n(z)$, $N_d^+(z)$, and $N_a^-(z)$ denote carrier densities of holes, electrons, ionized donors, and ionized acceptors. QCLs are basically n-type, so $p(z) = 0$ and $N_a^-(z) = 0$. Electrons' distribution is determined by wavefunction.

$$n(z) = \sum_i N_i |\psi_i(z)|^2 = \sum_i N_s \rho_i |\psi_i(z)|^2 \tag{2.119}$$

By using Equation (2.119), the sheet charge density $\sigma(z)$ is described in Equation (2.120).

$$\sigma(z) = q_0 \left[N_s \sum_i \rho_i |\psi_i(z)|^2 - N_d^+(z) \right] \delta z \tag{2.120}$$

Consider the electrical field made by a sheet charge located at z. Using Gauss' law, the electrical field is obtained.

$$E^H(z) = \frac{\sigma(z)}{2\varepsilon_s} \tag{2.121}$$

The net electrical field at z is a sum of the individual discretized parts.

$$E(z) = \sum_{z'=-\infty}^{\infty} E^H(z)\, sign(z-z') = \frac{1}{2\varepsilon_s}\sum_{z'=-\infty}^{\infty} \sigma(z)\, sign(z-z') \tag{2.122}$$

$$sign(z-z') = \begin{cases} 1\ (z > z') \\ 0\ (z = z') \\ -1\ (z < z') \end{cases}$$

Due to $E(z) = -\frac{\partial V(z)}{\partial z}$,

$$\therefore V_H(z) = -\int_{-\infty}^{z} E(z')dz' \tag{2.123}$$

By replacing $V(z)$ in Equation (2.1) with $V(z) + V_H(z)$, wavefunction and subband energy including band-bending effect are calculated from the Schrödinger equation. In THz QCLs, when doping density is not so high (~10^{10} cm^{-2}), the influence of band-bending is negligible. However, high doping density (>10^{11} cm^{-2}) induces remarkable band-bending and subband detuning.

2.9 Calculation Flow

In this section, a calculation flowchart of the developed rate equation model will be described. As described in Figure 2.2, the device simulator of this work bases some input parameters; electrical field, heat-sink temperature, and sheet doping density to calculate optical gain ultimately. Having said that, accurate calculation results require self-consistent loop calculation because the Hartree potential, subband carrier density (population fraction), lattice temperature, and electron temperature needs solutions of the rate equation, as described in the previous section and Figure 2.24. In the developed model, a single calculation for ionized-impurity and electron-electron scattering is a heavy task, so calculation time for even one electrical field conditions is time-consuming.

This work does not use self-consistent loop calculation to reduce calculation time and reuses the device parameters obtained in a previous calculation step of electrical field as described in Figure 2.25. If the initial values of the Hartree potential or temperatures are close to the true values (solutions of self-consistent loop calculation), the calculated results also tend to be close to the true values, too. This method, indeed, sacrifices the calculation accuracy, to some extent, but the difference from self-consistent loop is not so significant. As for dopant activation rate, self-consistent loop calculation is implemented because this parameter is independent of others which needs initial conditions.

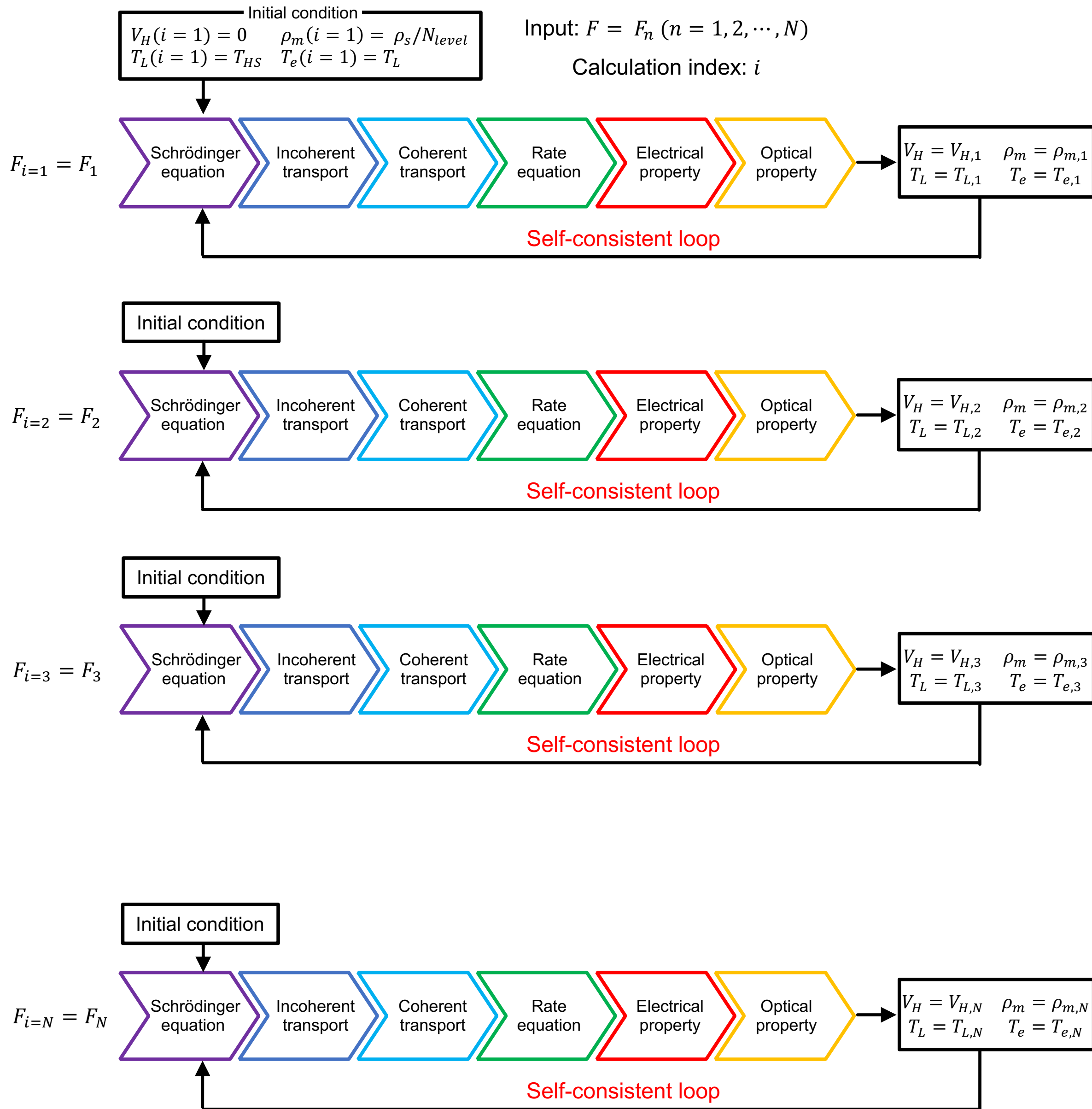

Figure. 2.24 Calculation flowchart with self-consistent loop.

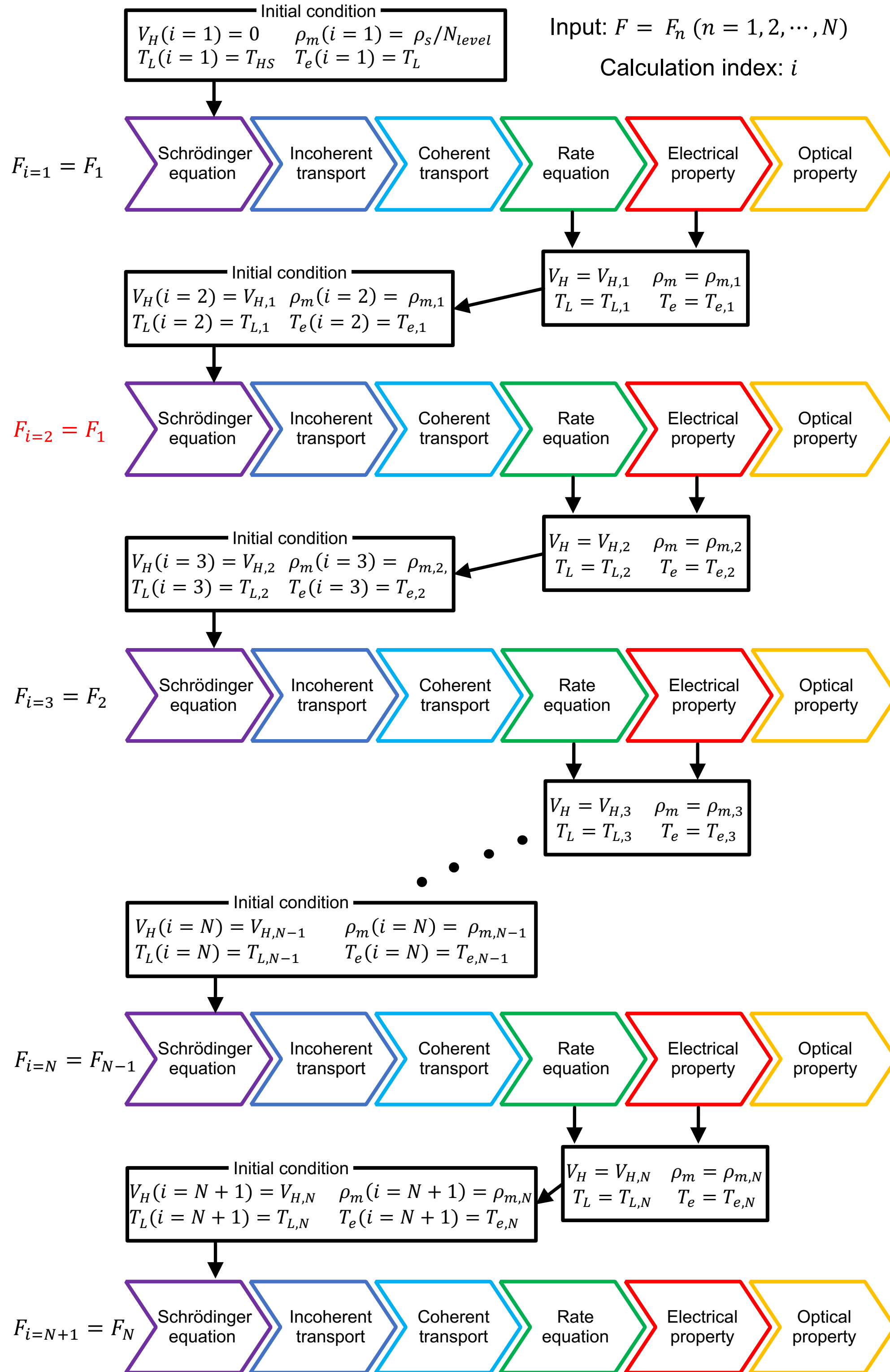

Figure. 2.25 Calculation flowchart without self-consistent loop (adopted in this work).

2.10 Calculation Examples

In this section, example calculation for previously published devices will be demonstrated. In 2.10.1, the high-performance two-well resonant-phonon THz QCL is calculated by the developed device simulator. In 2.10.2, the highest operation temperature of five devices is predicted.

2.10.1 High-Performance Two-Well Resonant-Phonon THz QCL

Figure 2.26 describes a two-well resonant-phonon device designed by Khalatpour *et al.*(G652) [224] which recorded the highest operation temperature of 250K, and the calculation results of this device at 200K of the heat-sink temperature is shown in Figure 2.27 and 2.28. This device is a standard in the research in Chapter 3 and 4.

A module of G652 is composed of GaAs/AlGaAs material system with 30% of Al-composition and has six subbands. A rectangular-shaped impurity doping is implemented over 30Å in the center of a phonon-well with 4.5×10^{10}cm^{-2} of sheet carrier density. The carrier transition for lasing occurs among the lowest three subbands. At an alignment condition between subband $|1'\rangle$ and $|3\rangle$, carriers are injected from subband $|1'\rangle$ to $|3\rangle$ (the upper lasing state ULS), and carriers in subband $|2\rangle$ (the lower lasing state LLS) are also extracted down to subband $|1\rangle$ by fast LO-phonon scattering, resulting in population inversion and stimulated emission between ULS and LLS. Other upper level subbands ($|4\rangle$ ~ $|6\rangle$) work as parasite states.

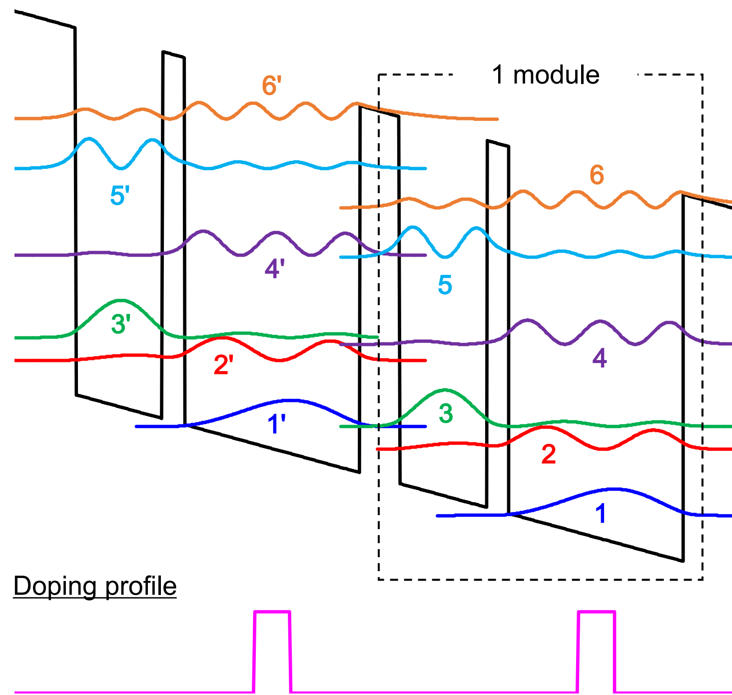

Figure. 2.26 A two-well resonant-phonon structure (G652).

The calculated J-V curve of G652 matches well with the experimental results as described in Figure 2.27 (a). Where, two times of subband alignment appear as kinks around 17 and 27kV/cm. The influence of carrier leakage into continuums is observed to be negligible, so most subband carriers contributed to tunneling transport as described in Figure 2.27 (b)~(d). Fractional population inversion reaches around 12% even at the alignment condition between $|1\rangle$ and $|3\rangle$. Lastly, calculated scattering rate of main three subbands is shown in Figure 2.28. At 200K of the heat-sink temperature, LO-phonon scattering is found to be the dominant factor in all inter-subband transition although Coulomb scatterings are dominant in intra-subband scattering. In the transition between the lasing states $|3\rangle$ and $|2\rangle$,

interface-roughness and ionized-impurity scattering become influential, so barrier height or impurity doping would need to be carefully designed depending on the conditions.

Due to structural simplicity, two-well resonant-phonon devices are considered to be suitable for investigating the impact of design parameters on performance. Therefore, further study would be implemented by using this type of structures.

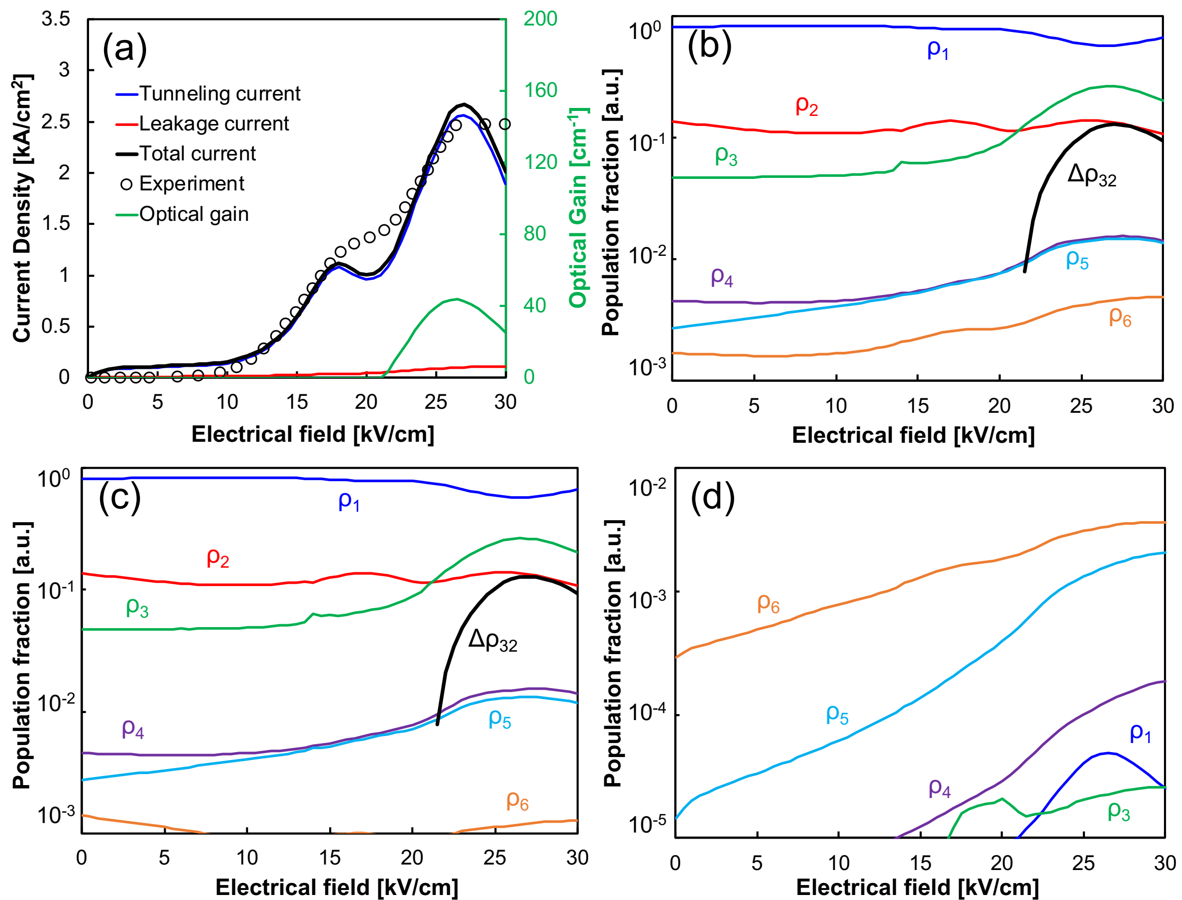

Figure. 2.27 Calculation results of G652. (a) J-V characteristics. Experimental data was taken at 10K. (b) Population fraction calculated by the rate equation. (c) Tunneling component of population fraction. (d) Leakage component of population fraction.

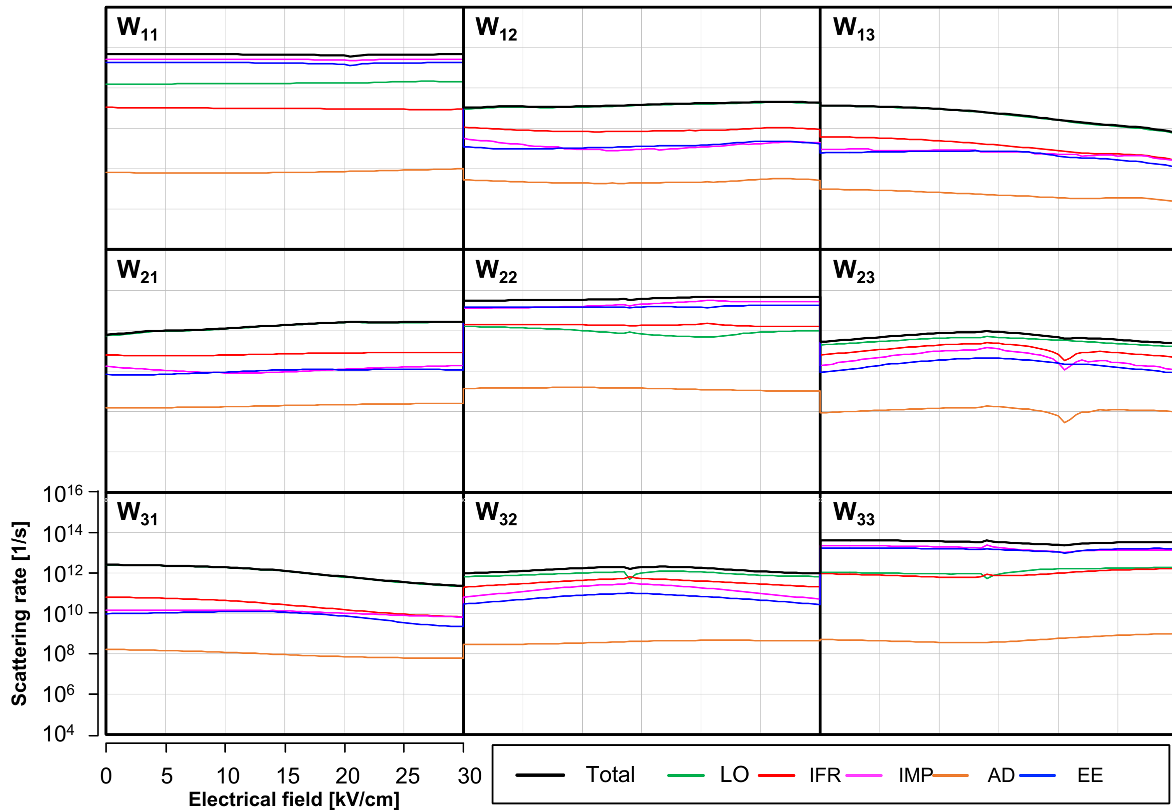

Figure. 2.28 Scattering rate between main subbands. In this calculation, electron temperature of each subband is individually calculated and shows abrupt change to electrical field. That change influence the current density and appears as small dents.

2.10.2 Prediction of the Highest Operation Temperature

The validity of the developed device simulator is implemented through a comparison in the highest operation temperature between simulation and experiment. In this investigation, five test devices which have already been published are simulated: an indirectly-pumped device (V843) [225], one three-well resonant-phonon device (F47) [282], and three two-well resonant-phonon devices (G652, EV2624, and TW246) [224, 283, 284], and the highest operation temperature is estimated as the one where the optical gain reaches the threshold gain set as 20cm^{-1}.

In the comparison described in Figure 2.29, simulation results and experimental values of three devices (V843, F47, and G652) match with small errors. However, large difference is observed in the other devices (EV2624 and TW246). This error would come from the precision of the device simulator, experimental uncertain errors, and difference in waveguide structures. Especially, the size of active cores of these devices are not the same, which can affect the threshold gain. For example, active cores of the three devices (V843, F47, and G652) are designed to be 10μm-thick, but the ones of the other devices (EV2624 and TW246) are different (12μm and 8μm, respectively).

As described in Figure 2.29, there is a room to improve the developed device simulator to predict the highest operation temperature very precisely. However, it is also a fact that this simulator can distinguish high-performance devices (F47, EV2624, G652) among the five samples even under a rough assumption (g_{th} = 20cm^{-1}). So, the author judges this simulator is enough for the investigation about the influence of design parameters on

device performance in Chapter 3 to 5.

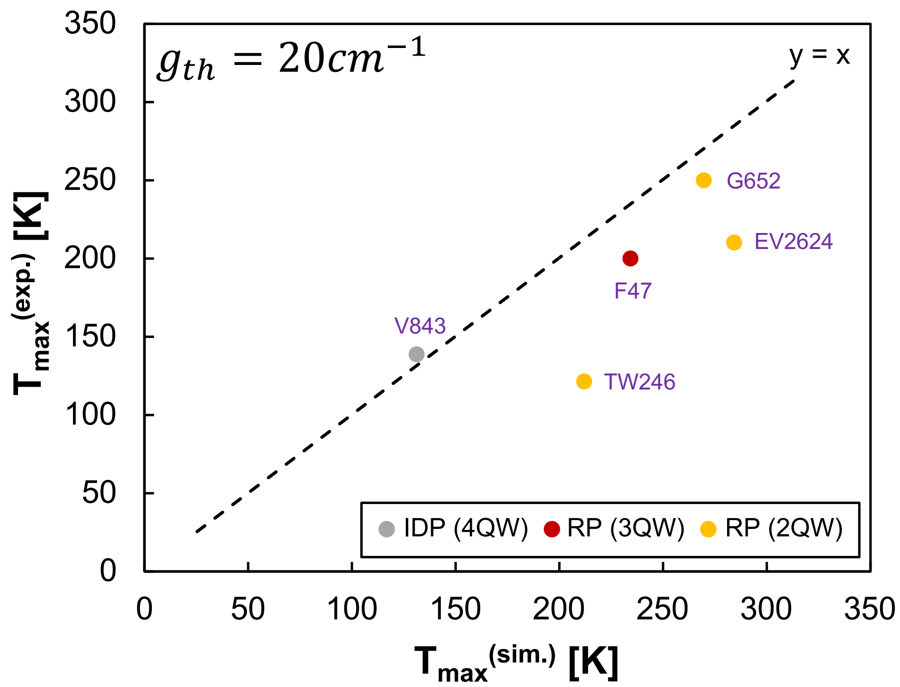

Figure. 2.29 Comparison in the highest operation temperature between simulation and experiment.

Even if 99 out of 100 people say otherwise, the remaining one may be right.

– Masatoshi Koshiba

Chapter 3 Doping Study

3.1 Introduction

Doping studies have been reported for both MIR QCLs [286-292] and THz QCLs with roughly seven factors: ionized-impurity scattering [137,221,234,245,293,294], doping amount [151,170,286-288,295-299], doping position [289,290,300,301,309], doping distribution [280,281], device polarity [291,302,187], band-bending [292,303], and free-carrier absorption [102,304,305].

The impact of ionized-impurity scattering on carrier transition rate and optical linewidth is the most important feature in doping studies [137,221,234,245,293,294]. In terms of carrier transition rate, the ionized-impurity scattering is not a dominant phenomenon in THz QCLs compared to the LO-phonon and interface-roughness scattering. However, in accordance with Fermi's golden rule, where scattering rate is determined by an overlap amongst wavefunctions of the initial and final states and dopants, when the doping position is close to the lasing sites, non-radiative scattering rate can increase due to the ionized-impurity scattering [289]. This effect is less influential in MIR QCLs and early-stage THz QCLs. Because a doping region (injection region) and an active region are spatially separated in these devices, the carrier transition between lasing subbands is less likely to be exacerbated by the ionized-impurity scattering. In recent THz QCLs composed of fewer wells, on the other hand, donor impurities are doped very close to lasing sites. In this case, the degradation

of population inversion is inevitable. This issue is thus thought to be more critical in short two-well THz QCLs [202,224,283,310]. As for optical linewidths, the ionized-impurity scattering is one of the main causes of optical linewidth broadening [137,245]. Therefore, ionized-doping greatly influences the optical gain through optical linewidths.

Studies on the optimal doping amount have been the most frequently reported, and representative works for THz QCLs are listed in Table 3.1. In these previous works [137,151,170,211,295-299], resonant-phonon (RP), bound-to-continuum (B-to-C), and split-well direct-phonon (SW-DP) structures are used with a different range of sheet doping densities from 4.3×10^{9} to 3.5×10^{11} cm^{-2}, and the highest operation temperature, optical gain, and output power are reported to have optimized values [170,295,299]. This fact is interpreted as that dopants are necessary to obtain a sufficient optical gain over the threshold gain; a too high impurity doping causes high free-carrier absorption [102,304,305] and band-bending [292,303], resulting in increase of waveguide loss and undesirable misalignment of subbands, respectively. Free-carrier absorption must be suppressed in THz QCLs because it is proportional to the square of dopant density (N_d^2) and wavelength to the power of three-and-half ($\lambda^{3.5}$) [102,304].

Despite relatively few studies, the influence of doping position has also been investigated [289,300,301,309]. Previous research using MIR QCLs reveals that when dopants are injected in the vicinity of the upper lasing state (ULS), device performance degrades remarkably [289]. In THz QCL research, Wang *et al.* also examined the influence of doping positions on the highest operation temperatures, using three-well resonant-phonon devices [301]. In comparison between a phonon-well doped device and a radiation-barrier

doped one with a typical sheet doping density (3.0×10^{10}cm^{-2}), the demonstrated highest operation temperatures were almost the same. Demić *et al.* also theoretically confirmed that device performance is independent of doping position with 2.0×10^{10}cm^{-2} of sheet doping density [309]. On the other hand, Grange demonstrates the possibility of improving device performance with different doping positions through his theoretical work [300]. Because this type of research is expected to be influenced by other components: doping amounts or distribution, more-detailed research is necessary.

Lastly, a few studies on doping distribution have also been reported. The most frequently used doping method for recent resonant-phonon devices is narrow-rectangular doping in the center of phonon-wells [224,282,283]. On the other hand, δ-doping method, minimizing interactions between doping regions and wavefunctions, is also effective to enhance performance [280,281]. In experiments, furthermore, the influence of dopant migration is also considered. During epitaxial growth, dopants diffuse into more freshly grown layers. If these diffused dopants reach radiation areas, device performance is degraded [187,302]. To avoid this issue, the order of layer growth should be carefully considered.

This study aims to theoretically examine doping methods composed of doping amount, position, and distribution for two-well resonant-phonon THz QCLs and to provide doping design guidelines for high-temperature operation. In Section 3.2, the calculation for investigation of the influence of impurity doping will be explained. Along with it, the influence of doping on device parameters are also investigated to understand the calculation results shown in the later sections. In Section 3.3, the optical gain of eight doping patterns is calculated for a single module by using the device simulator developed in Chapter 2, and the

best doping pattern will be determined based on the optical gain. The calculation results will also be analyzed by investigating the componential device parameters of optical gain. Finally, an effective doping scheme is suggested and discussed in Section 3.4, including the same phenomena occurring in waveguides that are not dealt with in the device simulation.

Year	Researcher	Sim. / Exp.	Basic device structure		Impurity doping method		
			Carrier transport	Material system	Position	Distribution	Sheet doping density [cm^{-2}]
2005	H. C. Liu / D. Ban	Exp.	RP (4QW)	GaAs / $Al_{0.15}Ga_{0.85}As$	Phonon-well	δ-doping	3.2×10^{10} ~ 4.8×10^{10}
2005	J. Alton		B-to-C		Two wide wells	homogeneous	1.6×10^{10} ~ 5.8×10^{10}
2006	L. Ajili		B-to-C		One wide well		3.3×10^{10} ~ 8.8×10^{10}
2007	A. Benz		RP (4QW)		Phonon-well		5.4×10^{9} ~ 1.9×10^{10}
2008	A. M. Andrews		RP (4QW)				4.3×10^{9} ~ 3.9×10^{10}
2015	T. Grange	Sim.	RP (3QW)			narrow-rectangular	very low ~ 1.0×10^{11}
2016	C. W. I. Chen	Exp.	RP (3QW)				3.0×10^{10} ~ 2.4×10^{11}
2021	N. L. Gower		SW-DP*			homogeneous	3.0×10^{10} ~ 6.0×10^{10}
2022	T.-T. Lin	Sim. & Exp.	RP (4QW)				6.4×10^{10} ~ 3.5×10^{11}
2022	This work	Sim.	RP (2QW)	GaAs / $Al_{0.30}Ga_{0.70}As$	Examined	Examined	1.0×10^{10} ~ 1.0×10^{12}

Table. 3.1 Previous doping studies of THz QCLs. (*Injection barriers are composed of $Al_{0.45}Ga_{0.55}As$, and phonon-wells are split.)

3.2 Method

The influence of impurity doping on device performance of a two-well resonant-phonon THz QCL is theoretically investigated in terms of doping density, position, and distribution. This section will explain the simulation conditions, and the advanced knowledge necessary for understanding the calculation results will also be described.

3.2.1 The Influence of Impurity-Doping on Device Parameters

The device simulator based on the rate equation has been developed in Chapter 2, and the relation between impurity doping and device parameters will be explained in Figure 3.1. Device parameters directly influenced by impurity doping: current density, optical gain, carrier scattering rate, optical linewidth, and band-bending have often been discussed. In addition to these direct influence, indirect effects on some of these parameters caused by band-bending is also important to consider simulation and experimental results. For example, band-bending issues subband detuning at lasing alignment conditions [303]. Such potential distortion affects other device parameters such as oscillator strength and tight-binding parameters via wavefunction and eigen energy calculated by Schrödinger equation, resulting in change in current density and optical gain.

In doping study, it is especially important to understand how the ionized-impurity scattering is influenced by impurity doping, and this effect is explained based on a simple double-quantum-well (DQW) structure.

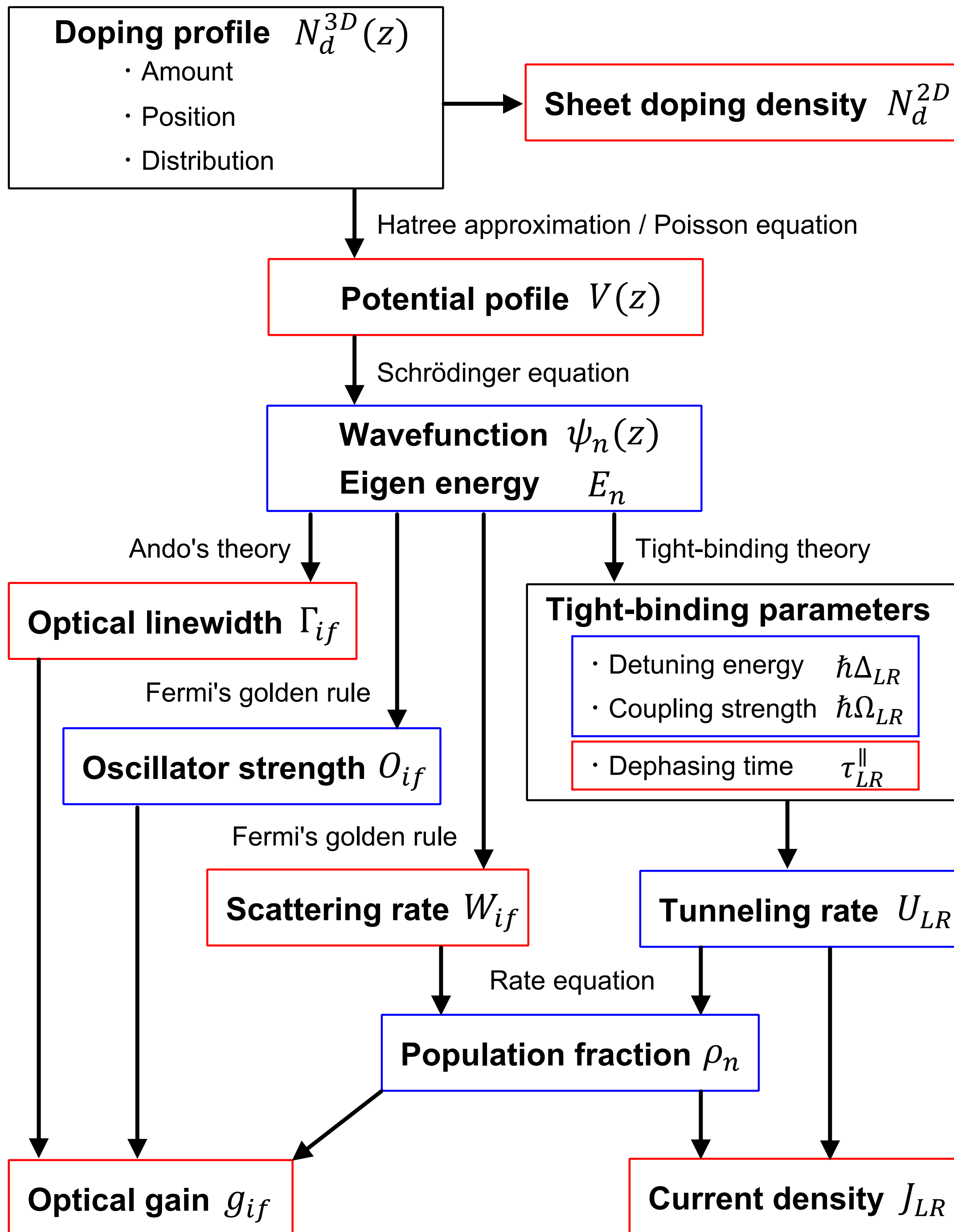

Figure. 3.1 The influence of impurity doping on device parameters in theory. The parameters directly influenced by doping are described by red boxes. Indirect influence is described by blue boxes. Some parameters are affected both directly and indirectly. In calculation, three-dimensional doping profiles are determined based on sheet doping density.

Ionized impurity affects carrier scattering and radiation spectrum, and scattering rate and optical linewidth are calculated as described in Chapter 2. Although the rate due to ionized impurities has been often investigated, the theoretical study of optical linewidth is scarce and the behavior of it is a little difficult for us to imagine from the theoretical form. To obtain a crude sense of the relation between optical linewidth and other parameters such as wavefunction and doping, a series of example calculations is implemented based on a GaAs/$Al_xGa_{1-x}As$-based double-quantum-well (70/**20**/140 in Å. **Bold** is the barrier. x denotes the Al-composition), and the results are summarized in Figure 3.2 where $|i\rangle$ and $|f\rangle$ denote the ground states in each well. Calculations are implemented with a sheet doping density $3.0\times10^{10}cm^{-2}$ and population fractions $(\rho_i,\ \rho_f)$ = (0.9, 0.1) under no electrical field and 200K of the heat-sink temperature conditions. Unlike the full rate equation model, some physical phenomena such as the Hartree potential and electron temperature model are ignored. In calculation, the wavefunctions of the initial and final states are fixed, and the 20Å-rectangular doping region is shifted among four different positions as described in Figure 3.2(a).

In the results, the scattering rate and optical linewidth take the highest values in Position C. In this condition, the wavefunction of the initial state peaks in the left well, and it has a marked overlap with the doping area. The scattering rate decreases as the doping position is further from the left well. The difference due to doping position becomes remarkable when barrier height lowers, and this would be attributed to wavefunction spreading. In Position B, the optical linewidth is one order smaller than the ones of other conditions. This is because the optical linewidth is mainly determined by an overlap of the

doping area and the probability density difference of the two wavefunctions as described in Equation (2.36). In radiative transition, optical gain can increase by small non-radiative scattering rate and optical linewidth. So, Position B is concluded to be the most advantageous doping position for the DQW structure.

Furthermore, the same tendency is observed even when population fractions and barrier height (Al-composition) are changed as in $(\rho_i,\ \rho_f)$ = (0.5, 0.5) and (0.2, 0.8), and the Al-composition changes from 15% to 30%.

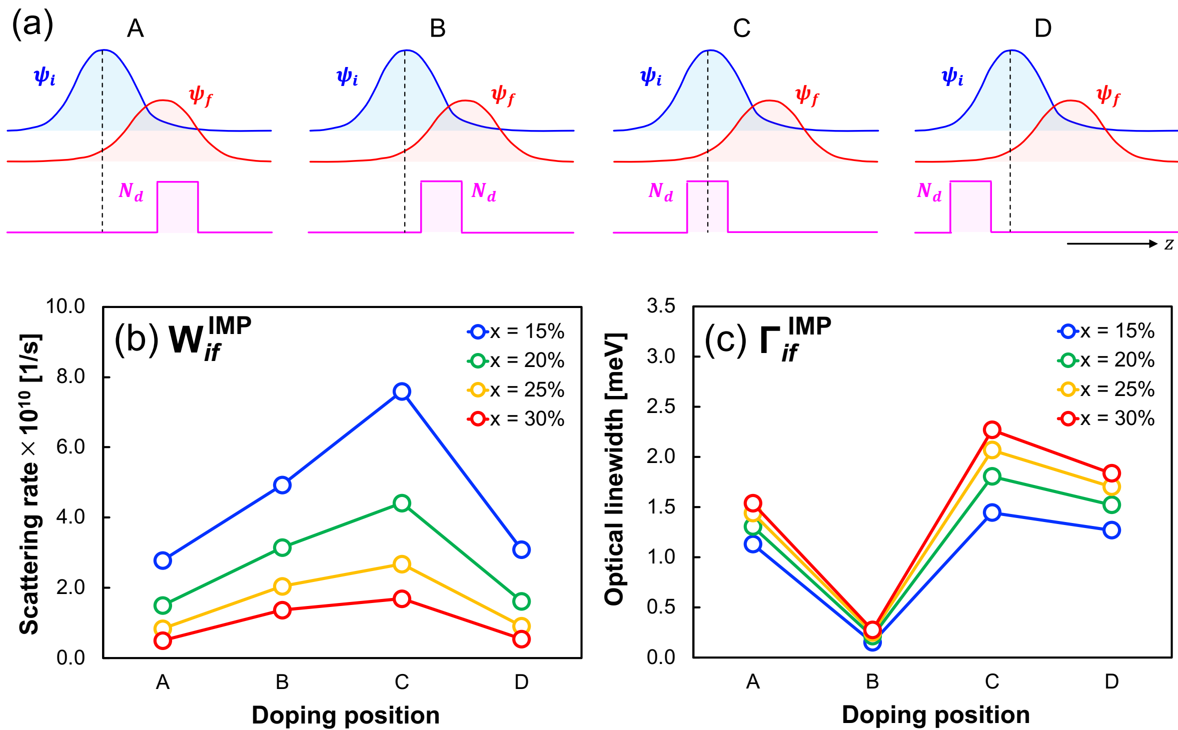

Figure. 3.2 The influence of doping position on the ionized-impurity scattering rate and optical linewidth in a double-quantum-well. (a) Different doping positions. (b) The ionized-impurity scattering rate. (c) Optical linewidth due to ionized-impurity scattering. In all doping positions, 20Å-rectangular doping is assumed.

3.2.2 Examined Doing Patterns

Doping conditions examined in this study are divided into eight patterns depending on positions and distributions (bottom figures in Figure 3.3). To investigate the influence of doping positions, narrow-rectangular doping patterns in phonon-wells (A), radiation-barriers (B), injection-wells (C), and injection-barriers (D) are simulated. Following that, δ-doping in phonon-wells (E), homogeneous doping in phonon-wells (F), and all-layer doping (G) are examined to observe the influence of doping distributions. Furthermore, the undoped condition (H), where electrons are assumed to be injected from external modules, is also investigated. In the undoped condition, sheet doping density and (injected) sheet carrier density are separately defined without using the equations introduced in Chapter 2, and sheet carrier density is used as a variable. In any doping conditions, n-type natural doping is assumed to be 1.0×10^{14}cm^{-3} over all regions. For comparison, optical gain is used as a figure-of-merit, and sheet doping density N_d^{2D} varys from 1.0×10^{10}cm^{-2} to 1.0×10^{12}cm^{-2}. All calculations are implemented under the heat-sink temperature T_{HS} = 200K.

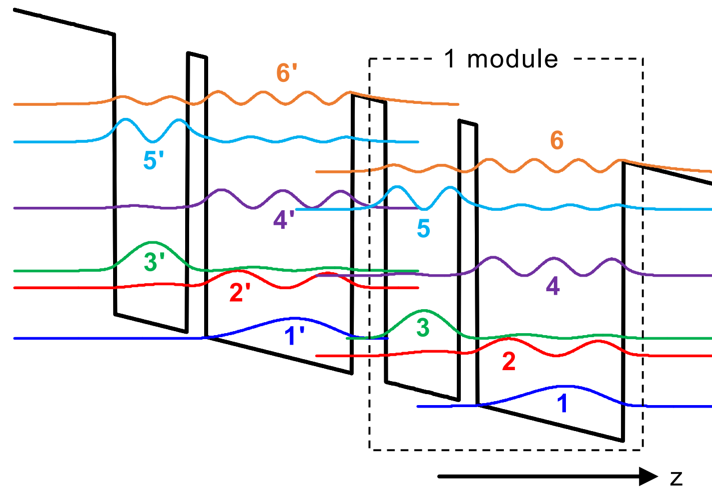

Rectangular doping

A. Phonon-well

B. Radiation-barrier

C. Collection-well

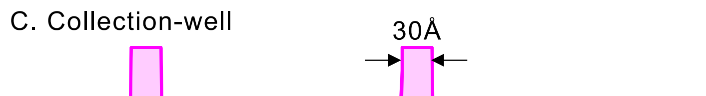

D. Injection-barrier

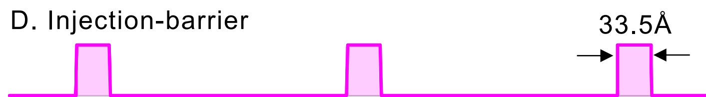

Others

E. Phonon-well (δ-doping)

F. Phonon-well (homogeneous)

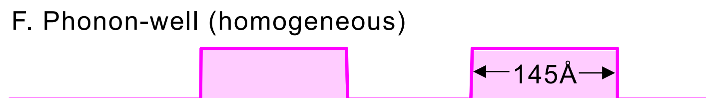

G. All-layer

H. Undoped (Only back-ground doping)

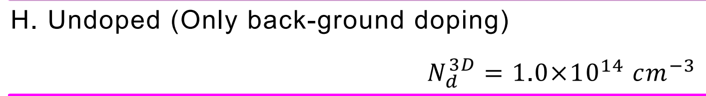

Figure. 3.3 A two-well resonant-phonon structure in the tight-binding condition and eight examined doping patterns. The layer thicknesses of the simulated structure are fixed as **33.5**/72.0/**18.5**/145.0 in Å (**Bold** = barrier). Segregation is considered only in Pattern E.

3.3 Simulation

3.3.1 Simulation Results

Simulation results for fundamental device parameters are described in Figure 3.4 ~ 3.6. First, as shown in Figure 3.4, calculated optical gain increases with doping density, and the discrepancy amongst all doping patterns is small in the low doping conditions. In the high doping conditions, however, maxima of optical gain appear within a doping range 3.0×10^{10} ~ $4.5\times10^{11}cm^{-2}$ in any doping patterns. In addition, doping position and distribution greatly influence not only optical gain maxima but also the doping window (a range of sheet doping densities with which gain peaks appear). In a comparison of doping patterns, the undoped condition (H) demonstrates the highest optical gain $222.7cm^{-2}$ at $4.5\times10^{11}cm^{-2}$. Amongst the other conditions, homogeneous doping in phonon-wells (F) shows the second-highest value 76.2 cm^{-1} at $3.0\times10^{11}cm^{-2}$. The influence of doping positions on gain is so significant that doping in layers except for phonon-wells (B, C, D, and G) deteriorates both gain maxima and the doping window. As for the influence of doping distributions, the optical gain of δ-doping device (E) is similar to that of the conventional narrow-rectangular doping device (A), but homogeneous doping (F) is effective for high optical gain and a wide doping window.

Next, current density and lasing frequency at gain peaks are described in Figure 3.5 and 3.6, respectively. With sheet doping density increasing, current density rises linearly, and the discrepancy is negligible amongst doping conditions until around $7.0\times10^{10}cm^{-2}$. However, in high doping conditions, a discrepancy becomes larger, and the difference reaches several

kA/cm^2. Despite a previous demonstration [292], the possibility of frequency tuning by doping position is shown in this calculation, too. When phonon-wells are doped (A, E, and F), lasing frequency blue-shifts with doping density. On the other hand, in other conditions, lasing frequency stays almost consistent (G) or red-shifts (B, C, D, and H).

In Subsection 3.3.2 and 3.3.3, doping position and doping distribution dependences are thoroughly investigated. In theory, optical gain peak is proportional to the sheet carrier density N_s, oscillator strength O_{if}, and population inversion $\Delta\rho_{if}$, and is inversely proportional to optical linewidth Γ_{if}. To identify the major causal phenomena for the calculation results in Figure 3.4 ~ 3.6, the influence of doping conditions on these parameters is investigated. Furthermore, we also analyze three carrier transition rates determinative for the population inversion: tunneling injection to the upper-lasing state, the non-radiative transition between the lasing states, and carrier extraction from the lower-lasing state.

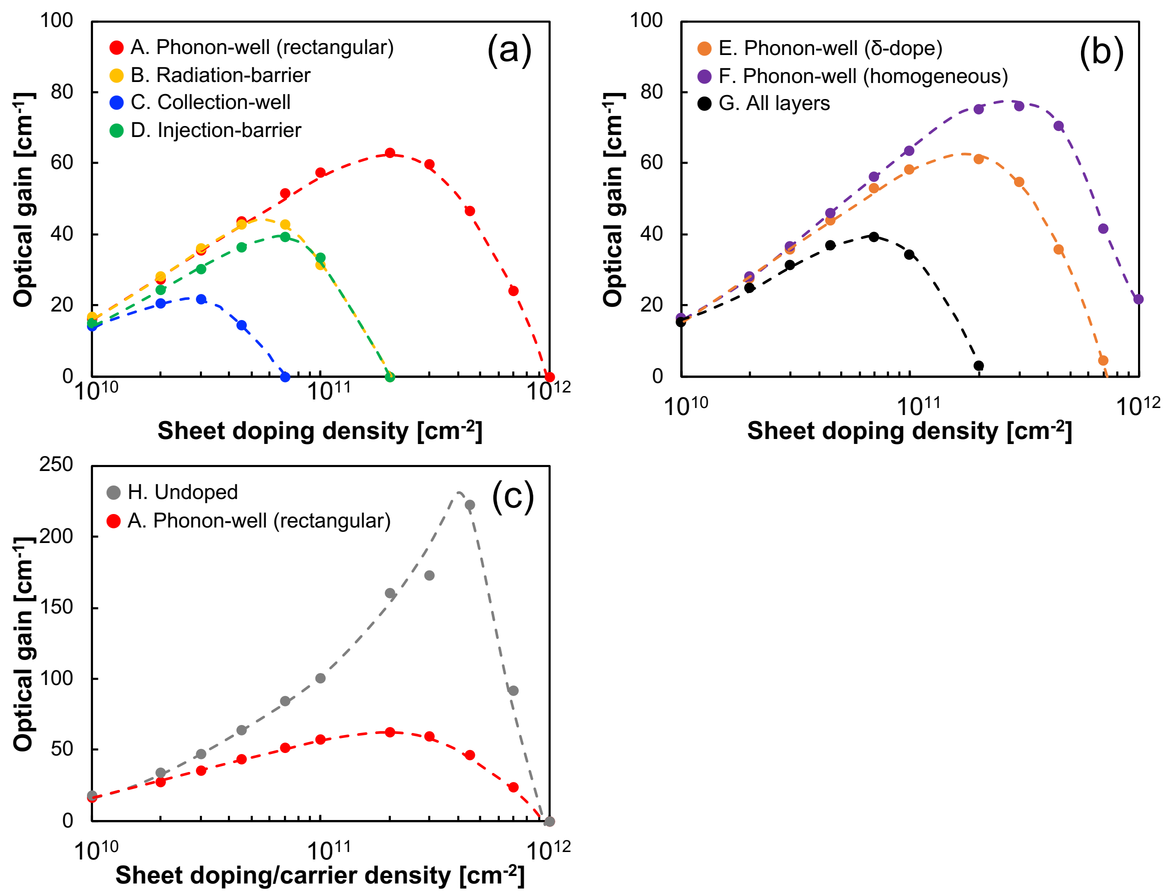

Figure. 3.4 The dependence of optical gain peak on sheet doping/carrier density. (a) Narrow-rectangular doping patterns (A~D), (b) Other doping patterns (E~G), (c) Undoped pattern (H). The thick dots are optical gain peaks abstracted from the gain-filed characteristics for each sheet doping/carrier density, and wiggly lines are trend curves. In (c), the calculation result of pattern A is inserted as a reference with sheet doping density, and sheet carrier density, assumed to be injected from external modules, is swept as a variable for pattern H instead of constant sheet doping density (2.69×10^{8} cm^{-2}).

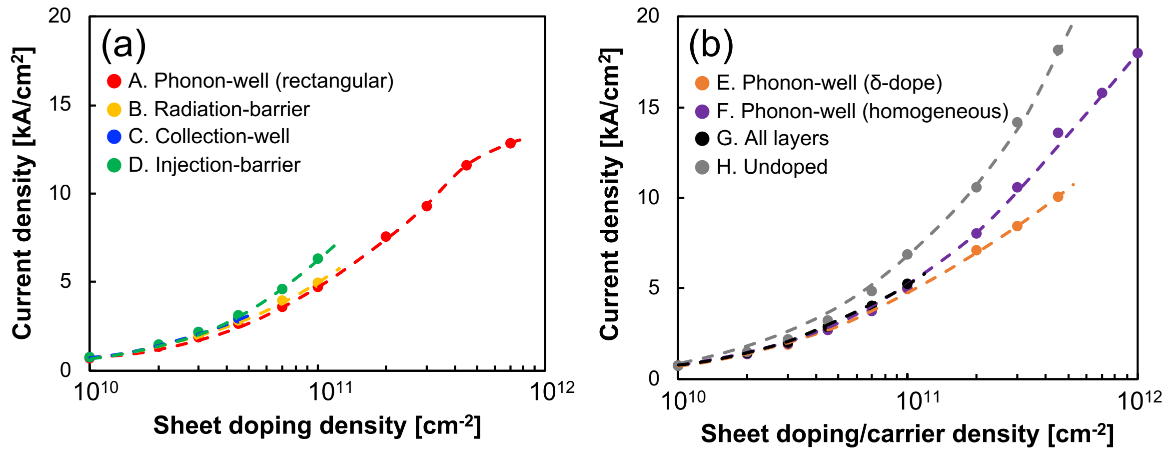

Figure. 3.5 The dependence of electrical current density on sheet doping/carrier density. (a) Narrow-rectangular doping patterns (A~D), (b) Other doping patterns (E~H). The plotted data are abstracted at the gain peak conditions. In (b), x-axis describes carrier density for pattern H and sheet doping density for others.

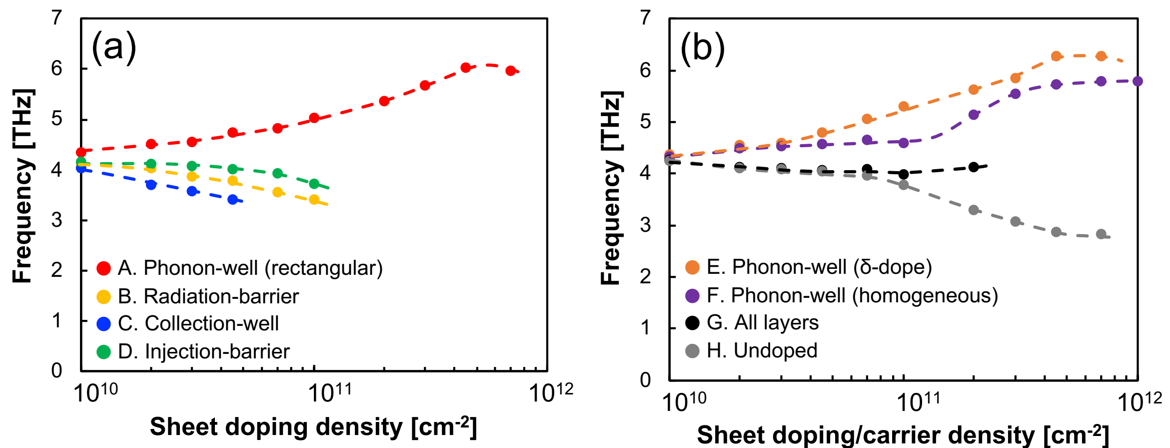

Figure. 3.6 The dependence of lasing frequency on sheet doping/carrier density. (a) Narrow-rectangular doping patterns (A~D), (b) Other doping patterns (E~H). The plotted data are abstracted at the gain peak conditions. In (b), x-axis describes carrier density for pattern H and sheet doping density for others.

3.3.2 Doping Position Dependence

The influence of doping positions on optical gain is studied by using narrow-rectangular doping distributions (A~D). As described in Figure 3.4(a), optical gain peaks and doping windows are clearly dependent on doping positions. Among these four patterns, when phonon-wells are doped (A), optical gain takes the highest maximum 63.1cm^{-1}, and gain peaks are observed up to around 1.0×10^{12}cm^{-2}. However, when doping positions get closer to collection-wells, device performance is exacerbated remarkably. Optical gain of radiation-barrier doping (B) takes almost the same values as the ones for phonon-well doping (A) in low doping conditions. These calculation results, to some extent, support an experimental result implemented by Wang *et al.* [301] despite small structural differences between two-well and three-well devices. However, the highest gain peak of this doping pattern is 43.0cm^{-1} at 4.5×10^{10}cm^{-2}, and its doping window shrinks to 2.0×10^{11}cm^{-2}. As for other conditions (C and D), the device performance is inferior to these patterns.

To analyze this result, componential parameters of optical gain; oscillator strength O_{32}, population inversion $\Delta\rho_{32}$, and optical linewidth Γ_{32} are carefully investigated in Figure 3.7. All plotted data are abstracted at the fields when optical gain peaks (25~28kV/cm). As seen in Figure 3.7(a), oscillator strength increases when doping positions are proximate to collection-wells, and this behavior is effective to improve optical gain. However, the decrease of population inversion described in Figure 3.7(b) surpasses the increase of oscillator strength and determines the behavior of optical gain. Therefore, the simulation results described in Figure 3.4(a) are mainly attributed to the degradation of population inversion. In all doping conditions, population inversion for phonon-well doping takes the

largest values and gradually decreases from 15% at 1.0×10^{10}cm^{-2} to below 5% at 7.0×10^{11}cm^{-2} with an increase of doping density. In other doping conditions, on the other hand, population inversion more rapidly decreases. For oscillator strength, the difference due to doping positions is thought to originate from band-bending. Even though band-bending is not so significant in lower doping conditions, wavefunction and eigen energies are very sensitive to potential profile deformation, and their change is reflected in oscillator strength. Optical linewidth increases with doping density except for radiation-barrier doping even though the change is not very impactful on optical gain.

As for the behavior of population inversion, further detailed analysis is implemented. In Figure 3.7 (d)~(f), the calculated tunneling injection rate $U_{1'3}$, non-radiative scattering rate between lasing subbands W_{32}, and carrier extraction rate W_{21} are described where non-radiative scattering rates are the most susceptive to doping positions and determinative to population inversion. The non-radiative scattering rate of phonon-well doping (A) is around almost 1.0×10^{12} 1/s over a whole doping density. However, when the doping position is closer to collection-wells, the non-radiative scattering drastically increases due to excessive ionized-impurity scattering. Moreover, a decrease of the carrier injection rate with doping density also determines the decrease of population inversion. This reduction in injection rate is considered attributable to subband detuning by band-bending effect. Carrier extraction rates are almost immune to these doping condition

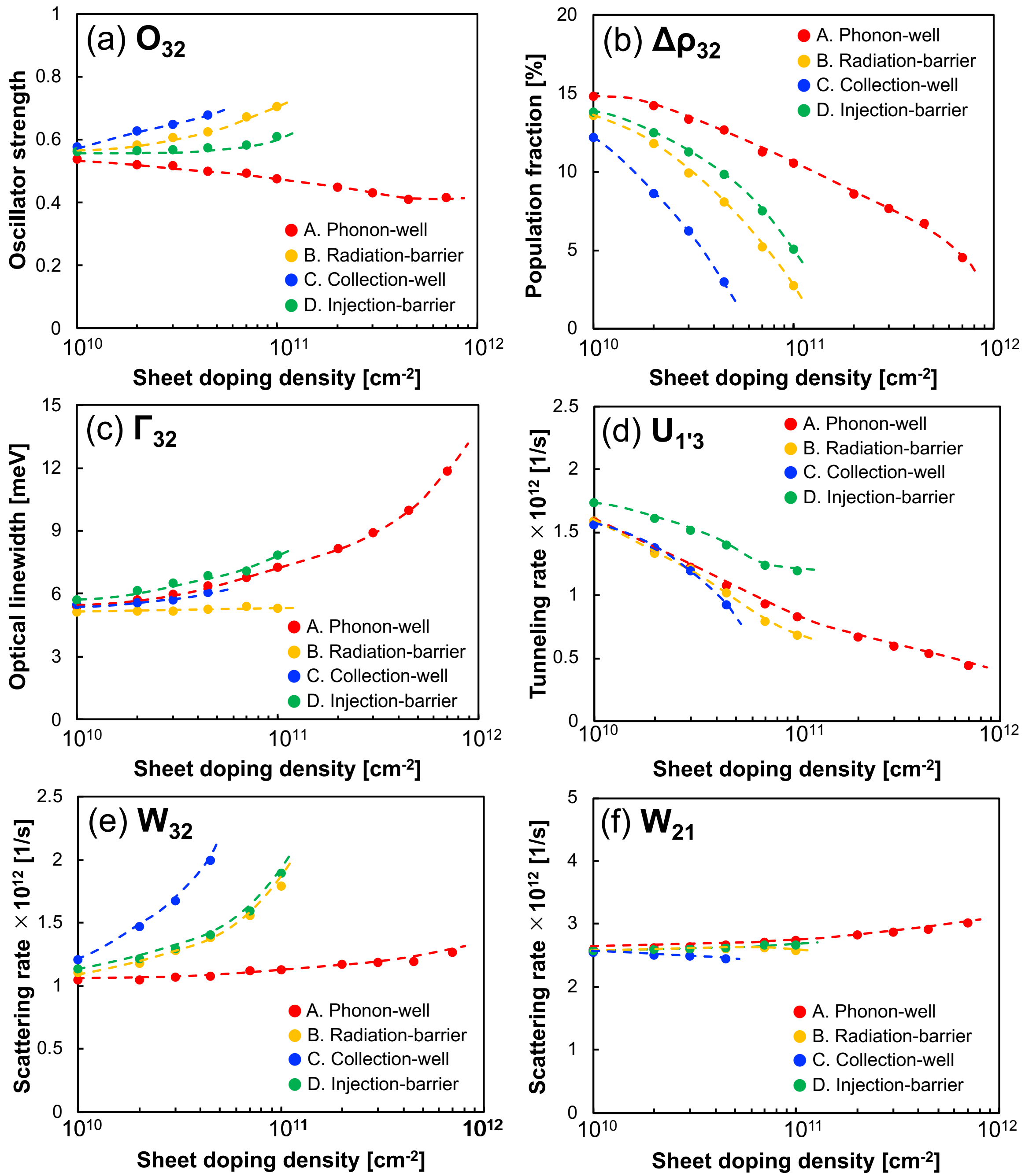

Figure. 3.7 The dependence of componential parameters and carrier transition rates on sheet doping density (A~D). (a) Oscillator strength. (b) Population inversion. (c) Optical linewidth. (d) Tunneling injection rate. (e) Non-radiative scattering rate. (f) Carrier extraction rate. The plotted data are abstracted at the gain peak conditions.

3.3.3 Doping Distribution Dependence

The influence of doping distributions is investigated by comparing the calculation results of the δ-doping (E), homogeneous-doping (F), and all layer doping (G) with those of conventional narrow-rectangular doping (A) as a reference. The reason for the highest optical gain under the undoped condition (H) is also analyzed in this section.

First, the δ-doping (E), and homogeneous-doping (F) in phonon-wells are compared with the rectangular-doping (A). As observed in Figure 3.4 ~ 3.6, doping distributions also influence electrical and optical characteristics greatly. In Figure 3.4(b), the optical gain of homogeneous-doping takes the second-highest value $76.2cm^{-1}$ at $3.0\times10^{11}cm^{-2}$, and the one of δ-doping takes almost similar values to the rectangular-doping. The doping window is observed to become wider when the doping region is wider. Furthermore, under the high doping conditions, a clear difference is seen in current density (Figure 3.5(b)) and lasing frequency (Figure 3.6(b)), as well.

To investigate such behavior in optical gain, the componential parameters are analyzed. In Figure 3.8, the difference in these componential parameters amongst the three doping distributions (A, E and F) is not so significant but is surely reflected in the calculation results in Figure 3.4(b). When a doping region is wider, higher oscillator strength and narrower optical linewidth are obtained. Thus, optical gain is also larger in the homogeneous-doping than that in the δ-doping. In the population inversion in Figure 3.8(b), a cross-over is seen between the δ-doping and homogeneous-doping at around $2.5\times10^{11}cm^{-2}$. This result is explained by the carrier transition rates shown in Figure 3.8 (d) ~ (f). In the low doping conditions, non-radiative scattering rate of homogeneous-doping is higher, and the other two

transition rates do not have so large difference, resulting in a higher population fraction of ULS and population-inversion in δ-doping. In the high doping conditions, the carrier injection rate and extraction rate of the homogeneous-doping are also higher than the ones of δ-doping, so the ULS population fractions increases, and the one of LLS decreases, resulting in a higher population-inversion with homogeneous-doping where the non-radiative transition rate and carrier extraction rate are enhanced by higher ionized impurity scattering due to wider doping.

To analyze these results based on the behavior of wavefunctions, the band-bending effect induced by localized space charges (electrons and dopants) is observed. In Figure 3.9, calculated potential profiles of doping patterns A, F, and H with $2.0\times10^{11}cm^{-2}$ at 25kV/cm are described. The top and bottom figures describe the conduction band edges and the Hartree potentials, respectively where different potential shapes are seen depending on the doping distributions. In rectangular-doping (A), a concave potential appears in the center of a phonon-well. In homogeneous-doping (F), an almost flat/ideal potential is obtained. In undoped condition (H), where the potential is determined only by electrons, a large difference between the calculated potential and the flat one is seen. In two-well resonant-phonon devices, substantial numbers of electrons accumulate in phonon-wells, resulting in a convex potential as seen in Figure 3.9(c). On the other hand, ionized impurities cause a concave potential. Therefore, doping in phonon-wells cancels out the convex potential created by electrons, and the potential distortion in a whole structure is mitigated.

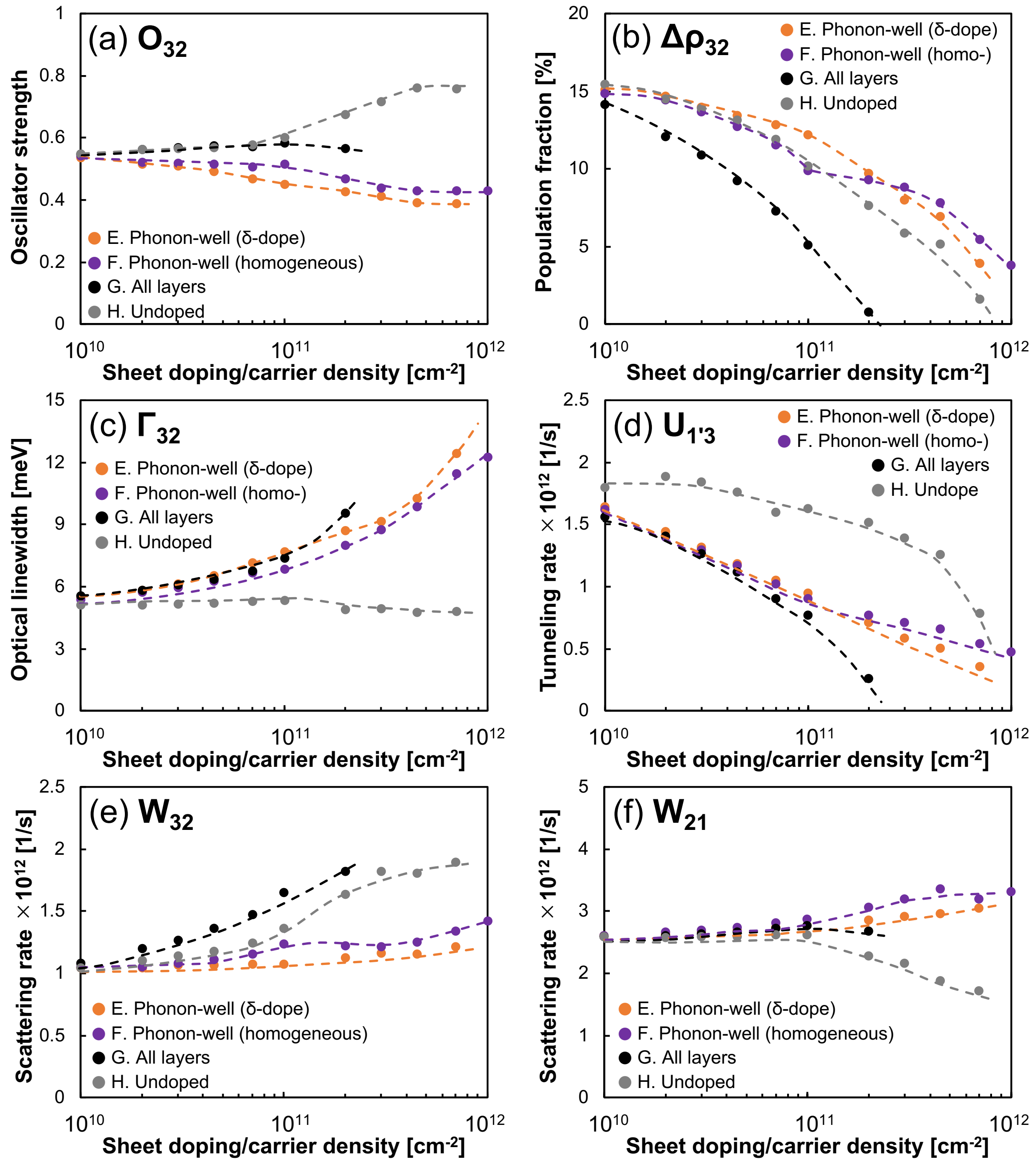

Figure. 3.8 The dependence of componential parameters and carrier transition rates on sheet doping/carrier density (E~H). (a) Oscillator strength. (b) Population inversion. (c) Optical linewidth. (d) Tunneling injection rate. (e) Non-radiative scattering rate. (f) Carrier extraction rate. The plotted data are abstracted at the gain peak conditions. The x-axis describes sheet carrier density for the condition (H).

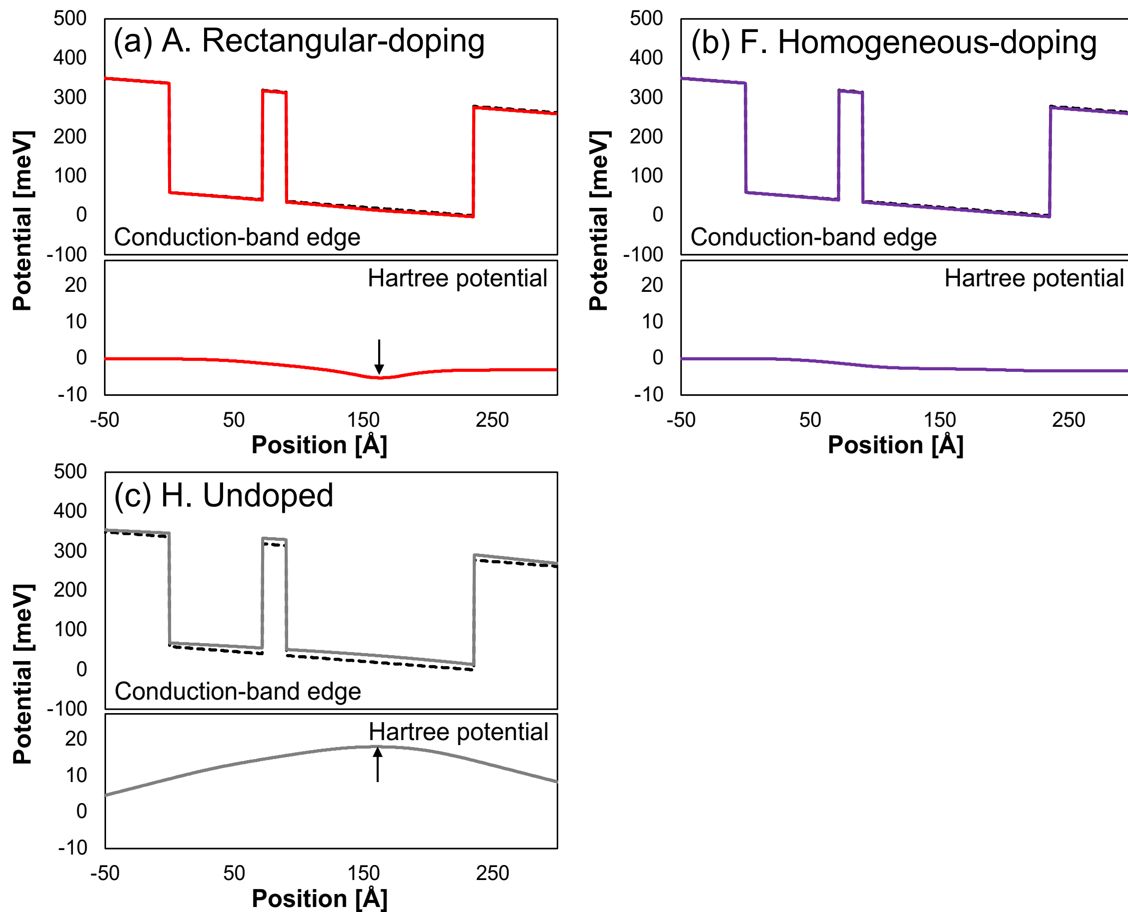

Figure. 3.9 Potential profile including band-bending effect with $2.0\times10^{11}cm^{-2}$ at 25kV/cm. (a) Rectangular-doping. (b) Homogeneous-doping. (c) Undoped condition. Black dotted lines describe a flat potential (no band-bending), and colored solid lines describe the total potential.

With impurity doping, band-bending varys depending on doping distributions. As described in Figure 3.1, the wavefunction and eigen energy calculated by the Schrödinger equation also shift, along with the complicated potential deformation, and ultimately modify electrical and optical characteristics as described in Figure 3.4~3.6 via componential parameters. Because unique doping distributions generate corresponding Hartree potentials, the wavefunction and eigen energies also vary. Under the homogeneous-doping condition, the error between the ideal potential and modified potential is the smallest. Thus, detuning of

the quantum states is minimized, and high injection and extraction rates are maintained, resulting in high optical gain even at high doping conditions. Practically, the band-bending effect becomes remarkable under high doping conditions, and designed alignment fields in simulation and actual ones confirmed in experiment are thought to make a large difference. Therefore, homogeneous-doping is expected to solve this problem.

Second, all layer doping (G) is not suitable for enhancing optical gain and the highest operation temperatures. Even though it is advantageous that lasing frequency is immune to doping amount, optical gain is also smaller than that of the reference conditions (A) due to population inversion degradation for the same reason as the doping patterns B~D.

Finally, the undoped condition (H) recorded the highest optical gain, as described in Figure 3.4(c), because a rather high oscillator strength and low optical linewidth are obtained even under the high doping condition (Figure 3.8). On the one hand, it is reasonable that the small optical linewidth is attributed to the absence of ionized-impurity scattering. On the other hand, the increase of oscillator strength is originally attributed to band-bending. With band-bending, a wavefunction overlap of ULS and LLS becomes greater, resulting in higher oscillator strength. The change of the non-radiative scattering rate and oscillator strength for doping pattern B~D is also explained by the same idea. The population inversion for the undoped condition is lower than that for the other three conditions (A, E, and F) because high tunneling injection works to increase ULS's population but the increased non-radiative scattering rate reduces ULS's population, and the lower carrier extraction rate increases LLS's population. Therefore, population inversion of the undoped condition is degraded.

3.4 Discussion

From the simulation results in Section 3.3, the undoped condition is the most preferable setup for high optical gain and high operation temperature in two-well resonant-phonon THz QCLs if only one module is doped. This setup is reasonable when we see that doping regions are separated from lasing regions in MIR QCLs. In reality, however, it is infeasible to drive THz QCLs completely without doping [298]. Therefore, homogeneous-doping in phonon-wells is concluded to be the best method when all modules in an active core are doped. Furthermore, because dopants can migrate and intrude into other layers due to heat during epitaxial growth, it is preferable to avoid doping in the vicinities of interfaces between wells and barriers (Figure 3.10).

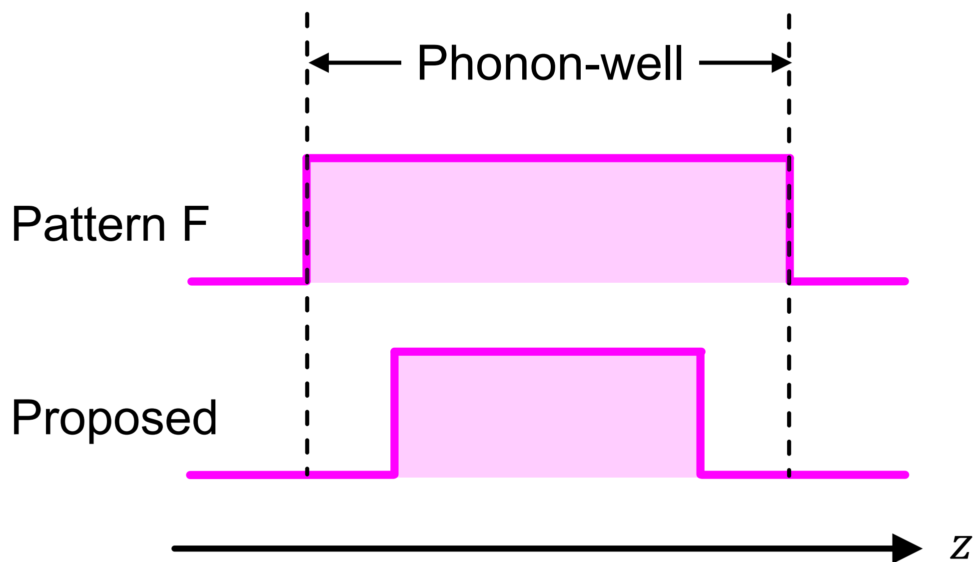

Figure. 3.10 A proposed doping pattern for a single module.

The knowledge obtained in the simulation is beneficial for expanding doping tactics. Conventionally, an active core of THz QCLs is composed of several hundred modules, and all modules are doped. Therefore, when an active core includes a great number of modules, the total impurity per active core increases simultaneously, resulting in high free-carrier absorption and threshold gain. Having said that, in principle, carriers of QCLs are recycled after radiation, so the authors think that not all modules need doping. A modulation doping scheme, with an active core that includes both doped and undoped modules, should be effective for simultaneously achieving high optical gain and low threshold gain (Figure 3.11).

In the recent design trend of THz-QCLs, devices composed of two wells have often been studied as a way to improve quantum efficiency by using fewer subbands. On the one hand, decreasing the number of quantum wells per module shortens the length of one module and is effective for high optical gain. On the other hand, it does not change that using an approximately 10-μm thick waveguide is preferable for low waveguide loss. Therefore, down-sizing of devices is expected to increase the net doping density in waveguides if all modules are equally doped.

For example, a long device, designed by Williams *et al.* with a 539Å of four-well resonant-phonon structure, has 186 modules per 10μm active core [106]. On the other hand, a short device, designed by Khalatpour *et al.* with a 269.3Å of two-well resonant-phonon structure, has 371 modules in the same size of active core as the long device [224]. Therefore, if all modules are doped in the two devices with the same condition such as around 4.5×10^{10}cm^{-2} of sheet doping density over 30Å-wide near the center of phonon-wells, the net doping density in the short device is almost double that of the long device. Therefore, the

highest operation temperature of the short device is thought to be suppressed by high threshold gain due to high free carrier loss instead of high optical gain. One of the solutions for this issue is a modulation doping scheme, and if every two modules are doped, the net doping density can remain constant as described in Figure 3.11. Furthermore, undoped modules are realized in the active core, so a higher optical gain and improved temperature characteristics are also expected. Although instability of the system due to the space charge effect by injection is also apprehensive [307,308], this issue would not be so serious unless the doping period is very long because Straub *et al.* already demonstrated an operational MIR QCL device by adopting a modulation doping scheme with longer than 100nm of doping period in the past [290]. Having said that, they did not discuss the influence of modulation doping on the temperature characteristics of QCLs. In THz QCLs, therefore, the validity of modulation doping schemes need to be confirmed experimentally.

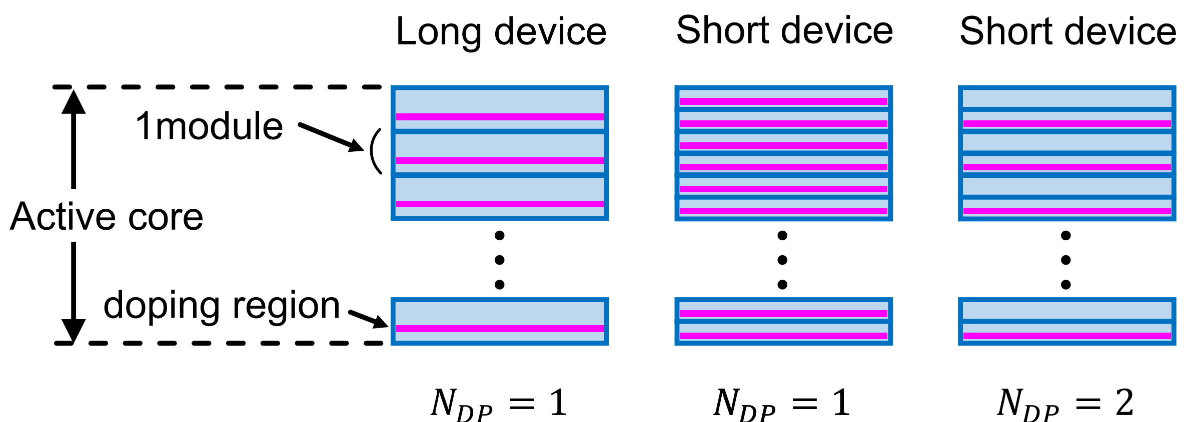

Figure. 3.11 The modulated doping scheme. The magnitude of doping period toward the structural period is described by N_{DP}. For example, when all modules are doped, N_{DP} = 1. When impurities are doped every two modules, it is described as N_{DP} = 2.

Finally, the duration of carrier recycling is also one of our great interests. The device designed by Straub *et al.* was already demonstrated to operate even if the doping period is longer than 100nm [290]. On the other hand, devices completely without doping have also been observed not to lase [298]. Thus, we predict that carrier recycling will have a limitation toward doping period, distance, or space charge effect, and the optimal modulation doping period needs to be adjusted by experiment.

3.5 Summary and Conclusion

Through theoretical investigation, doping profiles (amount, position, and distribution) have been found to greatly influence the performance of a two-well resonant-phonon THz QCL. In a comparison with a doped single module, it is concluded that wide-doping in phonon-wells is the best method due to high population inversion and immunity to band-bending. On the other hand, an undoped condition showed the highest gain among all doping patterns, and modulation doping method is suggested to exploit the undoped conditions. Even though the detuning of aligned subbands greatly increases under high doping conditions, combining the doping scheme and structural adjustment [303] is expected to further improve device performance.

Wherever there is a will, there is a way.

– Abraham Lincoln

Chapter 4 Barrier Height Study - Part I

4.1 Introduction

The influence of barrier height on device performance has also been investigated by many researchers like doping study [174,179,311-316]. In the research for improving highest operation temperature, the devices renewed the record temperature were fabricated with 15% ~ 30% of Al-composition, and it has been unclear whether or not the optimal barrier height exists [106,224,282,283]. For example, two works, one by Kainz *et al*. and the other by Khalatpour *et al*., are introduced here. In 2018, Kainz *et al.* modified the barrier height of a three-well resonant-phonon device by changing the Al-composition from 12% to 24% with fixed-layer thicknesses in order to investigate this issue theoretically and experimentally [282,316]. They concluded that 20% Al-composition is the optimal condition for the highest performance due to a trade-off between carrier leakage with a low barrier and oscillator strength lowering with a high barrier. In 2021, however, Khalatpour *et al.* reported a higher-performance device using a rather high Al-composition of 30% [224]. From these two attempts, the question of whether lower or higher barriers work better has yet to be settled, necessitating further investigation.

It is a little cumbersome to discuss the optimal barrier height. Wavefunction and subband energy are influenced by barrier height, and other device parameters calculated based on these components also change, resulting in different alignment conditions. Thus,

device structures need to be optimized. However, the design freedom is very large in QCLs composed of several layers, so determining the optimal barrier height requires comparison of many applicant devices. On the one hand, such investigation is not realistic by experiment due to very long time and effort. On the other hand, simulation also bears issues in the calculation accuracy and time. Delving deeply into this topic requires that one consider the influence of carrier leakage in simulations. In QCL studies, two types of carrier leakage are often discussed. One is leakage from bound states to other bound states, which mainly occurs due to thermally activated LO-phonon scattering [175,179,181] and is calculated by Fermi's golden rule. The other is leakage from bound states to continuum states (B-to-C leakage) [219], but it has seldom been treated in QCL simulations. B-to-C leakage can not only increase electrical current but also undesirably diminish subband carrier density, resulting in the deterioration of the optical gain. Therefore, in theoretical work, it is preferable that B-to-C leakage be dealt with, especially, in low barrier devices.

This study aims to develop a third-order tunneling current theory to demonstrate the influence of carrier leakage on subband carrier density by combining the second-order tunneling current model proposed by Terazzi *et al.* [264] and the leakage current model that is often used in studies for quantum-well infrared photodetectors [266]. In this new model, the total subband carrier density is divided into the components for bound states and for continuum states using a semi-classical tunneling coefficient theory. In the leakage current calculation, theoretically calculated mobility and drift velocity are used. The lattice temperature and electron temperature in the continuum states are also modeled. The developed theoretical models are incorporated in a simulation based on rate equation

introduced in Chapter 2, and three types of two-well resonant-phonon devices, designed and investigated in previous works, are selected to confirm the validity of the simulation. Using one of the examined device structures (G652), the influence of barrier height is also theoretically investigated by changing the Al-composition from 12.5% to 45%.

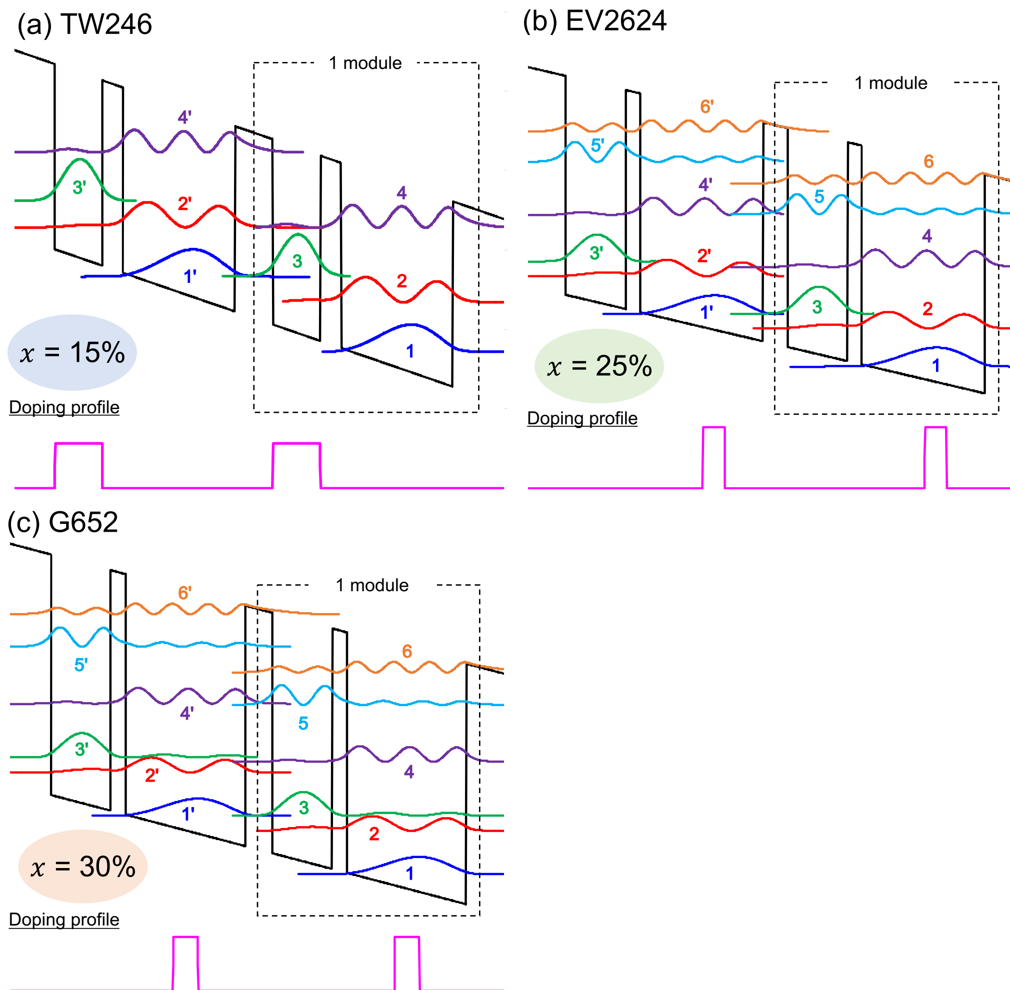

Figure. 4.1 Band diagrams of two-well resonant-phonon THz QCLs in tight-binding condition. (a) Low-barrier device (TW246), (b) Middle-barrier device (EV2624), and (c) High-barrier device (G652).

4.2 Method and Simulation Results

4.2.1 Validation of the Third-Order Tunneling Current Model

Figure 4.1 and Table 4.1 describe three designs for two-well resonant-phonon devices selected to verify the developed simulation method in Chapter 2. In addition to their capability of enhancing the carrier-use efficiency to produce high performance, two-well resonant-phonon structures' simplicity makes them suitable for investigating the impact of several design parameters on device performance. This advantage of this type of devices would be beneficial for research on other device design components.

Even though the number of bound states in these devices varys depending on barrier height, the carrier transport mechanism is the same in all structures. In this scheme, the carrier transition for lasing occurs among the lowest three subbands. At an alignment condition between subband $|1'\rangle$ and $|3\rangle$, carriers are injected from subband $|1'\rangle$ to $|3\rangle$ (the upper lasing state ULS), and carriers in subband $|2\rangle$ (the lower lasing state LLS) are also extracted down to subband $|1\rangle$ by fast LO-phonon scattering, resulting in population inversion and stimulated emission between ULS and LLS. Other upper level subbands ($|4\rangle \sim |6\rangle$) work as parasite states.

Selecting three devices for this work, composed of different Al-compositions between 15% and 30%, enables us to determine the influence of barrier height on device performance. The low-barrier device (TW246) with 15% Al-composition, designed by Kumar *et al.* in an early THz QCL study, lases up to 121K [284]. The middle-barrier device

(EV2624) designed by Bosco *et al.* has a 25% Al-composition and lases up to 210.5K [283]. The high-barrier device (G652) is designed by Khalatpour *et al.* with 30% Al-composition and relatively high impurity doping 4.5×10^{10} cm^{-2} in phonon-wells [224]. Although the waveguide designs and materials vary among these devices, their tendency is seen: when the barrier height is higher, the highest operation temperatures are also higher. The validity of our simulation is confirmed by comparing the theoretical and experimental results of J-V characteristics and the temperature dependence of optical gain. Except in calculations for temperature dependence, a heat-sink temperature $T_{HS}^{(sim)}$ = 200K is used in the simulation.

Device design	Low-barrier device (TW246)	Middle-barrier device (EV2624)	High-barrier device (G652)
Material system	GaAs/$Al_{0.15}Ga_{0.85}As$	GaAs/$Al_{0.25}Ga_{0.75}As$	GaAs/$Al_{0.30}Ga_{0.70}As$
Original structure [Å] (**bold**=barrier, underline=doping)	**56.0**/71.0/**31.0**/167.0	**32.6**/79.9/**19.0**/164.6	**33.7**/72.0/**18.7**/144.9
Simulated structure [Å]	**56.0**/71.0/**31.0**/167.0	**32.5**/80.0/**19.0**/164.5	**33.5**/72.0/**18.5**/145.0
Doping profile	2.17×10^{10} cm^{-2} Uniform in collection-wells	4.5×10^{10} cm^{-2} 29Å in phonon-wells	4.5×10^{10} cm^{-2} 30Å in the center of phonon-wells
Lasing frequency	4.60 THz	3.89 THz	3.94 THz
Alignment field	17.0 kV/cm	16.9 kV/cm	25.0 kV/cm*
Active core thickness	8 μm	12 μm	10 μm
Waveguide	Au-Au	Cu-Cu	Au-Au
Maximum operating temperature	121 K	210.5 K	250 K

Table. 4.1 Device information for examined two-well resonant-phonon THz QCLs. (*Estimated in this work.)

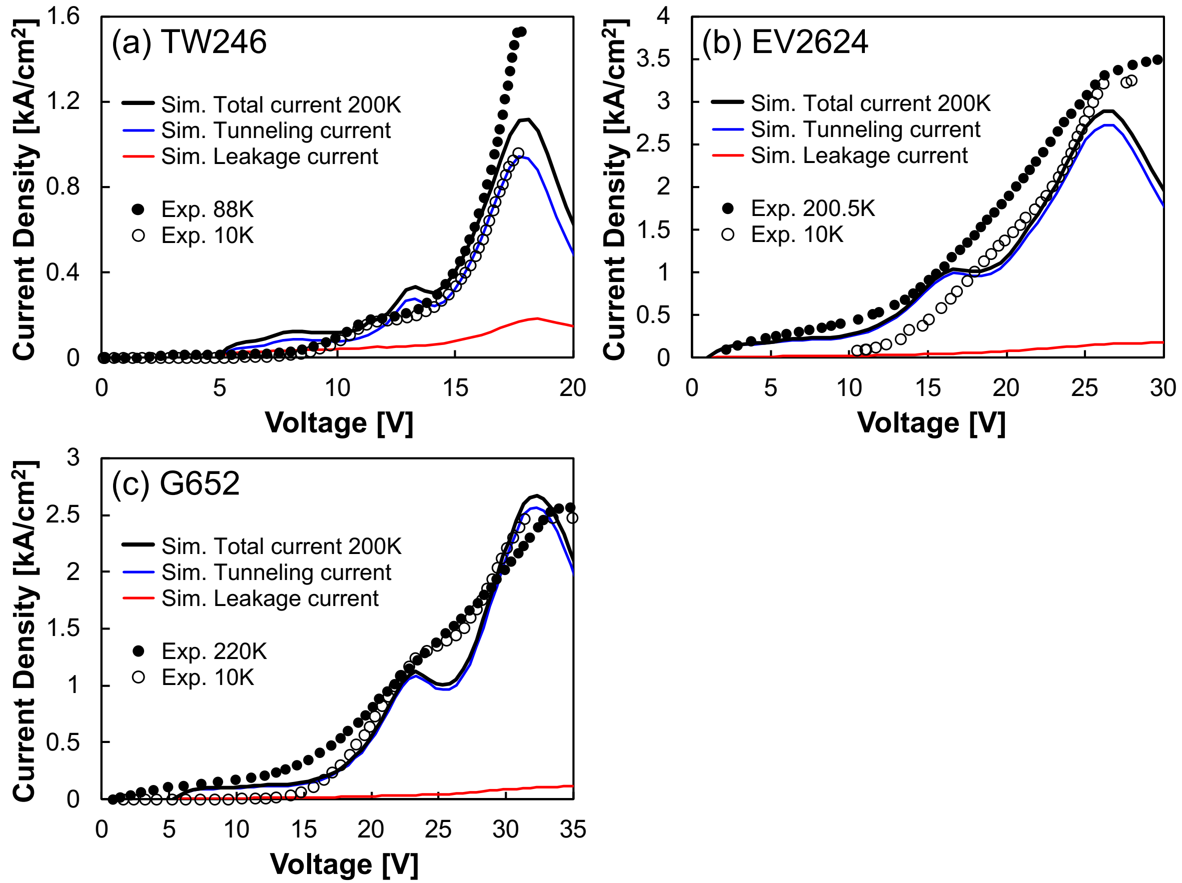

Figure. 4.2 J-V characteristics. (a) Low-barrier device (TW246). (b) Middle-barrier device (EV2624). (c) High-barrier device (G652).

The calculated J-V curves at 200K and experimental data exploited at low and high temperatures for the three devices are described in Figure 4.2. For curve fitting, an offset voltage of 1.0 ~ 5.3V, corresponding to the voltage drop due to Schottky-barrier effect and/or outer circuit resistance, is assumed for the simulation data. Generally, current peaks or plateaus are known to appear twice in the J-V characteristics of two-well resonant-phonon devices because the injection state $|1'\rangle$ aligns with subbands $|2\rangle$ and $|3\rangle$ during voltage

increases. For example, in G652 (Figure 4.2(c)), after a current plateau due to the alignment between subbands $|1'\rangle$ and $|2\rangle$ at around 23V, another alignment happens between $|1'\rangle$ and $|3\rangle$ at around 31V. At the second alignment designed for lasing, the tunneling current between $|1'\rangle$ and $|3\rangle$ becomes dominant due to the high tunneling rate $U_{1'3}$ = 1.07×10^{12} 1/s. On the other hand, the tunneling rate between $|1'\rangle$ and $|2\rangle$ is $U_{1'2}$ = 7.37×10^{9} 1/s, and this path no longer contributes to electrical conduction. This feature and the amount of current density are reproduced well in all devices.

Even though the simulation results match relatively well with the experimental results at low temperatures, discrepancies appear at high temperatures. One remarkable difference is that the experimental current density is higher than the calculated one over some of the voltage regions. For instance, this type of difference is seen beyond 16V in TW246 and EV2624, and before and after the first current plateau in G652. Even with the leakage current model, this phenomenon cannot be reproduced. The simulation does not include stimulated emission, so the discrepancy in the high voltage region would be attributed to lack of optical current. The discrepancy in the middle voltage region is considered to be attributed to subband broadening. Subband broadening is known to happen in actual devices, and the NEGF calculation considers this effect, so current density increases smoothly with rising voltage (Figure 4.3). However, the rate equation model does not consider subband broadening in resonant tunneling. Therefore, such calculated current density is a little smaller than the experimental values.

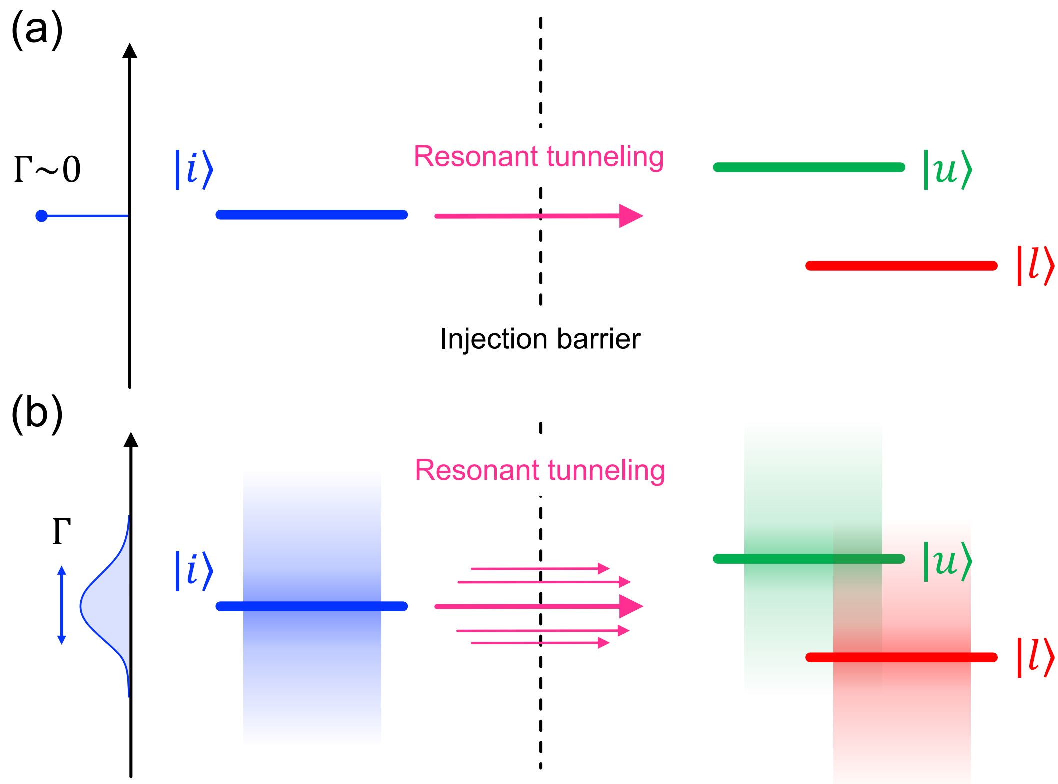

Figure. 4.3 Difference in resonant tunneling transport model between the rate equation and actual devices or the NEGF calculation. (a) a condition in the rate equation, and (b) in actual devices or the NEGF.

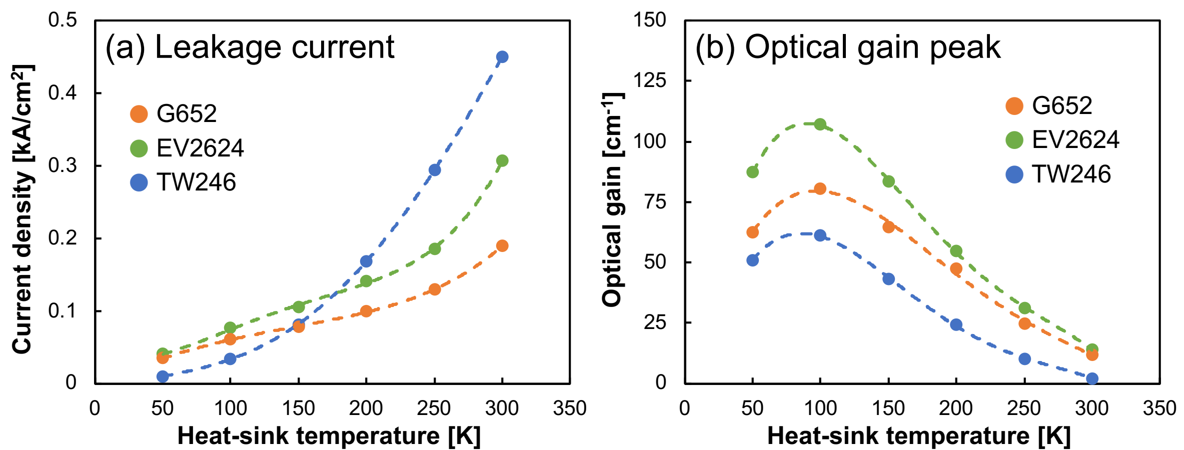

Figure. 4.4 Calculated temperature dependence. (a) Leakage current density. (b) Optical gain peak. The data are taken when optical gain peaks.

In terms of the leakage current calculations in Figure 4.2 and 4.3 (a), barrier height dependence is observed clearly at high temperature conditions. Although the difference in leakage current is not so remarkable below 200K, at 300K, the leakage current density of the low-barrier device reaches 0.45kA/cm^2 instead of below 0.2kA/cm^2 for the high-barrier device. Because the sheet doping density of the low-barrier device is less than half of the others, this result implies that if doping density of all devices is the same, the leakage current of the low-barrier device will greatly surpass that of others. Although the contribution of leakage current to total current density is not very large at 200K, a high barrier would be preferable for circumventing the increase of leakage current at high temperatures.

The results of calculating the temperature dependence of optical gain in Figure 4.4 (b) reflect the highest experimental operation temperatures to some extent. The peak gain of the low-barrier device, on the one hand, reaches 61.0cm^{-1} at 100K. On the other hand, those for the middle- and high-barrier devices reach 107.0cm^{-1} and 80.6cm^{-1}, respectively. As the highest operation temperature of the low-barrier device is 121K, and the ones for others are over 200K, these results are reasonable. Having said that, above 200K, the gain peak of the middle-barrier device is higher than that of the high-barrier device by 2 to 7cm^{-1}, which is contrary to the experimental results in which the highest operation temperatures of the middle- and high-barrier devices are 200.5K and 250K, respectively. This error may be caused by the lack of a stimulated emission model in the simulation or by fabrication-method differences. The decrease of the optical gain in the low temperature region is due to the low dopant activation ratio. The developed simulation would be enough to investigate the major device characteristics.

For the high-barrier device (G652), other calculated parameters whose theoretical models are introduced in this paper are mentioned below. Under a pulsing condition, 400ns at 500Hz [224], the calculated lattice temperature and continuum electron temperature at the alignment field are 201.5K and 211.9K, respectively, when the heat-sink temperature is 200K. There, a thickness of GaAs wafer H_{sub} = 650μm and thermal conductivity κ_{sub} = 55W/mK are used. A calculated pure dephasing time for aligned subbands $\tau^*_{1'3}$ is 0.16ps.

4.2.2 The Influence of Barrier Height on Device Characteristics

Next, the influence of barrier height on device characteristics is investigated by simulation at 200K heat-sink temperature. Based on the high-barrier device (G652), the barrier height is modified from 113.2meV to 363.9meV by changing the Al-composition from 12.5% to 45% with a fixed-layer thickness (Figure 4.5). Due to this modification, the number of subbands per module increases from four to seven, and all subbands are considered in the calculation. In the simulation results described in Figure 4.6 and Table 4.2, calculated data is abstracted when the optical gain reaches a peak.

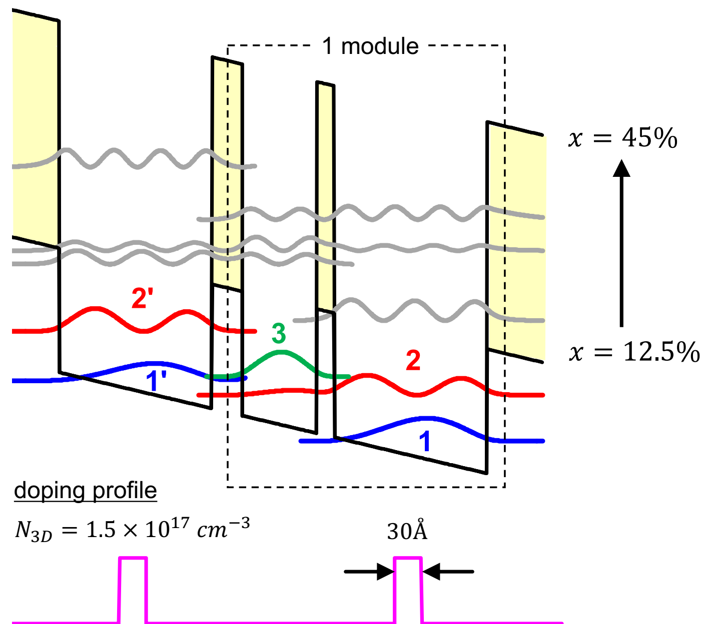

Figure. 4.5 Two-well resonant-phonon structure for barrier height study (A phonon-well + one module). The layer thicknesses are fixed as 33.5/72.0/18.5/145.0 in Å. (Bold = barrier, underline = doping).

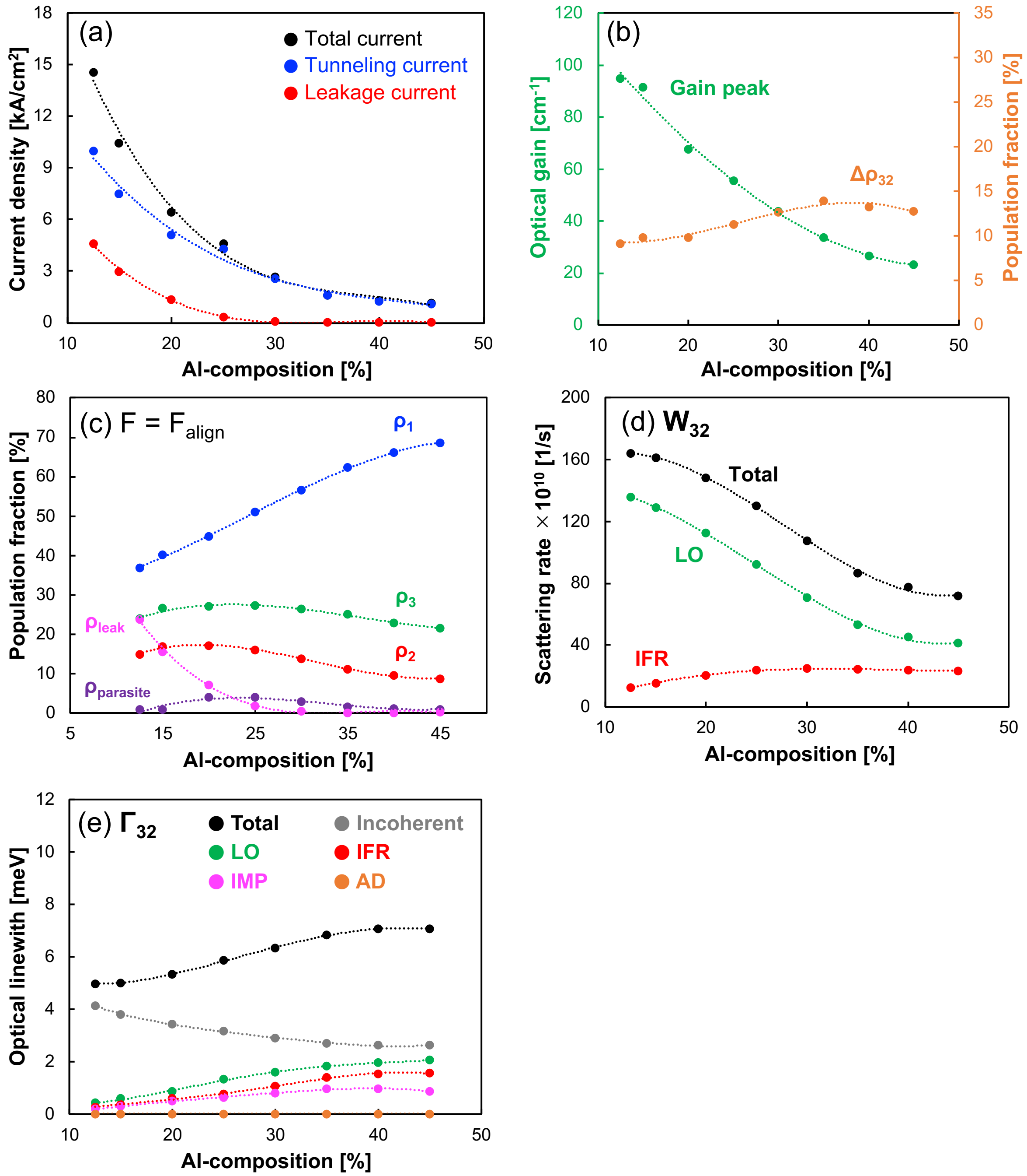

Figure. 4.6 Barrier height (Al-composition) dependence in simulation. (a) Electrical current density, (b) Optical gain peak and population inversion $\Delta\rho_{32}$, (c) Population fraction, (d) Scattering rate between lasing states, (e) Optical linewidth between lasing states. In (c), $\rho_{parasite}$ is the sum of population fractions for all parasite subbands. In (d), Total = LO + IFR + IMP + AD + EE. Dot-lines indicate trend curves.

As seen in Figure 4.6(a), the current density decreases with the Al-composition. The tunneling current dominates all Al-compositions, and the leakage current also rises remarkably below 25% Al-composition, occupying 29% of the total current at 15% Al-composition. This tendency is attributed to the fact that more carriers can escape to continuum states due to lower barriers as depicted in Figure 4.6(c). The reduction of tunneling current in higher barrier conditions originates from weaker coupling strength $\hbar\Omega_{1'3}$ between the injection state $|1'\rangle$ and ULS $|3\rangle$. Because the tunneling rate $U_{1'3}$ is proportional to a square of coupling strength, the tunneling current also concomitantly decreases [139].

The optical gain also decreases with Al-composition, and changes from 95.1cm^{-1} at 12.5% of Al-composition to 23.2cm^{-1} at 45% (Figure 4.6(b)). As shown in the calculation results in Table. 4.2, this result is mainly attributable to oscillator strength lowering. When Al-composition increases, it drops from 0.40 to 0.10. On the other hand, the change in the population inversion and optical linewidth are rather small, and almost cancel out each other in the gain calculation. Despite the maximum population inversion at 35% of Al-composition, this feature is not reflected in the optical gain.

The calculation results for population fraction in Figure 4.6(c) show strong carrier confinement due to high barriers. With a higher barrier, the population fraction of the injection state $|1\rangle$ becomes greater, and it increases from 36.7% to 68.7%. On the other hand, reduction of the population fraction is seen in other higher subbands, and the ones of ULS and LLS change from 23.9% and 14.8% to 21.5% and 8.7%. However, intriguingly, the population inversion does not change so remarkably, remaining at around 12%. In addition,

leakage carriers notably increase below 25% of Al-composition, reaching 23.8% at 12.5% of Al-composition. The total population fraction of parasite states is smaller than 4% even when the number of subbands increases. From these results, the number of carriers contributing to lasing is found to be suppressed by leakage to continuum states and strong confinement in the low and high barrier conditions, respectively.

Al-composition	12.5%	15%	20%	25%	30%	35%	40%	45%
Barrier height [meV]	113.2	136.2	182.7	229.9	277.8	326.5	352.8	363.9
Number of subbands per module	4	4	5	5	6	6	7	7
Field at optical gain peak [kA/cm]	22.5	24.0	25.5	26.0	26.5	27.0	27.0	27.0
Injection transport path $\|1'\rangle \rightarrow \|3\rangle$								
Tunneling rate $U_{1'3}\times10^{11}$ [1/s]	63.8	44.6	25.9	17.0	10.7	6.6	4.7	3.8
Coupling strength $\hbar U_{1'3}$ [meV]	3.38	2.96	2.24	1.70	1.30	1.01	0.86	0.77
Optical transport path $\|3\rangle \rightarrow \|2\rangle$								
Oscillator strength O_{32}	1.21	1.06	0.83	0.65	0.50	0.38	0.32	0.29
Optical linewidth Γ_{32} [meV]	4.98	5.00	5.34	5.85	6.35	6.83	7.06	7.07
Population inversion $\Delta\rho_{32}$ [%]	9.1	9.8	9.8	11.3	12.7	13.9	13.2	12.8
Extraction transport path $\|2\rangle \rightarrow \|1\rangle$								
Scattering rate W_{21} $\times10^{12}$ [1/s]	2.99	2.78	2.59	2.63	2.68	2.76	2.83	2.92

Table. 4.2 Calculated device parameters at optical gain peak (T_{HS} = 200K).

The influence of barrier height on carrier scattering rates and optical linewidths for lasing states (W_{32} and Γ_{32}) are also investigated. Generally, it is problematic that interface-roughness scattering worsens device performances such as population inversion and optical linewidth [184]. In the simulation results in this work, the total scattering rate is improved and the total optical linewidth deteriorates when a high barrier is used as described in Figure 4.6(d) and (e). The former is attributed to reduction of the dominant LO-phonon scattering rate, and the latter deterioration is caused not only by interface-roughness scattering but also other scattering phenomena. Therefore, it is hard to say that interface-roughness scattering predominantly degrades the device performance of the THz QCLs examined in this study even though it is still the second dominant scattering phenomenon.

4.3 Discussion

The calculation results described in the previous section are intuitively understood, but we can deepen our comprehension of them by considering more rudimentary phenomena such as the spreading/compression of the wavefunction and the change of carrier transport rates due to barrier height.

Lowering the non-radiative scattering rates between lasing subbands, shown in Figure 4.6(d), is thought to derive from the compression of wavefunction due to a high barrier. The inter-subband transition rate, calculated by Fermi's golden rule, is dependent on the degree of overlap of the two wavefunctions [59]. Because wavefunction in a high barrier quantum well is less likely to intrude into barriers and tends to be compressed inside wells, the overlap of two wavefunctions separated by a barrier is also likely to be small, resulting in a decreased scattering rate, as seen in LO-phonon scattering in Figure 4.6(d). As for interface-roughness scattering, enhancement of the scattering strength and shrinking of the wavefunction overlap would happen simultaneously. Therefore, these effects would cancel each other out beyond 30% Al-composition, and the scattering rate reaches a constant. In terms of oscillator strength, its change in Table. 4.2 is explained by the same consideration. In device design, oscillator strength is adjustable by getting two wavefunctions closer using a thinner barrier. In that case, however, the barrier becomes very thin, requiring tight control of epitaxial growth

Next, the population fraction in Figure 4.6(c) can be explained based on the carrier transition rates of major inflow and outflow among subbands (Figure 4.7. A carrier income

rate from LLS $|2\rangle$ to the injection state $|1\rangle$ does not change drastically regardless of barrier height and takes 2.8~2.9$\times 10^{12}$ 1/s. On the other hand, an outcome rate from the injection state $|1'\rangle$ to ULS $|3\rangle$ differs greatly depending on barrier height and is 4.5×10^{12} 1/s and 0.4×10^{12} 1/s for low and high barrier devices, respectively. Thus, carriers in a deeper well are more likely to accumulate in the injection state. In terms of electrical conduction, the transition paths with smaller rates limit the total current.

The authors wonder whether the strong confinement by high barriers, observed in this study, can explain a series of barrier height studies implemented previously. In the recent research for THz QCLs, a GaAs/AlGaAs material system has often been used, but other materials such as InGaAs/AlInAs, whose effective mass of electrons is smaller, have also been examined in THz QCLs [176,186,187,206]. In theory, the optical gain of QCLs is inversely proportional to an electron's effective mass, so it is reasonable to apply such different material systems to improve device characteristics. Against our expectation, having said that, it is hard to say that the highest operation temperature is enhanced in these experiments, and the reasons for that has not been clarified.

As one of the reasons, the difference in crystal quality between binary and tertiary materials has been proposed to affect device performance [186]. However, this explanation seems contradictory when considering the success of the lattice-matched InGaAs/AlInAs material system in mid-infrared QCL studies. Therefore, the authors focus on strong electron confinement and wavefunction compression occurring with high barriers to explain these issues.

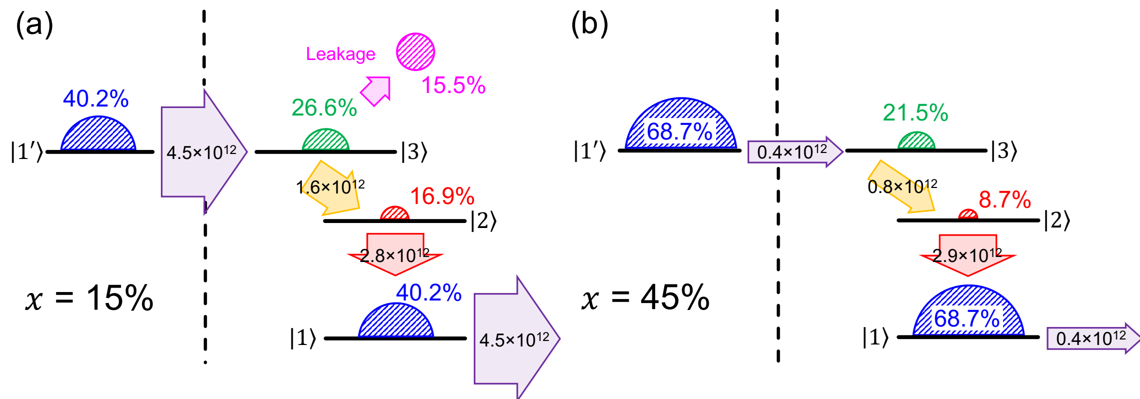

Figure. 4.7 Major carrier transition and population fraction. A unit of transition rate is 1/s. (a) Low barrier device (x = 15%), (b) High barrier device (x = 45%). The sum of population fraction of all parasite states is smaller than 1% in both cases, and their occupancy is not described.

Confinement effect by high barriers is estimated quantitatively by the simulation in this study, and it is observed to happen even in non-driving devices (Figure 4.8). So, if this phenomenon happens regardless of material systems, the lattice-matched InGaAs/AlInAs, whose band-offset is 520meV, could show stronger confinement of electrons in the ground state and wavefunction compression, and the experimental results shown in Table. 1.1 (Chapter 1) are considered to be reasonable. In Table. 1.1, the results for an InAs-based device and the GaAsSb-barrier device can also be explained by the same consideration. In terms of the AlInGaAs-barrier device, the barrier height is relatively low, so degradation of device performance would be attributed to carrier leakage.

Lastly, instead of renewing the highest operation temperature with a high barrier device, investigating the optimal barrier height would require more inclusive research. As shown in Figure 4.6(b), higher optical gain is obtained even in lower barrier conditions

instead of the increase of leakage current. Low barrier devices have several clear merits such as a high oscillator strength due to wavefunction spreading and lower interface-roughness scattering. Thus, there is still room to investigate low barrier device structures, and the third-order tunneling current theory, introduced in Chapter 2, will be important for predicting the device parameters of low barrier devices. Moreover, the quantum systems of QCLs have complicated variations not only due to barrier height but also other design components such as alignment field and layer thickness. Therefore, reaching a conclusion on the optimal barrier height will require further investigation considering the influence of these design parameters.

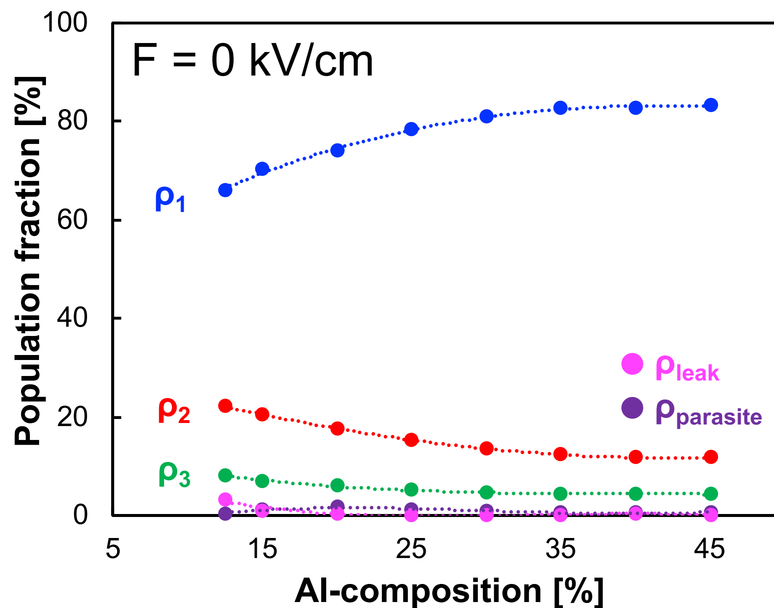

Figure. 4.8 Population fraction without electrical field.

4.4 Summary and Conclusion

The third-order tunneling and leakage currents for QCLs are modeled and explain electrical and optical characteristics of two-well resonant-phonon THz QCLs well. In simulation, when Al-composition/barrier height decreases, a drastic increase of leakage current is observed below 25% Al-composition. In high barrier conditions, electrons accumulate in the ground state due to strong confinement effect, and the population fraction of lasing subbands also becomes lower. In the devices examined in this study, with a fixed-layer thickness, interface-roughness scattering does not become so influential in terms of both scattering rate and optical linewidth even when a potential barrier becomes higher. It seems from Figure 4.4 that maintaining a high optical gain at elevated temperatures is the key to greatly enhancing the temperature performance of this type of THz QCLs, as it drops significantly as temperature increases. Otherwise, from this result, the leakage current essentially has to be completely suppressed in order to reach room temperature performance. Additionally, the suppression of carrier leakage by introducing high barriers would cause many practical issues in the material growth and device processing. Therefore, seeking prospective device designs using low barriers would still be necessary. To determine the optimal barrier height, more inclusive studies considering not only barrier height but also other quantum mechanical conditions will be required.

I do not compose with techniques. I weave melodies coming to me naturally.

– Koichi Sugiyama

Chapter 5 Barrier Height Study - Part II

5.1 Introduction

A comprehensive study about the influence of barrier height on device performance of two-well resonant-phonon devices (shown in Figure 5.1) is implemented in this chapter, aiming to seek effective device design concepts for high temperature operation. In Chapter 4, a prestige barrier height study is implemented by using a standard device structure designed by Khalatpour *et al.* [224] without changing the layer thicknesses and shows a possibility of low barrier condition to be advantageous for high optical gain and high temperature operation [265,317]. Barrier height of quantum wells, however, affects fundamental parameters such as wavefunction and subband energy, and other componential parameters which determine QCL's operation such as oscillator strength, subband carrier density (population fraction), optical linewidth, and so on can also be influenced. Thus, when only barrier height of an optimized device is changed without tuning layer thicknesses, the driving condition of the modified device can often become different from the one of the original structures. Therefore, in order to discuss the optimal barrier height conditions precisely, we need to optimize device structures totally by adjusting layer thicknesses and an alignment field as well as barrier height. Even if only one barrier height condition is focused, quite a few numbers of applicant device structures can be considered for high optical gain. So, the maximum optical gain for the barrier height and the optimized structure for it are

found from these applicants. A set of optical gain maxima are also obtained by the same way, and the dependence of optical gain maxima on barrier height which is necessary for the discussion for the optimal barrier height is finally obtained.

The purpose of this study is to determine the optimal barrier height for two-well resonant-phonon THz QCLs composed of GaAs and $Al_xGa_{1-x}As$ based on a relation between Al-composition and optical gain maxima, and to clarify the dynamic of barrier height on device characteristics. Two-well resonant-phonon devices can be designed with structural variation based on published research. For example, a device with different barrier heights (barrier heights of an injection-barrier and radiation-barrier are different) [188,208,209], with a stepped-well [207], and with a very thin AlAs barrier [210] have been proposed so far. Although these complexities would be necessary for high performance structures, that can complicate this research. Therefore, this work targets only most simple structure [111,138,224,284] designed with wells and barriers of GaAs and $Al_xGa_{1-x}As$ (AlGaAs composed of only one Al composition). Al-composition varys from 5% to 45%.

Details of this work will be described form the next section. In Section 5.2, a device structure exploration procedure and an optical gain calculation specified to this research are explained. In Section 5.3, simulation results obtained from a series of calculation in Section 5.2 are discussed. Finally, this work is summarized and concluded in Section 5.4.

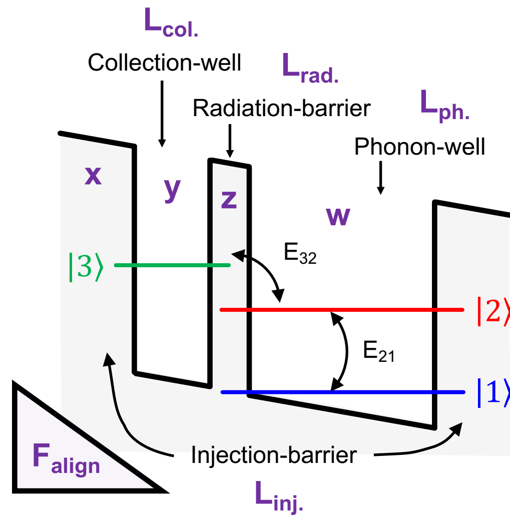

Design parameters

x : Al-composition of injection-barrier
y : Al-composition of injection-well
z : Al-composition of radiation-barrier
w : Al-composition of phonon-well

$L_{inj.}$: Injection-barrier thickness
$L_{col.}$: Collection-well thickness
$L_{rad.}$: Radiation-barrier thickness
$L_{ph.}$: Phonon-well thickness

F_{align} : Alignment field

Figure. 5.1 A basic structure of a two-well resonant-phonon terahertz quantum cascade laser and design parameters.

5.2 Method

A device structure exploration procedure and optical gain calculation method used in this work are described in this section. The focus of this research is a relation between Al-composition and optical gain maxima. In order to obtain the optical gain maxima in the relation, an effective exploration tactics is necessary to compare numerous device structures designed by tuning design parameters such as an alignment field and layer thicknesses.

First, QCL device design is exploration of device structures by adjusting layer thicknesses and alignment electrical field which affect subband energies inside quantum wells. For exploration, optical gain is often chosen as a figure-of-merit. (Other device parameters may be focused depending on research purposes.) In the case of two-well

resonant-phonon device structures, in which carrier transport for lasing is implemented by three main subbands: a ground state $|1\rangle$, a lower-lasing state $|2\rangle$ (LLS), and an upper-lasing state $|3\rangle$ (ULS), a set of the fundamental design rules described below need to be satisfied.

- A ground state of the adjacent module and ULS are aligned.
- An energy difference between ULS and LLS corresponds to the target/design lasing frequency.
- An energy difference between LLS and a ground state corresponds to the energy for high LO-phonon scattering rate.

Optical gain is calculated based on three main componential parameters: oscillator strength, population inversion, and optical linewidth, and the fundamental design rules are a requirement for large population inversion. Where, optical gain can be large by an efficient carrier injection from a ground state of the adjacent module aligned with ULS and by an efficient carrier extraction from LLS to a ground state. However, Fundamental design rule does not necessarily guarantee large population inversion. Another determinative condition for population inversion is a non-radiative carrier transition rate between ULS and LLS, and when this value is small, population inversion tends to become larger. However, a trade-off happens between a non-radiative transition rate and oscillator strength because these parameters are both calculated based on an overlap of the same wavefunctions by using Fermi's golden rule. Which means that if devices are designed for small non-radiative transition rate, oscillator strength can also become small, resulting in small optical gain. Therefore, we need to balance between oscillator strength and non-radiative transition rate in

design and cannot tell that applicant device structures can take high optical gain until calculation.

As depicted in Figure 5.1, a single module of a basic two-well resonant-phonon device is composed of four layers: an injection-barrier, collection-well, radiation-barrier, and phonon-well. So, even this simple structure, compared with other devices, has, totally, nine design parameters: Al-compositions of each layer (x, y, z, and w), layer thicknesses ($L_{inj.}$, $L_{rad.}$, $L_{col.}$, and $L_{ph.}$), and an alignment electrical field F_{align}, which can give a lot of structure design variation as depicted in Figure 5.2. Due to this freedom of device design, tremendous numbers of applicant device structures satisfying the fundamental design rule can be found. When a design parameter of an optimized device changes, the optimization brakes. However, that brake can be compensated for by tuning the other parameters. So, a new optimization condition is found. Calculation time of optical gain for such number of devises also increases. In device structure exploration, therefore, exploration ranges of design parameters and a set of screening conditions for selecting structures matching design purposes are necessary.

In this study, only simple structures composed of GaAs wells and $Al_xGa_{1-x}As$ barriers ($y = z = 0$, and $z = x$ in Figure 5.1, and Regular structure in Figure 5.2) are targeted. For precise discussion about the optimal barrier height for two-well resonant-phonon devices, all structural variations in Figure 5.2 should indeed be investigated and optical gain of these structures would be compared. (The research for other structural designs except for Regular structure in Figure 5.2 is called ‘structural study’ in this thesis.) Especially, investigation about the designs as $z \neq x$ is intriguing because an injection-barrier and

radiation-barrier take different roles in device operation. Having said that, such expansive research requires to deal with a massive volume of data. Besides, even research for Regular structures have never adequately been concluded theoretically and experimentally. Therefore, this work positions a barrier height study for Regular structure as the first step of structural studies that would be implemented in the future, and the influence of barrier height on characteristics of Regular structures is thoroughly investigated.

Calculation for optical gain in this exploration is developed as Rate equation – Limited model (Limited-RE) based on Rate equation – Full model (Full-RE) introduced in Chapter 2. Optical gain of quite a few device structures found in the structure exploration need to be calculated by Rate equation [59,224,236]. However, the calculation method, where optical gain peak is exactly estimated from the dependence of optical gain on electrical field as shown in Figure 2.18 or 2.27(a), is unrealistic to be applied. Therefore, the full model is modified for short calculation time.

In addition, optical gain map – a contour chart of optical gain versus two design parameters – is introduced [318]. Due to several design parameters and complexity of the theory, it is difficult to describe optical gain by an equation directly with these parameters. Instead, optical gain map can visualize the influence of design parameters on optical gain. In this study, the number of design parameters is reduced to four as described later, and the influence of all parameters is reflected in optical gain maps. Optical gain maxima obtained from gain maps for each Al-composition are focused in this study and are plotted to Al-composition. The optimal barrier height for two-well resonant-phonon devices is determined based on the relation between Al-composition and optical gain. As for other analysis, a range

of design parameters for high optical gain can be considered as durability against the difference between design and actual driving conditions, so this range is called 'structure tolerance' and its dependence on Al-composition is investigated. The distribution of design parameters for high-performance devices is also investigated.

Finally, device structures recording optical gain maxima in Rate equation – Limited model are re-calculated by the full model, and componential parameters relating to optical gain and electrical current density are also analyzed for clarifying the dynamics of barrier height. As described in Chapter 2, the calculation reliability of the full model is not guaranteed for devices with too thin injection-barriers. So, analysis by the full-model is separated depending on injection-barrier thickness: thin and thick injection-barrier device conditions.

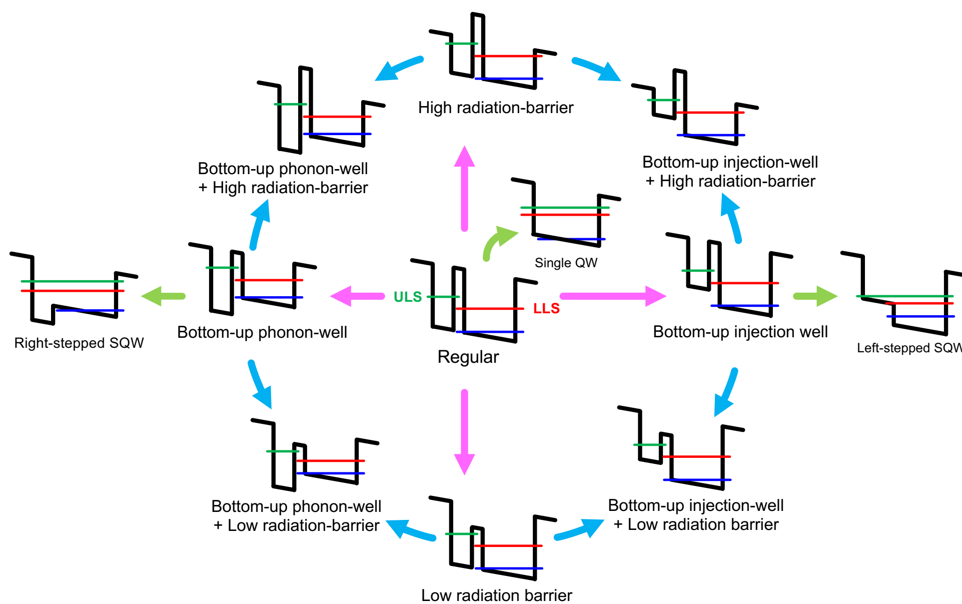

Figure. 5.2 Variations of two-well resonant-phonon structures.

5.2.1 Methodology of Device Structure Exploration

In this subsection. Componential conditions for structure exploration are explained from 5.2.1.1 to 5.2.1.4, and the exploration flow is show in 5.2.1.5.

5.2.1.1 Design Parameters

Reduction of the number of design parameters is explained below. This work limits the examining device structures, and only simple structures composed of GaAs quantum wells and $Al_xGa_{1-x}As$ barriers are basically considered with six design parameters: Al-composition of barrier x_{Al}, alignment field F_{align}, thicknesses of four layers $L_{inj.}$, $L_{inj.}$, $L_{inj.}$, and $L_{inj.}$. By considering a condition satisfying the fundamental design rules, one of the layer thicknesses is omitted by the relation established between these design parameters and subband energy differences calculated by Schrödinger equation.

Under a condition for subband alignment ($F = F_{align}$), an electron radiatively or non-radiatively transfers from ULS to LLS and is subtracted from LLS to an injection state while moving through one module. So, an energy-drop per module L_p is a sum of the energy difference between ULS and LLS E_{32} and the one between LLS and the injection state E_{21}. This relation is expressed by Equation (5.1).

$$F_{align}L_p = E_{32} + E_{21} \tag{5.1}$$

The length of one module L_p is described by a sum of thicknesses of all layers inside a

module.

$$L_p = L_{inj.} + L_{col.} + L_{rad.} + L_{ph.} \tag{5.2}$$

One of the design parameters can be reduced by combining the two equations. In this work, an injection-barrier thickness is expressed by the other design parameters in Equation (5.3), and this equation is applied to device structure exploration.

$$L_{inj.} = \frac{E_{32} + E_{21}}{F_{align}} - \left(L_{col.} + L_{rad.} + L_{ph.}\right) \tag{5.3}$$

Excluding Al-composition x_{Al}, determined in the beginning of the exploration, the other four design parameters – thicknesses of collection-well $L_{col.}$, radiation-barrier $L_{rad.}$, and phonon-well, and $L_{ph.}$, and an alignment field F_{align} are dealt as variables in the device structure exploration.

5.2.1.2 Structure Screening Conditions

Based on the fundamental design rules, screening conditions reflecting our purposes for devices are defined by adding a term about the number of subband, and applicant device structures for high optical gain are picked up from numerous ones that are randomly generated.

① More than three subbands exist per module.
② Under a designed alignment field, a ground state in the adjacent module ($|1'\rangle$) and ULS are aligned.
③ Under a designed alignment field, the energy difference between ULS and LLS corresponds to an energy of the target frequency.
④ Under a designed alignment field, the energy difference between LLS and a ground state corresponds to the one for high LO-phonon scattering rate.

These conditions will be written by using design parameters.

First, when four design parameters F_{align}, $L_{col.}$, $L_{rad.}$, and $L_{ph.}$ are determined, a structure of one module is calculated by Schrödinger equation, and wave function and eigen energy (subband energy) are calculated. As described in the condition ①, a two-well resonant-phonon device needs, at least, three subbands per module for carrier transition. The first condition is described with the number of subbands N_{level} ($\boldsymbol{N_{level} \geq 3}$). Under conditions with electrical field ($F \neq 0$), eigen states can be detected in the continuums from Schrödinger equation. To count the number of subbands per module automatically, calculation in implemented under a non-field condition ($F = 0$).

Next, a screening condition about an injection-barrier thickness $L_{inj.}$ is determined. An injection-barrier thickness is calculated by assigning values of other design parameters in Equation (5.3). However, the calculated injection-barrier thickness can be a negative or extremely large value because a set of these design parameters are randomly selected in the exploration program. Therefore, the lower limit of an injection-barrier thickness is determined as 5Å which is a controllable layer thickness by MBE, and the upper limit is determined to be 60Å based on a calculation in the past work so that a coupling strength of two subbands becomes higher than 1meV, which is required for high tunneling transition rate as shown in Figure 5.3 [263] ($\mathbf{5} \leq \boldsymbol{L_{inj.}} \leq \mathbf{60}$ [Å]).

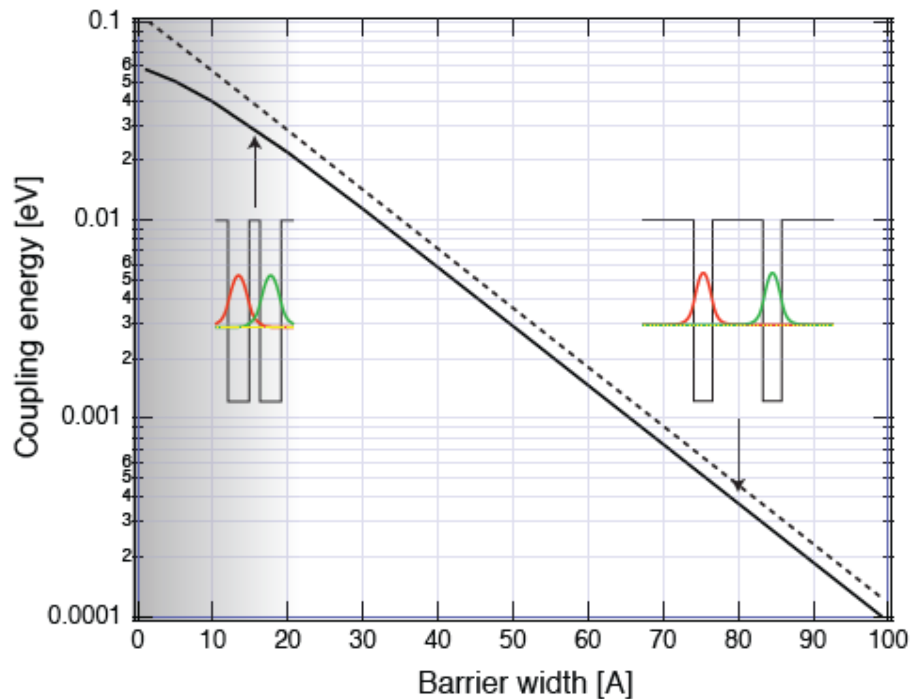

Figure. 5.3 The coupling energy between the ground-states of two coupled quantum-wells. (Solid line = coupling energy, Dashed line = detuning energy) [263].

Lasing frequency is one of the important parameters and is described in Equation (5.4) by using the energy difference between ULS and LLS E_{32}.

$$f_{32} = \frac{E_{32}}{2\pi\hbar} \tag{5.4}$$

Usually, GaAs-based THz QCLs are designed to lase at 1~5THz, so a corresponding energy range is determined as a screening condition ($\mathbf{4.5 \leq E_{32} \leq 20.5\ [meV]}$). In structure exploration, band-bending effect is not considered, so the energy difference of selected structures remains in this range. However, in optical gain calculation, band-bending effect can change the energy difference. As a results higher or lower energy difference than this energy range can be detected.

Lastly, a screening condition for the energy difference between LLS and an injection state E_{21} is determined. For large population inversion, not only efficient carrier injection to ULS but also carrier extraction from LLS is important, and the energy difference between LLS and an injection state is usually designed to be the same as the LO-phonon energy of the well material (In GaAs, 36.7meV) so that carriers in LLS are extracted by fast LO-phonon scattering. In this point, the screening condition for E_{21} is determined by a different way in this study. As described in Figure 5.4, LO-phonon scattering rate peaks when the energy difference between subbands corresponds to the LO-phonon energy of the well material regardless of the lattice temperature. So, the conventional determination method for E_{21} is thought to be reasonable. On the other hand, this study gives more freedom in designing the energy difference because LO-phonon scattering rate becomes high over a wide energy range

at high temperature conditions. As shown in the L-V characteristic of a two-well resonant-phonon device designed by Khalatpour *et al.* in Chapter 2, around 1.0×10^{12} [1/s] of carrier transition rate between subbands is high enough. Based on this calculation, 2.0×10^{12} [1/s] of thermally averaged LO-phonon scattering rate is set as a screening condition ($\mathbf{20 \leq E_{21} \leq 100\ [meV]}$).

The aforementioned screening conditions are summarized below. In the structure exploration program coded by MATLAB, true-false tables are used for screening (Figure 5.5).

$$\begin{cases} ① \ N_{level} \geq 3 \\ ② \ 5 \leq L_{inj.} \leq 60\ [Å] \\ ③ \ 4.5 \leq E_{32} \leq 20.5\ [meV] \\ ④ \ 20 \leq E_{21} \leq 100\ [meV] \end{cases}$$

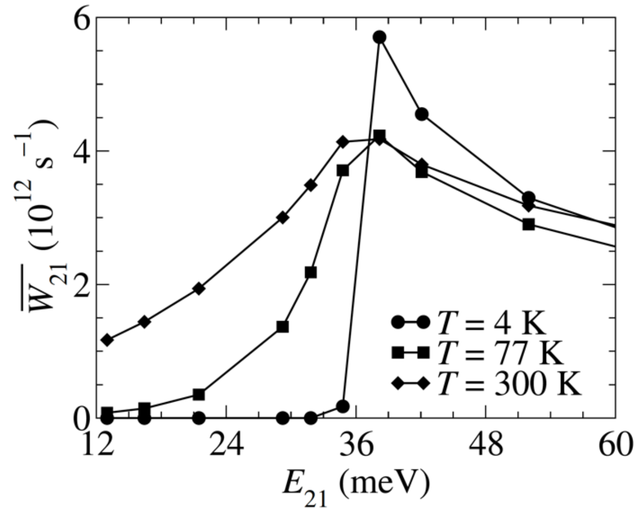

Figure. 5.4 Thermally averaged LO-phonon scattering rate versus subband energy difference in a 200Å-wide single quantum well structure [59]. Subband number 1 and 2 in this figure corresponds to a ground state and the first excited state of the 200Å-wide single quantum well.

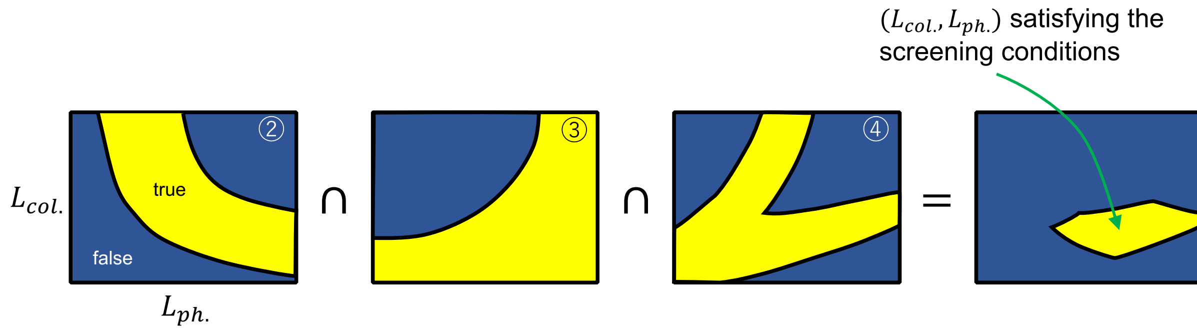

Figure. 5.5 An image picture of condition screening process by true-false tables in a MATLAB program. Images ②, ③, ④ correspond to the screening conditions shown in the previous page.

5.2.1.3 Optical Gain Map

In addition to the investigation for the optimal barrier height of two-well resonant-phonon THz QCLs, common features or tendency for high-performance devices are also investigated. There are many design parameters in two-well resonant-phonon devices, and these parameters affect the componential parameters of optical gain. However, the precise investigation of the influence of these design parameters on device characteristics or the mutual influence of these parameters is not so easy because optical gain cannot be directly expressed by equations with these parameters. So, such investigation needs to rely on numerical calculation, and optical gain map is introduced for this purpose.

Optical gain maps in this work are made from a massive amount of calculation data based on four design parameters and optical gain taking two of design parameters for x- and y- axes, and optical gain for z-axis, and optical gain can visualize relations amongst design parameters in a 3D-contour plot. Among four parameters dealt with in this study F_{align} and

$L_{rad.}$ are selected for the main analysis of optical gain because optical gain is susceptible to these two parameters. Although small change of $L_{col.}$ and $L_{ph.}$ do not affect optical gain, the influence of these parameters is also considered in calculation.

One of the two types of optical gain map is explained in Figure 5.6. The F_{align}-$L_{rad.}$ gain map described in the left is used in the main analysis later, every single point of optical gain at (F_{align}, $L_{rad.}$) is the maximum in the $L_{col.}$-$L_{ph.}$ gain map. So, the optical gain maximum of the F_{align}-$L_{rad.}$ gain map is the one for one Al-composition conditions. Even though this method takes too much time, the accuracy in calculation is also important. So, two types of design parameter discretization steps are introduced to seek the gain peak maxima efficiently balancing between the calculation accuracy and speed.

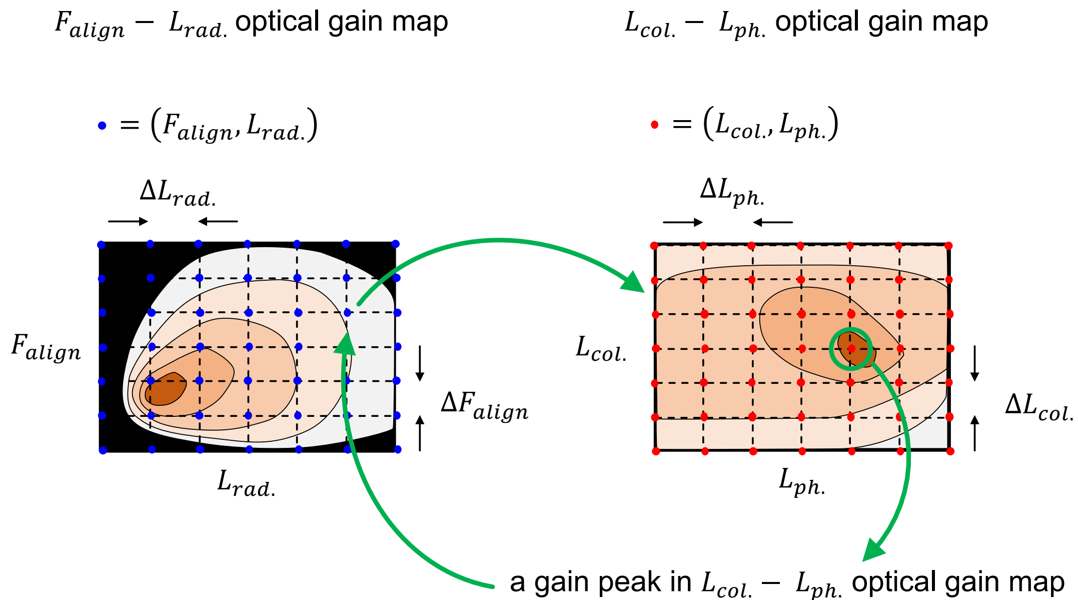

Figure. 5.6 How to make an optical gain map. Conditions in black parts do not have optical gain peaks. In other parts, thicker colors mean higher optical gain.

5.2.1.3 Rough and Fine Search

The other types of optical gain map is defined by discretization steps of design parameters, and totally four types of optical gain maps made by combination of F_{align}-$L_{rad.}$ gain map or $L_{col.}$-$L_{ph.}$ gain map and two more types depending on discretization steps are used for efficient device structure exploration. The other new types are explained below.

For the structure exploration, a set of exploration range is limited for four design parameters F_{align}, $L_{col.}$, $L_{rad.}$, and $L_{ph.}$ of two-well resonant-phonon devices. This range is determined based on the device structures published in the past.

$$\begin{cases} 10 \leq F_{align} \leq 70 \text{ [kV/cm]} \\ 30 \leq L_{col.} \leq 130 \text{ [Å]} \\ 10 \leq L_{rad} \leq 60 \text{ [Å]} \\ 80 \leq L_{ph.} \leq 220 \text{ [Å]} \end{cases}$$

A set of device parameters (F_{align}, $L_{col.}$, $L_{rad.}$, $L_{ph.}$) satisfying screening conditions are explored by changing these design parameters in this range. However, optical gain can greatly vary due to these parameters, so parameter discretization steps need to be selected carefully. For example, if the discretization is too large, optical gain maps may not show precise influence of design parameters. On the other hand, too small discretization steps can increase the number of calculation points, resulting in long calculation time. Considering the points above, this work uses Rough search using large discretization steps and Fine search using small ones for efficiency. These two searches are applied to all four design parameters, and the discretization steps below are used in the exploration.

・Rough search discretization steps

$$\begin{cases} \Delta F_{align}^{rough} = 5.0\ [\mathrm{kV/cm}] \\ \Delta L_{col.}^{rough} = 5.0\ [\text{Å}] \\ \Delta L_{rad.}^{rough} = 5.0\ [\text{Å}] \\ \Delta L_{ph.}^{rough} = 5.0\ [\text{Å}] \end{cases}$$

・Fine search discretization steps

$$\begin{cases} \Delta F_{align}^{fine} = 1.0\ [\mathrm{kV/cm}] \\ \Delta L_{col.}^{fine} = 0.5\ [\text{Å}] \\ \Delta L_{rad.}^{fine} = 1.0\ [\text{Å}] \\ \Delta L_{ph.}^{fine} = 0.5\ [\text{Å}] \end{cases}$$

These discretization steps are decided by several times of adjustment between the calculation amount and accuracy. In Fine search, 1.0 [Å] of discretization steps can also work for $\Delta L_{col.}^{fine}$ and $\Delta L_{ph.}^{fine}$. Example calculation data at $x_{Al} = 20\%$ is described in Figure 5.7.

On the one hand, Rough search is applied to a whole exploration range. On the other hand, Fine search is implemented to a limited range close to the gain maximum in Rough search, determined by ±2.5kV/cm of the optimal field and ±2.5Å of layer thickness. For instance, the $L_{col.}$-$L_{ph.}$ gain map in Figure 5.6 is created through these two types of searches as depicted in Figure 5.8. The gain maximum is first calculated by Rough search, and more detailed value is sought by Fine search.

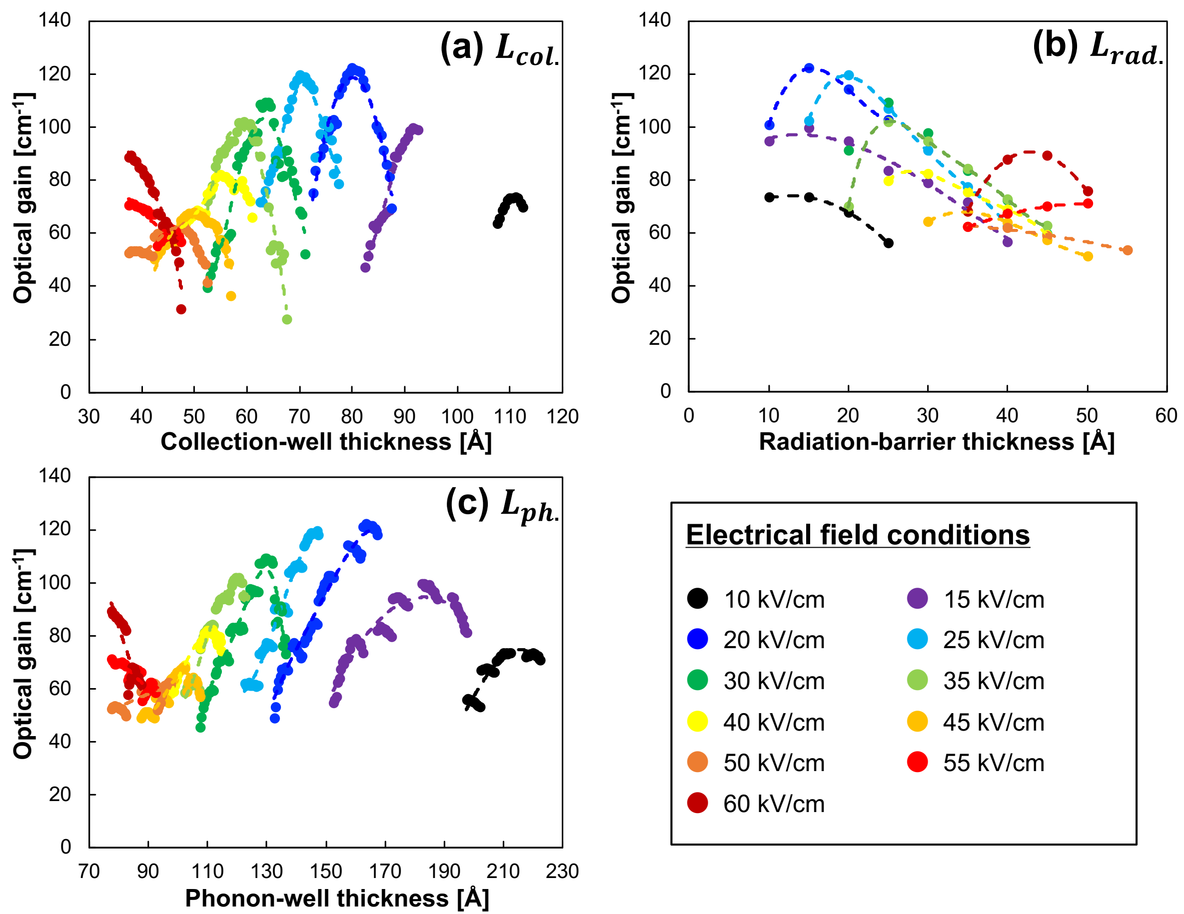

Figure. 5.7 The relation between optical gain and design parameters. (a) Collection-well thickness dependence, (b) radiation-barrier thickness dependence, and (c) phonon-well thickness dependence.

5.2.1.5 Device Structure Exploration Procedure for Optical Gain Map

A device structure exploration procedure constructed by combining essential exploration components described from 5.2.1.1 to 5.2.1.4 is described in Figure 5.9 and 5.10. In this study, 250K of the heat-sink temperature is consistently used for exploration.

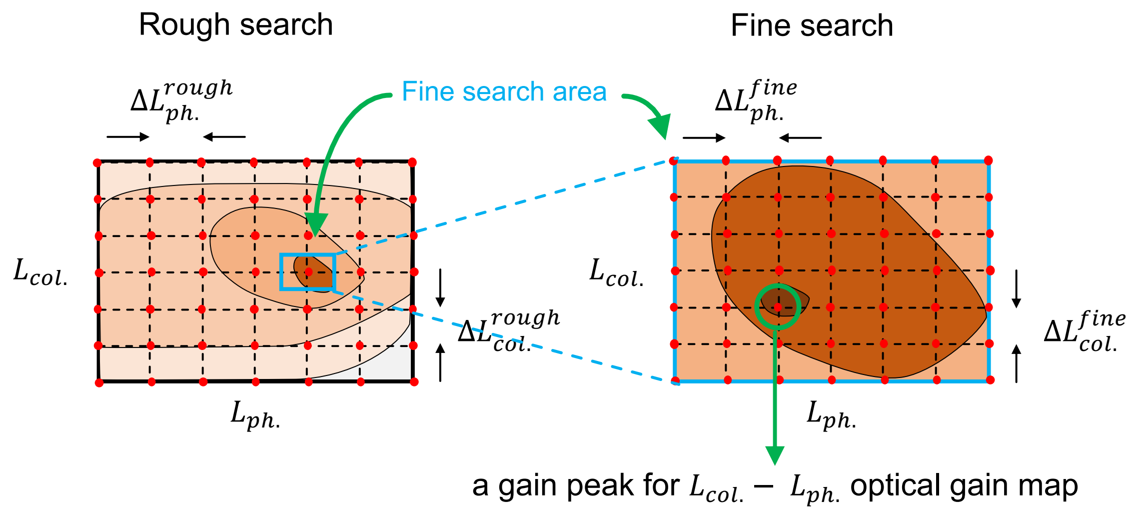

Figure. 5.8 A sketched image of Rough search and Fine search.

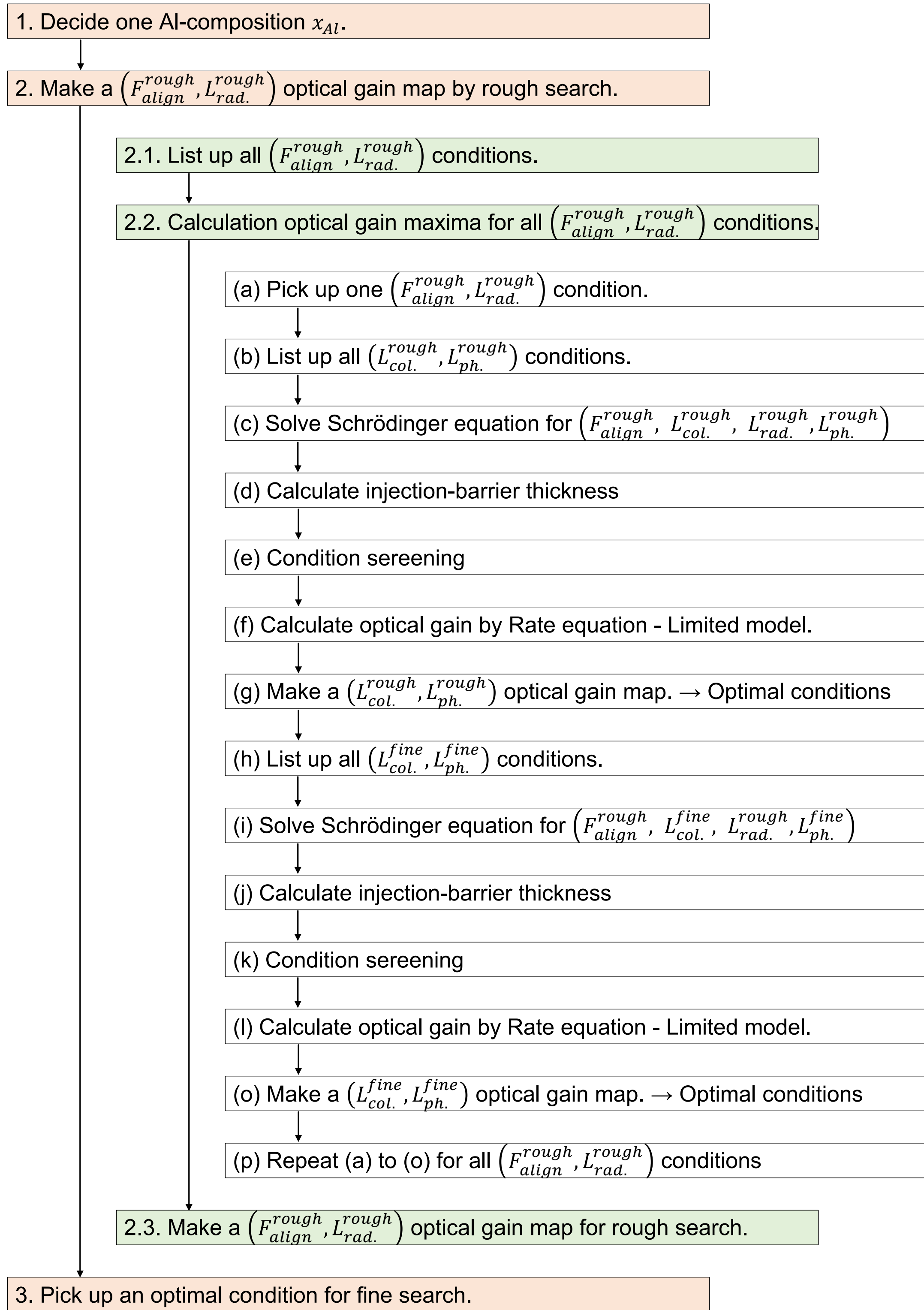

Figure. 5.9 Device structure exploration procedure – Part A.

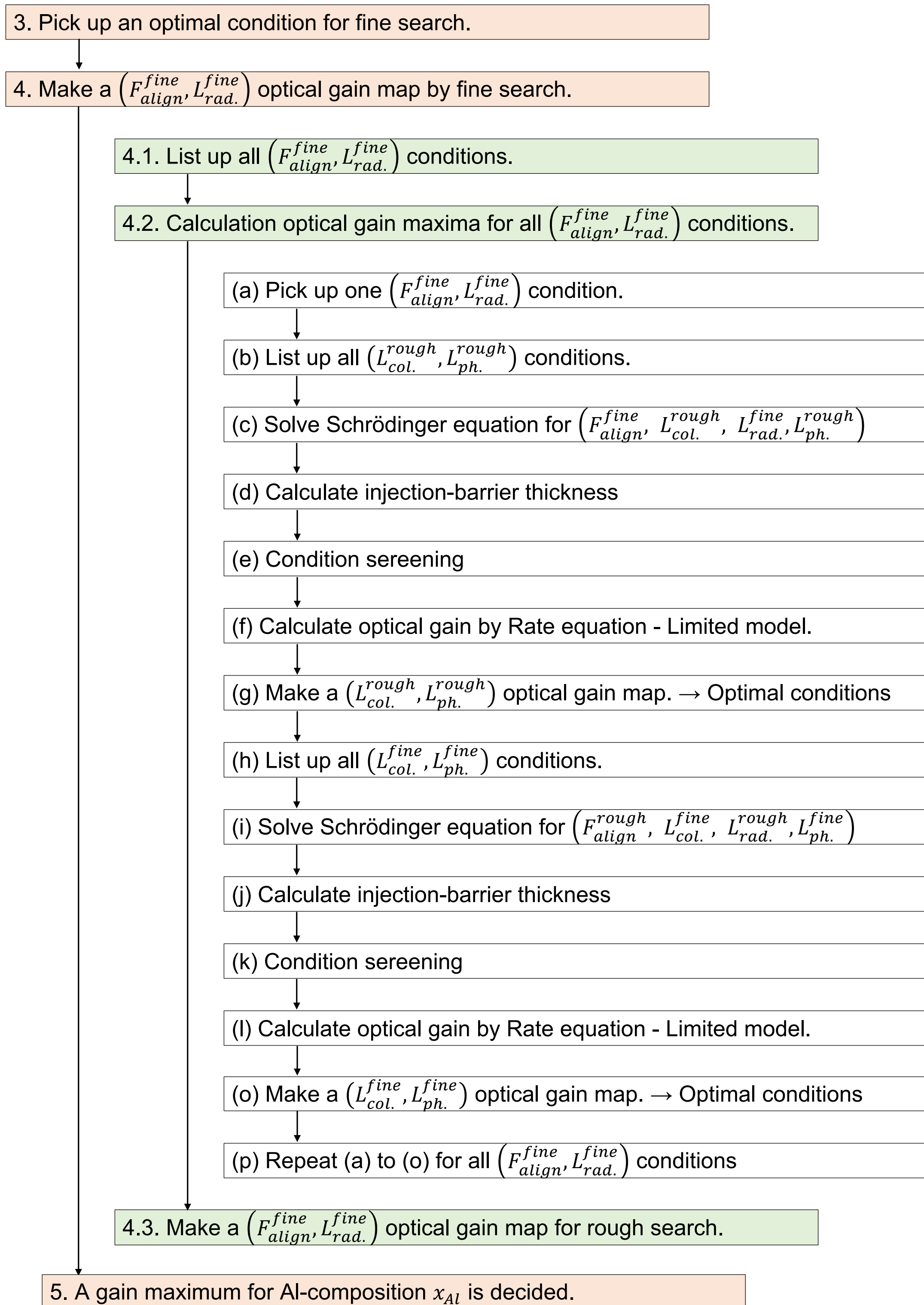

Figure. 5.10 Device structure exploration procedure – Part B.

5.2.2 Rate Equation – Limited Model

In device structure exploration, Rate equation – Limited model (Limited-RE) is used. The details and use of this model in exploration are explained in this subsection

Device parameters		Theory and considered phenomena	
		Full-RE	Limited-RE
Subband number		All	
Wave function / Eigen energy		Finite difference method – single band model with band non-parabolicity	
Intra-module carrier transport	Scattering rate	Fermi's golden rule LO* / IFR / **IMP*** / AD / **EE***	Fermi's golden rule LO* / IFR / AD
	Optical linewidth	Ando's theory LO* / IFR / **IMP*** / AD	Ando's theory LO* / IFR / AD
Inter-module carrier transport	Coupling strength Detuning energy	Tight-binding theory	
	Dephasing time	Ando's theory LO* / IFR / **IMP*** / AD	Ando's theory LO* / IFR / AD
Population fraction		Rate equation without stimulated emission	
Current density		3rd-order tunneling current model	
Optical gain		Fermi's golden rule	
Lattice temperature		Self-heating model	
Electron temperature	Bound state	Kinetic energy balance theory (LO* / IFR)	
	Continuums	Theoretical model	
Dopant activation		Theoretical model	
Band-bending effect		Schrödinger-Poisson system	

Table. 5.1 Comparison of the rate equation – Full model and – Limited model. *A screening effect model is considered.

As described in Chapter 2, Rate equation – Full model (Full-RE) can calculate device characteristics of two-well resonant-phonon devices with high accuracy. However, the demerit of this model is calculation time due to the ionized-impurity and electron-electron scattering. Thus, it is actually difficult to apply this model to all applicant structures found in the structure exploration to calculate optical gain. To resolve this issue, Rate equation – Limited model is developed by omitting calculation of ionized-impurity and electron-electron scattering and used for structure selection. The difference between Full model and Limited model are described in Table 5.1.

Omission of the ionized-impurity and electron-electron scattering calculation can degrade the calculation accuracy instead of speed. In Full model, calculation for the ionized-impurity scattering is included in intra-module carrier scattering rate and optical linewidth and inter-module pure dephasing time calculation. The electron-electron scattering is also considered in intra-module carrier scattering rate calculation. In carrier scattering rate, the LO-phonon scattering rate is the dominant parameter because 250K of the heat-sink temperature is used for calculation. The influence of the ionized-impurity and electron-electron scattering rate is small enough, so elimination of these calculation does not affect the calculation results of subband carrier density or population inversion at all. However, omission of optical linewidth broadening calculation by the ionized-impurity scattering can increase optical gain greatly because optical linewidth broadening by the ionized-impurity scattering is comparable to the ones due to the LO-phonon and interface-roughness scattering. Temperature dependence of optical gain of a two-well resonant-phonon THz QCL designed by Khalatpour is calculated by Full and Limited models, and the results are compared in

Figure 5.11. In Figure 5.11, optical gain from 0 to 30kV/cm of electrical field is calculated, and the gain maxima are plotted to the heat-sink temperature in both models. From this results, optical gain calculated by Limited model almost doubles compared to the ones by Full model. Such difference would be attributed to wavefunction or subband energy, so the difference can vary even among two-well resonant-phonon devices, to some extent.

In Rate equation – Limited model, rules for impurity doping and electrical field conditions are commonly applied to all structures described as below. Impurities are assumed to be doped over 30Å-wide in the center of a phonon-well with 4.5×10^{10}cm^{-2} of sheet doping density, which is a recent design trend (Figure 5.12). As for electrical field condition, optical gain is calculated twice at the same field condition $F = F_{align} + 1$ [kV/cm].

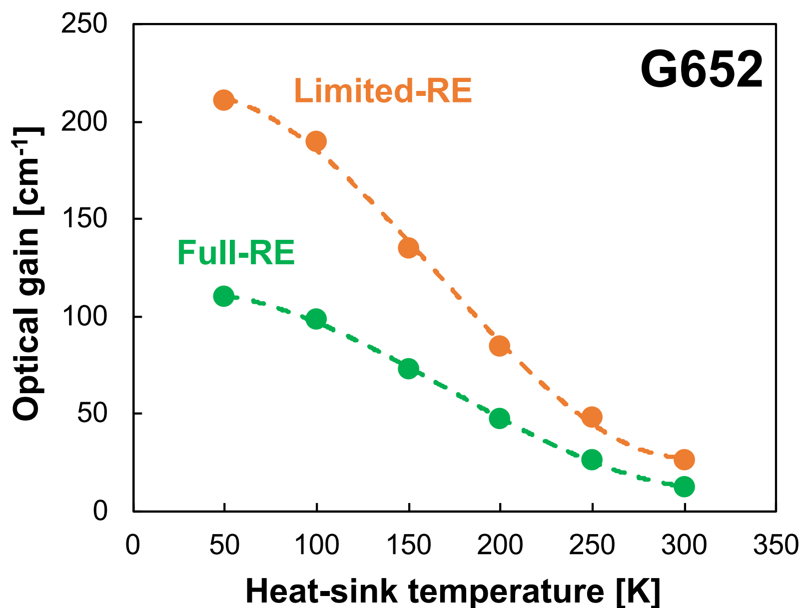

Figure. 5.11 Comparison between the rate equation – full model and – limited model in the dependence of optical gain on the heat-sink temperature.

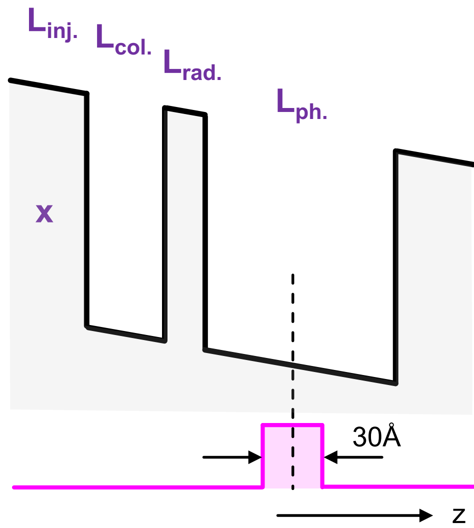

Doping

- $N_d^{2D} = 4.5 \times 10^{10}$ [cm^{-2}]
- 30Å of rectangular doping in the middle of a phonon-well

Electrical field

- $F = F_{align}$
- twice

Figure. 5.12 doping condition and electrical field conditions in device structure exploration.

The reason why optical gain is calculated under the electrical field condition $F = F_{align} + 1$ kV/cm is because optical gain is observed to peak 1~2kV/cm higher electrical field conditions than design field conditions in several device structures. Two times of optical gain calculation at the same field condition are able to offer almost the same values of the solution by self-consistent loop calculation as accurately as possible. For example, subband carrier density and band-bending effect (the Hartree potential) for one electrical field condition are calculated by self-consistent loop calculation, but even single loop takes too much time due to complexity of the QCL theory (Figure 5.13). So, using self-consistent loop calculation is not efficient for device structure exploration. Thus, a compromising calculation method is used for the L-I-V characteristics in Full model. Where, subband carrier density and band-bending effect are calculated without self-consistent loop calculation by using these values in the previous electrical field condition for the initial parameters. (Only first condition

is calculated twice.) In the Limited model of structure exploration, the same condition ($F = F_{align} + 1$ kV/cm) is calculated twice to keep acceptable level of accuracy.

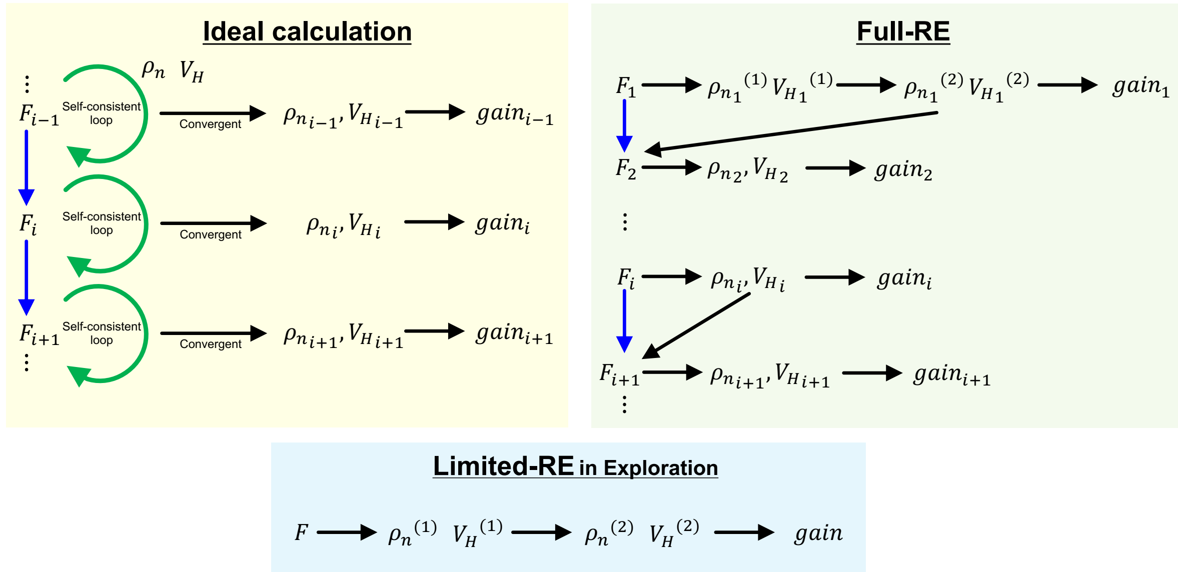

Figure. 5.13 Difference of calculation procedures. ρ_n and V_H denote population fraction of a subband $|n\rangle$ and Hartree potential, respectively.

5.3 Results and Discussion

In this section, calculation results of optical gain maps explained in the previous section and analyzed date are shown from 5.3.1 to 5.3.3, and high-performance devices are thoroughly analyzed by using Rate equation – Full model in 5.3.4.

5.3.1 Optical Gain Map

Optical gain maps of two-well resonant-phonon THz QCLs for 5~45% of Al-composition are described in Figure 5.14. These F_{align}-$L_{rad.}$ gain maps are created by Rough search shown in Figure 5.6 and 5.8. The evaluation points in these figures are the optical gain maxima, a set of design parameters for these maxima, ranges for high optical gain, and two types of gain peaks.

First, 182.5cm^{-1} of the maximum optical gain among all Al-composition conditions was recorded at 15%, and the maxima are found to decrease to around 100cm^{-1} in 5 or 15%. In the high barrier condition higher than 25% of Al-composition, the optical gain maxima decrease gradually. So, the optimal Al-composition for two-well resonant-phonon devices, the largest concern in this work, is determined as around 15%.

Next, a design parameter range (F_{align}, $L_{rad.}$) of high optical gain is called 'structure tolerance' in this work. Active cores of QCLs are composed of a stack of very thin layers in Å-order, so very sensitive layer control – in atomic layer level – is necessary for crystal growth. However, it takes around 20hours to pile up around 10μm thick of active cores, and

operation conditions of MBE such as temperature or ingredient gas flux can subtly vary during crystal growth. So, fabrication of several hundred repetitions of layers in the same quality is actually challenging, and thickness errors can normally happen between modules. Therefore, maintaining high optical gain even when layer thicknesses vary in optical gain map means the structure is durable to such design errors.

Furthermore, electrical field domain effect in QCLs was experimentally demonstrated [319,320]. Electrical field domain (EFD) is a phenomenon that several regions/domains with different fields are created in an active core. Because there are several hundred modules in one active core of THz QCLs, when EFD happens, parts of regions of active core do not contribute to lasing, resulting in radiation efficiency degradation. Considering this phenomenon, a wide range of optical gain to alignment field is preferable for high-performance devices to suppress radiation efficiency degradation due to EFD.

Structure tolerance describes durability against the errors of the aforementioned parameters (radiation-barrier thickness and alignment field) between design and actual device driving conditions and is visualized in optical gain maps as a thick-color regions in Figure 5.14. Considering that the optical gain calculated by Limited model is approximately two times larger than the ones by Full model and that normally $30cm^{-1}$ of optical gain is considered to match threshold gain of waveguide, structure tolerance in Figure 5.14 is defined as regions where optical gain surpass $75cm^{-1}$.

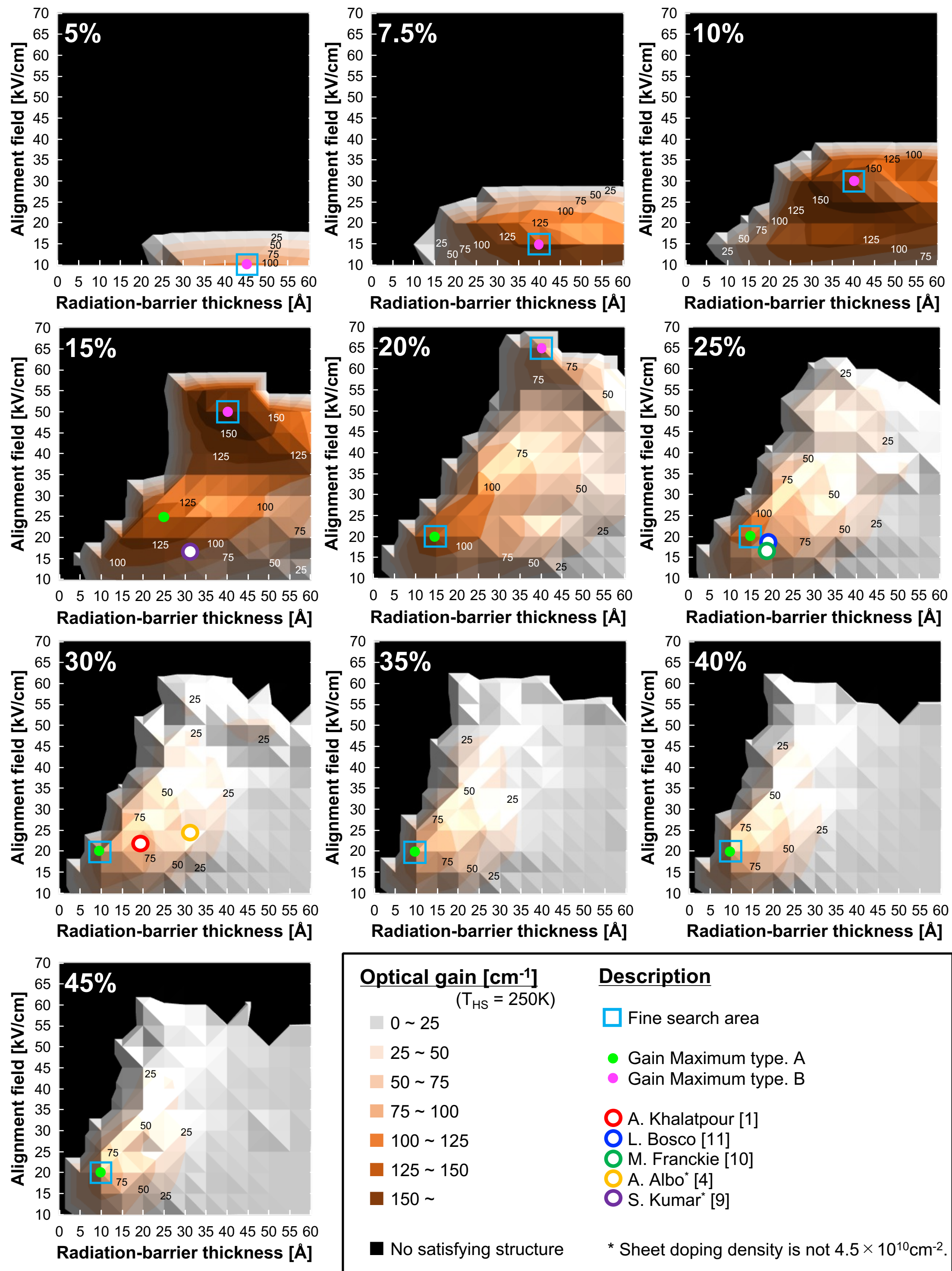

Figure. 5.14 Optical gain map of two-well resonant-phonon terahertz quantum cascade lasers by Rate equation – Limited model.

In Figure 5.14, structure tolerance becomes the largest when 15% of Al-composition, and when Al-composition becomes larger or smaller than 15%, the tolerance is observed to be small. Furthermore, the change of structure tolerance to Al-composition is different between the low and high barrier conditions. On the one hand, in low barrier conditions, structure tolerance shrinks along with decreasing of the number of device structure that can satisfy the high field conditions even though optical gain values are high. On the other hand, in high barrier conditions, decrease of the optical gain maxima with Al-composition determines the structure tolerance.

Lastly, the most important feature in optical gain in Figure 5.14 is two types of gain peaks. This means that two types of design concepts exist for high-performance devices. One of the concepts is a conventional one and appears in the thin radiation-barrier and low alignment field conditions (Type-A). Gain peaks for type-A are observed from 15 to 45% of Al-compositions, and the gain maximum peaks 141.6cm^{-1} at 15% and decreases to 90.2cm^{-1} at 45%. The device design information for published devices is plotted in Figure 5.14, then these high-performance devices are indicated to be designed under the concept of Type-A [111,138,188,224,284]. Another optimization (Type-B), featured by thick radiation-barrier (around 40Å), is observed from 5 to 20% of Al-compositions in optical gain map. Even though radiation-barrier thickness does not change so much in this concept, alignment field decreases along with Al-composition. Details of these two design concepts and the influence of barrier height of these devices are a little complicated and are explained in the later subsections.

5.3.2 Device Design Concepts

The two types of design concepts Type-A and -B are compared in this subsection. Band diagrams for 20% of Al-composition are described in Figure 5.15.

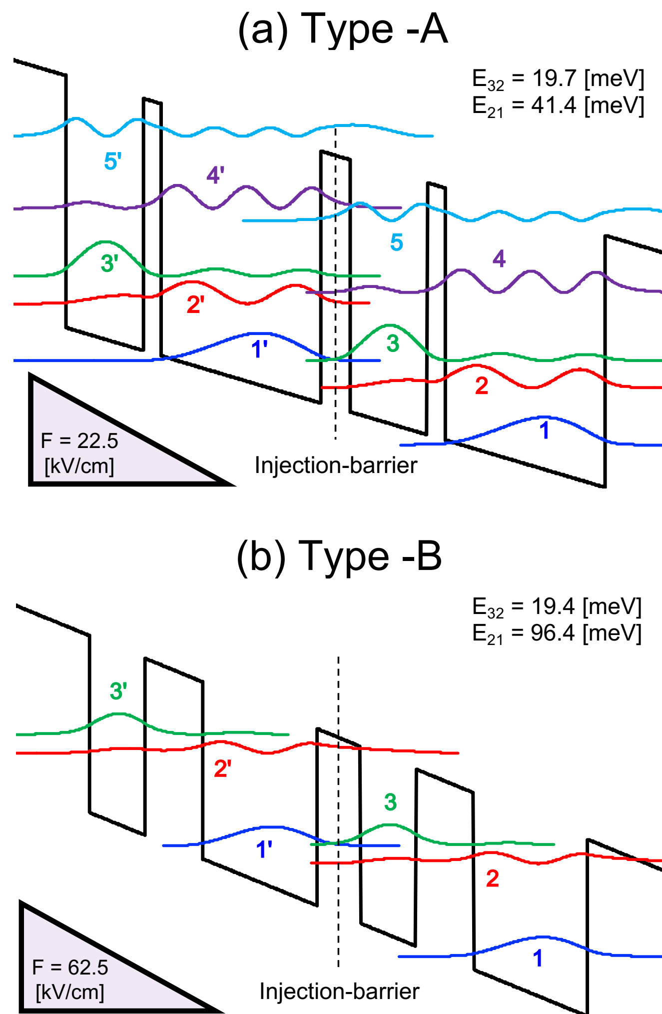

Figure. 5.15 Band diagrams of two types of devices. (20% of Al-composition under tight-binding condition.) (a) Type-A: 28/73.5/17.5/153 in Å (b) Type-B: 29/37.5/39.5/77.5 (**Bold** = barrier, underline = doping.).

A conventional design concept, Type-A, is featured so that the energy difference between LLS and an injection state E_{21} corresponds to the LO-phonon vibration energy of materials (In GaAs, 36.7meV) to efficiently abstract carriers from LLS by fast LO-phonon scattering. The subband number is often more than four, and the main three subbands, which are necessary for carrier transport, are located in rather deep energy level of quantum wells. Because wavefunction spreading is not remarkable compared to Type-B, wavefunctions need to be gotten close for high oscillator strength. Therefore, a radiation-barrier thickness needs to be thin enough, around 20Å.

On the other hand, Type-B is featured by a thick radiation-barrier around 40Å. The lasing states are designed to be high energy close to continuums, and E_{21} varys flexibly to realize such alignment conditions. So, spreading wavefunction also require thick radiation-barrier to balance non-radiative carrier transition rate and oscillator strength. The reason why Type-B appears up to 20% of Al-composition would be because the maximum of E_{21} is set at 100meV in a screening condition. If larger E_{21} is allowed, Type-B could be observed in higher barrier conditions, as well. Some merits are considered in Type-B. In Type-B devices composed of purely three subbands, horizontal leakage current does not happen due to absence of parasite states [175]. Furthermore, LLS is located near the continuums, so carriers in LLS may be abstracted not only by LO-phonon scattering but also thermal excitation into continuums. These features are summarized in Table 5.2.

Parameters	Type -A	Type -B
Al-composition x_{Al}	15 ~ 45% (High barrier condition)	5 ~ 20% (Low barrier condition)
Subband number N_{level}	≧4	3
Radiation barrier thickness $L_{rad.}$	≈ 20Å	≈ 40Å
Energy difference between LLS and injection state E_{21}	≈ E^{LO}	Vary
Alignment field F_{align}	~ 20kV/cm	Vary
Lasing state energy	Deep (Low energy)	Shallow (high energy)

Table. 5.2 Features of device design concepts type -A and -B.

5.3.3 High-Performance Device Design

Based on the calculation results in the structure exploration, design parameters for high-performance devises are investigated. Optical gain of explored devises in Figure 5.14 is plotted to lasing frequency in Figure 5.16. From Figure 5.16, when Al-composition is higher than 10%, high optical gain is found to be obtained over a wide range of lasing frequency. Lasing frequency of some explored devices are higher or lower than the screening condition 1~5THz. During the structure exploration, band-bending effect is not considered. On the other hand, when optical gain is calculated, band-bending effect is considered and affect the energy corresponding to lasing frequency. Very high optical gain also appears around 4~5THz. Under 10% of Al-composition, the number of device structures satisfying screening conditions decreases, the lasing frequency range also concomitantly becomes narrow. This means that the freedom of device design is small in low barrier conditions.

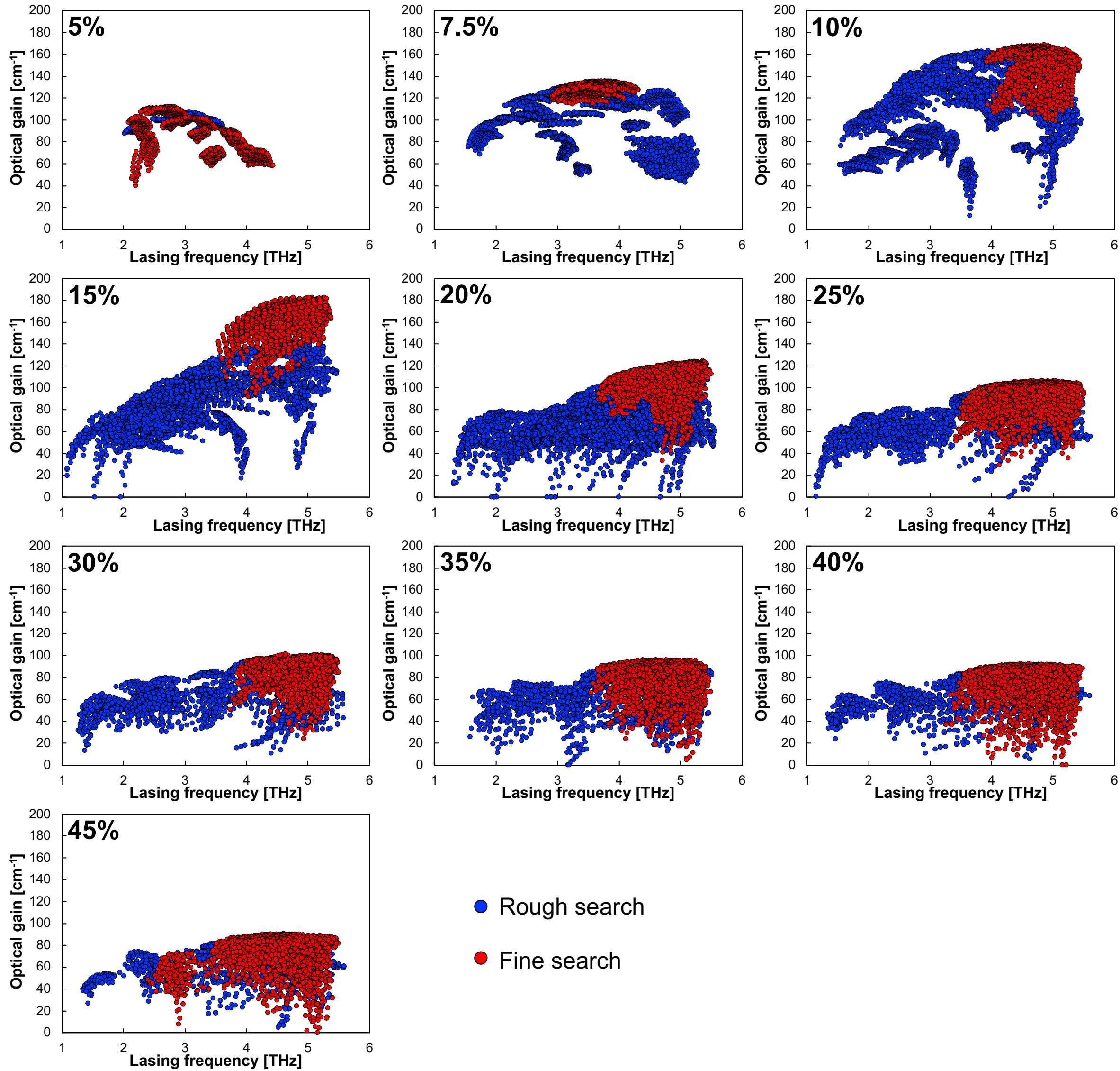

Figure. 5.16 A relation between optical gain and lasing frequency in explored devices.

Next, device parameter ranges of high-performance devices are analyzed in Figure 5.17. High-performance devices here are defined as the ones whose optical gain is higher than 90% of the maximum for each Al-composition. The data for Type-A is plotted to high Al-composition higher than 20% in green, and the data for Type-B is plotted to low Al-composition in pink.

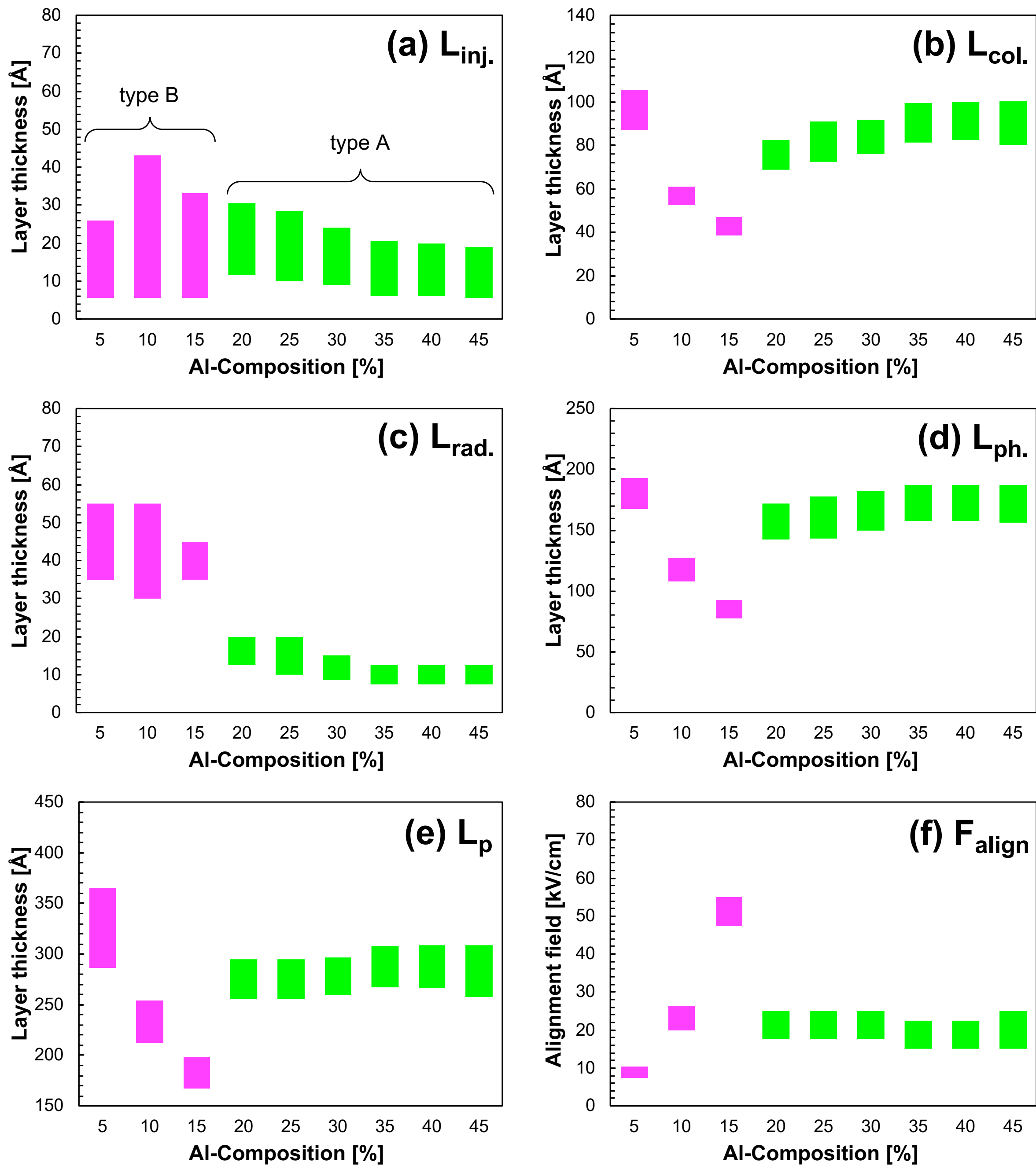

Figure. 5.17 The Al-composition dependence of design parameters. (a) Injection-barrier, (b) collection-well, (c) radiation-barrier, (d) phonon-well, (e) one period length, and (f) alignment field.

These data do not describe precise characteristics of each device but provide statistical tendencies of design parameters to Al-composition. First, Type-A devices are analyzed. In Type-A devices, it is observed that when Al-composition increases, injection-barrier and radiation-barrier thicknesses decrease, and collection-well and phonon-well thicknesses increase. As shown in Chapter 4, when barriers of quantum wells become high, wavefunction gets compressed inside wells, and tunneling rate and oscillator strength, determined by the interference between two subbands, become small. Therefore, the behavior of high-performance devices seen in Figure 5.17 is interpreted as the interference between subbands are maintained even when barriers become high by narrowing barrier thicknesses to get wavefunctions closer and by widening well thicknesses to mitigate wavefunction compression. Due to this behavior, the length of one period does not change and is kept from 260 to 290Å, and corresponding electrical field is also fixed at around 20kV/cm.

Type-B devices show different behavior from Type-A devices. In Type-B devices, injection-barrier thicknesses distribute over a little wider range than the ones of Type-A devices, and radiation-barrier thicknesses is larger than Type-A. However, both types of barrier thicknesses do not show the dependence of Al-composition. On the other hand, collection-well and phonon-well thicknesses become thinner with increase of Al-composition, resulting in decrease of one period length. Because of a relation established at alignment conditions shown in Equation (5.3), a corresponding alignment field also increases. ($F_{align}L_p = E_{32} + E_{21} = const.$)

5.3.4 Full Model Analysis

High-performance devices obtained in the device structure exploration are analyzed by using Rate equation – Full model. This analysis investigates the influence of barrier height on optical gain, electrical current density, and population fraction. Furthermore, the componential parameters which are necessary for calculating optical gain or electrical current density are also analyzed by the same way to clarify the mechanisms of the influence by barrier height on device characteristics.

In the structure exploration, a screening condition about injection-barrier thickness $5 \leq L_{inj.} \leq 60$ [Å] is applied. As a result, all high-performance devices found in the range of injection-barrier thickness narrower than 30Å. The rate equation model developed in Chapter 2 adopts only coherent tunneling transport theory for inter-module carrier transition, and the calculation accuracy can degrade with such thin injection-barrier thicknesses because incoherent carrier transition can be significant under thin injection-barrier conditions. So, in this work, high-performance devices are selected from different conditions: thin injection-barrier condition (an original screening condition) and thick injection-barrier condition $L_{inj.} \gtrsim 30$ [Å] and analyzed by Full model in 5.3.4.1 and 5.3.4.2, respectively.

5.3.4.1 Thin injection-barrier devices

Thin injection-barrier devices found in the structure exploration under an original screening condition ($5 \leq L_{inj.} \leq 60\ [\text{Å}]$) are analyzed in this section. The device structures and parts of calculation data are listed in Table 5.3. Al-composition and alignment field in design are described as x_{Al} and F_{align}^{design} (Alignment field is not estimated in Limited model.) In Full model, alignment field and lasing frequency are described as F_{align}^{full} and f_{32}^{full}, respectively. Calculation results of other device parameters are also abstracted at gain peak conditions.

The dependence of design parameters on Al-composition described in the previous section is also confirmed in Table 5.3, as well. In Type-A devices, barrier thicknesses decrease, and well thicknesses increase with increase of Al-composition. However, those design parameters stay almost constant when Al-composition is higher than 35%. This would be because wavefunction does not compress anymore in high barrier conditions, so parameters also do not change. Type-B devices also show similar tendency as the previous section. Radiation-barrier thicknesses are around 40Å, injection-barrier thicknesses change indifferent to Al-composition, and well thicknesses decrease with Al-composition. E_{21}, the energy determining carrier abstraction rate from LLS, increases from 22.9meV to 95.5meV along with barrier height.

x_{Al} [%]	Type	Device structure [Å] $\boldsymbol{L_{inj.}}/L_{col.}/\boldsymbol{L_{rad.}}/L_{ph.}$ **Bold** = barrier, Underline = doped	L_p [Å]	N_{level}	F_{align}^{design} [kV/cm]	F_{align}^{full} [kV/cm]	f_{32}^{full} [THz]	E_{21}^{full} [meV]
5	B	**6.0** / 94.5 / **45.5** / <u>181.5</u>	327.5	3	9.5	11.0	2.86	22.9
7.5		**20.0** / 72.5 / **38.5** / <u>148.0</u>	279.0	3	16.5	18.5	3.96	33.1
10		**8.5** / 57.5 / **38.5** / <u>117.5</u>	222.0	3	29.5	32.0	5.12	47.5
15		**12.0** / 44.0 / **38.5** / <u>89.5</u>	184.0	3	50.5	56.5	5.98	72.3
20		**26.0** / 37.5 / **38.5** / <u>77.5</u>	179.5	3	64.5	74.5	6.26	95.5
15	A	**27.5** / 67.0 / **25.0** / <u>135.0</u>	254.5	4	25.0	27.0	4.85	46.4
20		**20.0** / 76.0 / **15.5** / <u>157.0</u>	268.5	5	22.5	24.5	5.52	40.8
25		**19.0** / 82.0 / **13.5** / <u>164.0</u>	278.5	6	20.5	22.5	5.01	39.8
30		**16.5** / 84.5 / **12.5** / <u>164.5</u>	278.0	6	20.5	22.5	4.81	40.5
35		**13.0** / 86.5 / **10.5** / <u>167.5</u>	278.0	7	20.5	22.0	4.84	39.9
40		**13.0** / 87.0 / **10.5** / <u>167.5</u>	278.0	8	20.5	22.5	4.79	40.8
45		**11.5** / 88.0 / **10.0** / <u>169.5</u>	279.0	8	20.0	22.0	4.78	39.6

Table. 5.3 Device structures of high-performance THz-QCLs with a thin injection-barrier.

Optical gain of thin injection-barrier devices, calculated by Limited and Full models, is plotted to Al-composition in Figure 5.18, and the calculation results by Limited model and the ones by Full model show large difference. In Type-A, optical gain calculated by Full model is around 30~40% of the ones by Limited model. On the other hand, calculation results by Full model are around 60~70% of the ones by Limited model even though the difference is small only at 20% of Al-composition. Instead of such numerical difference, the dependence of optical gain on Al-composition is very similar between Limited and Full models, and the optimal Al-composition is 15% in Full model calculation, as well. The calculation in Figure 5.18 is implemented at 250K of heat-sink temperature, so optical gain is expected to decrease further at 300K. Therefore, it is expected that devices that can operate at room-temperature are difficult to design at Al-conditions higher than 20%.

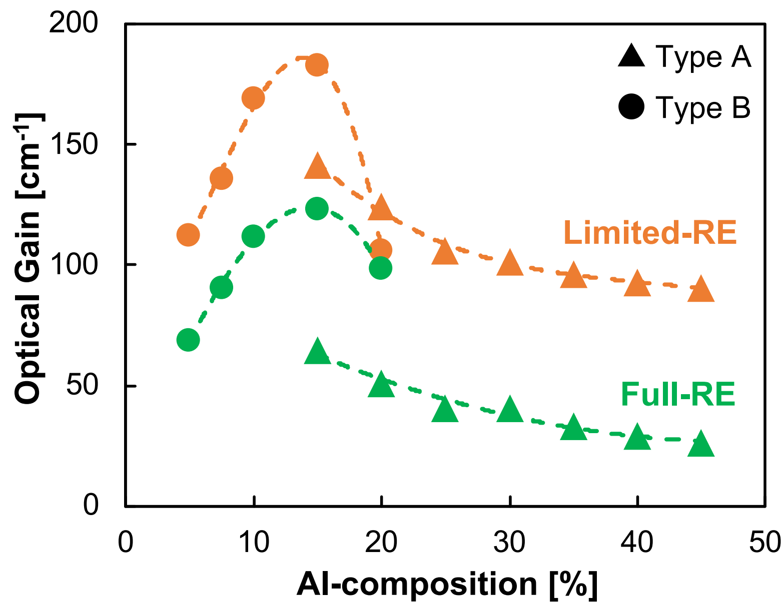

Figure. 5.18 The Al-composition dependence of optical gain maxima.

Current density at gain peak conditions is plotted to Al-composition in Figure 5.19. Large difference in total current is observed between Type-A and Type-B devices. On the one hand, in Type-A devices, tunneling and leakage current decrease gradually with increase of Al-composition, and total current greatly increases due to leakage current at low Al-composition. Tunneling current is rather large and solely occupy around 10kA/cm^2. This would be attributed to thin injection-barriers (= large coupling strength). On the other hand, in Type-B devices, tunneling and leakage current are further larger, and the dependence of these parameters on Al-composition is also different from the ones on Type-A devices. Further thinner injection-barrier thicknesses of Type-B devices (Table 5.3) would be attributed to larger tunneling current. Usually, leakage current is expected to decrease with high barriers like as Type-A devices. Contrary to our prediction, leakage current of Type-B devices increases with Al-composition.

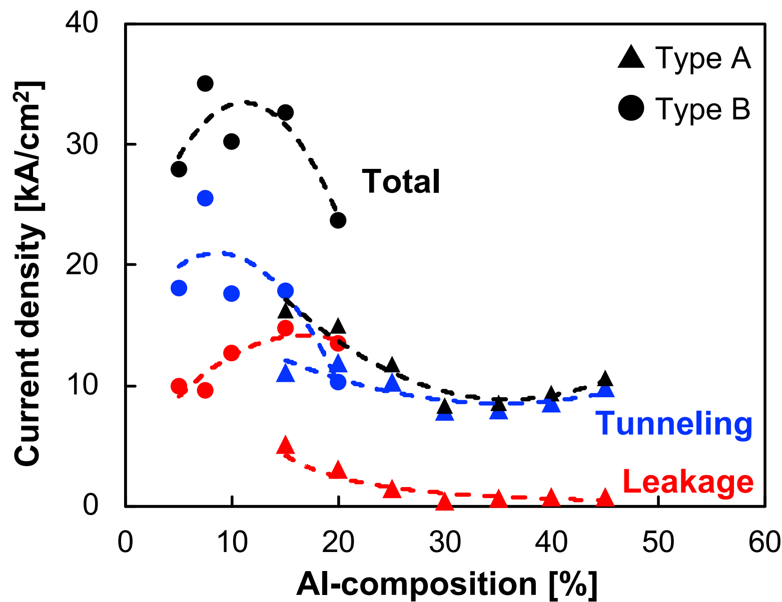

Figure. 5.19 The Al-composition dependence of electrical current at gain peak conditions.

The Al-composition dependence of population fraction is show in Figure 5.20, and this result is important to analyze other parameters. First, in Type-A devices, population fraction of the main three subbands are almost independent of Al-composition. On the other hand, leakage component decreases with increase of Al-composition, and this change is reflected in electrical current density in Figure 5.19. Even though population fraction of parasite states increases with Al-composition, this change does not show tunneling current. Over a whole Al-composition, the sum of leakage and parasite components in Type-A devices is almost constant, and it occupies about 25% of the total population. In Type-B devices, due to increased leakage population occupies about 55%, the population fraction of the main three states also decreases. However, the difference population inversion in Type-A and -B devices does not vary so remarkably depending on Al-composition.

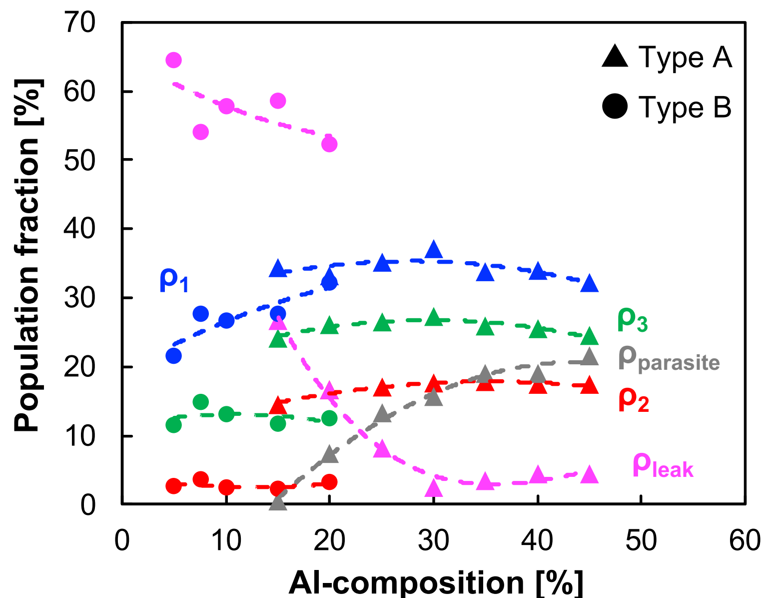

Figure. 5.20 The Al-composition dependence of population fraction at gain peak conditions. $\rho_{parasite} = \rho_4 + \rho_5 + \rho_6 + \cdots$.

Componential parameters of optical gain, current density, and population inversion respectively described in Figures 5.18, 19, and 20 are calculated and the dependence of these parameters on Al-composition are described in Figure 5.21 to analyze the mechanisms of quantum well barrier height on device characteristics.

First, the influence of Al-composition on optical gain is analyzed. In conclusion, the dependence of optical gain on Al-composition is determined by all componential parameters of it: oscillator strength, population inversion, and optical linewidth. Oscillator strength varys uniquely in Type-A and Type-B devices individually as shown in Figure 5.21(a). On the one hand, oscillator strength of Type-B devices is optimized at 15% of Al-composition, resulting in the maximum of optical gain at this condition. Even though such behavior of oscillator strength is difficult to understand qualitatively, this feature is interpreted due to complicated change of wavefunctions calculated by Schrödinger equation. On the other hand, decrease of oscillator strength in high barrier conditions, similar to the results seen in Chapter 4, is thought to be because of wavefunction compression by high barrier.

Second, the gradual decrease of population inversion described in Figure5.21(b), from about 10% in the low barrier conditions to 7% at 45%, is understood from the calculation results of carrier transition rate related to lasing subbands shown in (d)~(f). In the low barrier conditions, the carrier injection rate to ULS is rather high ($U_{1'3} = 2.4\times10^{12}$ [1/s]), and non-radiative transition rate between ULS and LLS is small ($W_{32} = 8.0\times10^{11}$ [1/s]). Therefore, population fraction of ULS and population inversion become rather higher. W_{21}, determinative to carrier abstraction rate from LLS, is not related to the dependence of Al-composition. In barrier height study, the influence of interface-roughness scattering is often

focused, and interface-roughness scattering rate indeed increases with increase of Al-composition in this work. However, under 250K of heat-sink temperature, which is high enough, LO-phonon scattering rate dominantly determines non-radiative scattering rate W_{32} and carrier abstraction rate W_{21}. So, interface-roughness scattering is not influential.

Third, smooth increase of optical linewidth to Al-composition is observed to be attributed to different causes between Type-A and Type-B devices as shown in Figure 5.21(c). On the one hand, optical linewidth broadening in the low barrier conditions of Type-B devices is attributed to interface-roughness scattering. On the other hand, LO-phonon scattering is the main factor in optical linewidth in the high barrier conditions of Type-A devices. In Type-A devices, the influence of interface-roughness scattering is observed, but not so influential. In theory, optical gain is proportional to oscillator strength and population inversion, and inversely proportional to optical linewidth. Therefore, the change of these componential parameters to Al-composition results in the optical gain characteristics described in Figure 5.18.

Lastly, the influence of barrier height on current density is analyzed separating tunneling and leakage currents individually. As described in Chapter 2, the determinative factors of tunneling current are a tunneling rate between aligned subbands $U_{1'3}$ and population fraction difference of them $\rho_{1'} - \rho_3$. As described in Figure 5.21(b), tunneling rate $U_{1'3}$ decreases with increase of Al-composition, and the difference in population fraction between subbands $|1'\rangle$ and $|3\rangle$ of Type-B devices is rather larger than the ones of Type-A devices. These characteristics are reflected in tunneling current in Figure 5.19. The decrease of leakage current to barrier height in Type-A devices is qualitatively understandable.

In Type-B devices, however, increase of leakage current with high barriers needs thinking of details of theories for analysis. Leakage current in this simulation is defined as a three-dimensional drift current which is determined not only by carrier density but also by drift velocity proportional to electrical field [321]. As described in Table 5.3, alignment field of Type-B devices increases with Al-composition. Therefore, drift velocity also increases, resulting in leakage current increase with Al-composition.

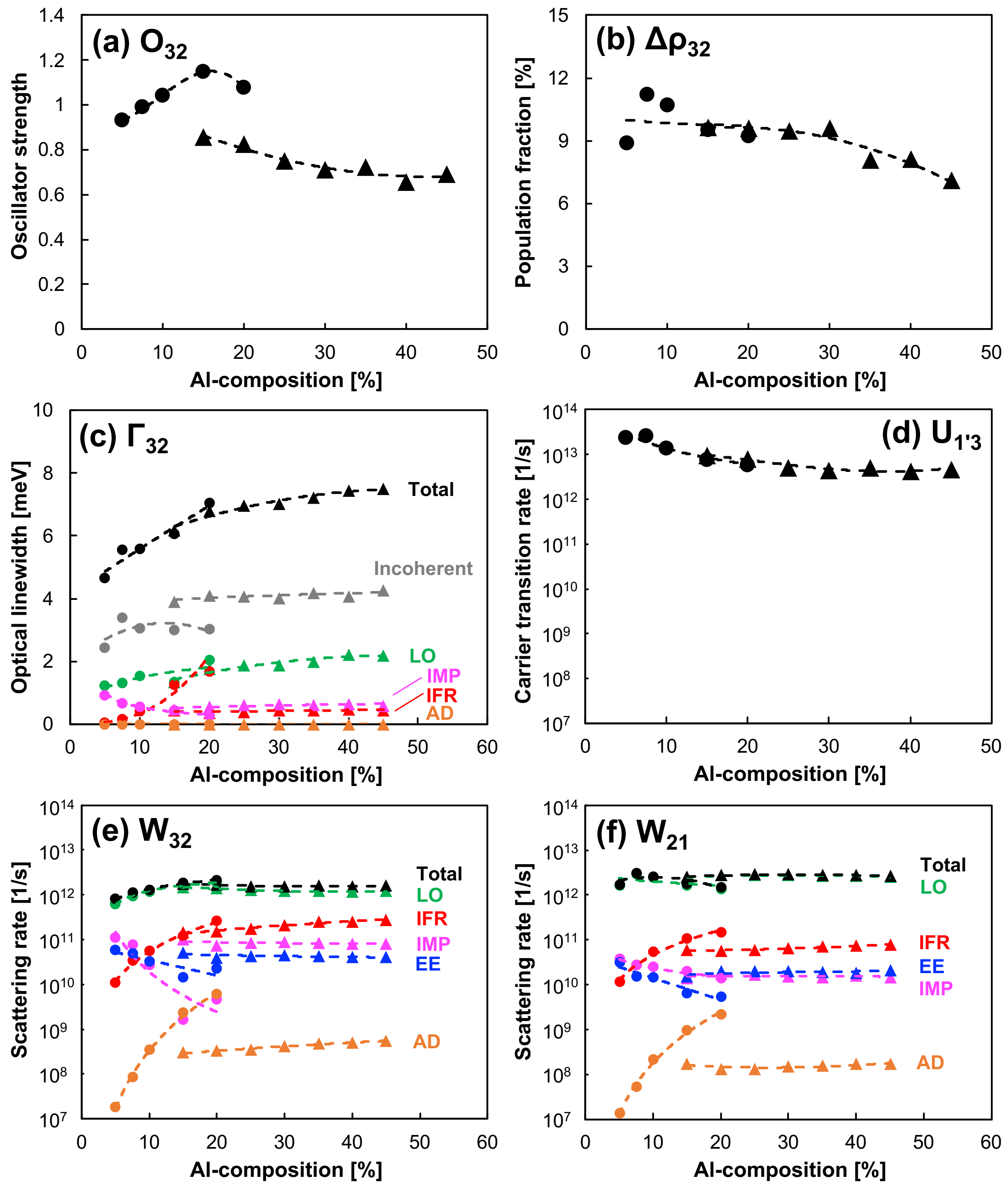

Figure. 5.21 The Al-composition dependence of componential parameters of thin injection-barrier devices at gain peak conditions. (▲= Type-A, ● = Type-B) (a) Oscillator strength, (b) population inversion, (c) optical linewidth, (d) carrier injection rate to ULS, (e) non-radiative scattering rate between lasing states, and (f) carrier extraction rate from LLS.

5.3.4.2 Thick injection-barrier devices

Subsequently, thick injection-barrier devices found under another screening condition ($L_{inj.} \gtrsim 30\ [\text{Å}]$) are explored, and the data of high-performance devices are listed in Table 5.4. Device characteristics observed in thin injection-barrier devices are found in Table 5.4, as well, with some difference. As for Type-A devices, layer thicknesses and a length of one period are not very different from the ones of thin injection-barrier devices in the low barrier conditions of 15~25% of Al-composition. However, radiation-barrier thicknesses become thicker, and collection-well and phonon-well thicknesses become thinner in the high barrier devices. Due to this change, the length of one period becomes longer and corresponding alignment fields also become larger. On the other hand, design parameters of Type-B devices are almost similar to the ones of Type-A devices except for injection-barrier thicknesses.

Optical gain for thick injection-barrier devices is calculated by Rate equation – Full model and described in Figure 5.22 with the results of Limited model. In thick injection-barrier devices, the Al-composition dependence of optical gain has similar tendency to the ones of thin injection-barrier devices. The optimized Al-composition is also around 15%. On the other hand, the calculation results by Limited model show drop of gain in high Al-composition. This drop is considered to reflect decrease of oscillator strength and population inversion shown in Figure 5.25 (a) and (b), respectively.

x_{Al} [%]	Type	Device structure [Å] $\boldsymbol{L_{inj.}}/L_{col.}/\boldsymbol{L_{rad.}}/L_{ph.}$ **Bold** = barrier, Underline = doped	L_p [Å]	N_{level}	F_{align}^{design} [kV/cm]	F_{align}^{full} [kV/cm]	f_{32}^{full} [THz]	E_{21}^{full} [meV]
5	B	**29.5** / 100.5 / **46.5** / 192.5	369.0	3	7.5	10.5	2.93	21.8
7.5	B	**28.5** / 69.0 / **40.5** / 145.5	283.5	3	16.5	18.5	3.96	33.8
10	B	**28.0** / 53.5 / **41.5** / 113.5	236.5	3	27.5	30.0	4.66	48.9
15	B	**28.0** / 41.0 / **40.5** / 86.0	195.5	3	47.5	52.5	5.37	74.4
20	B	**29.0** / 37.5 / **39.5** / 77.5	183.5	3	62.5	72.0	6.04	95.9
15	A	**28.0** / 66.5 / **25.0** / 136.0	255.5	4	25.0	27.0	4.92	46.4
20	A	**28.0** / 73.5 / **17.5** / 153.0	272.0	5	22.5	24.0	5.24	42.0
25	A	**28.0** / 78.0 / **16.5** / 155.0	277.5	6	21.5	23.5	4.71	43.4
30	A	**28.0** / 82.5 / **15.0** / 160.0	285.5	6	20.0	21.5	4.20	42.3
35	A	**28.0** / 75.5 / **15.0** / 147.5	266.0	6	25.0	26.5	4.66	49.8
40	A	**28.0** / 69.0 / **15.0** / 139.0	251.0	6	30.0	31.5	5.25	56.1
45	A	**28.0** / 69.0 / **15.0** / 139.0	251.0	6	30.0	31.5	5.17	56.4

Table. 5.4 Device structures of high-performance THz-QCLs composed of thick injection-barrier.

In electrical current density, tunneling current density greatly decreases compared to thin injection-barrier devices. This would be because thick injection-barriers lower coupling strength between aligned subbands, and carrier injection rate to ULS also decreases as shown in Figure 5.25(d). In terms of leakage current, no significant difference is seen between thick and thin injection-barrier devices.

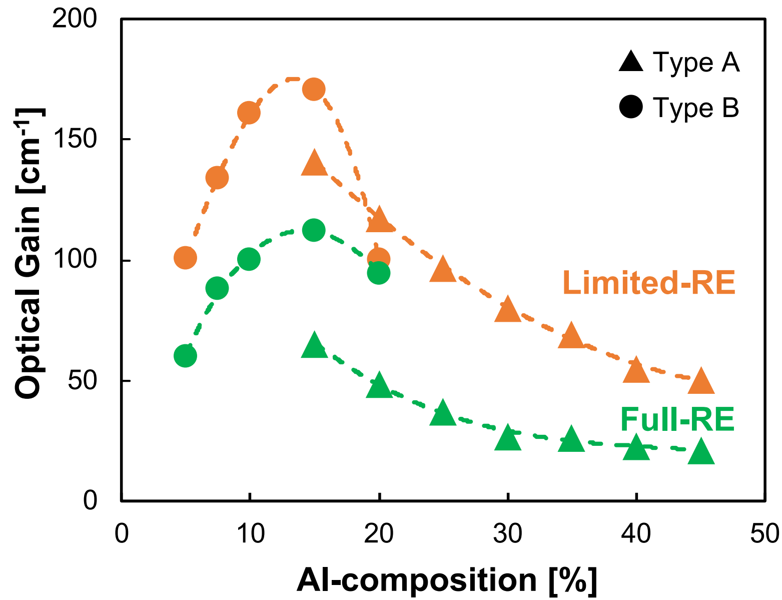

Figure. 5.22 The Al-composition dependence of optical gain maxima.

In population fraction calculation, an intriguing feature is observed. Population fractions of Type-B devices are almost same as the ones of thin injection-barrier devices, but the one of a ground state in Type-A devices increases with Al-composition instead of small population in parasite states. This phenomenon is interpreted with tunneling current in Figure 5.22 as that thick injection-barriers squeeze coherent carrier transport in injection-barriers, and electrons accumulate in a ground state.

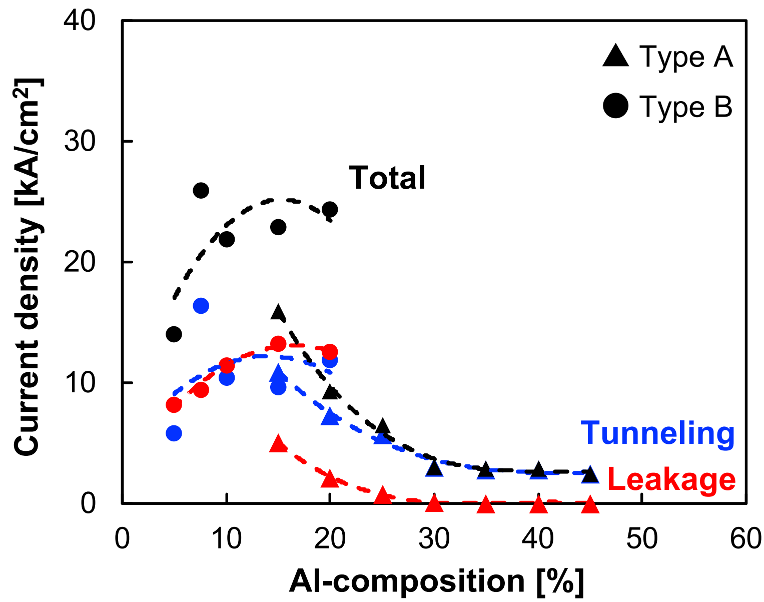

Figure. 5.23 The Al-composition dependence of electrical current at gain peak conditions calculated by the rate equation – full model.

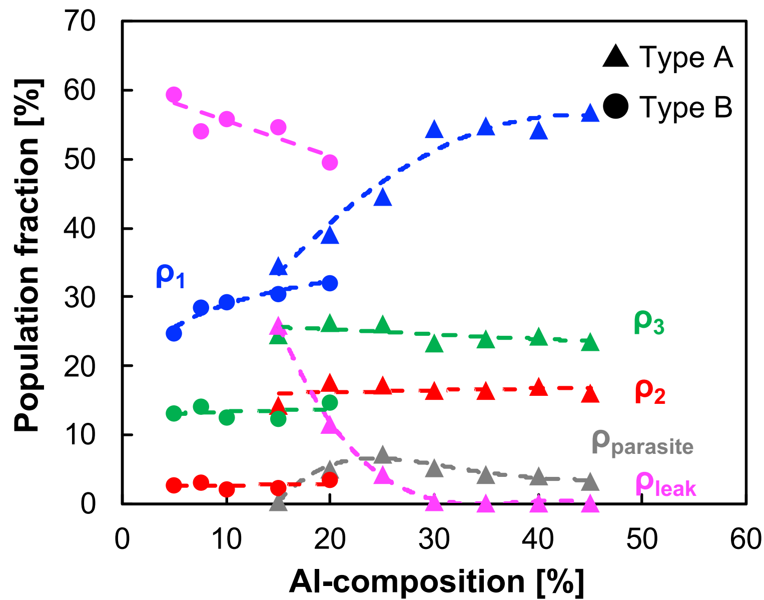

Figure. 5.24 The Al-composition dependence of population fraction at gain peak conditions. $\rho_{parasite} = \rho_4 + \rho_5 + \rho_6 + \cdots$.

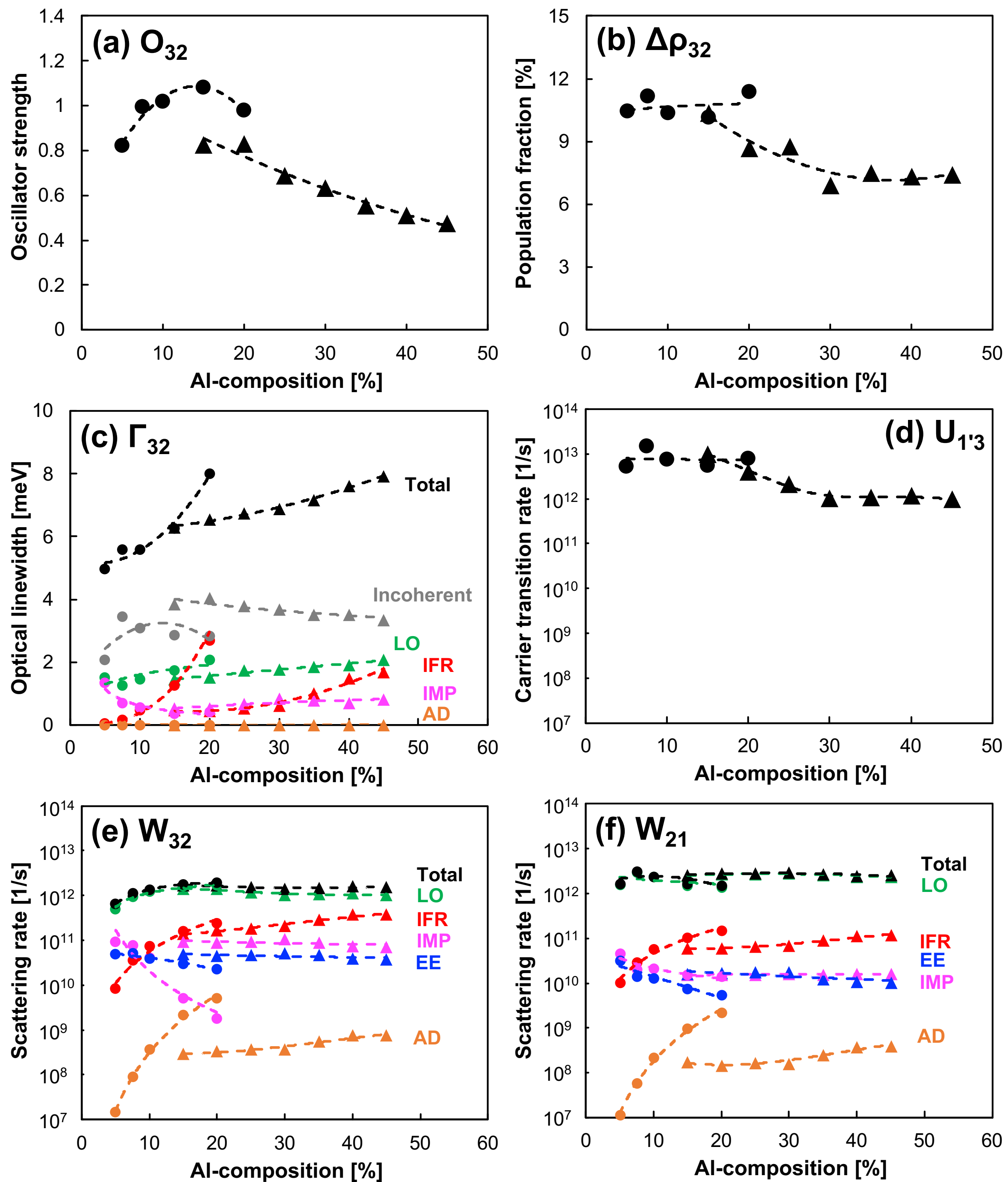

Figure. 5.25 The Al-composition dependence of componential parameters of thick injection-barrier devices at gain peak conditions. (▲ = Type-A, ● = Type-B) (a) Oscillator strength, (b) population inversion, (c) optical linewidth, (d) carrier injection rate to ULS, (e) non-radiative scattering rate between lasing states, and (f) carrier extraction rate from LLS.

5.4 Summary and Conclusion

Expansive barrier height study of two-well resonant-phonon THz QCLs is implemented by introducing flexible device design in this work. The explored device structures are limited as the simplest ones composed of GaAs-wells and $Al_xGa_{1-x}As$-barriers (of only one Al-composition), and the influence of Al-composition on optical gain is investigated. The devices are explored in certain ranges of alignment field, collection-well thickness, radiation-barrier thickness, and phonon-well thickness: $10 \leq F_{align} \leq 70 \left[\frac{\mathrm{kV}}{\mathrm{cm}}\right]$、$30 \leq L_{col.} \leq 130$ [Å]、$10 \leq L_{rad} \leq 60$ [Å]、$80 \leq L_{ph.} \leq 220$ [Å], and optical gain for applicant devices are calculated by Rate equation – Limited model. Form the results of the structure exploration and optical gain calculation, the optimal Al-composition for two-well resonant-phonon devices is turned out to be around 15%. At 15% of Al-composition, high optical gain is obtained over a wide range of alignment field and radiation-barrier thickness, and structure tolerance – allowable range of design parameters against errors between design and actual driving conditions – also becomes the largest among all Al-composition. Furthermore, two types of design concepts are discovered from optical gain maps: Type-A featured by thin radiation-barrier thickness and Type-B featured by thick radiation-barrier thickness. Higher-performance devices are anticipated to design by adopting the Type-B concept. In the future, this concept needs to be confirmed in experiment.

What were once only hopes for the future have now come to pass.

– Queen Elizabeth II

Chapter 6 Conclusion and Future Work

6.1 Conclusion

This work investigates and abstracts the issues of THz QCL development from previous research as described in Chapter 1 and theoretically approaches to these issues for solution in Chapter 2 to 5. In the theoretical research of this work, a device simulator based on the rate equation is developed, and the influence of design parameters (impurity doping and barrier height) on device performance of two-well resonant-phonon THz QCLs is clarified by simulation. New design guidelines or concepts are also proposed.

In Chapter 2, a device simulator is developed based on the rate equation. The simulator bases a previous calculation method proposed by Razavipour and is modified for improvement of the calculation accuracy and speed. First, this study applies the discretized Fourier transform (DFT) to speed up the calculation of electron-electron scattering rate and improves the calculation time by three orders without impairing accuracy. Next, the calculation accuracy is improved by adding new models of some physical phenomena. A screening effect model, which is necessary for the Coulomb scattering rate calculation, is also carefully selected. In addition, the developed simulator also includes optical linewidth and pure dephasing time models based on Ando's theory and the third-order tunneling current theory to describe bound-to-continuum carrier leakage.

In Chapter 3, the influence of impurity doping on GaAs-based two-well resonant-

phonon terahertz quantum cascade lasers is investigated theoretically, and efficient doping schemes are discussed. By using the rate equation model, the impacts of dopant amount, position, and distribution on the performance of a high-performance device is simulated focusing on a single module. The calculated optical gain is found to have a peak over the range of sheet doping density from 1.0×10^{10} to 1.0×10^{12} cm^{-2} in all eight doping conditions examined in this work. Among these patterns, the devices with the undoped condition and homogeneous-doping in phonon-wells mark high optical gain, and the latter is also resistant against the detuning of subband alignment due to band-bending under the high doping conditions. Furthermore, based on the simulation results, a modulation doping scheme whose active cores include both doped and undoped modules is suggested and discussed.

In Chapter 4, the influence of barrier height is theoretically investigated through the third-order tunneling current theory. Three types of GaAs/AlGaAs-based two-well resonant-phonon THz QCLs published in the past, are simulated by the device simulator, and the dependence of bound-to-continuum carrier leakage on barrier height is clarified. Furthermore, based on the latest high-performance device, the influence of barrier height is investigated by changing the Al-composition from 12.5% to 45% with a fixed-layer thickness. As a result, it turns out that there are carrier dynamics that diminish the carrier density of lasing subbands in both high and low barrier conditions. On the one hand, carrier leakage into continuum states increases drastically below 25% Al-composition. On the other hand, in high barrier conditions, quite a few carriers accumulate in the ground state due to a strong confinement effect in addition to oscillator strength lowering.

In Chapter 5, more inclusive computation work theoretically determines the optimal barrier height for two-well resonant-phonon THz QCLs. This work clarifies that there are two types of device design concepts for one barrier height condition: Type-A concept, a conventional design, uses deep subbands for lasing, and Type-B, found in this work, uses shallow subbands. In both cases, optical gain is found to peak around 15% of Al-composition as a result of layer thickness and alignment field tuning. Furthermore, the design tolerance which allows error in optical gain between ideal design and actual device conditions also wide when the Al-composition is close to 15%.

6.2 Future Works

The current research goal of THz QCL research is to achieve room-temperature operation and is expected to shift to high output power and wide-frequency radiation after the first goal. To achieve the above goals, it is meaningful to clarify the impact of design parameters on device characteristics, so this work investigates the optimal conditions of impurity doping and barrier height for two-well resonant-phonon THz QCLs. Even though the optimal design conditions can vary depending on carrier transport methods, the information and device design guidelines which come from simple structures such as two-well resonant-phonon structure are considered to be essential in physics and appliable for more complicated structure design. As for two-well resonant-phonon THz QCLs, the influence of structural complexity described in Figure 5.2 has yet been investigated in this work and is expected to be studied in the future by the methods like shown in Chapter 5. The

experimental verification of the proposals obtained in this work is also necessary.

In terms of carrier transport method except for two-well resonant-phonon devices, three-level carrier transports such as resonant-phonon and scattering assisted methods should be investigated for feasibility within single quantum well structures because optical gain is inversely proportional to the one-module length as described in Equation (2.99). As described in Chapter 3, more modules can be stacked in a 10μm-active core when one module is short, so higher optical gain is expected in theory. With conventional doping method, however, the net doping density of an active core increases, which would require optimization in modulation doping. (The idea of modulation doping originally comes from the design of single-well resonant-phonon structure.)

When we go back to the research by Bosco *et al.*, a two-level carrier transport can also be a research topic because the theoretical minimum number of subbands for carrier transport is two. This carrier transport method does not use resonant-tunneling which has been traditionally used for THz QCLs with no exception, instead use only carrier scattering for optical transition and carrier abstraction from LLS (Non-resonant-tunneling THz QCL). Although the author is rather skeptical about the feasibility of this carrier transport, the idea about device structures of two-level carrier transport will be explained below.

Carrier transport by two subbands provides two device structures composed of single quantum well depending on the role of a ground state as depicted in Figure 6.1. In both device structures, the LO-phonon scattering works to abstract carriers from LLS and to inject to ULS, but the author predicts that the feasible method is the one shown in Figure 6.1(a), where a ground state works as ULS, and optical transition happens between a ground state

and a first excited state in an adjacent module. (Carrier injection and radiation happen ove a barrier.) Due to a fact that one module length is determined based on LO-phonon scattering rate, short length of modules could be realized despite higher alignment field.

On the other hand, the device structure described in Figure 6.1(b) is disadvantageous for building population inversion because a ground state, where carriers are more likely to accumulate, is used for LLS. It would also be challenging to get a ground and first excited states in a module close to around 4.5~20.5meV (corresponding to lasing at 1~5THz). To realize such situation, a one module length needs to be very large, and increase of parasite states would lower the carrier use efficiency or unable carrier transport itself.

In both single-well structures, tuning wavefunction spreading and subband energy needs structural complexities such as a step-well structure as well as only one barrier.

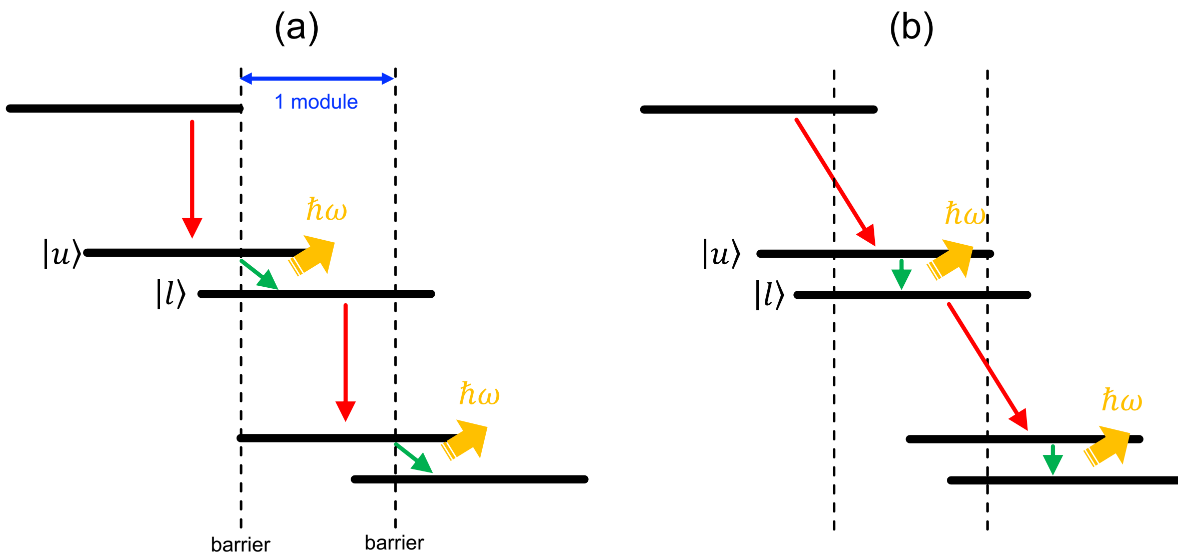

Figure. 6.1 Ideas of carrier transport by two subbands. (a) a ground state is used as ULS, and (b) a ground state is used as LLS.

Reference

[1] ‘WHITE PAPER Information and Communication in Japan Heisei 4-nen’, Ministry of Internal Affairs and Communications, Japan (1992).

[2] ‘WHITE PAPER Information and Communication in Japan 2021’, Ministry of Internal Affairs and Communications, Japan (2021).

[3] Carter M. Armstrong, ‘The Truth About Terahertz’, IEEE Spectrum **49**, 9 (2012).

[4] Peter H. Siegel, ‘Terahertz Technology’ IEEE Transactions on Microwave Theory and Techniques, **50**, 3 (2002)

[5] Masayoshi Tonouchi, ‘Cutting-edge terahertz technology’ Nature Photonics **1**, 97 (2007).

[6] Bradley Ferguson, and Xi-Chen Zhang, ‘Materials for terahertz science and technology’ Nature Materials, **1**, 26 (2002).

[7] Tadao Nagatsuma, ‘Terahertz technologies: present and future’ IEICE Electronics Express, **8**, 14, 1127-1142 (2011).

[8] John F Federici, Brian Schulkin, Feng Huang, Dale Gary, Robert Barat, Filipe Oliveira, and David Zimdars, ‘THz imaging and sensing for security applications – explosives, weapons and drugs’ Semiconductor Science and Technology **20**, S266 (2005).

[9] Gang Chen, Jie Pei, Fei Yang, Xiao Yang Zhou, Z. L. Sun, and Tie Jun Cui, ‘Terahertz-Wave Imaging System Based on Backward Wave Oscillator’ IEEE Transactions on Terahertz Science and Technology **2**, 5 (2012).

[10] Kodo Kawase, ‘Terahertz Imaging For Drug Detection and Large-Scale Integrated Circuit Inspection’ Optics and Photonics News **15**, 10, (2004).

[11] Nicholas Karpowicz, Hua Zhong, Cunlin Zhang, Kuang-I Lin, Jenn-Shyong Hwang, Jingzhou Xu, and X.-C. Zhang, ‘Compact continuous-wave subteraherts system for inspection applications’ Applied Physics Letters **86**, 054105 (2005).

[12] Atsushi Nakanishi, Kazuue Fujita, Kazuki Horita, and Hironori Takahashi, ‘Terahertz imaging with room-temperature terahertz difference-frequency quantum-cascade laser sources’ Optics Express **27**, 3 (2019).

[13] Adrian Dobroiu, Masatsugu Yamashita, Yuichi N. Ohshima, Yasuyuki Morita, Chiko Otaki, and Kodo Kawase, ‘Terahertz imaging system based on a backward-wave oscillator’ Applied Optics **43**, 30 (2004).

[14] Hai Zhang, Stefano Sfarra, Karan Saluja, Jeroen Peeters, Julien Fleuret, Yuxia Duan, Henrique Fernandes, Nicolas Avdelidis, Clemente Ibarra-Castanedo, and Xavier Maldague, ‘Non-destructive

Investigation of Paintings on Canvas by Continuous Wave Terahertz Imaging and Flash Thermography' Journal of Nondestructive Evaluation **36**, 34 (2017).

[15] Hai-Bo Liu, Hua Zhong, Nicholas Karpowicz, Yunqing Chen, and Xi-Cheng Zhang, 'Terahertz Spectroscopy and Imaging for Defense and Security Applications' Proceedings of the IEEE **95**, 8 (2007).

[16] Tetsuro Sasaki, 'Terahertz wave imaging' The Journal of the Institute of Image Information and Television Engineers **67**, 6 (2013).

[17] W. H. Fan, A. Burnett, P. C. Upadhya, J. Cunningham, E. H. Linfield, and A. G. Davies, 'Far-Infrared Spectroscopic Characterization of Explosives for Security Applications Using Broadband Terahertz Time-Domain Spectroscopy' Applied Spectroscopy **61**, 6 (2007).

[18] Hiromichi Hoshina, Yoshiaki Sasaki, Aya Hayashi, Chiko Otani, and Kodo Kawase, 'Noninvasive Mail Inspection System with Terahertz Radiation' Applied Spectroscopy **63**, 1 (2009).

[19] Kodo Kawase, Yuichi Ogawa, Yuuki Watanabe, and Hiroyuki Inoue, 'Non-destructive terahertz imaging of illicit drugs using spectral fingerprints' Optics Express **11**, 20 2549 (2003).

[20] Mikiya Kato, Saroj R. Tripathi, Kosuke Murate, Kazuki Imayama, and Kodo Kawase, 'Non-destructive drug inspection in covering materials using a terahertz spectral imaging system with injection-seeded terahertz parametric generation and detection' Optics Express **24**, 6, 6425 (2016).

[21] Yao-Chun Shen, and Philip F. Taday, 'Development and Application of Terahertz Pulsed Imaging for Nondestructive Inspection of Pharmaceutical Tablet' IEEE Journal of Selected Topics in Quantum Electronics **14**, 2 (2008).

[22] Yuma Takida, Kouji Nawata, and Hiroaki Minamide, 'Security screening system based on terahertz-wave spectroscopic gas detection' Optics Express **29**, 2, 2529 (2021).

[23] Takeshi Ikeda, Akira Matsushita, Michiaki Tatsuno, and Yukio Minami, Mariko Yamaguchi, Kohji Yamamoto, Masahiko Tani, and Masanori Hangyo, 'Investigation of inflammable liquids by terahertz spectroscopy' Applied Physics Letters **87**, 034105 (2005).

[24] Sachiko Nakajima, Hiromichi Hoshina, Masatsugu Yamashita, and Chiko Otani, Norio Miyoshi, 'Terahertz imaging diagnostics of cancer tissues with a chemometrics technique' Applied Physics Letters **90**, 041102 (2007).

[25] Lyubov V. Titova, Ayesheshim K. Ayesheshim, Andrey Golubov, Dawson Fogen, Rocio Rodriguez-Juarez, Frank A. Hegmann, and Olga Kovalchuk, 'Intense THz pulses cause H2AX phosphorylation and activate DNA damage response in human skin tissue' Biomedical Optics Express **4**, 4, 559 (2013).

[26] Young Bin Ji, Seung Jae Oh, Seok-Gu Kang, Jung Heo, Sang-Hoon Kim, Yuna Choi, Seungri Song, Hye Young Son, Se Hoon Kim, Ji Hyun Lee, Seung Joo Haam, Yong Min Huh, Jong Hee Chang, Chulmin Joo, and Jin-Suck Suh, 'Terahertz reflectometry imaging for low and high grade gliomas' Scientific

Reports **6**, 36040 (2016).
[27] Joo-Hiuk Son, Seung Jae Oh, and Hwayeong Cheon, 'Potential clinical applications of terahertz radiation' Journal of Applied Physics 125, 190901 (2019).
[28] Hiromichi Hoshina, Aya Hayashi, Norio Miyoshi, Fumiaki Miyamaru, and Chiko Otani, 'Terahertz pulsed imaging of frozen biological tissues' Applied Physics Letter 94, 123901 (2009).
[29] Seppo Yrjölä, Petri Ahokangas and Marja Matinmikko, 'Evaluation of recent spectrum sharing concepts from business model scalability point of view' IEEE International Symposium on Dynamic Spectrum Access Networks (DySPAN), DOI:10.1109/DySPAN.2015.7343907 (2015).
[30] Ian F. Akyildiz, Josep Miquel Jornet, Chong Hana, 'Terahertz band: Next frontier for wireless communications' Physical Communication **12**, 16 (2014).
[31] [Investigation on wireless communication techniques contributing to efficient use of terahertz waves] Teraherutsuhatai no yuukouriyou ni sisuru musentsuushingijutsu ni kannsuru chousakenntou (in Japanese). Telecom Advanced Technology Research Support Center (2013).
[32] Tadao Nagatsuma, Akifumi Kasamatsu, 'Terahertz Communications for Space Applications' Proceedings of 2018 Asia-Pacific Microwave Conference' DOI:10.23919/APMC.2018.8617598 (2018).
[33] Wikipedia commons, 'Atmospheric electromagnetic opacity'
https://commons.wikimedia.org/wiki/File:Atmospheric_electromagnetic_opacity.svg
[34] Lothar Moeller, John Federici, and Ke Su, 'THz Wireless Communications: 2.5 Gb/s Error-free Transmission at 625 GHz using a Narrow-bandwidth 1mW THz Source' 30th URSI General Assembly and Scientific Symposium (URSI GASS), Istanbul (2011).
[35] X. Pang, S. Jia, O. Ozolins, X. Yu, H. Hu, L. Marcon, P. Guan, F. Da Ros, S. Popov, G. Jacobsen, M. Galili, T. Morioka, D. Zibar, L. K. Oxenløwe, '260 Gbit/s Photonic-Wireless Link in the THz Band' Proceedings IEEE Photonics Conference, Postdeadline paper, DOI: 10.1109/IPCon.2016.7830951 (2016).
[36] Yuji Sakai, Iwao Kawayama, Hidetoshi Nakanishi, and Masayoshi Tonouchi, 'Visualization of GaN surface potential using terahertz emission enhanced by local defects' Scientific Reports **5**, 13860 (2015).
[37] Masatsugu Yamashita, Kodo Kawase, and Chiko Otani, 'Imaging of large-scale integrated circuits using laser terahertz emission microscopy' Optics Express **13**, 1 (2005).
[38] Megnkun Liu, Harold Y. Hwang, Hu Tao, Andrew C. Strikwerda, Kebin Fan, George R. Keiser, Aaron J. Sternbach, Kevin G. West, Salinporn Kittiwatanakul, Jiwei Lu, Stuart A. Wolf, Fiorenzo G. Omenetto, Xin Zhang, Keith A. Nelson, and Richard D. Averitt, 'Terahertz-field-induced insulator-to-metal transition in vanadium dioxide metamaterial' Nature **487**, 345-348 (2012).
[39] Hiromichi Hoshina, Hal Suzuki, Chiko Otani, Masaya Nagai, Keigo Kawase, Akinori Irizawa, and Goro Isoyama, 'Polymer Morphological Change Induced by Terahertz Irradiation' Scientific Reports **6**,

27180 (2016).
[40] Antanas Reklaitis, ‘Terahertz emission from InAs induced by photo-Dember effect: Hydrodynamic analysis and Monte Carlo simulations’ Journal of Applied Physics **108**, 053102 (2010).
[41] Kodo Kawase, Jun-ichi Shikata, and Hiromada Ito, ‘Terahertz wave parametric source’ Journal of Physics D: Applied Physics **35**, R1-R14 (2002).
[42] D. J. Cook, and R. M. Hochstrasser, ‘Intense terahertz pulses by four-wave rectification in air’ Optics Letters **25**, 16 (2000).
[43] Masahiko Tani, Osamu Morikawa, Shuji Matsuura, and Masanori Hangyo, ‘Generation of terahertz radiation by photomixing with dual- and multiple-mode lasers’ Semiconductor Science and Technology 20, S151-S163 (2005).
[44] Hiroshi Ito, Satoshi Kodama, Yoshifumi Muramoto, Tomofumi Furuta, Tadao Nagatsuma, and Tadao Ishibashi, ‘High-Speed and High-Output InP-InGaAs Unitraveling-Carrier Photodiodes’ IEEE Journal of Selected Topics in Quantum Electronics **10**, 4 (2004).
[45] Tadao Ishibashi, Yoshifumi Muramoto, Toshihide Yoshimatsu, and Hiroshi Ito, ‘Unitraveling-Carrier Photodiodes for Terahertz Applications’ IEEE Journal of Selected Topics in Quantum Electronics **20**, 6 (2014).
[46] J. B. Gunn, ’The Gunn Effect’ Solid State Communication **1**, 88 (1963).
[47] F. Amir, C. Mitchell, N. Farrington, and M. Missous, ‘Advanced Gunn Diode as High Power Terahertz Source for a Millimetre Wave High Power Multiplier’ Proceedings of SPIE 7485, 748501, DOI:10.1117/12.830296 (2019).
[48] S. Chung, and N. Balkan, ‘The anatomy of the Gunn laser’ Journal of Applied Physics 104, 073101 (2008).
[49] Piotr Płotka, Jun-ichi Nishizawa, Toru Kurabayashi, and Hiroki Makabe, ‘240-325-GHz GaAs CW Fundamental-Mode TUNNETT Diodes Fabricated With Molecular Layer Epitaxy’ IEEE Transactions on Electron Devices **50**, 4 (2003).
[50] Jun-ichi Nishizawa, Piotr Płotka, Hiroki Makabe, and Toru Kurabayashi, ‘GaAs TUNNETT Diodes Oscillating at 430-655 GHz in CW Fundamental Mode’ IEEE Microwave and Wireless Components Letters **15**, 9 (2005).
[51] T. T. Fong, and H. J. Kuno, ‘Millimeter-Wave Pulsed IMPATT Sources’ IEEE Transactions on Microwave Theory and Techniques **27**, 5 (1979).
[52] Masahiro Asada, and Safumi Suzuki, ‘Terahertz oscillators using electron devices – an approach with Resonant tunneling diodes’ IEICE Electronics Express **8**, 14 (2011).
[53] Masahiro Asada, and Safumi Suzuki, ‘Terahertz Emitter Using Resonant-Tunneling Diode and

Applications' Sensors **21**, 1384 (2021).
[54] Iwao Hosako, and Norihisa Hiromoto, 'Research and developments on p-type Germanium lasers I the frequency range from 0.1 terahertz to few terahertz' Journal of Communications Research Laboratory **49**, 1 (2002).
[55] S. Komiyama, 'Far-Infrared Emission from Population-Inverted Hot-Carrier System in p-Ge' Physical Review Letters **48**, 4 (1982).
[56] Alan W. M. Lee, Qi Qin, Sushil Kumar, Benjamin S. Williams, Qing Hu, and John L. Reno, 'Real-time terahertz imaging over a standoff distance (>25 meters)' Applied Physics Letters **89**, 141125 (2006).
[57] J. Faist, F. Capasso, D. L. Sivco, C. Sirtori, A. Hutchinson, and A. Y. Cho, 'Quantum cascade laser' Science 264, 553-556 (1994).
[58] Shun Lien Chuang, '*Physics of Photonics Devices* – 2nd edition' John Wiley & Sons Inc. (2009).
[59] Paul Harrison and Alex Valavanis, 'Quantum Wells, Wires, and Dots – 4th edition' John Wiley & Sons, Ltd. (2016).
[60] Chih-Hsiang Lin, Rui Q. Yang, D. Zhang, S. J. Murry, S. S. Pei, A. A. Allerman, S. R. Kurtz, 'Type-II interband quantum cascade laser at 3.8μm' Electronics Letters 33, 7, 598 (1997).
[61] R. Köhler, A. Tredicucci, F. Beltram, H. E. Beere, E. H. Linfield, A. G. Davies, D. A. Ritchie, R. C. Iotti, and F. Rossi, 'Terahertz semiconductor-heterostructure laser' Nature **417**, 156 (2002).
[62] Mikhail A. Belkin, Federico Capasso, Alexey Belyanin, Deborah L. Sivco, Alfred Y. Cho, Douglas C. Oakley, Christopher J. Vineis, and George W. Turner, 'Terahertz quantum-cascade-laser source based on intracavity difference-frequency generation' Nature Photonics 1, 288 (2007).
[63] R. F. Kazarinov and R. A. Suris Soviet Physics – Semiconductors **5**, 4, 707 (1971).
[64] Jérôme Faist, Federico Capasso, Carlo Sirtori, Deborah L. Sivco, James N. Baillargeon, Albert L. Hutchinson, Sung-Nee G. Chu, and Alfred Y. Cho, 'High power mid-infrared (λ∼5μm) quantum cascade lasers operating above room temperature' Applied Physics Letters 68, 3680 (1996).
[65] O. Cathabard, R. Teissier, J. Devenson, J. C. Moreno, and A. N. Baranova, 'Quantum cascade lasers emitting near 2.6μm' Applied Physics Letters **96**, 141110 (2010).
[66] Raffaele Colombelli, Federico Capasso, Claire Gmachl, Albert L. Hutchinson, Deborah L. Sivco, Alessandro Tredicucci, Michael C. Wanke, A. Michael Sergent, and Alfred Y. Cho, 'Far-infrared surface-plasmon quantum-cascade lasers at 21.5μm and 24μm wavelengths' Applied Physics Letters **78**, 2620 (2001).
[67] Miriam Serena Vitiello, Giacomo Scalari, Benjamin Williams, and Paolo De Natale, 'Quantum cascade lasers: 20 years of challenges' Optics Express **23**, 4, 5167 (2015).
[68] Carlo Sirtori, Hideaki Page, Cyrille Becker, and Valentin Ortiz, 'GaAs-AlGaAs Quantum Cascade

Lasers: Physics, Technology, and Prospects' IEEE Journal of Quantum Electronics **38**, 6 (2002).
[69] S. M. S. Rassel, L. Li, Y. Li, R. Q. Yang, J. A. Gupta, X. Wu, and Geof C. Aers, 'High temperature and low threshold interband cascade lasers at wavelengths longer than 6μm' Optical Engineering 57, 1 (2017).
[70] Ali Khalatpour, Man Chun Tam, Sadhvikas J. Addamane, John Reno, Zbig Wasilewski and Qing Hu, 'Terahertz semiconductor laser source at -12°C' arXiv:2211.08125 (2022).
[71] Christoph Walther, Milan Fischer, Giacomo Scalari, Romain Terazzi, Nicolas Hoyler, and Jérôme Faist, 'Quantum cascade lasers operating from 1.2 to1.6THz' Applied Physics Letters **91**, 131122 (2007).
[72] M. Wienold, B. Röben, X. Lü, G. Rozas, L. Schrottke, K. Biermann, and H. T. Grahn, 'Frequency dependence of the maximum operating temperature for quantum-cascade lasers up to 5.4 THz' Applied Physics Letters **107**, 202101 (2015).
[73] Mikhail A. Belkin, Federico Capasso, Feng Xie, Alexey Belyanin, Milan Fischer, Andreas Wittmann, and Jérôme Faist, 'Room temperature terahertz quantum cascade laser source based on intracavity difference-frequency generation' Applied Physics Letters **92**, 201101 (2008).
[74] M. Austerer, H. Detz, S. Schartner, M. Nobile, W. Schrenk, A. M. Andrews, P. Klang, and G. Strasser, 'Čerenkov-type phase-matched second-harmonic emission from GaAs⁄AlGaAs quantum-cascade lasers' Applied Physics Letters **92**, 111114 (2008).
[75] Quanyong Lu, and Manijeh Razeghi, 'Recent Advances in Room Temperature, High-Power Terahertz Quantum Cascade Laser Sources Based on Difference-Frequency Generation' Photonics **3**, 3, 42 (2016).
[76] Kazuue Fujita, Seungyong Jung, Yifan Jiang, Jae Hyun Kim, Atsushi Nakanishi, Akio Ito, Masahiro Hitaka, Tadataka Edamura, and Mikhail A. Belkin, 'Recent progress in terahertz difference-frequency quantum cascade laser sources' Nanophotonics **7**, 11, 1795 (2018).
[77] E. Benveniste, A. Vasanelli, A. Delteil, J. Devenson, R. Teissier, A. Baranov, A. M. Andrews, G. Strasser, I. Sagnes, and C. Sirtori, 'Influence of the material parameters on quantum cascade devices' Applied Physics Letters **93**, 131108 (2008).
[78] V. D. Jovanović, D. Indjin, Z. Ikonić, and P. Harrison, 'Simulation and design of GaN/AlGaN far-infrared (λ~34μm) quantum-cascade laser' Applied Physics Letters **84**, 16 (2004).
[79] L. Esaki, and R. Tsu, 'Superlattice and Negative Differential Conductivity in Semiconductors' IBM Journal of Research and Development **14**, 1 (1970).
[80] L. L. Chang, L. Esaki, W. E. Howard, R. Ludeke, and G. Schul, 'Structures Grown by Molecular Beam Epitaxy' Journal of Vacuum Science and Technology **10**, 5, 655 (1973).
[81] L. L. Chang, L. Esaki, and R. Tsu, 'Resonant tunneling in semiconductor double barriers' Applied Physics Letters **24**, 12, 593 (1974).

[82] Federico Capasso, Khalid Mohammed, and Alfred Y. Cho, 'Sequential resonant tunneling through a multiquantum well superlattice' Applied Physics Letters **48**, 7, 478 (1986).

[83] Norihiko Sekine and Hosako Iwao, 'GaAs-based Quantum Cascade Lasers' Journal of the National Institute of Information and Communications Technology **55**, 1, 11 (2008).

[84] Masamichi Yamanishi, Kazuue Fujita, Tadataka Edamura, and Hirofumi Kan, 'Indirect pump scheme for quantum cascade lasers: dynamics of electron-transport and very high T_0-values' Optics Express **16**, 25 (2008).

[85] Alessandro Tredicucci, Federico Capasso, Claire Gmachl, Deborah L. Sivco, Albert L. Hutchinson, and Alfred Y. Cho, 'High performance interminiband quantum cascade lasers with graded superlattices' Applied Physics Letters **73**, 15 (1998).

[86] Michel Rochat, Daniel Hofstetter, Mattias Beck, and Jérôme Faist, 'Long-wavelength ($\lambda \approx 16\mu m$), room-temperature, single-frequency quantum-cascade lasers based on a bound-to-continuum transition' Applied Physics Letters **79**, 26 (2001).

[87] Stephen Kohen, Benjamin S. Williams, and Qing Hu, 'Electromagnetic modeling of terahertz quantum cascade laser waveguides and resonators' Journal of Applied Physics **97**, 053106 (2005).

[88] Jérôme Faist, Lassad Ajili, Giacomo Scalari, Marchella Giovannini, Mattias Beck, Michel Rochat, Harvey Beere, A. Giles Davies, Edmund H. Linfield, and David Ritchie, 'Terahertz Quantum Cascade Lasers' Philosophical Transaction The Royal Society London A **362**, 215 (2004).

[89] Karl Unterrainer, Raffaele Colombelli, Claire Gmachl, Federico Capasso, Harold Y. Hwang, A. Michael Sergent, Deborah L. Sivco, and Alfred Y. Cho, 'Quantum cascade lasers with double metal-semiconductor waveguide resonators' Applied Physics Letters **80**, 17 (2002).

[90] Benjamin S. Williams, Sushil Kumar, Hans Callebaut, and Qing Hu, 'Terahertz quantum-cascade laser operating up to 137 K' Applied Physics Letters **83**, 25 (2003).

[91] Mikhail A. Belkin, Jonathan A. Fan, Sahand Hormoz, Federico Capasso, Suraj P. Khanna, Mohamed Lachab, A. Giles Davies, and Edmund H. Linfield, 'Terahertz quantum cascade lasers with copper metal-metal waveguides operating up to 178 K' Optics Express **16**, 5 (2008).

[92] S. Fathololoumi, E. Dupont, C. W. I. Chen, Z. R. Wasilewski, S. R. Laframboise, D. Ban, A. Mátyás, C. Jirauschek, Q. Hu, and H. C. Liu, 'Terahertz quantum cascade lasers operating up to ~200K with optimized oscillator strength and improved injection tunneling' Optics Express **20**, 4 (2012).

[93] Lianhe Li, Li Chen, Jingxuan Zhu, J. Freeman, P. Dean, A. Valavanis, A. G. Davies and E. H. Linfield, 'Terahertz quantum cascade lasers with >1W output powers' Electronics Letters **50**, 4, 309 (2014).

[94] L. H. Li, L. Chen, J. R. Freeman, M. Salih, P. Dean, A. G. Davies and E. H. Linfield, 'Multi-Watt high-power THz frequency quantum cascade lasers' Electronics Letters **53**, 12, 799 (2017).

[95] Tsung-Tse Lin, Li Wang, Ke Wang, Thomas Grange, Stefan Birner, and Hideki Hirayama, 'Over One Watt Output Power Terahertz Quantum Cascade Lasers by Using High Doping Concentration and Variable Barrier-Well Height' Physica Status Solidi Rapid Research Letters **16**, 7 (2022).
[96] S. Fathololoumi, E. Dupont, Z. R. Wasilewski, C. W. I. Chen, S. G. Razavipour, S. R. Laframboise, Shengxi Huang, Q. Hu, D. Ban, and H. C. Liu, 'Effect of oscillator strength and intermediate resonance on the performance of resonant phonon-based terahertz quantum cascade lasers' Journal of Applied Physics **113**, 113109 (2013).
[97] Lukas Mahler, Rüdeger Köhler, Alessandro Tredicucci, Fabio Beltram, Harvey E. Beere, Edmund H. Linfield, David A. Ritchie, and A. Giles Davies, 'Single-mode operation of terahertz quantum cascade lasers with distributed feedback resonators' Applied Physics Letters **84**, 26 (2004).
[98] Lukas Mahler, Alessandro Tredicucci, Rüdeger Köhler, Fabio Beltram, Harvey E. Beere, Edmund H. Linfield, and David A. Ritchie, 'High-performance operation of single-mode terahertz quantum cascade lasers with metallic gratings' Applied Physics Letters **87**, 181101 (2005).
[99] Miriam Serena Vitiello, and Alessandro Tredicucci, 'Tunable Emission in THz Quantum Cascade Lasers' IEEE Transactions on Terahertz Science and Technology **1**, 1 (2011).
[100] Nikita W. Almond, Xiaoqiong Qi, Riccardo Degl'Innocenti, Stephen J. Kindness, Wladislaw Michailow, Binbin Wei, Philipp Braeuninger-Weimer, Stephan Hofmann, Paul Dean, Dragan Indjin, Edmund H. Linfield, A. Giles Davies, Aleksandar D. Rakić, Harvey E. Beere, and David A. Ritchie, 'External cavity terahertz quantum cascade laser with a metamaterial/graphene optoelectronic mirror' Applied Physics Letters **117**, 041105 (2020).
[101] Joosun Yun, Tsung-Tse Lin, and Hideki Hirayama, 'Surface-emitting photonic crystal terahertz cascade laser adopting uniform triangular prism photonic crystal with a double-metal waveguide' Japanese Journal of Applied Physics **61**, 062001 (2022).
[102] W. Walukiewicz, L. Lagowski, L. Jastrzebski, M. Lichtensteiger, and H. C. Gatos, 'Electron mobility and free-carrier absorption in GaAs: Determination of the compensation ratio' Journal of Applied Physics 50, 2 (1979).
[103] I. Vurgaftman, and J. R. Meyer, 'TE- and TM-polarized roughness-assisted free-carrier absorption in quantum wells at midinfrared and terahertz wavelengths' Physical Review B 60, 20 (1999).
[104] Benjamin S. Williams, Sushil Kumar, Hans Callebaut, Qing Hu, and John L. Reno, 'Terahertz quantum-cascade laser operation up to 137K' Applied Physics Letters **83**, 25 (2003).
[105] Qing Hu, Benjamin S Williams, Sushil Kumar, Hans Callebaut, Stephen Kohen, and John L Reno, 'Resonant-phonon-assisted THz quantum-cascade lasers with metal-metal waveguides' Semiconductor Science and Technology **20**, S228 (2005).

[106] Benjamin S. Williams, Sushil Kumar, Qing Hu, and John L. Reno, 'Operation of terahertz quantum-cascade lasers at 164K in pulsed mode and at 117K in continuous-wave mode' Optics Express **13**, 9, 3331 (2005).

[107] H. Luo, S. R. Laframboise, Z. R. Wasilewski, G. C. Aers, H. C. Liu, and J. C. Cao, 'Terahertz quantum-cascade lasers based on a three-well active module' Applied Physics Letters **90**, 041112 (2007).

[108] S. Fathololoumi, E. Dupont, C. W. I Chan, Z. R. Wasilewski, S. R. Laframboise, D. Ban, A. Mátyás, C. Jirauschek, Q. Hu, and H. C. Liu, 'Terahertz quantum cascade lasers operating up to ~200K with optimized oscillator strength and improved injection tunneling' Optics Express **20**, 4, 3866 (2012).

[109] A. Wade, G. Fedorov, D. Smirnov, S. Kumar, B. S. Williams, Q. Hu, and J. L. Reno, 'Magnetic-field-assisted terahertz quantum cascade laser operation up to 225K' Nature Photonics 3, 41, (2009).

[110] Martin Brandstetter, Christoph Deutsch, Michael Krall, Hermann Detz, Donald C. MacFarland, Tobias Zederbauer, Aaron M. Andrews, Werner Schrenk, Gottfried Strasser, and Karl Unterrainer, 'High power terahertz quantum cascade lasers with symmetric wafer bonded active regions' Applied Physics Letters **103**, 171113 (2013).

[111] L. Bosco, M. Franckié, G. Scalari, M. Beck, A. Wacker, and J. Faist, 'Thermoelectrically cooled THz quantum cascade laser operating up to 210K' Applied Physics Letters **115**, 010601 (2019).

[112] Sushil Kumar, Chun Wang I. Chan, Qing Hu, and John L. Reno, 'A 1.8-THz quantum cascade laser operating significantly above the temperature of $\frac{\hbar\omega}{k_B}$'Nature Physics , 167 (2011).

[113] Christian Jirauschek, and Tillmann Kubis, 'Modeling techniques for quantum cascade lasers' Applied Physics Review **1**, 011307 (2014).

[114] E. Dupont, S. Fathololoumi, Z. R. Wasilewski, G. Aers, S. R. Laframboise, M. Lindskog, S. G. Razavipour, A. Wacker, D. Ban, and H. C. Liu, 'A phonon scattering assisted injection and extraction based terahertz quantum cascade laser' Journal of Applied Physics **111**, 073111 (2012).

[115] D. Indjin, P. Harrison, R. W. Kelsall, and Z. Ikonić, 'Mechanisms of temperature performance degradation in terahertz quantum-cascade lasers' Applied Physics Letters **82**, 1347 (2003).

[116] S. G. Razavipour, E. Dupont, S. Fathololoumi, C. W. I. Chan, M. Lindskog, Z. R. Wasilewski, G. Aers, S. R. Laframboise, A. Wacker, Q. Hu, D. Ban, and H. C. Liu, 'An indirectly pumped terahertz quantum cascade laser with low injection coupling strength operating above 150 K' Journal of Applied Physics **113**, 203107 (2013).

[117] C. Weber, A. Wacker, and A. Knorr, 'Density-matrix theory of the optical dynamics and transport in quantum cascade structures: The role of coherent' Physical Review B, 79, 165322 (2009).

[118] Sushil Kumar, and Qing Hu, 'Coherence of resonant-tunneling transport in terahertz quantum-

cascade lasers' Physical Review B **80**, 245316 (2009).
[119] E. Dupont, S. Fathololoumi, and H. C. Liu, 'Simplified density-matrix model applied to three-well terahertz quantum cascade lasers' Physical Review B **81**, 205311 (2010).
[120] G. Beji, Z. Ikonić, C. A. Evans, D. Indjin, and P. Harrison, 'Coherent transport description of the dual-wavelength ambipolar terahertz quantum cascade laser' Journal of Applied Physics **109**, 013111 (2011).
[121] T. V. Dinh, A. Valavanis, L. J. M. Lever, Z. Ikonić, and R. W. Kelsall, 'Extended density-matrix model applied to silicon-based terahertz quantum cascade lasers' Physical Review B **85**, 235427 (2012).
[122] Andrew Pan, Benjamin A. Burnett, Chi On Chui, and Benjamin S. Williams, 'Density matrix modeling of quantum cascade lasers without an artificially localized basis: A generalized scattering approach' Physical Review B **96**, 085308 (2017).
[123] Rita Claudia Iotti, and Fausto Rossi, 'Nature of Charge Transport in Quantum-Cascade Lasers' Physical Review Letters **87**, 14 (2001).
[124] F. Compagnone, A. Di Carlo, and P. Lugli, 'Monte Carlo simulation of electron dynamics in superlattice quantum cascade lasers' Applied Physics Letters **80**, 6 (2002).
[125] Hans Callebaut, Sushil Kumar, Benjamin S. Williams, and Qing Hu, 'Analysis of transport properties of tetrahertz quantum cascade lasers' Applied Physics Letters **83**, 2 (2003).
[126] M. Manenti, F. Compagnone, A. Di Carlo, and P. Lugli, 'Monte Carlo Simulation s of THz Quantum-Cascade Lasers' Journal of Computational Electronics 2: 433 (2003).
[127] Christian Jirauschek, Giuseppe Scarpa, and Paolo Lugli, 'Comparative analysis of resonant phonon THz quantum cascade lasers' Journal of Applied Physics **101**, 086109 (2007).
[128] Christian Jirauschek, and Paolo Lugli, 'Monte-Carlo-based spectral gain analysis for terahertz quantum cascade lasers' Journal of Applied Physics **105**, 123102 (2009).
[129] Hans Callebaut, and Qing Hu, 'Importance of coherence for electron transport in terahertz quantum cascade lasers' Journal of Applied Physics **98**, 104505 (2005).
[130] S.-C Lee, and A. Wacker, 'Nonequilibrium Green's function theory for transport and gain properties of quantum cascade structures' Physical Review B **66**, 245314 (2002).
[131] S.-C Lee, F. Banit, M. Woerner, and A. Wacker, 'Quantum mechanical wavepacket transport in quantum cascade laser structures' Physical Review B **73**, 245320 (2006).
[132] T. Kubis, C. Yeh, P. Vogl, A. Benz, G. Fasching, and C. Deutsch, 'Theory of nonequilibrium quantum transport and energy dissipation in terahertz quantum cascade lasers' Physical Review B **79**, 195323 (2009).
[133] H. Yasuda, T. Kubis, P. Vogl, N. Sekine, I. Hosako, and K. Hirakawa, 'Nonequilibrium Green's

function calculation for four-level scheme terahertz quantum cascade lasers' Applied Physics Letters **94**, 151109 (2009).
[134] T. Schmielau, and M. F. Pereira, Jr., 'Nonequilibrium many body theory for quantum transport in terahertz quantum cascade lasers' Applied Physics Letters **95**, 231111 (2009).
[135] Andreas Wacker, Rikard Nelander, and Carsten Weber, 'Simulation of gain in quantum cascade lasers' Proceedings of SPIE **7230**, 72301A (2009).
[136] Tao Liu, Tillmann Kubis, Qi Jie Wang, and Gerhard Klimeck, 'Design of three-well indirect pumping terahertz quantum cascade lasers for high optical gain based on nonequilibrium Green's function analysis' Applied Physics Letters **100**, 122110 (2012).
[137] Thomas Grange, 'Contrasting influence of charged impurities on transport and gain in terahertz quantum cascade lasers' Physical Review B **92**, 241306(R) (2015).
[138] M. Franckié, L. Bosco, M. Beck, C. Bonzon, E. Mavrona, G. Scalari, A. Wacker, and J. Faist, 'Two-well quantum cascade laser optimization by non-equilibrium Green's function modelling' Applied Physics Letter **112**, 021104 (2018).
[139] Giacomo Scalari, Romain Terazzi, Marcella Giovannini, Nicolas Hoyler, and Jérôme Faist, 'Population inversion by resonant tunneling in quantum wells' Applied Physics Letters **91**, 032103 (2007).
[140] Jérôme Faist, Lassaad Ajili, Giacomo Scalari, Marcella Giovannini, Mattias Beck, Michel Rochat, Harvey Beere, A. Giles Davies, Edmund H. Linfield and David Ritchie, 'Terahertz quantum cascade lasers' Philosophical Transactions of the Royal Society A, **362**, 215 (2004).
[141] Benjamin S. Williams, 'Terahertz quantum-cascade lasers' Nature Photonics **1**, 517 (2007).
[142] Michel Rochat, Lassaad Ajili, Harald Willenberg, Jérôme Faist, Harvey Beere, Giles Davies, Edmund Linfield, and David Ritchie, 'Low-threshold terahertz quantum-cascade lasers' Applied Physics Letters **81**, 8 (2002).
[143] L. Ajili, G. Scalari, D. Hofstetter, M. Beck, J. Faist, H. Beere, G. Davies, E. Linfield and D. Ritchie, 'Continuous-wave operation of far-infrared quantum cascade lasers' Electronic Letters **38**, 25 (2002).
[144] Stefano Barbieri, Jesse Alton, Sukhdeep S. Dhillon, Harvey E. Beere, Michael Evans, Edmund H. Linfield, A. Giles Davies, David A. Ritchie, Rüdeger Köhler, Alessandro Tredicucci, and Fabio Beltram, 'Continuous-Wave Operation of Terahertz Quantum-Cascade Lasers' IEEE Journal of Quantum Electronics **39**, 4 (2003).
[145] Rüdeger Köhler, Alessandro Tredicucci, Fabio Beltram, Harvey E. Beere, Edmund H. Linfield, A. Giles Davies, David A. Ritchie, Sukhdeep S. Dhillon, and Carlo Sirtori, 'High-performance continuous-wave operation of superlattice terahertz quantum-cascade lasers' Applied Physics Letters **82**, 10 (2003).
[146] Rüdeger Köhler, Alessandro Tredicucci, Fabio Beltram, Harvey E. Beere, Edmund H. Linfield, A.

Giles Davies, and David A. Ritchie, 'Low-threshold quantum-cascade lasers at 3.5THz (λ=85μm)' Optics Letters **28**, 10 (2003).
[147] Rüdeger Köhler, Alessandro Tredicucci, Cosimo Mauro, Fabio Beltram, Harvey E. Beere, Edmund H. Linfield, A. Giles Davies, and David A. Ritchie, 'Terahertz quantum-cascade lasers based on an interlaced photon-phonon cascade' Applied Physics Letters **84**, 8 (2004).
[148] Giacomo Scalari, Lassaad Ajili, Jérôme Faist, Harvey Beere, Edmund Linfield, David Ritchie, and Giles Davies, 'Far-infrared (λ≃87μm) bound-to-continuum quantum-cascade lasers operating up to 90K' Applied Physics Letters **82**, 19, 3165 (2003).
[149] S. Barbieri, J. Alton, H. E. Beere, J. Fowler, E. H. Linfield, and D. A. Ritchie, '2.9 THz quantum cascade lasers operating up to 70K in continuous wave' Applied Physics Letters **85**, 10 (2004).
[150] Lassaad Ajili, Giacomo Scalari, Jérôme Faist, Harvey Beere, Edmund Linfield, David Ritchie, and Giles Davies, 'High power quantum cascade lasers operating at λ≃87 and 130μm' Applied Physics Letters **85**, 18 (2004).
[151] J. Alton, S. Barbieri, C. Worrall, M. Houghton, H. E. Beere, E. L. Linfield, and D. A. Ritchie, 'Optimum resonant tunnelling injection and influence of doping density on the performance of THz bound-to-continuum cascade lasers' Proceedings of SPIE **5727**, 65 (2005).
[152] Chris Worrall, Jesse Alton, Mark Houghton, Stefano Barbieri, Harvey E. Beere, David Ritchie, Carlo Sirtori, 'Continuous wave operation of a superlattice quantum cascade laser emitting at 2THz' Optics Express **14**, 1, 171 (2006).
[153] Suraj Khanna, Mohamed Lachab, A. Giles Davies, and Edmund H. Linfield, 'Surface emitting terahertz quantum cascade laser with a double-metal waveguide' Optics Express **14**, 24, 11672 (2006).
[154] Christoph Walther, Giacomo Scalari, Jérôme Faist, Harvey Beere, and David Ritchie, 'Low frequency terahertz quantum cascade laser operating from 1.6 to 1.8THz' Applied Physics Letters **89**, 231121 (2006).
[155] S. P. Khanna, S. Chakraborty, M. Lachab, N. M. Hinchcliffe, P. Dean, E. H. Linfield, and A. G. Davies, 'Terahertz frequency quantum cascade lasers: growth and measurement' Terahertz Science and Technology **1**, 1 (2008).
[157] Lassaad Ajili, Giacomo Scalari, Nicolas Hoyler, Marcella Giovannini, and Jérôme Faist, 'InGaAs-AlInAs/InP terahertz quantum cascade laser' Applied Physics Letters **87**, 141107 (2005).
[158] M. Fischer, G. Scalari, K. Celebi, M. Amanti, Ch. Walther, M. Beck, and J. Faist, 'Scattering processes in terahertz InGaAs/InAlAs quantum cascade lasers' Applied Physics Letters **97**, 221114 (2010).
[159] Giacomo Scalari, Nicolas Hoyler, Marcella Giovannini, and Jérôme Faist, 'Terahertz bound-to-continuum quantum-cascade lasers based on optical-phonon scattering extraction' Applied Physics Letters

86, 181101 (2005).
[160] Lorenzo Sirigu, Alok Rudra, Eli Kapon, Maria I. Amanti, Giacomo Scalari, and Jérôme Faist, 'A terahertz quantum cascade laser grown by low-pressure metalorganic vapor phase epitaxy' Applied Physics Letters **92**, 181111 (2008).
[161] Maria I Amanti, Giacomo Scalari, Romain Terazzi, Milan Fischer, Mattias Beck, Jérôme Faist, Alok Rudra, Pascal Gallo and Eli Kapon, 'Bound-to-continuum terahertz quantum cascade laser with a single-quantum-well phonon extraction/injection stage' New Journal of Physics **11**, 125022 (2009).
[162] M. Wienold, L. Schrottke, M. Giehler, R. Hey, W. Anders, and H.T. Grahn, 'Low-voltage terahertz quantum-cascade lasers based on LO-phonon-assisted interminiband transitions' Electronics Letters **45**, 20 (2009).
[163] Xuemin Wang, Changle Shen, Tao Jiang, Zhiqiang Zhan, Qinghua Deng, Weihua Li, Weidong Wu, Ning Yang, Weidong Chu, and Suqing Duan, 'High-power terahertz quantum cascade lasers with ~0.23W in continuous wave mode' AIP Advances **6**, 075210 (2016).
[164] M. Fischer, G. Scalari, Ch. Walther, J. Faist, 'Terahertz quantum cascade lasers based on $In_{0.53}Ga_{0.47}As/In_{0.52}Al_{0.48}As/InP$' Journal of Crystal Growth **311**, 1939 (2009).
[165] Benjamin S. Williams, Sushil Kumar, Hans Callebaut, Qing Hu, and John L. Reno, 'Terahertz quantum-cascade laser at $\lambda \approx 100\mu m$ using metal waveguide for mode confinement' Applied Physics Letters **83**, 11 (2003).
[166] Benjamin S. Williams, Hans Callebaut, Sushil Kumar, Qing Hu, and John L. Reno, '3.4-THz quantum cascade laser based on longitudinal-optical-phonon scattering for depopulation' Applied Physics Letters **82**, 7 (2003).
[167] B. S. Williams, S. Kumar, H. Callebaut, Q. Hu, and J. L. Reno, '3.4THz quantum cascade laser operating above liquid nitrogen temperature' Electronics Letters **39**, 12 (2003).
[168] B. S. Williams, S. Kumar, Q. Hu and J. L. Reno, 'Resonant-phonon terahertz quantum-cascade laser operating at 2.1 THz ($\lambda \simeq 141\mu m$)' Electronics Letters **40**, 7 (2004).
[169] Sushil Kumar, Benjamin S. Williams, Stephen Kohen, Qing Hu, and John L. Reno, 'Continuous-wave operation of terahertz quantum-cascade lasers above liquid-nitrogen temperature' Applied Physics Letters **84**, 14 (2004).
[170] D. Ban, M. Wächter, H. C. Liu, Z. R. Wasilewski, M. Buchanan, and G. C. Aers, 'Terahertz quantum cascade lasers: Fabrication, characterization, and doping effect' Journal of Vacuum Science & Technology A **24**, 778 (2006).
[171] Sushil Kumar, Benjamin S. Williams, Qing Hu, and John L. Reno, '1.9THz quantum-cascade lasers with one-well injector' Applied Physics Letters **88**, 121123 (2006).

[172] Benjamin S. Williams, Sushil Kumar, Qing Hu, and John L. Reno, 'High-power Terahertz Quantum Cascade Lasers' Electronics Letters **42**, 2 (2006).
[173] L. Lever, N. M. Hinchcliffe, S. P. Khanna, P. Dean, Z. Ikonić, C. A. Evans, A. G. Davies, P. Harrison, E. H. Linfield, and R. W. Kelsall, 'Terahertz ambipolar dual-wavelength quantum cascade laser' Optics Express **17**, 22 (2009).
[174] Tsung-Tse Lin, and Hideki Hirayama, 'Improvement of operation temperature in GaAs/AlGaAs THz-QCLs by utilizing high Al composition barrier' Physica Status Solidi C **10**, 11 (2013).
[175] Tsung-Tse Lin, Li Wang, Ke Wang, Thomas Grange, and Hideki Hirayama, 'Optimization of terahertz quantum cascade lasers by suppressing carrier leakage channel via high-energy state' Applied Physics Express **11**, 11 (2018).
[176] K. Ohtani, M. Beck, G. Scalari, and J. Faist, 'Terahertz quantum cascade lasers based on quaternary AlInGaAs barriers' Applied Physics Letters **103**, 041103 (2013).
[177] Sushil Kumar, Qing Hu, and John L. Reno, '186 K operation of terahertz quantum cascade lasers based on a diagonal design' Applied Physics Letters **94**, 131105 (2009).
[178] Y. Chassagneux, Q. J. Wang, S. P. Khanna, E. Strupiechonski, J.-R. Coudevylle, E. H. Linfield, A. G. Davies, F. Capasso, M. A. Belkin, and R. Colombelli, 'Limiting Factors to the Temperature Performance of THz Quantum Cascade Lasers Based on the Resonant-Phonon Depopulation Scheme' IEEE Transactions on Terahertz Science and Technology **2**, 1, 83 (2011).
[179] Asaf Albo, Qing Hu, and John L. Reno, 'Room temperature negative differential resistance in terahertz quantum cascade laser structures' Applied Physics Letters **109**, 081102 (2016).
[180] Sudeep Khanal, Liang Gao, Le Zhao, John L. Reno & Sushil Kumar, 'High-temperature operation of broadband bidirectional terahertz quantum-cascade lasers' Scientific Report **6**, 32978 (2016).
[181] Asaf Albo and Yuri V. Flores, 'Carrier Leakage Dynamics in Terahertz Quantum Cascade Lasers' IEEE Journal of Quantum Electronics **53**, 5 (2017).
[182] Martin Alexander Kainz, Sebastian Schönhuber, Aaron Maxwell Andrews, Hermann Detz, Benedikt Limbacher, Gottfried Strasser, and Karl Unterrainer, 'Barrier Height Tuning of Terahertz Quantum Cascade Lasers for High-Temperature Operation' ACS Photonics **5**, 4687 (2018).
[183] A. N. Baranov, H. Nguyen-Van, Z. Loghmari, M. Bahriz, and R. Teissier, 'Terahertz quantum cascade laser with non-resonant extraction' AIP Advances **9**, 055214 (2019).
[184] Liang Gao, John L. Reno, and Sushil Kumar, 'Short Barriers for Lowering Current-Density in Terahertz Quantum Cascade Lasers' Photonics **7**, 7 (2020).
[185] Christoph Deutsch, Alexander Benz, Hermann Detz, Pavel Klang, Michele Nobile, Aaron Maxwell Andrews, Werner Schrenk, Tillmann Kubis, Peter Vogl, Gottfried Strasser, and Karl Unterrainer,

'Terahertz quantum cascade lasers based on type II InGaAs/GaAsSb/InP' Applied Physics Letters **97**, 261110 (2010).

[186] C. Deutsch, M. Krall, M. Brandstetter, H. Detz, A. M. Andrews, P. Klang, W. Schrenk, G. Strasser, and K. Unterrainer, 'High performance InGaAs/GaAsSb terahertz quantum cascade lasers operating up to 142K' Applied Physics Letters **101**, 211117 (2012).

[187] Christoph Deutsch, Martin Alexander Kainz, Michael Krall, Martin Brandstetter, Dominic Bachmann, Sebastian Schönhuber, Hermann Detz, Tobias Zederbauer, Donald MacFarland, Aaron Maxwell Andrews, Werner Schrenk, Mattias Beck, Keita Ohtani, Jérôme Faist, Gottfried Strasser, and Karl Unterrainer, 'High-Power Growth-Robust InGaAs/InAlAs Terahertz Quantum Cascade Lasers' ACS Photonics **4**, 957 (2017).

[188] Asaf Albo, Yuri V. Flores, Qing Hu, and John L. Reno, 'Two-well terahertz quantum cascade lasers with suppressed carrier leakage' Applied Physics Letters **111**, 111107 (2017).

[189] M. Franckié, L. Bosco, M. Beck, C. Bonzon, E. Mavrona, G. Scalari, A. Wacker, and J. Faist, 'Two-well quantum cascade laser optimization by non-equilibrium Green's function modelling' Applied Physics Letters **112**, 021104 (2018).

[190] Wataru Terashima, and Hideki Hirayama, 'GaN-based terahertz quantum cascade lasers' Proceedings of SPIE **9483**, 948304 (2015).

[191] Benjamin S. Williams, Sushil Kumar, Qi Qin, Qing Hu, and John L. Reno, 'Terahertz quantum cascade lasers with double-resonant-phonon depopulation' Applied Physics Letters **88**, 261101 (2006).

[192] Robert W. Adams, Karun Vijayraghavan, Qi Jie Wang, Jonathan Fan, Federico Capasso, Suraj P. Khanna, A. Giles Davies, Edmund H. Linfield, and Mikhail A. Belkin, 'GaAs/$Al_{0.15}Ga_{0.85}As$ terahertz quantum cascade lasers with double-phonon resonant depopulation operating up to 172K' Applied Physics Letters **97**, 131111 (2010).

[193] Andreas Wacker, 'Extraction-controlled quantum cascade lasers' Applied Physics Letters **97**, 081105 (2010).

[194] E. Dupont, S. Fathololoumi, Z. R. Wasilewski, G. Aers, S. R. Laframboise, M. Lindskog, S. G. Razavipour, A. Wacker, D. Ban, and H. C. Liu, 'A phonon scattering assisted injection and extraction based terahertz quantum cascade laser' Applied Physics Letter **111**, 073111 (2012).

[195] S. G. Razavipour, E. Dupont, C. W. I. Chan, C. Xu, Z. R. Wasilewski, S. R. Laframboise, Q. Hu, and D. Ban, 'A high carrier injection terahertz quantum cascade laser based on indirectly pumped scheme' Applied Physics Letters **104**, 041111 (2014).

[196] Sudeep Khanal, John L. Reno, and Sushil Kumar, '2.1 THz quantum-cascade laser operating up to 144 K based on a scattering-assisted injection design' Optics Express **23**, 15 (2015).

[197] Boyu Wen, Chao Xu, Kaixi Wang, Man Chun Tam, Zbig Wasilewski, and Dayan Ban, 'Dual-lasing channel quantum cascade laser based on scattering-assisted injection design' Optical Express **26**, 7 (2018).
[198] Aleksandar Demić, 'Density Matrix Modelling of Terahertz Frequency Quantum Cascade Lasers: Steady State Analysis and Maxwell-Bloch Dynamics' A dissertation to the University of Leeds (2019).
[199] Boyu Ben, Chris Deimert, Chao Xu, S. M. Shazzad Rassel, Zbignew Wasilewski, and Dayan Ban, 'Six-level hybrid extraction/injection scheme terahertz quantum cascade laser with suppressed thermally activated carrier leakage' Optics Express **28**, 18 (2020).
[200] Kazuue Fujita, Masamichi Yamanishi, Shinichi Furuta, Kazunori Tanaka, Tadataka Edamura, Tillmann Kubis, and Gerhard Klimeck, 'Indirectly pumped 3.7 THz InGaAs/InAlAs quantum-cascade lasers grown by metal-organic vapor-phase epitaxy' Optics Express **20**, 18 (2012).
[201] Li Wang, Tsung-Tse Lin, Ke Wang, Thomas Grange, Stefan Birner, and Hideki Hirayama, 'Short-period scattering-assisted terahertz quantum cascade lasers operating at high temperature' Scientific Reports **9**, 9446 (2019).
[202] Li Wang, Tsung-Tse Lin, Ke Wang, and Hideki Hirayama, 'Parasitic transport paths in two-well scattering-assisted terahertz quantum cascade lasers' Applied Physics Express **12**, 082003 (2019).
[203] Chun Wang I. Chan, Qing Hu, and John L. Reno, 'Ground state terahertz quantum cascade lasers' Applied Physics Letters **101**, 151108 (2012).
[204] H. Yasuda, I. Hosako, S. Miyashita, and M. Patrashin, 'Terahertz electroluminescence from GaAs/AlSb quantum cascade laser' Electronics Letters 41, 19 (2005).
[205] Hiroaki Yasuda, and Iwao Hosako, 'Terahertz Waveguide Design for GaSb/AlGaSb Quantum Cascade Laser' Japanese Journal of Applied Physics **47**, 3, 1575 (2008).
[206] Martin Brandstetter, Martin A. Kainz, Tobias Zederbauer, Michael Krall, Sebastian Schönhuber, Hermann Detz, Werner Schrenk, Aaron Maxwell Andrews, Gottfried Strasser, and Karl Unterrainer, 'InAs based terahertz quantum cascade lasers' Applied Physics Letters **108**, 011109 (2016).
[207] Will Freeman, and Gamani Karunasiri, 'Temperature effects in terahertz step well quantum cascade structures with diagonal optical transitions' Proceedings of SPIE **8119**, 81190A (2011).
[208] Alpar Matyas, Reza Chashmahcharagh, Istvan Kovacs, Paolo Lugli, Karun Vijayraghavan, Mikhail A. Belkin, and Christian Jirauschek, 'Improved terahertz quantum cascade laser with variable height barriers' Journal of Applied Physics **111**, 103106 (2012).
[209] Aiting Jiang, Alpar Matyas, Karun Vijayraghavan, Christian Jirauschek, Zbig R. Wasilewski, and Mikhail A. Belkin, 'Experimental investigation of terahertz quantum cascade laser with variable barrier height' Journal of Applied Physics **115**, 163103 (2014).
[210] Asaf Albo, Yuri V. Flores, Qing Hu, and John L. Reno, 'Split-well direct-phonon terahertz quantum

cascade lasers' Applied Physics Letters **114**, 191102 (2019).
[211] Nathalie Lander Gower, Silvia Piperno, and Asaf Albo, 'The Effect of Doping in Split-Well Direct-Phonon THz Quantum-Cascade Laser Structures' Photonics, **8**, 195 (2021).
[212] Vincent Berger, 'Three-level laser based on intersubband transitions in asymmetric quantum well: a theoretical study' Semiconductor Science Technology **9**, 1493 (1994).
[213] Giacomo Scalari, Maria I. Amanti, Milan Fischer, Romain Terazzi, Christoph Walther, Mattias Beck, and Jérôme Faist, 'Step well quantum cascade laser emitting at 3THz' Applied Physics Letters **94**, 041114 (2009).
[214] H. Li, J. C. Cao, Z. Y. Tan, Y. J. Han, X. G. Guo, S. L Feng, H. Luo, S. R. Laframboise, and H. C. Liu, 'Temperature performance of terahertz quantum-cascade lasers: experiment versus simulation' Journal of Physics D: Applied Physics **42**, 025101 (2009).
[215] Y. Chassagneux, Q. J. Wang, S. P. Khanna, E. Strupiechonski, J.-R. Coudevylle, E. H. Linfield, A. G. Davies, F. Capasso, M. A. Belkin, and R. Colombelli, 'Limiting Factors to the Temperature Performance of THz Quantum Cascade Lasers Based on the Resonant-Phonon Depopulation Scheme' IEEE Transactions on Terahertz Science and Technology **2**, 1 (2012).
[216] Asaf Albo, and Qing Hu, 'Investigation temperature degradation in THz quantum cascade lasers by examination of temperature dependence of output power' Applied Physics Letters **106**, 131108 (2015).
[217] C. Jirauschek, and P. Lugli, 'Limiting factors for high temperature operation of THz quantum cascade lasers' Physica Status Solidi C **5**, 1, 221 (2008).
[218] M. Lindskog, D. O. Winge, and A. Wacker, 'Injection schemes in THz quantum cascade lasers under operation' Proceedings of SPIE 8846, 884603 (2013).
[219] Asaf Albo, and Qing Hu, 'Carrier leakage into the continuum in diagonal GaAs/$Al_{0.15}$GaAs terahertz quantum cascade lasers' Applied Physics Letters **107**, 241101 (2015).
[220] Tsung-Tse Lin, Li Wang, Ke Wang, Thomas Grange, and Hideki Hirayama, 'Optimization of terahertz quantum cascade lasers by suppressing carrier leakage channel via high-energy state' Applied Physics Express **11**, 112702 (2018).
[221] Rikard Nelander, and Andreas Wacker, 'Temperature dependence of the gain profile for terahertz quantum cascade lasers' Applied Physics Letters **92**, 081102 (2008).
[222] Jacob B. Khurgin, 'Inhomogeneous origin of the interface roughness broadening of intersubband transitions' Applied Physics Letters **93**, 091104 (2008).
[223] Alpar Matyas, Paolo Lugli, and Christian Jirauschek, 'Role of collisional broadening in Monte Carlo simulations of terahertz quantum cascade lasers' Applied Physics Letters **102**, 011101 (2013).
[224] Ali Khalatpour, Andrew K. Paulsen, Chris Deimert, Zbig R. Wasilewski and Qing Hu, 'High-power

portable terahertz laser systems' Nature Photonics **15**, 16 (2021).

[225] Seyed Ghasem Razavipour, 'Design, Analysis, and Characterization of Indirectly-pumped Terahertz Quantum Cascade Lasers' a dissertation in the University of Waterloo (2013).

[226] J. D. Cooper, A. Valavanis, Z. Ikonić, P. Harrison, and J. E. Cunningham, 'Finite difference method for solving the Schrödinger equation with band nonparabolicity in mid-infrared quantum cascade lasers' Journal of Applied Physics **108**, 113109 (2010)

[227] D. F. Nelson, R. C. Miller, and D. A. Kleinman, 'Band non-parabolicity effects in semiconductor quantum wells' Physical Review B, **35**, 14 (1987).

[228] Xunpeng Ma, Kangwen Li, Zuyin Zhang, Haifeng Hu, Qing Wang, Xin Wei, and Guofeng Song, 'Two-band finite difference method for the bandstructure calculation with nonparabolicity effects in quantum cascade lasers' Journal of Applied Physics **114**, 063101 (2013).

[229] Carlo Sirtori, Federico Capasso, and Jérôme Faist, 'Nonparabolicity and a sum rule associated with bound-to-bound and bound-to-continuum intersubband transitions in quantum wells' Physical Review B **50**, 12 (1994).

[230] I. Vurgaftman, J. R. Meyer, and L. R. Ram-Mohan, 'High-Power/Low-Threshold Type-II Interband Cascade Mid-IR Laser – Design and Modeling' IEEE Photonics Technology Letters **9**, 2 (1997).

[231] Tsuneya Ando, 'Broadening of Inter-Subband Transitions in Image-Potential-Induced Surface States outside Liquid Helium' Journal of the Physical Society of Japan, **44**, 3 (1978).

[232] Tsuneya Ando, 'Line Width of Inter-Subband Absorption in Inversion Layers: Scattering from Charged Ions' Journal of the Physical Society of Japan, **54**, 7 (1985).

[233] Takeya Unuma, Teruyuki Takahashi, Takeshi Node, Masahiro Yoshita, Hiroyuki Sakaki, Motoyoshi Baba, and Hidefumi Akiyama, 'Effects of interface roughness and phonon scattering on intersubband absorption linewidth in a GaAs quantum well' Applied Physics Letters **78**, 22 (2001).

[234] Takeya Unuma, Masahiro Yoshita, Takeshi Noda, Hiroyuki Sakaki, and Hidefumi Akiyama, 'Intersubband absorption linewidth in GaAs quantum wells due to scattering by interface roughness, phonons, alloy disorder, and impurities' Journal of Applied Physics **93**, 3 (2003).

[235] Olivier Bonno, Jean-Luc Thobel, and François Dessenne, 'Modeling of electron–electron scattering in Monte Carlo simulation of quantum cascade lasers' Journal of Applied Physics **97**, 043702 (2005).

[236] Teppei Miyoshi, and Dayan Ban, 'Investigation of Coulomb scattering in terahertz quantum cascade

lasers' Journal of Applied Physics **129**, 153102 (2021).

[237] G. Bastard, 'Wave mechanics applied to semiconductor heterostructures' Editions de Physique, France (1988).

[238] K. A. Krivas, D. O. Winge, M. Franckié, and A. Wacker, 'Influence of interface roughness in quantum cascade lasers' Journal of Applied Physics **118**, 114501 (2015).

[239] David K. Ferry, 'Semiconductors: Bonds and Bands' Institute of Physics Publishing Inc. (2013).

[240] Wikipedia A 'Dephasing' https://wiki.edu.vn/en/wiki5/dephasing-wikipedia/

[241] J. L. Skinner, and D. Hsu, 'Pure Dephasing of a Two-Level System' The Journal of Physical Chemistry **90**, 21, 4931 (1986).

[242] K. L. Campman, H. Schmidt, A. Imamoglu, and A. C. Gossard, 'Interface roughness and alloy-disorder scattering contributions to intersubband transition linewidths' Applied Physics Letters **69**, 17 (1996).

[243] Will Freeman, 'Self-consistent calculation of dephasing in quantum cascade structures within a density matrix method' Physical Review B **93**, 205301 (2016).

[244] Will Freeman, and Gamani Karunasiri 'Nonequilibrium electron leakage in terahertz quantum cascade structures' Physical Review B **85**, 195326 (2012).

[245] Will Freeman, 'Decoherence in high barrier quantum cascade structures' Journal of Applied Physics **122**, 045701 (2017).

[246] Rikard Nelander, and Andreas Wacker, 'Temperature dependence and screening models in quantum cascade structures' Journal of Applied Physics **106**, 063115 (2009).

[247] S. Tsujino, A. Borak, E. Müller, M. Scheinert, C. V. Falub, H. Sigg, D. Grützmacher, M. Giobannini, and J. Faist, 'Interface-roughness-induced broadening of intersubband electroluminescence in *p*-SiGe and *n*-GaInAs/AlInAs quantum-cascade structures' Applied Physics Letters **86**, 062113 (2005).

[248] A. Wittmann, Y. Bonetti, J. Faist, E. Gini, and M. Giovannini, 'Intersubband linewidths in quantum cascade laser designs' Applied Physics Letters **93**, 141103 (2008).

[249] Jacob B. Khurgin, Yamac Dikmelik, Peter Q. Liu, Anthony J. Hoffman, Matthew D. Escarra, Kale J. Franz, and Claire F. Gmachl, 'Role of interface roughness in the transport and lasing characteristics of quantum-cascade lasers' Applied Physics Letters **94**, 091101 (2009).

[250] Yuri V. Flores, and Asaf Albo, 'Impact of Interface Roughness Scattering on Performance of

$GaAs/Al_xGa_{1-x}As$ Terahertz Quantum Cascade Lasers' IEEE Journal of Quantum Electronics **53**, 3 (2017).

[251] H. Bruus, and K. Flensberg, '*Introduction to many-body quantum theory in condensed matter physics*' Oxford university press, Oxford (2016).

[252] Ivan Ezhov, and Christian Jirauschek, 'Influence of screening on longitudinal-optical phonon scattering in quantum cascade lasers' Journal of Applied Physics **119**, 033102 (2016).

[253] J. T. Lü, and J. C. Cao 'Coulomb scattering in the Monte Carlo simulation of terahertz quantum-cascade lasers' Applied Physics Letters **89**, 211115 (2006).

[254] David O. Winge, Martin Franckié, Claudio Verdozzi, Andreas Wacker, and Mauro F. Pereira, 'Simple electron-electron scattering in non-equilibrium Green's function simulations' Journal of Physics: Conference Series **696**, 012013 (2015).

[255] S.-C. Lee, and I. Galbraith 'Intersubband and intrasubband electronic scattering rates in semiconductor quantum wells' Physical Review B 59, 24 (1999).

[256] M. Asada, *'Quantum well lasers* – 1st edition' P. S. Zory Jr. published by Academic press, San Diego (1993).

[257] Pierre F. Maldague, 'Many-body corrections to the polarizability of the two-dimensional electron gas' Surface Science **73**, 296-302 (1978).

[258] Jurgen H. Smet, Clifton G. Fonstad, and Qing Hu 'Intrawell and interwell intersubband transitions in multiple quantum wells for far-infrared sources' Journal of Applied Physics **79**, 9305 (1996).

[259] H. Haug, and S. W. Koch '*Quantum theory of the optical and electronic properties of semiconductors* – 3rd ed.' World Scientific publishing Co. Pte. Ltd., Singapore (1990).

[260] Per Hyldgaard and John W. Wilkins, 'Electron-electron scattering in far-infrared quantum cascade lasers' Physical Review B **53**, 6889 (1996).

[261] Seoung-Hwan Park, Doyeol Ahn, and Yong-Tak Lee 'Screening Effects on Electron-Longitudinal Optical-Phonon Intersubband Scattering in Wide Quantum Well and Comparison with Experiment' Japanese Journal of Applied Physics **39**, 6601 (2000).

[262] Amnon Yariv, Chris Lindsey, and Uri Sivan, 'Approximate analytic solution for electronic wave functions and energies in coupled quantum wells' Journal of Applied Physics **59**, 9 (1985).

[263] Romain Léon Terazzi 'Transport in Quantum Cascade Lasers' a dissertation to the University of Neuchâtel (2012).

[264] Romain Terazzi, Tobias Gresch, Andreas Wittmann, and Jérôme Faist 'Sequential resonant tunneling in quantum cascade lasers' Physical Review B 78, 155328 (2008).

[265] Teppei Miyoshi, and Dayan Ban, 'Barrier height study of two-well resonant-phonon terahertz quantum cascade lasers. I. The third-order tunneling current theory' Journal of Applied Physics 130, 183103 (2021).

[266] S. Harald, and H. C. Liu, '*Quantum well infrared photodetectors*' Springer, Berlin/Heidelberg (2007).

[267] S. M. Sze, Y. Li, and K. K. Ng, *Physics of semiconductor devices*, 4th ed. (John Wiley & Sons, Inc, New York, 2021).

[268] C. Jacoboni, '*Theory of electron transport in semiconductors*' Springer, Berlin/Heidelberg, (2010).

[269] R. Quay, C. Moglestue, V. Palankovski, and S. Selberherr, 'A temperature dependent model for the saturation velocity in semiconductor materials' Material Science in Semiconductor Processing. **3**, 149 (2000).

[270] S. Fathololoumi, D. Ban, H. Luo, E. Dupont, S. R. Laframboise, A. Boucherif, and H. C. Liu, 'Thermal Behavior Investigation of Terahertz Quantum-Cascade Lasers' IEEE Journal of Quantum Electronics **44**, 12 (2008).

[271] K. Pierścińsk, D. Pierścińska, M. Iwińska, K. Kosiel, A. Szerling, P. Karbownik, and M. Bugajski, 'Investigation of thermal properties of mid-infrared AlGaAs/GaAs quantum cascade lasers' Journal of Applied Physics **112**, 043112 (2012).

[272] P. Harrison, D. Indjin, and R. W. Kelsall 'Electron temperature and mechanisms of hot carrier generation in quantum cascade lasers' Journal of Applied Physics **92**, 11 (2002).

[273] D. Indjin, P. Harrison, R. W. Kelsall, and Z. Ikonić 'Self-Consistent Scattering Model of Carrier Dynamics in GaAs-AlGaAs Terahertz Quantum-Cascade Lasers' IEEE Photonics Technology Letters **15**, 3 (2003).

[274] P. Harrison, D. Indjin, V. D. Jovanović, A. Mirčetić, Z. Ikonić, R. W. Kelsall, J. McTavish, I. Savić, N. Vukmirović and V. Milanović 'Carrier Dynamics in Quantum Cascade Lasers' ACTA Physica Polonica A **107**, 1 (2005).

[275] Z. Ikonić, P. Harrison, and R. W. Kelsall, 'Self-consistent energy balance simulations of hole dynamics in SiGe/Si THz quantum cascade structures' Journal of Applied Physics **96**, 11 (2004).

[276] D. Indjin, Z. Ikonić, V. D. Jovanović, N. Vukmirović, P. Harrison, and R. W. Kelsall 'Relationship between carrier dynamics and temperature in terahertz quantum cascade structures: simulation of GaAs/AlGaAs, SiGe/Si and GaN/AlGaN devices' Semiconductor Science and Technology **20**, S237 (2005).

[277] V. D. Jovanović, S. Höfling, D. Indjin, N. Vukmirović, Z. Ikonić, P. Harrison, J. P. Reithmaier and A. Forchel 'Influence of doping density on electron dynamics in GaAs/AlGaAs quantum cascade lasers' Journal of Applied Physics 99, 103106 (2006).

[278] Philip Slingerland, Christopher Baird, and Robert H. Giles 'Application of multi-subband self-consistent energy balance method to terahertz quantum cascade lasers' Semiconductor Science and Technology **27**, 065009 (2012).

[279] Christopher S. Baird, Marissa D. Lafferty, 'Analysis of approximations used in terahertz quantum cascade laser doing calculations' Proceedings of SPIE **10917** (2019).

[280] H. C. Liu, Z. R. Wasilewski, M. Buchanan, and H. Chu 'Segregation of Si δ doping in GaAs-AlGaAs quantum wells and the cause of the asymmetry in the current-voltage characteristics of intersubband infrared detectors' Applied Physics Letters **63**, 761 (1993)

[281] Z. R. Wasilewski, H. C. Liu, and M. Buchanan, 'Studies of Si segregation in GaAs using current–voltage characteristics of quantum well infrared photodetectors' Journal of Vacuum Science & Technology B **12**, 1273 (1994).

[282] S. Fathololoumi, E. Dupont, C. W. I. Chan, Z. R. Wasilewski, S. R. Laframboise, D. Ban, A. Mátyás, C. Jirauschek, Q. Hu, and H. C. Liu, 'Terahertz quantum cascade lasers operating up to ~ 200 K with optimized oscillator strength and improved injection tunneling' Optics Express **20**, 4, 3866 (2012).

[283] L. Bosco, M. Franckié, G. Scalari, M. Beck, A. Wacker, and J. Faist, 'Thermoelectrically cooled THz quantum cascade laser operating up to 210 K' Applied Physics Letters **115**, 010601 (2019).

[284] Sushil Kumar, Chun Wang I. Chan, Qing Hu, and John L. Reno, 'Two-well terahertz quantum-cascade laser with direct intrawell-phonon depopulation' Applied Physics Letters **95**, 141110 (2009).

[285] Miriam Serena Vitiello, Gaetano Scamarcio, and Vincenzo Spagnolo, 'Temperature Dependence of Thermal Conductivity and Boundary Resistance in THz Quantum Cascade Lasers' IEEE Journal of Selected Topics in Quantum Electronics **14**, 2 (2008).

[286] M. Giehler, R. Hey, H. Kostial, S. Cronenberg, T. Ohtsuka, L. Schrottke, and H. T. Grahn, 'Lasing

properties of GaAs/(Al,Ga)As quantum-cascade lasers as a function of injector doping density' Applied Physics Letters **82**, 671 (2003).

[287] V. D. Jovanović, D. Indjin, N. Vukmirović, Z. Ikonić, P. Harrison, E. H. Linfield, H. Page, X. Marcadet, C. Sirtori, C. Worrall, H. E. Beere, and D. A. Ritchie, 'Mechanisms of dynamic range limitations in GaAs⁄AlGaAs quantum-cascade lasers: Influence of injector doping' Applied Physics Letters **86**, 211117 (2005).

[288] E. Mujagić, M. Austerer, S. Schartner, M. Nobile, L. K. Hoffmann, W. Schrenk, G. Strasser, M. P. Semtsiv, I. Bayrakli, M. Wienold, and W. T. Masselink, 'Impact of doping on the performance of short-wavelength InP-based quantum-cascade lasers' Journal of Applied Physics **103**, 033104 (2008).

[289] J. Faist, F. Capasso, C. Sirtori, D. L. Sivco, A. L. Hutchinson, S. N. G. Chu, and A. Y. Cho, 'Narrowing of the intersubband electroluminescent spectrum in coupled-quantum-well heterostructures' Applied Physics Letters **65**, 94 (1994).

[290] A. Straub, T. S. Mosely, C. Gmachl, R. Colombelli, M. Troccoli, F. Capasso, D. L. Sivco, and A. Y. Cho, 'Threshold reduction in quantum cascade lasers with partially undoped, dual-wavelength interdigitated cascades' Appl. Phys. Lett. **80**, 2845 (2002).

[291] P. M. Bouzi, Y. T. Chiu, C. Deutsch, Y. Dikmelik, Y. Song, V. Tokranov, S. Oktyabrsky, and C. Gmachl, 'Importance of growth direction in mid-infrared quantum cascade lasers' Journal of Applied Physics **116**, 034504 (2014).

[292] G. Hałdaś, A. Kolek, D. Pierścińska, P. Gutowski, K. Pierściński, M. Bugajski, 'Tuning quantum cascade laser wavelength by the injector doping' Applied Physics B **124**, 144 (2018).

[293] E. B. Dupont, D. Delacourt, D. Papillon, J. P. Schnell, and M. Papuchon, 'Influence of ionized impurities on the linewidth of intersubband transitions in GaAs/GaAlAs quantum wells' Applied Physics Letters **60**, 2121 (1992).

[294] H. Challebaut, S. Kumar, B. S. Williams, and Q. Hu, 'Importance of electron-impurity scattering for electron transport in terahertz quantum-cascade lasers' Applied Physics Letters **84**, 645 (2004).

[295] H. C. Liu, M. Wächter, D. Ban, Z. R. Wasilewski, M. Buchanan, G. C. Aers, J. C. Cao, S. L. Feng, B. S. Williams, and Q. Hu, 'Effect of doping concentration on the performance of terahertz quantum-cascade lasers' Appl. Phys. Lett. **87**, 141102 (2005).

[296] L. Ajili, G. Scalari, M. Giovannini, N. Hoyler, and J. Faist, 'Doping in quantum cascade lasers. II.

$GaAs/Al_{0.15}Ga_{0.85}As$ terahertz devices' Journal of Applied Physics **100**, 043102 (2006).

[297] A. Benz, G. Fasching, A. M. Andrews, M. Martl, K. Unterrainer, T. Roch, W. Schrenk, S. Golka, and G. Strasser, 'Influence of doping on the performance of terahertz quantum-cascade lasers' Applied Physics Letters **90**, 101107 (2007).

[298] A. M. Andrews, A. Benz, C. Deutsch, G. Fasching, K. Unterrainer, P. Klang, W. Schrenk, and G. Strasser, 'Doping dependence of LO-phonon depletion scheme THz quantum-cascade lasers' Material Science and Engineering B **147**, 152 (2008).

[299] C. W. I. Chan, A. Albo, Q. Hu, and J. L. Reno, 'Tradeoffs between oscillator strength and lifetime in terahertz quantum cascade lasers' Applied Physics Letters **109**, 201104 (2016).

[300] T. Grange, 'Doping engineering in THz QCLs' *Proceeding of the 14th Infrared Terahertz Quantum Workshop*, Marina Bay Sands, Singapore, 10-17 September (2017).

[301] Kai Xie (Cathy) Wang (Laboratory report, 2018).

[302] C. Deutsch, H. Detz, M. Krall, M. Brandstetter, T. Zederbauer, A. M. Andrews, W. Schrenk, G. Strasser, and K. Unterrainer, 'Dopant migration effects in terahertz quantum cascade lasers' Applied Physics Letters **102**, 201102 (2013).

[303] T.-T. Lin, L. Wang, K. Wang, T. Grange, S. Birner, T. Miyoshi and H. Hirayama, 'Increase in the output power from a terahertz quantum cascade laser due to high doping concentrations with strong band bending' Journal of Applied Physis on press (2022).

[304] M. Giehler, H. Kostial, R. Hey, and H. T. Grahn, 'Effect of free-carrier absorption on the threshold current density of GaAs/(Al,Ga)As quantum-cascade lasers' Journal of Applied Physics **96**, 4755 (2004).

[305] F. Carosella, C. Ndebeka-Bandou, R. Ferreira, E. Dupont, K. Unterrainer, G. Strasser, A. Wacker, and G. Bastard, 'Free-carrier absorption in quantum cascade structures' Physical Review B **85**, 085310 (2012).

[306] C. S. Baird, M. D. Lafferty, 'Analysis of approximations used in terahertz quantum cascade laser doping calculations' Proceedings of SPIE 10917 (2019).

[307] C. Sirtori, F. Capasso, J. Faist, A. L. Hutchinson, D. L. Sivco, and A. Y. Cho, 'Resonant tunneling in quantum cascade lasers' IEEE Journal of Quantum Electronics **34**, 9 (1998).

[308] C. Gmachl, F. Capasso, D. L. Sivco, and A. Y. Cho, 'Recent progress in quantum cascade lasers and applications' Report on Progress in Physics **64**, 11, 1533, (2001).

[309] A. Demić, Z. Ikonić, P. Dean, and D. Indjin, 'Dual resonance phonon–photon–phonon terahertz quantum-cascade laser: physics of the electron transport and temperature performance optimization' Optics Express **28**, 26, 38788 (2020).

[310] L. Wang, T.-T. Lin, K. Wang, T. Grange, S. Birner, and H. Hirayama, 'Short-period scattering-assisted terahertz quantum cascade lasers operating at high temperatures' Scientific Reports **9**, 9446 (2019).

[311] M. Wienold, L. Schrottke, M. Giehler, R. Hey, W. Anders, and H. T. Grahn, 'Low-threshold terahertz quantum-cascade lasers based on $GaAs/Al_{0.25}Ga_{0.75}As$ heterostructures' Applied Physics Letters **97**, 071113 (2010).

[312] Tsung-Tse Lin, Leiying Ying, and Hideki Hirayama, 'Threshold Current Density Reduction by Utilizing High-Al-Composition Barriers in 3.7THz $GaAs/Al_xGa_{1-x}As$ Quantum Cascade Lasers' Applied Physics Express **5**, 012101 (2012).

[313] Chun Wang I. Chan, Qing Hu, and John L. Reno, 'Tall-barrier terahertz quantum cascade lasers' Applied Physic Letters **103**, 151117 (2013).

[314] L. Schrottke, X. Lü, G. Rozas, K. Biermann, and H. T. Grahn, 'Terahertz GaAs/AlAs quantum-cascade lasers' Applied Physics Letters **108**, 102102 (2016).

[315] Asaf Albo and Yuri V. Flores, 'Carrie Leakage Dynamics in Terahertz Quantum Cascade Lasers' IEEE Journal of Quantum Electronics **53**, 5 (2017).

[316] Martin Alexander Kainz, Sebastian Schönhuber, Aaron Maxwell Andrews, Hermann Detz, Benedikt Limbacher, Gottfried Strasser, and Karl Unterrainer, 'Barrie Height Tuning of Terahertz Quantum Cascade Lasers for High-Temperature Operation' ACS Photonics **5**, 4687 (2018).

[317] Teppei Miyoshi, and Dayan Ban, 'Erratum: "Barrier height study of two-well resonant-phonon terahertz quantum cascade lasers. I. The third-order tunneling current theory" [J. Appl. Phys. 130 183103 (2021)' Journal of Applied Physics 131, 249901 (2022).

[318] Saeed Fathololoumi, 'Terahertz Quantum Cascade Lasers: towards high performance operation' a dissertation in the University of Waterloo (2010).

[319] Z. Y. Han, S. F. Yoon, K. Radhakrishnan, and D. H. Zhang, 'High-field domain formation in GaAs/AlGaAs superlattices' Applied Physics Letter **66**, 9 (1995).

[320] Rudra Sankar Dhar, Seyed Ghasem Razavipour, Emmanuel Dupont, Chao Xu, Sylvain Laframboise, Zbig Wasilewski, Qing Hu, and Dayan Ban, 'Direct Nanoscale Imaging of Evolving Electric Field

Domains in Quantum Structures' Scientific Reports **4**, 7183 (2014).

[321] B. F. Levine, C. G. Bethea, G. Hasnain, V. O. Shen, E. Pelve, R. R. Abbott, and S. J. Hsieh, 'High sensitivity low dark current 10μm GaAs quantum well infrared photodetectors' Applied Physics Letter **56**, 9 (1990).